

THÈSE

présentée par

Mathieu Blanchard

pour l'obtention du

GRADE de DOCTEUR

Formation doctorale : Mécanique

Laboratoires d'accueil : LadHyX du CNRS
et de l'École polytechnique,
Laboratoire d'Énergétique Moléculaire
et Macroscopique, Combustion (EM2C)
du CNRS et de l'ECP

Linear and nonlinear dynamics of laminar premixed flames submitted to flow oscillations

Soutenue le 9 décembre 2015

Jury : Mme Morgans A. S. Rapporteur
M Nicoud F. Rapporteur
M Huerre P. Examineur
M Schmid P. J. Directeur de thèse
M Schuller T. Co-Directeur
M Sipp D. Co-Directeur

Remerciements

De nombreuses personnes ont contribué à la réussite de ce projet ; la liste en sera nécessairement incomplète, mais je tenais néanmoins à exprimer ces quelques remerciements.

Merci à Peter, pour avoir accepté d'assumer le rôle de directeur de thèse, et pour son soutien constant. Merci à Thierry d'en avoir assuré l'encadrement au quotidien, au travers des moments simples mais aussi des plus compliqués. Merci également à Denis pour ses avis toujours avisés.

Merci ensuite à Aimee Morgans, Franck Nicoud et Patrick Huerre pour avoir accepté de prendre part à mon jury.

Merci également à Daniel Durox et Olivier Giquel pour m'avoir accueilli à l'EM2C. Merci à Lutz Lesshaft et Camille Duprat pour leurs conseils et les discussions que nous avons pu partager. Merci à Daniel Guy, Toai Vu, Sébastien Turgis et Matthieu Boileau sans qui le travail en simulation numérique ne serait pas possible.

Merci à ma chère Clémence, de m'avoir soutenu - et supporté! - durant ces trois années. Merci également à nos deux familles pour leur soutien constant, inconditionnel et bien entendu parfaitement objectif.

Enfin, merci aux doctorants et post-doc qui ont su, jour après jour, apporter bonne humeur, expériences improbables et parfois science tout cours dans nos recherches et pauses café. En particulier, merci à Miguel, Nicolas et Fabien pour m'avoir accueilli dans l'équipe. Merci à Eunok pour sa bonne humeur inoxydable ; à Gaétan pour sa capacité à dévoiler la subtilité et l'intérêt scientifique cachés dans nos quotidiens ; à Marine pour sa chaleur humaine pleine de compassion et d'objectivité; et enfin à Nancy pour montrer qu'humour et professionnalisme sont des valeurs trans-frontalières. Finalement, je citerais volontiers Xavier, Océane, Manu (les deux), Timothée, ... (au Ladhyx) et Pedro, Benjamin, Antoine, Wenjie,... (à l'EM2C) en leur adressant de chaleureux remerciements accompagnés de mon amitié.

Abstract

Self-sustained thermoacoustic oscillations cause recurrent problems in numerous combustion systems. These instabilities, which couple the reacting flow dynamics and the system acoustics, remain difficult to predict at the design stage of a combustor. The response of flames to flow oscillations is central to obtain an accurate description of this closed loop. The objective for this thesis is to develop new numerical tools capable of providing a better understanding of the flame dynamics. The first tool relies on the linearisation of a Direct Numerical Simulation (DNS) solver of the Navier-Stokes equations. An initially non-reactive, axisymmetric compressible code has been adapted to compute laminar premixed flames. A steady solution is first computed by solving the full non-linear Navier Stokes equations. The flame response to small flow oscillations is then determined by the linearised DNS solver (L-DNS). The results of these simulations unveil the mechanisms controlling the response of a conical flame and an M-flame to incoming flow disturbances. Linear algebra techniques were employed to get detailed insight into the flame dynamics at small amplitudes. In these linear computations, each physical mechanism corresponds to a distinct linear operator. An impact of a specific mechanism can then be isolated by simply adding or subtracting the corresponding matrices. The hydrodynamical modes stemming from the interaction of the flame with acoustic waves were thus analysed. It has been shown that the strong temperature gradient across the flame front is responsible for the creation of an upstream velocity mode. This result has been obtained by a direct evaluation of the response of an M-flame to an acoustic impulse. These data were then used to determine the unsteady heat release rate and the flame transfer function. The results were validated with experimental results. A method to convert an impulse response to an accurate low-order state-space representation has also been developed. An eigenvalue problem has then been solved to maximize the flame linear acoustic levels. These results inspired the development of a 1-D axisymmetric model of the flame response. The respective contributions of heat release rate and vorticity to acoustics in a near-field domain have been estimated quantitatively. These simulations highlighted the importance of vorticity-induced dipolar sources in the close-range acoustic field. The insight gained from this analysis at small perturbation levels allows us to tackle the more challenging issue of non-linear effects. A second flow solver based on a level-set description of the flame front has been developed for Graphic Processing Units (GPUs). This Navier-Stokes solver includes an original model for the effect of heat release on the gas dynamics. It relies on GPUs to allow a determination of the flame impulse response and flame transfer function at a reasonable CPU cost. This methodology allows a quick determination of the flame response to any finite-amplitude forcing. This new code has then been validated with experiments conducted on a methane-air conical flame. Two system identification algorithms have been tested on this configuration. These results highlight the need for a proper modelling of the bifurcated flow dynamics, especially at low forcing levels. The tools presented throughout this project have proven valuable at unveiling important aspects on the linear flame dynamics. The analysis of nonlinearities offers interesting perspectives for future work, with the overall objective of predicting the growth rates and the limit-cycle amplitudes of thermoacoustic instabilities, and eventually of their control.

Résumé

Les oscillations thermoacoustiques sont la source de problèmes récurrents dans de nombreux systèmes de combustion. Ces instabilités restent difficiles à prédire au cours de la conception du moteur. Améliorer la description de la réponse des flammes aux oscillations de l'écoulement est essentiel pour mieux décrire cette amplification acoustique. L'objectif de cette thèse est de développer des méthodes numériques permettant d'approfondir notre compréhension de la dynamique de flamme. Le premier outil envisagé est basé sur la linéarisation d'un solveur des équations de Navier et Stokes par Simulation Numérique Directe (DNS). Un code axisymétrique, compressible, non réactif a été adapté pour simuler des flammes prémélangées, laminaires. Une solution stationnaire des équations de Navier et Stokes non-linéaires est d'abord calculée. La réponse de la flamme à de petites oscillations est ensuite déterminée à l'aide d'un solveur DNS Linéarisé (L-DNS). Ces résultats permettent d'identifier les mécanismes contrôlant la réponse d'une flamme conique et d'une flamme en M à des perturbations incidentes. Des éléments d'algèbre linéaire ont été mis en oeuvre pour obtenir une description détaillée de la dynamique de flamme à faible amplitude. Dans ces simulations, chaque phénomène physique correspond à un opérateur linéaire distinct. Un mécanisme précis peut être isolé en ajoutant ou en soustrayant les différentes matrices correspondantes. Les modes hydrodynamiques résultant de l'interaction de la flamme avec des ondes acoustiques ont ainsi été analysés. Il a été montré que le gradient de température élevé présent au travers de la flamme est responsable de la création d'une perturbation de vitesse dans le mélange réactif. Ce résultat a été obtenu par une évaluation directe de la réponse d'une flamme en M à une impulsion acoustique. Ces données ont ensuite été utilisées pour déterminer le taux de dégagement de chaleur instationnaire et la fonction de transfert de flamme. Une méthode permettant de convertir la réponse impulsionnelle vers un espace d'états d'ordre faible mais précis a été développée. Un problème aux valeurs propres a ensuite été résolu de manière à maximiser les niveaux acoustiques rayonnés par la flamme. Ces résultats ont inspiré le développement d'une modélisation 1-D de la réponse de flamme. Une estimation quantitative des contributions respectives du taux de dégagement de chaleur et de la vorticit  au champ acoustique proche a été menée. Ces simulations ont mis en  vidence l'importance des sources dipolaires induites par la vorticit  sur le champ proche acoustique. Les m canismes r v l s par ces analyses   faible niveau d'amplitude sont ensuite mod lis s afin d' tudier les effets non-lin aires correspondants. Un second solveur incluant une description de la flamme comme un iso-niveau d'une fonction a ainsi  t  d velopp  sur carte graphique (GPU). Ce solveur Navier-Stokes inclut un mod le traitant l'influence du d gagement de chaleur sur l' coulement par une approche innovante. Il s'appuie sur la technologie GPU pour  valuer la r ponse impulsionnelle de flamme et sa fonction de transfert   un coup CPU raisonnable. Cette m thode permet une d termination rapide de la r ponse de la flamme   n'importe quel for age d'amplitude finie. Ce nouveau code a ensuite  t  valid  avec des donn es exp rimentales obtenues pour des flammes m thane-air. Deux techniques d'identification de syst me ont  t  test es sur cette configuration. Ces r sultats soulignent le besoin de m thodes de mod lisation adapt es   la dynamique des  coulements bifurqu s, particuli rement pour des niveaux de for age faibles. Les outils pr sent s dans ce manuscrit se sont montr s particuli rement efficaces   d voiler des aspects importants de la dynamique lin aire des flammes. L'analyse des non-lin arit s ouvre des perspectives int ressantes pour de futurs travaux, afin de pr dire les taux de croissance et les cycles-limites d'instabilit s thermo-acoustiques, et de finalement les contr ler.

Contents

Abstract	v
Résumé	vii
Introduction	1
1 Flames and Sound	1
2 Non-reactive Dynamics	4
2.1 Non-Reactive Hydrodynamic Instabilities	4
2.2 Resolvent Operator	5
2.3 Acoustic Waves in Instabilities: from Local to Global	5
3 Flame Instabilities	7
3.1 Flame Local Instabilities	7
3.2 Thermoacoustics of Finite Dimension Flames	8
3.3 Hydrodynamics of Flames	10
4 Flames Stabilized on an Annular Burner	14
5 Thesis Objectives	15
1 Governing Equations and Numerical Methods	17
1.1 Governing Equations	17
1.1.1 Assumptions	17
1.1.2 Detailed Equations	18
1.1.3 Code Presentation	22
1.1.3.1 Computation of Space Derivatives	22
1.1.3.2 Time Integration of Chemistry	25
1.1.3.3 Parallelism in CNS2D	26
1.1.4 Linear Algebra Algorithms	28
1.1.4.1 Creating the Linear and Adjoint Operators	28
1.1.4.2 Optimizing the System's Linear Frequency Response	28
1.1.4.3 Derivative of the Eigenvalue of the Optimal Frequency Response	30
1.2 Geometry and Baseflow	31
1.2.1 Geometry Presentation	31
1.2.2 Baseflow	33
1.2.3 Acoustic Sources	34
1.3 Conclusion	36
2 Linear Acoustic Forcing	37
2.1 Motivation	37

2.2	Article: Response Analysis of a Laminar Premixed M-Flame to Flow Perturbations	38
2.3	Going Further with Linear Results	78
2.3.1	State Space Identification Algorithm Layout	80
2.3.2	Detailed Description of the Wavelets Used	80
2.3.3	Detailed Description of the Algorithm	81
2.3.4	Validation Test Case	82
2.4	Conclusion	84
3	Optimal Linear Acoustic Generation	87
3.1	Motivation	87
3.2	Optimal Forcing of the M-flame	88
3.2.1	Presentation of the Optimization Procedure	88
3.2.2	Full Field Approach	90
3.2.3	Pressure Optimization Approach	93
3.3	Article: Pressure waves generation from perturbed premixed flames	96
3.4	From near-field to far-field combustion noise	110
3.5	Conclusion	114
4	Heating Effects with a G-Equation	115
4.1	Motivation	115
4.2	Governing Equations	116
4.2.1	Flow Equations	116
4.2.2	Boundary Conditions	117
4.2.3	Flame Region	120
4.3	Implementation on GPU	122
4.3.1	Algorithm Structure	122
4.3.2	Poisson Solver	124
4.4	Non-Linear Acoustic Forcing of a Conical Flame	127
4.4.1	Harmonic Forcing	129
4.4.2	Impulse Response Identification	136
4.4.2.1	ARMarkov Algorithm	136
4.4.2.2	Wiener-filtered impulse response	136
4.4.2.3	Impulse Response Estimate of a Conical Flame: the Problem of Flame Instabilities.	137
4.5	Conclusion	143
	Conclusion	145
	References	160

List of Figures

1	Typical 1-D flame structures with temperature profiles for a) a premixed flame and b) a diffusion flame.	2
2	Superposition of three images of luminous emission of flame front just before, during and just after formation of a tulip flame. From Clanet & Searby, 1996.	3
3	Sketch of a typical impulse response: (a) absolutely unstable flow; (b) convectively unstable flow. The parameter σ denotes the local growth rate of the instability. From Huerre & Monkewitz [1985].	4
4	Evolution of an upward propagating flame front with a Darrieus-Landau instability. Red: flame front. Arrows: Lagrangian displacement of the flame front. On the last position, a cusp is observed.	7
5	Schlieren images of a premixed methane-air flame, acoustically forced. The equivalence ratio is 0.95, the injection velocity is 0.96 m.s^{-1} . Top: steady conical flame. Modulation frequency: 25 Hz (middle), 75 Hz (bottom). Images of the perturbed flame are in phase opposition. From Ducruix <i>et al.</i> [2000].	11
6	Schematic presentation of flame pinching.	12
7	Dilatation field of a numerical flame, pinching at $Le = 1$. From Talei <i>et al.</i> [2013].	13
8	Schematic presentation of flame roll-up.	13
9	Sketch of the annular injector used as a reference with an M-flame attached.	14
10	Flames stabilized on an annular burner. a: conical flame; b: V-flame; c: M-flame. Images from [Schuller <i>et al.</i> , 2003a].	15
11	M-flame forced acoustically at high amplitude, at four different times of the acoustic cycle. Images from [Schuller <i>et al.</i> , 2003a].	15
1.1	Sketch of the annular configuration considered.	18
1.2	Comparison between dispersion relations of some differentiation operators. Dashed curve: optimal result based on Fourier transform. Black: centered finite difference. (1): order 2, (2): order 6, (3): order 10. Blue (4): 11-points stencil used in CNS2D. Red (5): Compact difference scheme CULD.	24
1.3	Gain of the filter used to damp non-resolved wavelengths.	25
1.4	Mesh distribution on processors. Gray areas are ghost cells.	27
1.5	Numerical Geometry used in CNS2D simulations. Top: reference case computed. Bottom: corresponding numerical implementation.	32
1.6	Typical M-flame mesh used in chapter 2, coarsened four times in each direction. The shaded regions are treated as non-slipping walls.	33
1.7	Chapter 2 M-flame baseflow temperature profile.	34

1.8	Acoustic forcing shapes in axial velocity (right) and total energy (left). Continuous black line: reference acoustic wave, computed with a linear simulation. Point-dotted blue line: linear acoustic forcing shape. Dotted red line: non-linear acoustic forcing shape.	36
2.1	Linear heat release rate response to an acoustic impulse for an M-flame. . .	79
2.2	Real part of a Morlet wavelet, $\sigma=5$	80
2.3	Impulse Response to State Space Algorithm. Continuous black arrows: pre-processing steps. Red arrows: identification steps. Dotted black arrows: post-processing steps.	83
2.4	Comparison of the initial signal and the reconstructed impulse response using our algorithm, with an order $k' = 40$. The 2-norm error is of 4%. Black: initial signal. Dotted red: reconstructed signal.	84
3.1	Setup of the optimal forcing computations. Top: full field optimization. Bottom: pressure optimization.	89
3.2	Optimal forcing shapes for a full field maximization, $\omega = 3$, presented in (r,z) coordinates.	91
3.3	Optimal forcing shapes for a full field maximization, $\omega = 10.125$, presented in (r,z) coordinates.	92
3.4	Optimal forcing eigenvalues for a full field optimization.	93
3.5	Comparison of the pressure and density outputs at $\omega = 3$ for an optimal (top) and an acoustic (bottom) forcing.	94
3.6	Comparison of the pressure and density outputs at $\omega = 10.125$ for an optimal (top) and an acoustic (bottom) forcing.	95
3.7	Optimal forcing shapes for the pressure maximization, $\omega = 3$, presented in (r,z) coordinates.	97
3.8	Optimal forcing pressure and heat release rate output for a pressure-optimized forcing at $\omega = 3$, presented in (r,z) coordinates.	98
3.9	Optimal forcing pressure and heat release rate output for a pressure-optimized forcing at $\omega = 10.125$, presented in (r,z) coordinates.	99
3.10	Values of $\tilde{\lambda}$ for: black cross, full field optimization; red circle, pressure optimization.	99
3.11	p_2 values, computed for pressure fields from full field optimization (left) and pressure optimization (right), at $\omega = 3$	111
3.12	p_3 values, computed for $\omega = 3$ (top) and $\omega = 10.125$ (bottom).	112
3.13	Left: masked pressure field. Right: vorticity. All field results from optimization procedures at $\omega = 3$	113
4.1	Set-up used for a weakly confined axisymmetric flame. α is defined as the half cone angle of the flame.	118
4.2	Boundary conditions implemented, along with the indicative position of the flame (in red). Boundary conditions on the sides of the domain (black lines) are implemented with ghost nodes. Inner walls non-slip boundary conditions are implemented with immersed boundary conditions.	119
4.3	Local mesh in the vicinity of a wall. Grey: wall. Blue dots: wall nodes. Red circles: interior wall points.	120

4.4	Interpolation of sources from the flame front to the mesh. Black lines: initial mesh. Red line: Flame Front. Blue dots: mesh compressible vorticity or dilatation sources. Red circles: flame front compressible vorticity or dilatation sources. Arrows: linear interpolation from flame front to mesh sources. . . .	121
4.5	Main integration loop. Blue arrows: initialization. Red: internal convergence procedure.	123
4.6	CPU/GPU memory structure.	125
4.7	V-cycle multigrid method for a 1D-problem. Blue arrows: restriction step. Red arrows: expanding step. Black points: interior nodes. Grey points: ghost nodes. Descending operations are described on the left, ascending operations on the right. Relaxation using an SOR algorithm is performed before restrictions, after expansions and at the coarsest level.	126
4.8	Red-Black ordering for over-relaxed Gauss-Seidel operations.	128
4.9	Longitudinal velocity (top left), radial velocity (top right) and streamlines (bottom left) of the flame harmonically forced of flame (a). $v_{bulk} = 0.89$ m.s ⁻¹ , $S_L = 0.28$ m.s ⁻¹ , $\mathcal{L} = 5.10^{-4}$ m. Bottom right: corresponding experimental flame configuration from Cuquel et al. [2013b] , $v_{bulk} = 0.89$ m.s ⁻¹ , $\phi = 0.86$	130
4.10	Comparison of numerical (left) and experimental (right) flames forced at a rms level $v'/v_{bulk} = 10\%$, with $v_{bulk} = 0.89$ m.s ⁻¹ . Left: $S_L = 0.28$ m.s ⁻¹ , $\mathcal{L} = 5.10^{-4}$ m. Color is based on local flame velocity, scaled between 0.2 and 0.93 m.s ⁻¹ . Axisymmetry is enforced to generate 3D visualizations. Right: methane-air flame, $v_{bulk} = 0.89$ m.s ⁻¹ , $\phi = 0.86$. White lines indicate the solid walls location.	132
4.11	Comparison of numerical (crosses) and experimental (triangles) flame transfer function , with $v_{bulk} = 0.89$ m.s ⁻¹ . Numerical parameters: $S_L = 0.28$ m.s ⁻¹ , $\mathcal{L} = 5.10^{-4}$ m, flame is forced at 10 %. Experiment: methane-air flame, $v_{bulk} = 0.89$ m.s ⁻¹ , $\phi = 0.86$	133
4.12	Phase of the principal longitudinal velocity mode on the axis of symmetry upstream the flame, rescaled with forcing frequency at a rms level $v'/v_{bulk} = 10\%$. a): 20 Hz, b): 40 Hz, c): 55 Hz, d): 80Hz, e): 200Hz. $x = 0.02$ m corresponds to the injector exit plane. In this computation, the average position of the flame tip is at $x = 0.05$ m.	134
4.13	Phase of the principal longitudinal velocity mode on the axis of symmetry upstream the flame, rescaled with forcing frequency at a rms level $v'/v_{bulk} = 10\%$. a): 20 Hz, b): 40 Hz, c): 55 Hz, d): 80Hz, e): 200Hz. $x = 0.02$ m corresponds to the injector exit plane. In this computation, the average position of the flame tip is at $x = 0.05$ m.	135
4.14	Results of both system identification techniques for an over-damped flame. $v_{bulk} = 0.89$ m.s ⁻¹ , $S_L = 0.28$ m.s ⁻¹ , $\mathcal{L} = 9.10^{-4}$ m. Dotted black: output from the ARMarkov algorithm, n=2000, $\mu = 40$. Red: output from the Wiener Filter, n=2000.	138
4.15	Longitudinal and radial velocity of flame (b). $v_{bulk} = 1.56$ m.s ⁻¹ , $S_L = 0.41$ m.s ⁻¹ , $\mathcal{L} = 5.10^{-4}$ m.	139
4.16	Results of both system identification techniques for an over-damped flame. $v_{bulk} = 1.56$ m.s ⁻¹ , $S_L = 0.41$ m.s ⁻¹ , $\mathcal{L} = 5.10^{-4}$ m. Dotted black: output from the ARMarkov algorithm, n=2000, $\mu = 40$. Red: output from the Wiener Filter, n=2000.	140

- 4.17 Flame Transfer Function obtained from discrete harmonic forcing of a methane-air flame at $\phi = 1.03$, $v_{bulk} = 1.56 \text{ m.s}^{-1}$. Data from [Cuquel \[2013\]](#). 141
- 4.18 Flame Transfer Function obtained from discrete harmonic forcing of a methane-air flame at $\phi = 1.03$, $v_{bulk} = 1.56 \text{ m.s}^{-1}$. Data from [Cuquel \[2013\]](#). 142

Introduction

1 Flames and Sound

What is a flame? This question, as simple as it may look, actually hides a very wide range of possible configurations. Flames are ubiquitous in industrial systems: rockets, plane and car engines, power plants, ... The potential combination of fuels, oxidizers, injection technologies, combustion chamber's dimensions makes each system quite unique: a large number of parameters is involved, and a mere choice of the Reynolds number, for instance, does not allow to retrieve similarity properties. However, some physical characteristics are common to all flames. This allows a first definition of a flame as a thermal layer, dominated by diffusion, and characterized by a strong temperature gradient induced by a localized exothermic reaction layer. This definition does not describe all the complexity of flames, and in particular does not allow to understand its chemistry. However, it is retained here to describe the coupling between heat release, acoustics and the flow. More detailed definitions of flames can be found in textbooks such as [Zeldovich *et al.* \[1985\]](#); [Williams \[1985a\]](#).

Three ingredients are necessary to generate a flame: a fuel, an oxidizer and some heating. Modern combustion regulations focus on the reduction of pollutant emissions, especially NOx and soot particles. For instance, European rules strengthen every three to four years [[Parliament & of the European Union, 2007](#)]. In order to achieve such performances, it is necessary to keep flame temperatures in an optimal range [[Böhm *et al.*, 1989](#); [Lewis & Elbe, 2012](#)]. One of the keys to achieve this objective is the control of mixing of fuel and oxidizer [[Nathan *et al.*, 2006](#)]. Flames are then traditionally separated between premixed and diffusion flames, with most flames being in fact partially premixed [[Poinot & Veynante, 2012](#)].

In the case of premixed flames, such as sketched in figure 1 (b), fuel and oxidizer are mixed before being burnt. The temperature increase in a thermal diffusion layer then triggers the chemical reaction. In figure 1, T_0 is the cold gas temperature, T_b is the burnt gas temperature, and x is the normal space coordinate through the flame. In contrast, in diffusion flames, oxidizer and fuel are initially separated, injected at potentially different temperatures T_{ox} and T_f , and mixed while burning, as sketched in figure 1 (a). Such flames are associated with locally high temperatures, on the order of the adiabatic flame temperature T_{ad} of a stoichiometric mixture, which is usually larger than the burnt gas temperature T_b observed in premixed systems operating with an excess of oxidizer. Modern combustion technologies are designed to operate with an excess of oxidizer, also referred to as 'lean combustion mode', in order to reduce flame temperature and to save fuel [[Lefebvre, 1998](#)]. A detailed analysis of flame structures and combustion equations can be found in

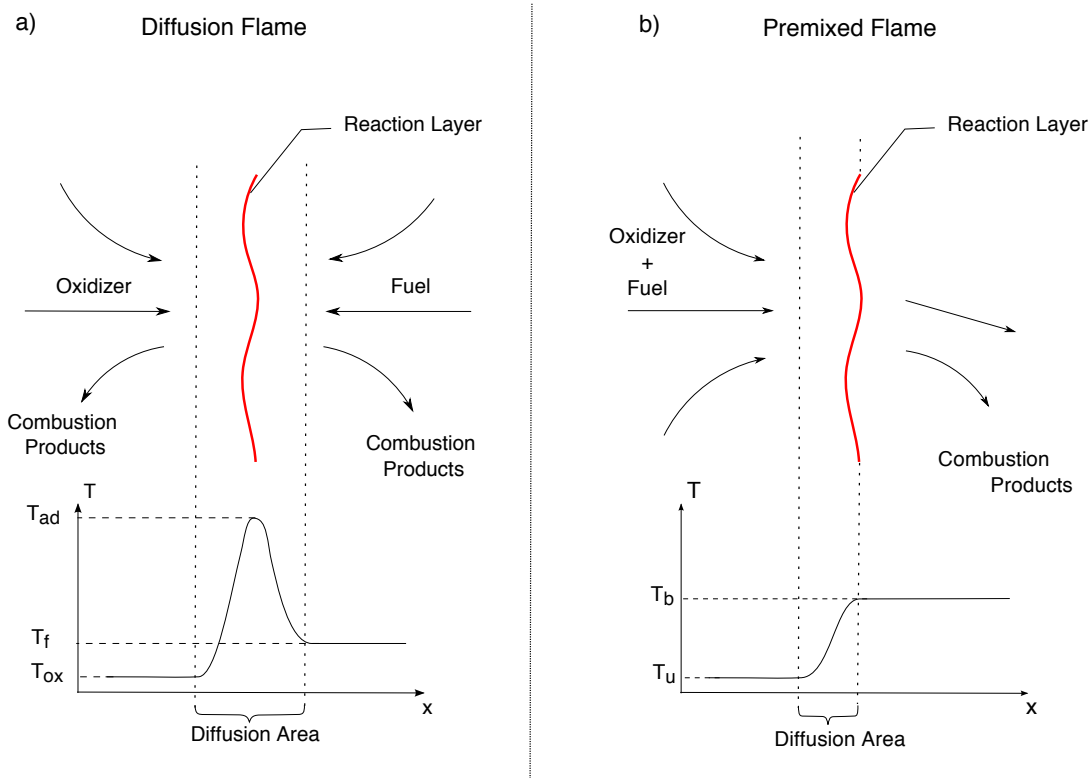


Figure 1: Typical 1-D flame structures with temperature profiles for a) a premixed flame and b) a diffusion flame.

Zeldovich *et al.* [1985], Williams [1985b] and Poinot & Veynante [2012].

The main advantage of diffusion flames over premixed flames is safety. Premixing creates a highly flammable mixture, which is dangerous to store and to manipulate. However, in view of increasingly ambitious ecological objectives, the premixed combustion mode has seen a strong interest during the last decades. This work will also focus on premixed flames.

For aeronautical or power generation engines, once performance and pollutant emissions are set, the next major issue is associated with the transient dynamics occurring during ignition and extinction phases, or with structural vibrations and sound emissions appearing during steady operations [Candel, 2002]. Again, regulations limit noise generation for engines. But this issue goes deeper. Very early, the presence of a localized heat source in a tube was observed to lead to acoustic oscillations of large amplitudes. The ‘Rijke tube’ [Rijke, 1859] is also one of the simplest thermoacoustically unstable system. The same principle can be used as a base for a musical instrument, the ‘flame organ’ or pyrophone. But in high performance engines, energy densities are so large that thermoacoustic instabilities can be destructive as well [Lieuwen & Yang, 2005]. The experiment of a planar flame propagating in a tube [Kaskan, 1953; Clavin *et al.*, 1990; Clanet & Searby, 1996] exemplifies this issue. The experimental set-up is rather simple: a planar premixed flame travels downstream in a half-open tube, closed at the bottom. During the process, a succession of very strong thermoacoustic instabilities occurs. The flame front becomes strongly deformed, as presented in figure 2, which generates large noise emissions.

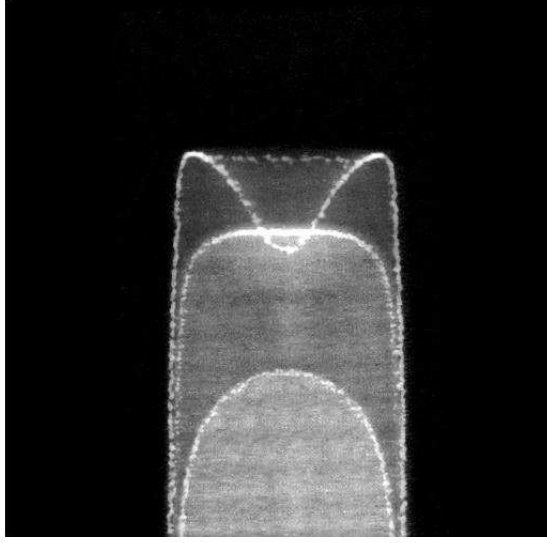


Figure 2: Superposition of three images of luminous emission of flame front just before, during and just after formation of a tulip flame. From Clanet & Searby, 1996.

Such high acoustic amplitudes endanger the structural integrity of an engine. Their occurrences also needs to be understood and predicted. A first insight is gained through the analysis of Lighthill's equations for acoustics [Lighthill, 1952]. A close examination of these equations in the context of flames shows that the dominant acoustic source term is associated with the unsteady heat release rate [Strahle, 1971]. In particular, the local flame-induced noise can be approximated by [Crighton *et al.*, 1992; Candel *et al.*, 2009]:

$$p_{ac}(t) = \frac{\partial}{\partial t} \int_{\Omega} \frac{(\gamma - 1)}{4\pi r' c_0^2} \dot{q} \left(r', t - \frac{r'}{c_0} \right) d\Omega(r'). \quad (1)$$

where p_{ac} is the acoustic pressure, r' is the distance between the source and the measurement point, c_0 is the speed of sound, γ is the ratio of specific heats, \dot{q} is the volumetric heat release rate with an integral carried out over the flame volume Ω . This relation between heat release and sound can then be used to derive a stability criterion. This was first understood by Rayleigh [1878] who derived the so-called Rayleigh criterion. If a system oscillates at an angular frequency ω , then a thermo-acoustic instability may be triggered, if

$$\int_0^{2\pi/\omega} p_{ac} \dot{q} dt > 0. \quad (2)$$

This equation proved quite useful at analyzing thermoacoustic systems [Nicoud & Poinot, 2005; Brear *et al.*, 2012]. However, this criteria provides only a very general context for thermoacoustic instabilities. In order to analyze practical cases, a more detailed review of flow instabilities is required.

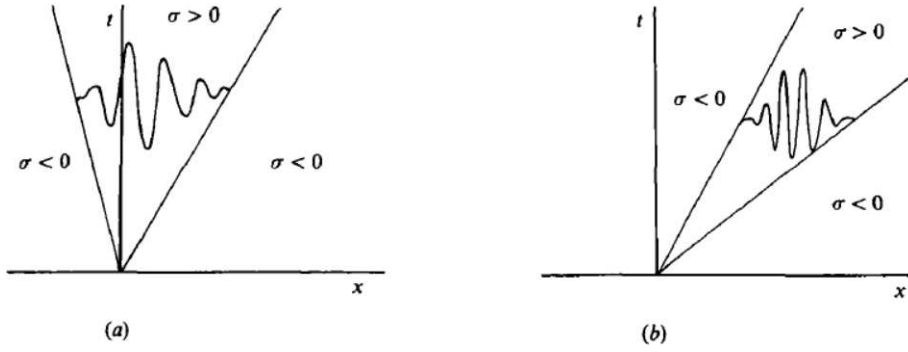


Figure 3: Sketch of a typical impulse response: (a) absolutely unstable flow; (b) convectively unstable flow. The parameter σ denotes the local growth rate of the instability. From [Huerre & Monkewitz \[1985\]](#).

2 Non-reactive Dynamics

2.1 Non-Reactive Hydrodynamic Instabilities

There exists a vast body of literature about flow instabilities (see [Joseph \[1976\]](#); [Michalke \[1984\]](#); [Schmid & Henningson \[2001\]](#)). A good starting point is linear stability analysis. Assuming that a flow is linearly unstable, two categories of instabilities can be distinguished within a local framework. If the disturbances grow in time while remaining at the same position in space, the instability is ‘absolute’. If the disturbances grow in time while propagating in space, the instability is ‘convective’. This difference is shown in figure 3 and was treated theoretically by [Huerre & Monkewitz \[1985\]](#) for shear layers. The advantage of this local analysis is the possibility to derive the growth rate and the wavenumber of the instability. Flow configurations such as shear layers [[Huerre & Monkewitz, 1985](#)], boundary layer [[Klebanoff *et al.*, 1962](#)] or jets [[Monkewitz & Sohn, 1988](#)] have been studied with such techniques.

However, this approach fails to represent more complex situations, and, instead, a global approach is required. Indeed, while absolute instabilities automatically induce an in-place growth of local perturbations, convectively unstable flows depend on a feedback phenomenon to be amplified in time at a constant space location [[Huerre & Monkewitz, 1990](#)]. Cold round jets for instance exhibit a strong self-sustained convective instability [[Monkewitz & Sohn, 1988](#); [Garnaud, 2012](#)]. The corresponding mechanisms are not captured by a purely local analysis. There is also a global instability, described by the most unstable eigenvalue of the full system [[Monkewitz & Sohn, 1988](#)]. This physical observation can be formalized, quantified and confirmed by numerical computations [[Ghaddar *et al.*, 1986](#)]. More specifically, when performing a non-linear numerical simulation, the system to be solved can be represented in the form:

$$\dot{\Upsilon} = \mathcal{L}(\Upsilon) \quad (3)$$

where Υ is the state vector of the simulation at a given time. If Υ_0 is a state such that

$$\dot{\Upsilon}_0 = \mathcal{L}(\Upsilon_0) = 0 \quad (4)$$

then Υ_0 is referred to as the baseflow, and the operator \mathcal{L} can be linearized around Υ_0 :

$$A = \frac{\partial \mathcal{L}}{\partial \Upsilon_0}. \quad (5)$$

The operator A is then linear. Its eigenvectors are called ‘global modes’, the corresponding eigenvalues give the growth rate and the characteristic frequency of each mode. But the properties of A extend further [Trefethen *et al.*, 1993].

2.2 Resolvent Operator

It is indeed sometimes useful to consider the steady-state response of the harmonically forced operator with a zero initial condition:

$$\Upsilon_\infty = (A - i\omega Id)^{-1}f \quad (6)$$

where Υ_∞ is the steady state response to the forcing $-f$ at the angular frequency ω . Then:

$$R = (A - i\omega Id)^{-1} \quad (7)$$

is called the resolvent. A and R operators have in general very similar stability properties, which has been used to circumvent a poor numerical conditioning of A in jet noise studies [Garnaud *et al.*, 2012]. The linear structure of A and R allows us as well to carry out optimizations in the least-square sense. This proves useful for numerous applications, from the shape optimization of airfoils [Reuther *et al.*, 1999] to the study of the amplification of streaks in a turbulent Couette flow [Hwang & Cossu, 2010]. In this thesis, we will focus on maximizing the acoustic output of a flame.

The validity of the linear approach may be questioned for combustion flows as flames are known to exhibit strongly nonlinear behaviours due to the very stiff, exponential form of their reaction rates [Zeldovich *et al.*, 1985]. Extensions of linear theories to weakly non-linear approximations offer an interesting answer to this issue by adding a non-linear correction to linear models. The resulting amplitude equations have been successfully implemented in the case of cylinder flow [Sipp & Lebedev, 2007]. In particular, a progressive weakly non-linear correction to the baseflow allows the retrieval, from a linear study, of the correct saturated mode shape and frequency [Mantič-Lugo *et al.*, 2014].

2.3 Acoustic Waves in Instabilities: from Local to Global

When a flow exhibits a local absolute instability, it is quite clear that the corresponding linear operator A will present an unstable global mode. However, creating a global instability from a convectively unstable flow is not as straightforward. Very often, acoustic waves will play this role. In a subsonic regime, they can propagate upstream and thus close an unstable feedback loop. The most straightforward definition for acoustic waves stems from the analysis of a linear perturbations of an inert flow with a uniform, low Mach number hydrodynamic velocity. In this case Doak [1973], following Chu & Kovásznyai [1958], developed an analytic expansion of the perturbation field in three components: acoustic waves, vortical waves and entropy waves. In this description, acoustic perturbations appear in the form of isentropic pressure waves travelling at a phase and group velocity of:

$$c_0 = \left(\frac{\partial p}{\partial \rho} \Big|_s \right)^{1/2}. \quad (8)$$

In this formulation, acoustic waves are independent of vortical and entropy structures. They are also associated with an eigenspace of the local linearized compressible Navier-Stokes operator. In order to expand this definition to more complex flow topologies this model needs to be refined. An interesting approach consists of correcting the previous wave equation with the appropriate source terms [Lighthill, 1952]. This results in an inhomogeneous wave equation that can be derived from the full fluid equations. We proceed along classical lines by defining the excess density [Crighton *et al.*, 1992]:

$$\rho_e = \rho - \rho_0 - \frac{p - p_0}{c_0^2}. \quad (9)$$

We continue by using the hypothesis of multiple species and of Fick's law for species diffusion which, after several manipulations with details given in Crighton *et al.* [1992], results in

$$\frac{1}{c_0^2} \frac{\partial^2 p'}{\partial t^2} - \Delta p' = \mathcal{T}_1 + \mathcal{T}_2 + \mathcal{T}_3 + \mathcal{T}_4 \quad (10)$$

with

$$\mathcal{T}_1 = \frac{\partial^2}{\partial x_i \partial x_j} (\rho u_i u_j - \tau_{ij}), \quad (11)$$

$$\mathcal{T}_2 = \frac{\partial^2 \rho_e u_i}{\partial t \partial x_i}, \quad (12)$$

$$\mathcal{T}_3 = \frac{1}{c_0^2} \frac{\partial}{\partial t} \left[\left(1 - \frac{\rho_0 c_0^2}{\rho c^2} \right) \frac{Dp}{Dt} - \frac{p - p_0}{\rho} \frac{D\rho}{Dt} \right], \quad (13)$$

$$\mathcal{T}_4 = \frac{\partial}{\partial t} \left[\frac{\alpha \rho_0}{\rho c_p} \left(\dot{q} - \frac{\partial q_i}{\partial x_i} + \tau_{ij} : \frac{\partial u_i}{\partial x_j} + \sum_{m=1}^N h_m \frac{\partial J_{m,i}}{\partial x_i} \right) \right]. \quad (14)$$

where \dot{q} denotes the volumetric heat release rate, \mathbf{q} denotes the heat flux, $J_{m,i}$ is the flux of species m , α is the thermal diffusivity and c_p is the specific heat capacity of the gas mixture. The source term \mathcal{T}_1 typically describes quadrupole sources stemming from flow noise. It usually scales as the eighth power of the flow Mach number [Crighton *et al.*, 1992]. The second acoustic source \mathcal{T}_2 describes dipolar sources due to flow inhomogeneities including, in particular, density perturbations. The third term \mathcal{T}_3 is important in regions of strong variations of density and speed of sound. Finally, \mathcal{T}_4 is associated with monopolar sound sources due to irreversible processes. The \dot{q} term is dominant in most reactive systems [Kidin & Librovich, 1983; Truffaut *et al.*, 1998].

This set of equations may help understand the main causes of noise. But they do not provide any insight in the causality that associates flow structures and acoustic waves. This problem is especially important as acoustic waves propagate quasi-isotropically at low Mach numbers. They are also candidates for numerous feedback mechanisms in hydrodynamic instabilities. For instance, jets and boundary layers are known to be very receptive to acoustic waves [Crow & Champagne, 1971; Nishioka & Morkovin, 1986]. This can lead to resonances for convectively unstable flows. In the case of an airfoil at low Mach number [Miguel Ángel Fosas De Pando, 2012], the acoustic waves, created by the shear layer past the airfoil, can resonate with the airfoil's boundary layer. This results in a characteristic tonal noise that can be heard on gliders or wind turbines. Such self-sustained noise can lead to extremely large amplitudes. The screech instability of supersonic jets [Powell, 1953; Norum, 1983; Beneddine *et al.*, 2015] relies on the same type of acoustic feedback and can result in structural damages.

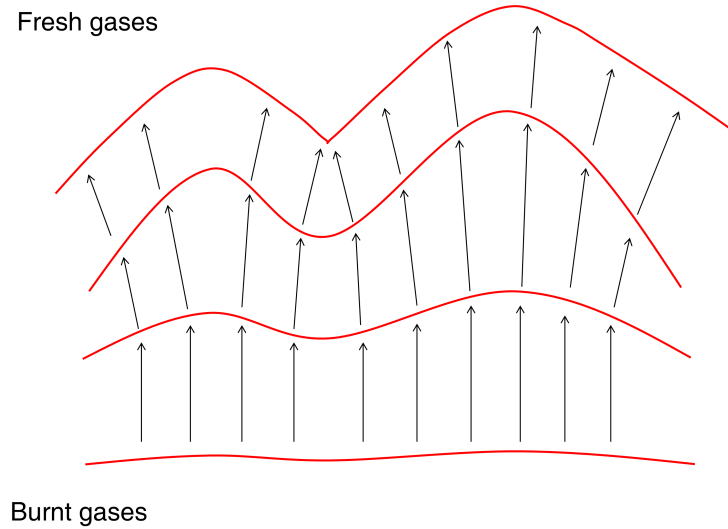


Figure 4: Evolution of an upward propagating flame front with a Darrieus-Landau instability. Red: flame front. Arrows: Lagrangian displacement of the flame front. On the last position, a cusp is observed.

Flames, of course, are another family of flows that are very sensitive to acoustic waves. Understanding thermoacoustic instabilities triggered by unsteady flames also requires a good knowledge of the flame dynamics and of its sensitivity to flow perturbations [Ducruix *et al.*, 2003].

3 Flame Instabilities

3.1 Flame Local Instabilities

Global modes have only recently been investigated in the combustion community [Nichols & Schmid, 2008; Qadri, 2014]. Some recent studies of flame-intrinsic instabilities have explored the role of global modes on thermoacoustic interactions [Emmert *et al.*, 2015]. Nevertheless, the practical evaluation of linear modes is still a serious challenge due to the very high computational cost of reactive computations. However, a strong local analysis background has been built in studies of laminar flames. The Landau-Darrieus instability [Darrieus, 1938; Landau, 1944] has received particular attention. This hydrodynamic instability stems from the dilatation of the flow by the flame. The upstream streamlines are curved by the heat released by the flame, thus amplifying any flame front disturbance. The saturation of this instability very often leads to cusps. This situation is outlined in figure 4.

The linear properties of the Darrieus-Landau instability have been studied by Pelce & Clavin [1982], Matalon & Matkowsky [1982] and Zeldovich *et al.* [1985]. In particular, it has been shown that transverse diffusion leads to a stabilization of the flame front at high wavenumbers. This effect was introduced by Markstein [1964] in the form of a stretch-rate correction on the flame-front velocity [Davis *et al.*, 2002a,b]:

$$S_f = S_{f0} (1 + \mathcal{L}_1 \kappa) + \mathcal{L}_2 (\mathbf{n} \cdot \nabla \mathbf{u} \cdot \mathbf{n} - \nabla \cdot \mathbf{u}) \quad (15)$$

where S_{f0} denotes the laminar burning velocity, κ the local flame front curvature, \mathbf{n} the normal to the flame front oriented from fresh to burnt gas, \mathcal{L}_1 and \mathcal{L}_2 are respectively the first and second Markstein lengths. In literature \mathcal{L}_1 is often taken equal to \mathcal{L}_2 [Poinsot & Veynante, 2012] or \mathcal{L}_2 may be neglected [Piana *et al.*, 1997] as a first approximation. Gravitational effects can as well be accounted for [Pelce & Clavin, 1982]. They are stabilizing for a downward propagating flame while a Rayleigh-Taylor instability may occur for a flame travelling upward [Bychkov & Liberman, 2000]. When destabilised, a flame typically quickly saturates by generating cusps such as shown in figure 4. Non-linear effects of the Landau-Darrieus instability have important consequences in turbulence, and have also been thoroughly studied [Cambray & Joulin, 1994; D’angelo *et al.*, 2000; Creta & Matalon, 2011]. However, a full and comprehensive study of regions of high curvature is still lacking. This issue is difficult to track theoretically; even adapted linear numerical tools are quite recent.

Another vast field of instabilities are thermo-diffusive instabilities [Joulin & Clavin, 1979], associated for instance with cellular flames. For the analysis of such instabilities, the Lewis number has to be introduced:

$$Le = \frac{k}{\rho C_p D} \quad (16)$$

where k is the thermal conductivity of the gas, ρ is its density, C_p is its specific heat capacity and D the mass diffusivity of the fuel. Typically, for $Le < 1$, diffusion is destabilizing, while for $Le > 1$ the flame tends to be stabilized [Zeldovich *et al.*, 1985]. In this study, we will choose $Le = 1$. With a flame of finite thickness and finite activation temperature, this corresponds to the diffusively stable case [Joulin & Clavin, 1979].

Understanding the flame’s local dynamics is a crucial step for further progress. To this end, this thesis provides a new perspective on practical combustor instabilities and, more precisely, on thermoacoustic instabilities.

3.2 Thermoacoustics of Finite Dimension Flames

Similar to non-reactive flows, flames are subject to global instabilities at the injector’s scale. For instance, the flickering phenomenon of a flame is related to the interaction of the Kelvin-Helmholtz instabilities generated by the burnt gases with the flame [Buckmaster & Peters, 1988; Yuan *et al.*, 1994]. Such instabilities rarely generate very large acoustic amplifications by themselves. In practice, thermoacoustic instabilities often arise when a coupling occurs between the engine acoustics and the flame. There is then a spatial scale separation between the combustion zone and the characteristic size of the acoustic waves. This property allows the treatment of thermo-acoustic problems in two parts: first, a reduced-order model for the forced flame dynamics is computed or measured [Ducruix *et al.*, 2000; Paschereit *et al.*, 2002; Palies *et al.*, 2010]; second, this approximation is then implemented in an engine model to evaluate its overall acoustic stability properties [Morgans & Stow, 2007; Nicoud *et al.*, 2007; Noiray *et al.*, 2008; Palies *et al.*, 2011; Bauerheim *et al.*, 2013; Silva *et al.*, 2013]. Computing accurate reduced-order models is consequently of prime interest.

A first, direct approach consists of computing the impedance matrix — or transfer matrix — associated with the acoustic characteristics of the flame [Paschereit *et al.*, 2002;

[Sattelmayer & Polifke, 2003]. Recently, this technique has been applied to study the onset of a flame-induced global instability, or ‘intrinsic instability’ with acoustic criteria [Emmert *et al.*, 2015]. A second possible strategy is based on the study of the flame’s forced dynamics. Such attempts rely on two assumptions.

- First, the heat release rate contribution to the radiated noise (from Eq. 1) is dominant when compared to other sound output in flames [Strahle, 1971; Kidin *et al.*, 1984].
- Second, the flame is only weakly sensitive to acoustic pressure only the acoustic velocity needs to be considered [Markstein, 1964; Ducruix *et al.*, 2003].

These assumptions considerably simplify the study of the flame-induced acoustic field: the problem reduces to an unique input-output relation [Dowling & Morgans, 2005; Sattelmayer & Polifke, 2003; Poinso & Veynante, 2012]. If the perturbation amplitudes are kept within the linear regime, three equivalent representations of the flame acoustic feedback are possible:

- A state-space representation: the flame response is described by linear Ordinary Differential Equations (ODEs) [Bellucci *et al.*, 2004].
- An impulse response: the flame response is analyzed by its response to an infinitesimal impulse [Tay-Wo-Chong, 2012].
- A transfer function: the flame is considered with respect to its permanent regime response to an harmonic forcing.

The latter solution is typically preferred in experiments [Ducruix *et al.*, 2000; Durox *et al.*, 2009; Palies *et al.*, 2010; Schimek *et al.*, 2011] as it allows a frequency-by-frequency systematic approach. The ‘Flame Transfer Function’ (FTF) is then defined as [Merk, 1956; Fleifil *et al.*, 1996]:

$$FTF = \frac{\tilde{Q}/Q_0}{\tilde{u}_b/u_{b,0}} \quad (17)$$

where Q_0 is the average integral heat release rate, \tilde{Q} is the Fourier transform of the heat release rate, $u_{b,0}$ is the average bulk velocity inside the injector, and \tilde{u}_b is the Fourier transform of the bulk velocity. Recently, impulse response identification has seen a rise in both the numerical [Polifke *et al.*, 2001] and experimental [Cuquel, 2013] communities, but is limited to low-amplitude analysis and, in theory, to globally stable configurations.

FTF-based techniques have been extended to weakly non-linear formulations. The most popular choice is the Flame Describing Function (FDF): a dependency on the acoustic amplitude is introduced in the flame transfer function [Noiray *et al.*, 2008; Durox *et al.*, 2009; Palies *et al.*, 2010; Schimek *et al.*, 2011; Krediet *et al.*, 2012]. The response of the flame to each individual forcing frequency and amplitude is computed. The amplitude and delay of the output at the forcing frequency are then used to locally define the value of the FDF. This method has been successful at estimating limit cycle amplitudes [Noiray *et al.*, 2008; Han *et al.*, 2015]. It has also been used to analyze post-Hopf bifurcation systems in the case of two simultaneously unstable modes [Boudy *et al.*, 2013]. This technique has

been further extended by Ghirardo *et al.* [2015] in order to extract a non-linear state space model from an FDF.

However, in spite of all these achievements, analyzing a combustion system in which two or more eigenmodes coexist and interact is still beyond current capabilities. Combustion chambers with an annular plenum and multiple burners [Evesque & Polifke, 2002; Bourgouin *et al.*, 2013; Worth & Dawson, 2013] are an excellent example of this limitation. The longitudinal and azimuthal modes can couple non-linearly. In such a chamber, two different acoustic forcing directions — longitudinal and azimuthal — can also be involved, with equal or different characteristic frequencies [Bourgouin *et al.*, 2014, 2015]. New tools need to be developed to tackle this type of non-linear instabilities.

More computationally intensive solutions can also be considered. They typically rely on the temporal integration of a simplified, non-linear flame propagation equation. A popular choice consists of representing the flame as a level-set: this leads to the G -equation, introduced by Markstein [1964] and since then frequently used and improved upon [Piana *et al.*, 1997; Luzzato *et al.*, 2013]. This technique introduces a fundamental novelty with respect to the transfer matrix, FTF or FDF measurements: the flame is no longer considered as a black box. The relevant features of the detailed flame dynamics need to be understood and modeled in this case.

3.3 Hydrodynamics of Flames

The most fundamental wave controlling the flame dynamics is related to flame wrinkling [Petersen & Emmons, 1961; Boyer & Quinard, 1990]. Even when the Darrieus-Landau mechanism is not absolutely or convectively unstable, large-scale — with respect to the flame thickness — flame front perturbations are weakly damped. This leads to the convection of waves along the flame front that can be amplified and eventually saturate, forming a cusp. Figure 5 presents a flame which is acoustically forced at 75 Hz (bottom images); the wrinkles induce a cusp. Due to the very general character of flame wrinkling, numerous flow perturbations can trigger it. For instance, entropy or fuel mass fraction inhomogeneities change the local flame speed, thus inducing flame perturbations; the velocity component of acoustic waves can locally displace the flame; finally, flames can strongly interact with vortices [Ducruix *et al.*, 2003]. Overall, wrinkles generate noise, at first order, when they induce a change in the flame area. Their propagation is typically related to slow variations of the integral unsteady heat release rate and induce, as a consequence, low acoustic levels. However, this general dynamics drastically changes when wrinkles lead to flame pinching [Schuller *et al.*, 2002b].

When two parts of the flame front coalesce, a quick process leads to the rupture of the flame front. This situation is outlined in figure 6. During this pinching phase, fast variations of the heat release rate are observed as the flame front gets disrupted [Schuller *et al.*, 2003a]. Sometimes, a flame pocket is released and will burn all the fuel it contains. Both of these phenomena are associated with large acoustic amplitudes [Kidin *et al.*, 1984]. Numerical simulations of this phenomenon computed by Talei *et al.* [2013] are presented in figure 7. Two acoustic impulses are generated during the phases of fast flame front destruction. But pinching is not the only phenomenon related to such an intense acoustic output. The same

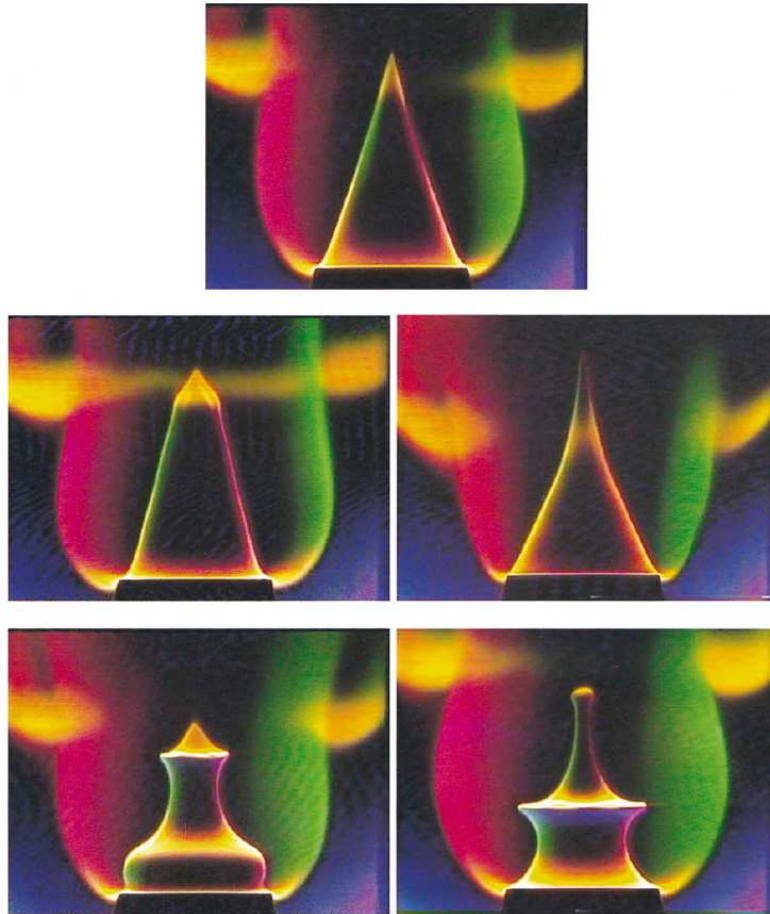


Figure 5: Schlieren images of a premixed methane-air flame, acoustically forced. The equivalence ratio is 0.95, the injection velocity is $0.96 \text{ m}\cdot\text{s}^{-1}$. Top: steady conical flame. Modulation frequency: 25 Hz (middle), 75 Hz (bottom). Images of the perturbed flame are in phase opposition. From [Ducruix et al. \[2000\]](#).

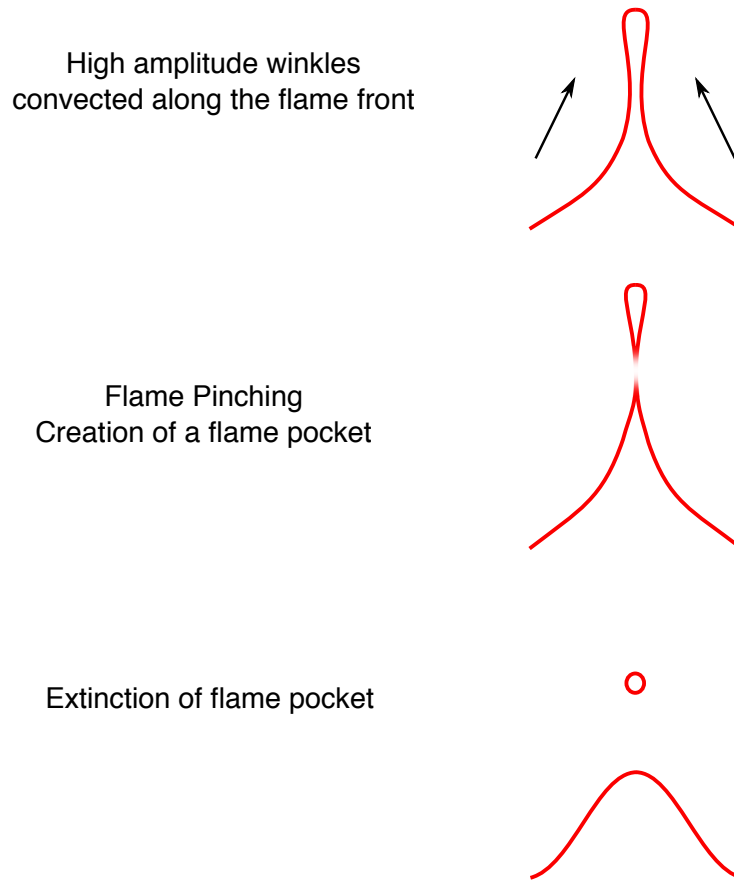


Figure 6: *Schematic presentation of flame pinching.*

type of pressure impulse can be observed during the extinction of the flame front associated with a flame-vortex interaction [Candel *et al.*, 2004].

This vortex-flame dynamics is especially interesting as it influences numerous flame-flow interactions. It has been studied in a number of investigations [Mueller *et al.*, 1998; Renard *et al.*, 2000; Kadowaki & Hasegawa, 2005; Ahn & Kenneth, 2012]. When vortices are small, they get damped by the flame [Mueller *et al.*, 1998]. However, larger-scale structures roll up the flame, leading to strongly non-linear behaviours [Renard *et al.*, 2000]. This interaction typically has two phases. First, the vortex will roll the flame around itself. This can isolate a portion of the fuel. When this fuel is depleted, or when the flame is stretched too violently, simultaneous quenching of multiple portions of the flame front occurs. This phenomenon is outlined in figure 8. The first phase is associated with a slow increase of flame area, the second phase with its quick destruction [Candel *et al.*, 2009]. Because of the form of the heat-release-based acoustic source term, this series of event is associated with drastic variations in noise levels.

The flame dynamics also has the particularity of alternating slow and fast temporal scales. With noise being related to the time derivative of the integral unsteady heat release rate

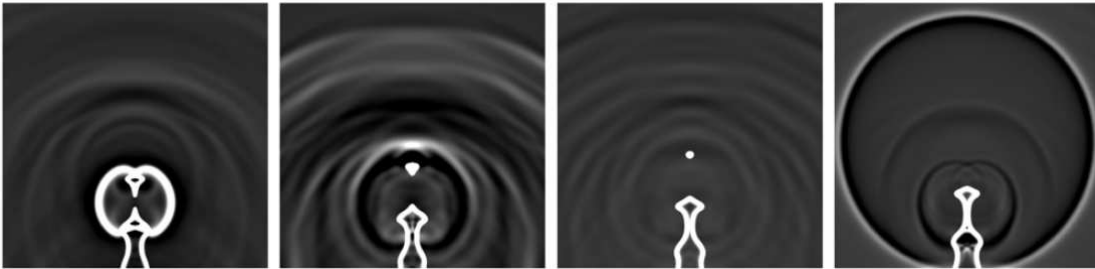


Figure 7: Dilatation field of a numerical flame, pinching at $Le = 1$. From Talei et al. [2013].

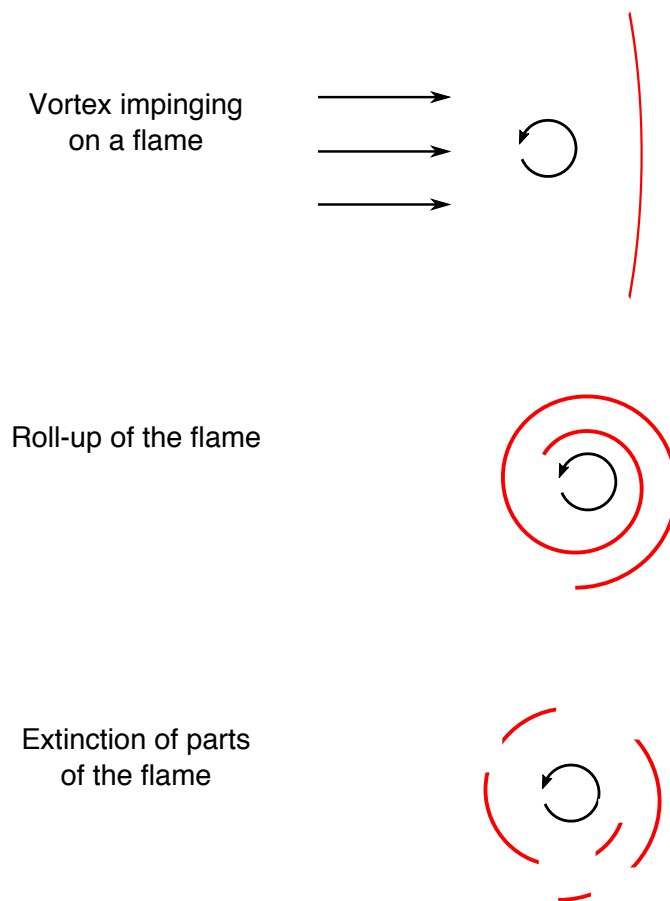


Figure 8: Schematic presentation of flame roll-up.

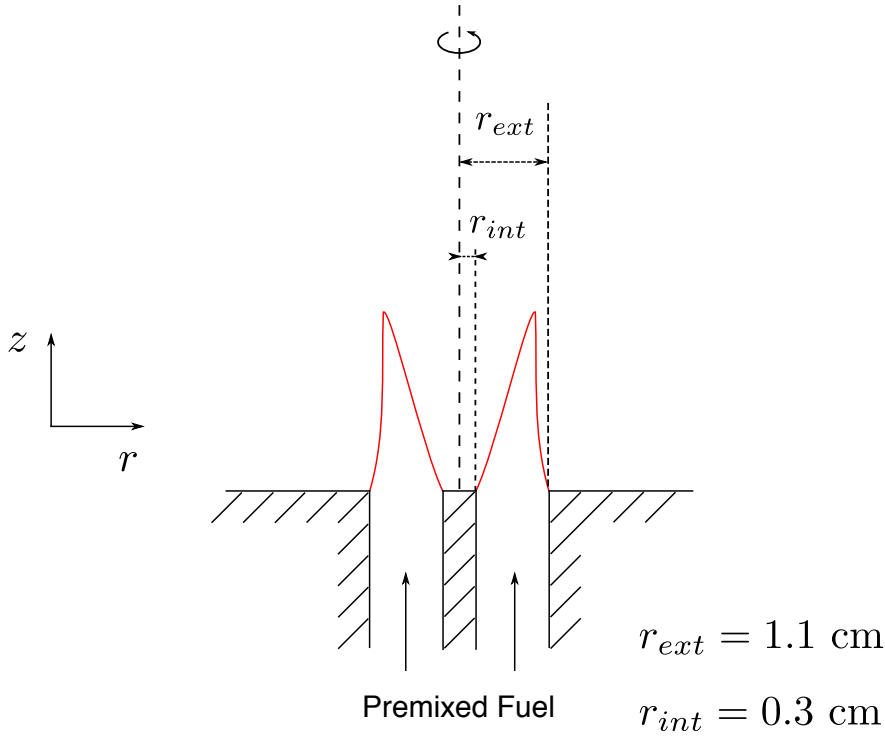


Figure 9: Sketch of the annular injector used as a reference with an M-flame attached.

[Strahle, 1971], the associated phenomena have strong implications in terms of acoustic generation. Interestingly, the three processes presented here can be observed and studied on an annular injector. This configuration is also sufficiently simple to allow a reasonable degree of reproducibility, yet sufficiently complex to contain most of the dynamical features found in many industrial combustors. Throughout this study, we will consider either a circular or, mostly, an annular injector.

4 Flames Stabilized on an Annular Burner

The burner used as a reference in this study is sketched in figure 9. The inner and outer dimensions correspond to the burner used in Schuller *et al.* [2003a]; Birbaud *et al.* [2006]; Durox *et al.* [2009]. Three different types of flames can be stabilized on such an injector:

- A conical flame: the flame is only attached on the exterior wall of the annulus.
- A V-flame: the flame is only attached on the interior rod.
- An M-flame: the flame is attached both on the interior rod and on the exterior wall.

The three configurations are presented in figure 10. These flames have rather different physical properties. The conical flame has been studied in numerous publications [Schuller *et al.*, 2003b; Durox *et al.*, 2009; Duchaine *et al.*, 2011; Cuquel *et al.*, 2013a,b]. It is also a good reference case to experimentally validate a numerical code. The M-flame induces a torus of fuel when acoustically forced at large amplitudes, as shown in figure 11. The

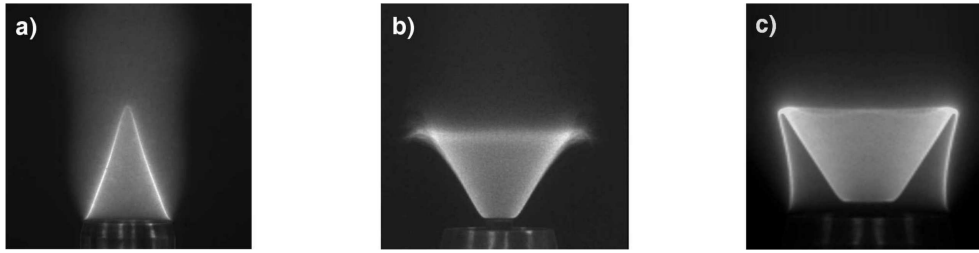


Figure 10: *Flames stabilized on an annular burner. a: conical flame; b: V-flame; c: M-flame. Images from [Schuller et al., 2003a].*

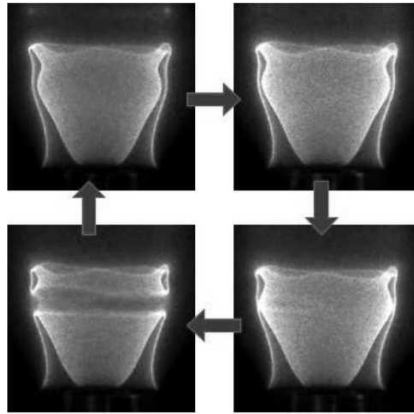


Figure 11: *M-flame forced acoustically at high amplitude, at four different times of the acoustic cycle. Images from [Schuller et al., 2003a].*

rapid destruction of this torus is responsible for high acoustic amplitudes [Schuller et al., 2003a]. This saturation effect is related to the presence of a large, circular flame tip area. This high-curvature flame front zone participates in the low-amplitude flame-induced acoustics. M-flames make more noise than conical flames at all acoustic amplitudes while being, in our configuration, linearly stable. Lastly, the V-flame flame front terminates at the mixing layer induced by the exterior wall of the injector. This interaction destabilizes the flame front, which induces a strongly non-linear behaviour [Durox et al., 2009]. These three configurations also offer a variety of physical phenomena, sufficiently rich to allow a comprehensive analysis of flame-generated noise.

5 Thesis Objectives

Black-box approaches, such as FDF, proved valuable in understanding thermoacoustic instabilities. However, they rely on assumptions that strongly restrict their applicability. For instance, using a transfer-function-based model in an engine model supposes that acoustic disturbances are dominated by a single frequency; that their growth is slow compared to the oscillation time scale; that the acoustic forcing on the flame is identical to the forcing used to evaluate the FDF. Going beyond these limitations implies abandoning the black-box techniques in favor of a more computational approach which involves a closer look at flame dynamics. This thesis will focus on identifying relevant physical phenomena for thermoacoustic studies.

The atomistic decomposition of linear operators allows us to consider separately each physical process and its effect on the flow. This approach proved especially useful at analyzing the linear response of a flame to acoustic forcing. Chapter 1 will present the main numerical methods used in this thesis, while chapter 2 will focus on the effects of flame-induced heating on the M-flame hydrodynamics in the linear limit. Using an in-house linear code, a quick method to compute an accurate impulse response will be presented, along with a numerical strategy to convert it to a state-space model.

Once the flame dynamics is better understood, an accurate model of sound generation at flames is important. Most studies make the assumption that flames-induced acoustics can be accounted for by considering the volume integral of the heat release rate. However, the range of validity of this model is not clear. Transfer of energy between entropic, vortical and acoustic modes near flame fronts is complex and may depend on the local stretch of the flame. Chapter 3 will tackle this issue by first presenting optimal-forcing computations on M-flames. The results will then be analyzed with the help of a 1D axisymmetric model. This novel methodology will highlight the importance of vorticity-generated acoustic waves at small scales. The overall objective is to understand how stretch, on one hand, and disturbances wavelength, on the other hand, affect noise generation near flame fronts.

The previous analyses are all conducted within the linear limit. Flames, however, are often intrinsically unstable, settling into a limit-cycle behaviour. Large-scale computations, commonly the method of choice for this regime, are typically extremely expensive, which prevents us from adopting a try-and-error approach and system identification for a possible control design. An intermediate solution between Large Eddy Simulations (LES) and simplified weakly non-linear models has to be developed.

An attempt to introduce non-linear heating effects in a flame model will thus be presented in chapter 4. This model relies on a level-set formulation and will be compared to experimental measurements. The objective is to converge to a pleasing trade-off between computational cost and modeling accuracy while taking advantage of an implementation on Graphic Processing Unit (GPU) hardware. Such a tool opens up new possibilities for the estimation of limit-cycles amplitudes in practical combustion chambers and for the design of accurate control strategies.

Chapter 1

Governing Equations and Numerical Methods

A reactive axisymmetric code has been adapted from a previous non-reactive compressible jet code. Performances are the subject of a specific care. The equations, the numerical implementation novelties, the geometry and the baseflow used in linear simulations are presented in this chapter.

1.1 Governing Equations

1.1.1 Assumptions

In this project, the reactive Navier-Stokes equations are solved using the following assumptions:

- A compressible viscous flow is assumed.
- The flame is premixed and lean : fuel is always the limiting component.
- Thermodynamic properties between fuel, oxidizer, products and ambient air are supposed identical.
- A simple one step irreversible reaction is considered.
- As a consequence of previous assumptions, we suppose the medium being constituted of only two species (namely the fuel and the ambient air).
- Fick's law [Poinsot & Veynante, 2012] is used to model diffusion velocities.

It is further assumed that all the heat capacities of reactants and reaction products are identical. This set of hypotheses is intended to capture bulk premixed flame properties while using a simplified chemistry modeling. They will be validated in chapter 2 against experimental measurements of laminar flames submitted to flow perturbations. The equations are then expressed in a conservative form:

$$\frac{\partial \tilde{\rho}}{\partial t} + \nabla \cdot (\tilde{\rho} \mathbf{u}) = 0 \quad (1.1)$$

$$\frac{\partial \tilde{\rho} \mathbf{u}}{\partial t} + \nabla \cdot (\tilde{\rho} \mathbf{u} \otimes \mathbf{u}) = -\nabla \tilde{p} + \nabla \cdot \underline{\boldsymbol{\tau}}, \quad (1.2)$$

$$\frac{\partial \tilde{\rho} \tilde{E}}{\partial t} + \nabla \cdot (\tilde{\rho} \mathbf{u} \tilde{E}) = -\nabla \cdot (\tilde{p} \mathbf{u}) + \widetilde{\Delta Q} \dot{\omega}_f - \nabla \cdot \mathbf{q} + \nabla \cdot (\underline{\boldsymbol{\tau}} \cdot \mathbf{u}) \quad (1.3)$$

$$\frac{\partial \tilde{\rho} Y_f}{\partial t} + \nabla \cdot (\tilde{\rho} \mathbf{u} Y_f) = -\dot{\omega}_f + \nabla \cdot (\tilde{\rho} \tilde{D} \nabla Y_f) \quad (1.4)$$

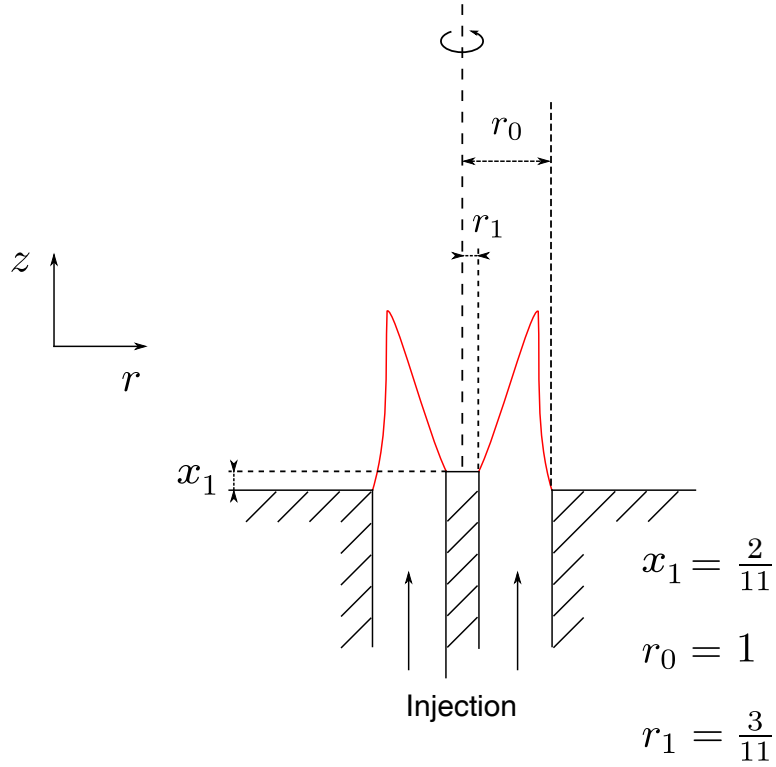


Figure 1.1: Sketch of the annular configuration considered.

with $\tilde{\rho}$ denoting the density, \mathbf{u} the flow velocity, p the pressure, $\underline{\boldsymbol{\tau}}$ the stress tensor, \tilde{E} the total energy per unit of mass, \mathbf{q} the heat flux, Y_f the fuel mass fraction, \tilde{D} the diffusivity of the species and $\tilde{\Delta Q}$ the enthalpy of the reaction. The reaction rate $\dot{\omega}_f$ is taken of the form:

$$\dot{\omega}_f = \tilde{A}\tilde{\rho}Y_f \exp\left(-\frac{\tilde{T}_a}{\tilde{T}}\right) \quad (1.5)$$

where \tilde{A} is the Arrhenius prefactor and \tilde{T}_a is the activation temperature of the fuel.

The equations are implemented in a dimensionless form. The reference length is chosen as the tube radius r_0 , as defined on figure 1.1, the reference velocity is the maximum velocity u_{\max} in the injector, the reference viscosity, temperature and density are chosen as the cold gases corresponding values, the reference fuel mass fraction being the unburnt fuel mass fraction Y_0 entering the tube.

1.1.2 Detailed Equations

If \tilde{f} is a dimensional variable, let f be the corresponding dimensionless value. Some useful relations can then be expressed from these equations [Sandberg, 2007; Garnaud, 2012].

First, a perfect gas is assumed:

$$p = \frac{\rho T}{\gamma \text{Ma}^2} \quad (1.6)$$

Where γ is the specific heat ratio and Ma is the Mach number. The internal energy is then

$$e = \frac{T}{\gamma(\gamma - 1) \text{Ma}^2} \quad (1.7)$$

and the entropy is expressed as

$$s = \frac{1}{\gamma(\gamma - 1) \text{Ma}^2} (\log(p) - \gamma \log(\rho)) \quad (1.8)$$

In cylindrical coordinates (x, r, θ) , the velocity and fuel mass fraction are redefined as

$$\mathbf{u} = (u_x \mathbf{e}_x + u_r \mathbf{e}_r + u_\theta \mathbf{e}_\theta) u_{\max} \quad (1.9)$$

$$Y = \frac{Y_f}{Y_0} \quad (1.10)$$

In cylindrical coordinates, the corresponding conservative compressible Navier-Stokes equations take following the form [Sandberg, 2007; Poinso & Veynante, 2012] of

$$\frac{\partial \Upsilon}{\partial t} + \frac{\partial \mathbf{F}_e^x - \mathbf{F}_v^x}{\partial x} + \frac{\partial \mathbf{F}_e^r - \mathbf{F}_v^r}{\partial r} + \frac{1}{r} \frac{\partial \mathbf{F}_e^\theta - \mathbf{F}_v^\theta}{\partial \theta} + \frac{\mathbf{F}_e - \mathbf{F}_v}{r} - \mathbf{f}_{vol} = 0 \quad (1.11)$$

Where Υ denotes the state vector, \mathbf{F}_e^i are the inviscid fluxes in the i direction, \mathbf{F}_v^j refer to the diffusion fluxes in the j -direction, and \mathbf{f}_{vol} groups the volumetric forces acting on the fluid along with chemistry effects. The state vector chosen is chosen as:

$$\Upsilon = \begin{pmatrix} \rho \\ \rho u_x \\ \rho u_r \\ \rho u_\theta \\ \rho E \\ \rho Y \end{pmatrix} \quad (1.12)$$

Inviscid fluxes are expressed as:

$$\mathbf{F}_e^x = \begin{pmatrix} \rho u_x \\ \rho u_x u_x + p \\ \rho u_x u_r \\ \rho u_x u_\theta \\ (\rho E + p) u_x \\ \rho Y u_x \end{pmatrix} \quad (1.13)$$

$$\mathbf{F}_e^r = \begin{pmatrix} \rho u_r \\ \rho u_r u_x \\ \rho u_r u_r + p \\ \rho u_r u_\theta \\ (\rho E + p) u_r \\ \rho Y u_r \end{pmatrix} \quad (1.14)$$

$$\mathbf{F}_e^\theta = \begin{pmatrix} \rho u_\theta \\ \rho u_\theta u_x \\ \rho u_\theta u_r \\ \rho u_\theta u_\theta + p \\ (\rho E + p) u_\theta \\ \rho Y u_\theta \end{pmatrix} \quad (1.15)$$

$$\mathbf{F}_e = \begin{pmatrix} \rho u_r \\ \rho u_r u_x \\ \rho u_r u_r - \rho u_\theta u_\theta \\ 2\rho u_r u_\theta \\ (\rho E + p) u_r \\ \rho Y u_r \end{pmatrix} \quad (1.16)$$

Diffusion fluxes take the form:

$$\mathbf{F}_v^x = \begin{pmatrix} 0 \\ \tau_{xx} \\ \tau_{xr} \\ \tau_{x\theta} \\ \tau_{xx} u_x + \tau_{xr} u_r + \tau_{x\theta} u_\theta - q_x \\ -\tau_{Y,x} \end{pmatrix} \quad (1.17)$$

$$\mathbf{F}_v^r = \begin{pmatrix} 0 \\ \tau_{xr} \\ \tau_{rr} \\ \tau_{r\theta} \\ \tau_{xr} u_x + \tau_{rr} u_r + \tau_{r\theta} u_\theta - q_r \\ -\tau_{Y,r} \end{pmatrix} \quad (1.18)$$

$$\mathbf{F}_v^\theta = \begin{pmatrix} 0 \\ \tau_{x\theta} \\ \tau_{r\theta} \\ \tau_{\theta\theta} \\ \tau_{x\theta} u_x + \tau_{r\theta} u_r + \tau_{\theta\theta} u_\theta - q_\theta \\ -\tau_{Y,\theta} \end{pmatrix} \quad (1.19)$$

$$\mathbf{F}_v = \begin{pmatrix} 0 \\ \tau_{rx} \\ \tau_{rr} - \tau_{\theta\theta} \\ 2\tau_{\theta r} \\ \tau_{rx}u_x + \tau_{rr}u_r + \tau_{\theta r}u_\theta - q_r \\ -\tau_{Y,r} \end{pmatrix} \quad (1.20)$$

the stress tensor τ is defined as:

$$\tau_{xx} = \frac{2}{3\text{Re}} \left[2 \frac{\partial u_x}{\partial x} - \frac{\partial u_r}{\partial r} - \frac{1}{r} \left(\frac{\partial u_\theta}{\partial \theta} + u_r \right) \right], \quad (1.21)$$

$$\tau_{rr} = \frac{2}{3\text{Re}} \left[-\frac{\partial u_x}{\partial x} + 2 \frac{\partial u_r}{\partial r} - \frac{1}{r} \left(\frac{\partial u_\theta}{\partial \theta} + u_r \right) \right], \quad (1.22)$$

$$\tau_{\theta\theta} = \frac{2}{3\text{Re}} \left[-\frac{\partial u_x}{\partial x} - \frac{\partial u_r}{\partial r} + \frac{2}{r} \left(\frac{\partial u_\theta}{\partial \theta} + u_r \right) \right], \quad (1.23)$$

$$\tau_{xr} = \frac{1}{\text{Re}} \left[\frac{\partial u_x}{\partial r} + \frac{\partial u_r}{\partial x} \right], \quad (1.24)$$

$$\tau_{x\theta} = \frac{1}{\text{Re}} \left[\frac{\partial u_\theta}{\partial x} + \frac{1}{r} \frac{\partial u_x}{\partial \theta} \right], \quad (1.25)$$

$$\tau_{r\theta} = \frac{1}{\text{Re}} \left[\frac{\partial u_\theta}{\partial r} + \frac{1}{r} \left(\frac{\partial u_r}{\partial \theta} - u_\theta \right) \right] \quad (1.26)$$

The heat flux takes the form:

$$q_x = -\frac{1}{(\gamma - 1) \text{PrReMa}^2} \frac{\partial T}{\partial x} \quad (1.27)$$

$$q_r = -\frac{1}{(\gamma - 1) \text{PrReMa}^2} \frac{\partial T}{\partial r} \quad (1.28)$$

$$q_\theta = -\frac{1}{(\gamma - 1) \text{PrReMa}^2} \frac{1}{r} \frac{\partial T}{\partial \theta} \quad (1.29)$$

Species diffusion terms are written:

$$\tau_{Y,x} = -\frac{1}{\text{LePrRe}} \frac{\partial Y}{\partial x} \quad (1.30)$$

$$\tau_{Y,r} = -\frac{1}{\text{LePrRe}} \frac{\partial Y}{\partial r} \quad (1.31)$$

$$\tau_{Y,\theta} = -\frac{1}{\text{LePrRe}} \frac{1}{r} \frac{\partial Y}{\partial \theta} \quad (1.32)$$

The Prandtl number Pr and the Lewis number Le are assumed constant. On the contrary, a Sutherland temperature correction of the viscosity is considered for the Reynolds number:

$$\frac{1}{\text{Re}} = \frac{1}{\text{Re}_0} T^{2/3} \frac{1+S}{T+S} \quad (1.33)$$

Where S is the Sutherland constant and Re_0 is the reference Reynolds number.

Finally, as gravity is neglected, the volumetric term is expressed here as

$$\mathbf{f}_{vol} = \begin{pmatrix} 0 \\ 0 \\ 0 \\ 0 \\ \Delta Q \dot{\omega} \\ -\frac{1}{Y_0} \dot{\omega} \end{pmatrix} \quad (1.34)$$

where $\dot{\omega}$ is the fuel reaction rate, modelled by an Arrhenius law:

$$\dot{\omega} = A \rho Y Y_0 \exp\left(-\frac{T_a}{T}\right) \quad (1.35)$$

where A is the Arrhenius prefactor, Y_0 the initial mass fuel fraction (in order to keep Y between 0 and 1) and T_a is the activation temperature of the chemical reaction.

In this code,

$$u_\theta = 0 \quad (1.36)$$

and

$$\frac{\partial \cdot}{\partial \theta} = 0 \quad (1.37)$$

The \mathbf{e}_θ direction is also not considered and:

$$\tau_{x\theta} = \tau_{r\theta} = q_\theta = \tau_{Y,\theta} = 0 \quad (1.38)$$

1.1.3 Code Presentation

The main code used during this project is called CNS2D (Combustion Navier-Stokes 2D). This implementation expands a previous non reactive jet code implemented by Xavier Garnaud at LadHyX. The previous equations are solved on a large number of processors for both linear and non-linear regimes. The details of the implementation being presented in [Garnaud \[2012\]](#), only the most important features and developments will be recalled in this part.

1.1.3.1 Computation of Space Derivatives

When solving for acoustic-related instabilities, specific care must be taken when computing gradients. Acoustic waves indeed usually appear as almost negligible, high velocity perturbations in subsonic flows. Inappropriate numerical techniques would result in their damping by numerical diffusion or in their deformation by numerical dispersion.

In order to evaluate the quality of the computation of space derivatives, several criteria are possible. The most basic one is based on an analytical Taylor expansion. By writing for instance, for a \mathcal{C}^∞ function f

$$f(x + dx) = f(x) + f'(x) dx + f''(x) \frac{dx^2}{2} + \mathcal{O}(dx^3) \quad (1.39)$$

it is possible to isolate the derivative term $f'(x)$. This allows to prove that centered differences schemes lead to a second-order gradient evaluation:

$$\frac{f(x + dx) - f(x - dx)}{2 dx} = f'(x) + \mathcal{O}(dx^2) \quad (1.40)$$

This scheme uses two values of the function, at $x+dx$ and $x-dx$. Arbitrary order schemes could thus be created by using more points. However, this theoretical solution leads to unsatisfactory results. Numerical computations are carried out with a fixed precision. For a double (64 bits) representation of real numbers, 52 bits are used to model the significant figures of the number. A maximum relative precision of $\epsilon = 2^{-53} \simeq 1.1e^{-16}$ is also reachable. For instance, assuming a domain of size 1, a reasonable well resolved mesh would typically achieve a minimum local grid size of $dx \simeq 1e^{-4}$. In the following, all the values and derivatives of f are supposed to be of order 1. A gradient computation that involves a division by dx would then have a maximum theoretical precision of $\epsilon/dx \simeq 1e^{-12} \simeq dx^3$. This order of precision is completely independent from the method used to compute gradients, and is an emanation of machine's limitations. This estimate can also be compared with the result from Taylor expansions such as Eq. 1.39. In this example, a scheme with a theoretical order larger than 3 would apparently not lead to any observable improvement of the actual order of the method. When high precision gradients are aimed at, numerical methods also need being analysed and optimized using other criteria.

Computing derivatives is equivalent to multiplying by ik in the Fourier space. Studying the dispersion properties of the discrete operators on this operation is also quite meaningful. To do so, the derivative of \exp^{ikx} is computed and divided by $(i \exp(ikx))$. The numerical value is then compared with the theoretical value. Examples of such computations are presented on figure 1.2. By optimizing the numerical schemes in the Fourier space, new techniques arise. A popular solution consists in constructing banded matrices A and B such that:

$$Af' = Bf \quad (1.41)$$

where f is the numerical vector to be differentiated and f' denotes the corresponding numerical approximation evaluated. An inversion of A is then required in this 'compact scheme' technique. Fosas de Pando *et al.* [2012] used for instance the Compact Upwind Low Dissipation (CULD) method developed by Adams & Shariff [1996]. Compact schemes have very good properties but are rather expensive as they require large mesh overlap between processors in parallel computations.

Another popular solution is to automatically optimize the coefficients associated with a stencil of a given width. This operation was for instance run by Berland *et al.* [2007] on an 11 points stencil. This method is the one used in our code, CNS2D. The interest of such an approach is visible on figure 1.2: 10-th order centered difference (3) and Berland's scheme (4) use the same number of points, but result in quite different performances in Fourier's domain.

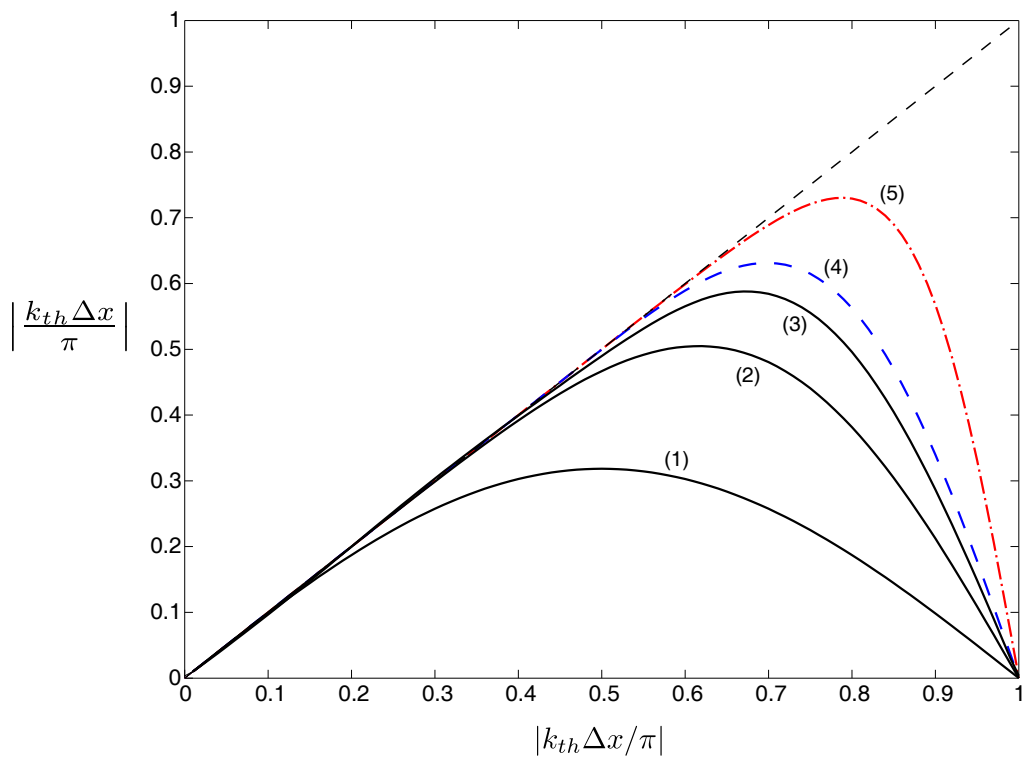


Figure 1.2: Comparison between dispersion relations of some differentiation operators. Dashed curve: optimal result based on Fourier transform. Black: centered finite difference. (1): order 2, (2): order 6, (3): order 10. Blue (4): 11-points stencil used in CNS2D. Red (5): Compact difference scheme CULD.

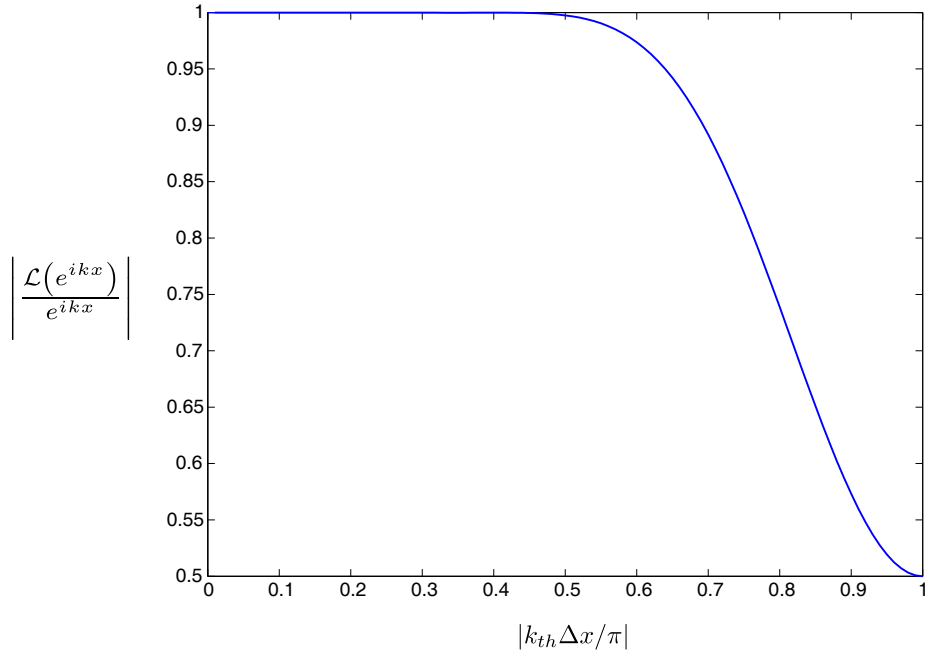


Figure 1.3: Gain of the filter used to damp non-resolved wavelengths.

Berland *et al.* [2007]’s operator provides an excellent precision on resolved wavenumbers. However, very little numerical damping is involved in such high-precision techniques. These computations also require for accuracy and stability purposes to damp non resolved frequencies. On figure 1.2, the CULD scheme curve (5) drops almost immediately to 0 when the results start differing from the theory. No filtering is required. On the contrary, the transition between non resolved and damped wavenumbers is much more progressive for our scheme (4). For $\frac{k_{th}\Delta x}{\pi} > 0.6$, additional dissipation is necessary. An appropriate filtering [Berland *et al.*, 2007] was also implemented. The gain of this filter is presented on figure 1.3. As expected, this filters preserves long wavelengths while damping wavenumbers larger than $\frac{\pi}{2\Delta x}$. This leads to accurate and reasonably stable computations. It is applied at the end of every time-step.

Once the fluxes are estimated, differentiated, computing the sources terms seems quite straightforward in compressible simulations. However, the CFL condition creates a theoretical constraint on the time step. But most of all, reaction rates can be extremely stiff, often replacing acoustics as the time-step limiting term in combustion computations.

1.1.3.2 Time Integration of Chemistry

Time-stepping is handled through an explicit fourth-order Strong Stability Preserving Runge-Kutta method [Ketcheson, 2008]. Optionally, during each intermediate Runge-Kutta step, the reaction rate $\dot{\omega}$ is computed by solving the system:

$$\frac{\widetilde{\rho E}(t+dt) - \rho E(t)}{dt} = \Delta Q \dot{\omega}(t+dt), \quad (1.42)$$

$$\frac{\widetilde{\rho Y}(t+dt) - \rho Y(t)}{dt} = -\dot{\omega}(t+dt). \quad (1.43)$$

where the reaction rate $\dot{\omega}(t+dt)$ will be the one used for time integration during the current time-step. In this technique, $\widetilde{\rho E}(t+dt)$ and $\widetilde{\rho Y}(t+dt)$ are estimated and exclusively used to compute $\dot{\omega}$. The time step dt refers to the simulation's time step -and not to the intermediate Runge Kutta step. This procedure is also not a fractional time stepping method, but a technique intended to relax the reaction term. This algorithm was used for the critical phases of initialization, ignition and baseflow computation. The procedure was switched off during non-linear simulations as it locally reduces the precision of the time stepper to first order.

Once the numerical techniques is chosen, implementing them as a highly scalable software is quite challenging. In CNS2D, this is achieved using MPI communications with the PETSc library.

1.1.3.3 Parallelism in CNS2D

CNS2D is a massively parallelisable code. It was written in C. MPI communications are handled through the PETSc library. Linear algebra operations are done with the SLEPc library. Throughout the development phase, performance was of prime interest. Indeed, a technical constraint for our computations was the 24h walltime limit on national clusters (Curie (TGCC), Jade and Occigen (CINES)). Besides, no restart procedure is implemented in the SLEPc library. Reaching a good scaling was also crucial. This was achieved by minimizing MPI communications. In parallel computations, each processor owns a specific piece of the mesh along with some regularly updated ghost values used to compute fluxes. This situation is illustrated on figure 1.4 A naive way to compute for instance inviscid fluxes would lead to the following algorithm:

Data: Υ

Result: $\partial \mathbf{F}_e^x / \partial x, \partial \mathbf{F}_e^r / \partial r$

Compute \mathbf{F}_e^x ;

Update ghost values of \mathbf{F}_e^x with MPI ;

Compute $\partial \mathbf{F}_e^x / \partial x$;

Compute \mathbf{F}_e^r ;

Update ghost values of \mathbf{F}_e^r with MPI ;

Compute $\partial \mathbf{F}_e^r / \partial r$;

end

In this process, two MPI communications phases are required. If viscous fluxes were computed as well, six MPI communications phases would be required. On modern hardware, transferring data between processors takes significantly more time than computing local multiplications. A way to take advantage of this situation is to do:

Data: Υ

Result: $\partial \mathbf{F}_e^x / \partial x, \partial \mathbf{F}_e^r / \partial r$

Update ghost values of Υ with MPI ;

Compute \mathbf{F}_e^x ;

Compute \mathbf{F}_e^x on ghost cells ;

Compute $\partial \mathbf{F}_e^x / \partial x$;

Compute \mathbf{F}_e^r ;

Compute \mathbf{F}_e^r on ghost cells ;

Compute $\partial \mathbf{F}_e^r / \partial r$;

end

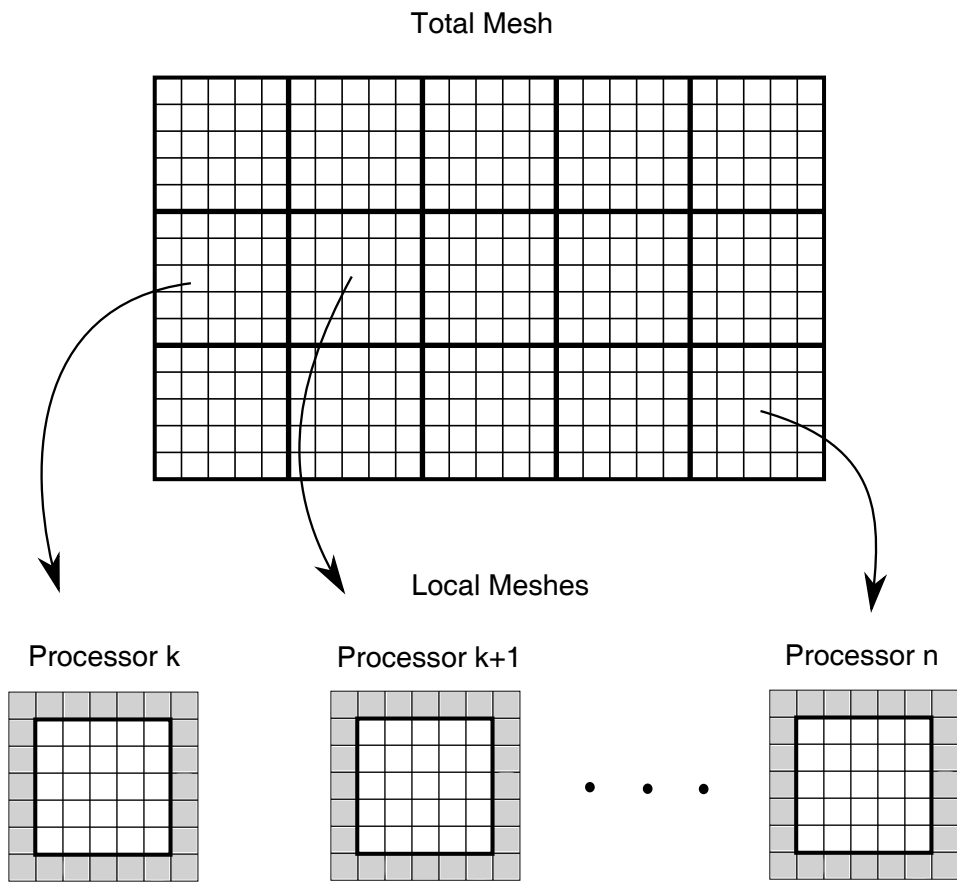


Figure 1.4: Mesh distribution on processors. Gray areas are ghost cells.

In this algorithm, only one MPI communication phase is required, and only four when viscous fluxes are computed. This presents two advantages: first, when keeping the number of CPU constant, the total computational time is reduced by about 20%; second, the scalability of the code is improved by 10% to 20% depending on the platform. A scalability factor of 1 was thus preserved with up to 800 processors for the largest configuration tested with 10.9 millions degrees of freedom, and an overall speed-up factor of 2 in walltime was measured on CEA's Curie cluster.

1.1.4 Linear Algebra Algorithms

1.1.4.1 Creating the Linear and Adjoint Operators

In our problem, the state space vector Υ is of the order of a few millions of degrees of freedom. No explicit inversion or direct computation of eigenvalues is possible. All the algorithms presented in this section can also be used in a matrix-free mode: no explicit access to matrices elements is necessary. Only the images of vectors by the linear operator and its adjoint are required. In order to generate such images, two families of strategies coexist in the fluid mechanics community. A first possibility is to derive the direct and adjoint linear equations from the continuous equations [Marquet *et al.*, 2008]. However, this solution is technically complex for compressible reactive flows and may be imprecise from a numerical point of view. Indeed, in order to keep a good conditioning of our methods, the operator A and its adjoint A^* should respect for all vectors \mathbf{x} and \mathbf{y} the scalar product relation

$$\mathbf{y}^* A \mathbf{x} = (A^* \mathbf{y})^* \mathbf{x} \quad (1.44)$$

Relying on an equation-based adjoint makes the result implementation-dependent, which may create numerical discrepancies in equation 1.44. Instead, the numerical adjoint method will be used here [Fosas de Pando *et al.*, 2012]. This technique relies on the separation of the non-linear computation into a succession of individual simple steps. Each step is linearised individually to provide functions emulating linear operators A_i , the succession of which create the linear operator:

$$A \Upsilon = A_0(A_1(\dots(A_n \Upsilon)\dots)) \quad (1.45)$$

For the adjoint operator, the adjoint of each individual step is taken, and the structure of the linear code is reversed:

$$A^* \Upsilon = A_n^*(A_{n-1}^*(\dots(A_0^* \Upsilon)\dots)) \quad (1.46)$$

During this project, the previous formalism was used to optimize the frequency response of the system in order to carefully study noise-generation mechanisms in flames.

1.1.4.2 Optimizing the System's Linear Frequency Response

In the following, the variable $\lambda_i(M)$ denotes the i -th eigenvalue of the operator M . Moreover, we define:

$$\lambda_{max}(M) = \max_i \lambda_i(M) \quad (1.47)$$

Using the previous definitions, it is possible to solve 2-norm based optimization problems. In this thesis, the case of the permanent regime response to a forcing f at the frequency ω is considered. This corresponds to the infinite-time limit of:

$$\frac{\partial \Upsilon}{\partial t} = A\Upsilon - e^{i\omega t} f \quad (1.48)$$

The solution can then be written as:

$$\Upsilon(t \rightarrow \infty) = \Upsilon_{\infty} e^{i\omega t} \quad (1.49)$$

and, using the definition of the resolvent from equation 7:

$$\Upsilon_{\infty} = (A - i\omega Id)^{-1} f = Rf \quad (1.50)$$

This equation can be generalized: if a windowing in space, a limitation on the form of the forcing or a norm is imposed, a multiplication by a matrix M_{in} can be added. The same reasoning can be applied on the output with another matrix M_{out} . Taking into account these additions, the resolvent becomes:

$$R = M_{out}(A - i\omega Id)^{-1} M_{in} \quad (1.51)$$

In the following, this generalized definition will be assumed. We wish to maximize an output λ_{out} of R based on a unitary forcing f_0 .

$$\lambda_{out} = \max_{\|f\|=1} \|\Upsilon_{\infty}\|^2 = \max_{\|f\|=1} \|Rf\|^2 \quad (1.52)$$

As we are working with the 2-norm:

$$\lambda_{out} = \max_f \frac{f^* R^* R f}{f^* f} \quad (1.53)$$

The matrix R^*R is Hermitian. Then:

$$\lambda_{out} = \lambda_{max}(R^*R) = f_{opt}^* R^* R f_{opt} \quad (1.54)$$

where f_{opt} is the normalized eigenvector of R^*R corresponding to λ_{max} . This eigenvalue problem was solved using the explicitly restarted Arnoldi algorithm implemented in the SLEPc library [Hernandez *et al.*, 2005]. This method is based on the construction of a Krylov subspace. The main technical difficulty then lies in the evaluation of images of vectors by the operators $(A - i\omega Id)^{-1}$ and $(A^* + i\omega Id)^{-1}$. We proceed along classical lines by computing $(A - i\omega Id)^{-1}f$ through the time-stepping of:

$$\frac{\partial \Upsilon}{\partial t} = A\Upsilon - i\omega\Upsilon - f \quad (1.55)$$

$$\Upsilon(t=0) = 0 \quad (1.56)$$

Or equivalently:

$$\frac{\partial \tilde{\Upsilon}}{\partial t} = \tilde{A}\tilde{\Upsilon} \quad (1.57)$$

$$\tilde{\Upsilon}(t=0) = \begin{pmatrix} 0 \\ f \end{pmatrix} \quad (1.58)$$

where:

$$\tilde{\Upsilon} = \begin{pmatrix} \Upsilon \\ f \end{pmatrix} \quad (1.59)$$

$$\tilde{A} = \begin{pmatrix} A - i\omega Id & -Id \\ 0 & 0 \end{pmatrix} \quad (1.60)$$

The adjoint of this equation is straightforward:

$$\frac{\partial}{\partial t} \begin{pmatrix} \Upsilon \\ f \end{pmatrix} = \frac{\partial \tilde{\Upsilon}}{\partial t} = \tilde{A}^* \tilde{\Upsilon} = \begin{pmatrix} A^* + i\omega Id & 0 \\ -Id & 0 \end{pmatrix} \begin{pmatrix} \Upsilon \\ f \end{pmatrix} \quad (1.61)$$

$$\tilde{\Upsilon}(t=0) = \begin{pmatrix} \Upsilon_\infty \\ 0 \end{pmatrix} \quad (1.62)$$

which is integrated in time until a steady state is achieved. It is quite straightforward to see that the steady-state of Eq. 1.55 computes $\Upsilon_\infty = (A - i\omega Id)^{-1}f$. For the adjoint, simply rewriting the previous set of equations in terms of f leads to:

$$\frac{\partial^2 f}{\partial t^2} = A^* \frac{\partial f}{\partial t} + i\omega \frac{\partial f}{\partial t} \quad (1.63)$$

$$f(t=0) = 0 \quad (1.64)$$

$$\frac{\partial f}{\partial t}(t=0) = -\tilde{\Upsilon}(t=0) = -\Upsilon_\infty \quad (1.65)$$

By integrating Eq. 1.63 with respect to time between 0 and t , the previous set of equations becomes:

$$\frac{\partial f}{\partial t} + \Upsilon_\infty = A^* f + i\omega f \quad (1.66)$$

$$f(t=0) = 0 \quad (1.67)$$

When reaching a steady state, the expected expression $f = (A^* + i\omega Id)^{-1}\Upsilon_\infty$ is thus obtained. The advantage of using Eq. 1.61 over Eq. 1.66 lies in the numerical precision of the adjoint. Equation 1.61 is the strict computational adjoint of Eq. 1.55, which ensures the convergence of our eigenvalues algorithms.

1.1.4.3 Derivative of the Eigenvalue of the Optimal Frequency Response

Because of the estimation of R and R^* , and even though R^*R is an Hermitian matrix, computing its eigenvectors is an expensive process. When the user's interest is focused on $\lambda_{out}(\omega)$, it is possible to quickly evaluate $\partial\lambda_{out}/\partial\omega$ by a mere matrix multiplication sequence on the eigenvector

$$\frac{\partial\lambda_{out}}{\partial\omega} = 2\text{Re} (if_{opt}^* R^* M_{out} (A - i\omega Id)^{-1} (A - i\omega Id)^{-1} M_{in} f_{opt}) \quad (1.68)$$

This expression can be proved quickly by noticing that Id and A commute, thus leading to

$$\frac{\partial(A - i\omega Id)^{-1}}{\partial\omega} = i(A - i\omega Id)^{-2} \quad (1.69)$$

This expression implies

$$\frac{\partial R}{\partial\omega} = iM_{out}(A - i\omega Id)^{-2}M_{in} \quad (1.70)$$

The second useful intermediate result stems from the normality of the (real-valued) eigenvector f_{opt}

$$\|f_{opt}\|^2 = f_{opt}^* f_{opt} = 1 \quad (1.71)$$

which implies

$$f_{opt}^* \frac{\partial f_{opt}}{\partial\omega} = 0 \quad (1.72)$$

Last, by definition, λ_{out} is the eigenvalue of R^*R associated with the eigenvector f_{opt}

$$R^*Rf_{opt} = \lambda_{out}f_{opt} \quad (1.73)$$

Using these equations, and differentiating Eq. 1.54 with respect to ω leads to

$$\frac{\partial\lambda_{out}}{\partial\omega} = \frac{\partial f_{opt}^*}{\partial\omega} R^*Rf_{opt} + f_{opt}^* \frac{\partial R^*}{\partial\omega} Rf_{opt} + f_{opt}^* R^* \frac{\partial R}{\partial\omega} f_{opt} + f_{opt}^* R^* R \frac{\partial f_{opt}}{\partial\omega} \quad (1.74)$$

$$= 2\text{Re} \left(\lambda_{out} f_{opt}^* \frac{\partial f_{opt}}{\partial\omega} + f_{opt}^* R^* \frac{\partial R}{\partial\omega} f_{opt} \right) \quad (1.75)$$

$$= 2\text{Re} \left(f_{opt}^* R^* \frac{\partial R}{\partial\omega} f_{opt} \right) \quad (1.76)$$

Hence Eq. 1.68 is found.

In the special case of $M_{in} = M_{out} = Id$, Eq. 1.68 can be further simplified to

$$\frac{\partial\lambda_{out}}{\partial\omega} = 2\lambda_{out}\text{Re} \left(i f_{opt}^* R f_{opt} \right) \quad (1.77)$$

Those very general equations were applied to an M-flame stabilized on an annular injector. The following section presents useful details on this specific geometry.

1.2 Geometry and Baseflow

1.2.1 Geometry Presentation

CNS2D handles multidomain rectilinear structured geometries. The numerical set-up used in the computation is presented on figure 1.5. The computational domain is separated in two regions, the injection annular tube and an expanding area. The annular injector has wall boundary conditions. The inlet is imposed through mono-dimensional characteristic

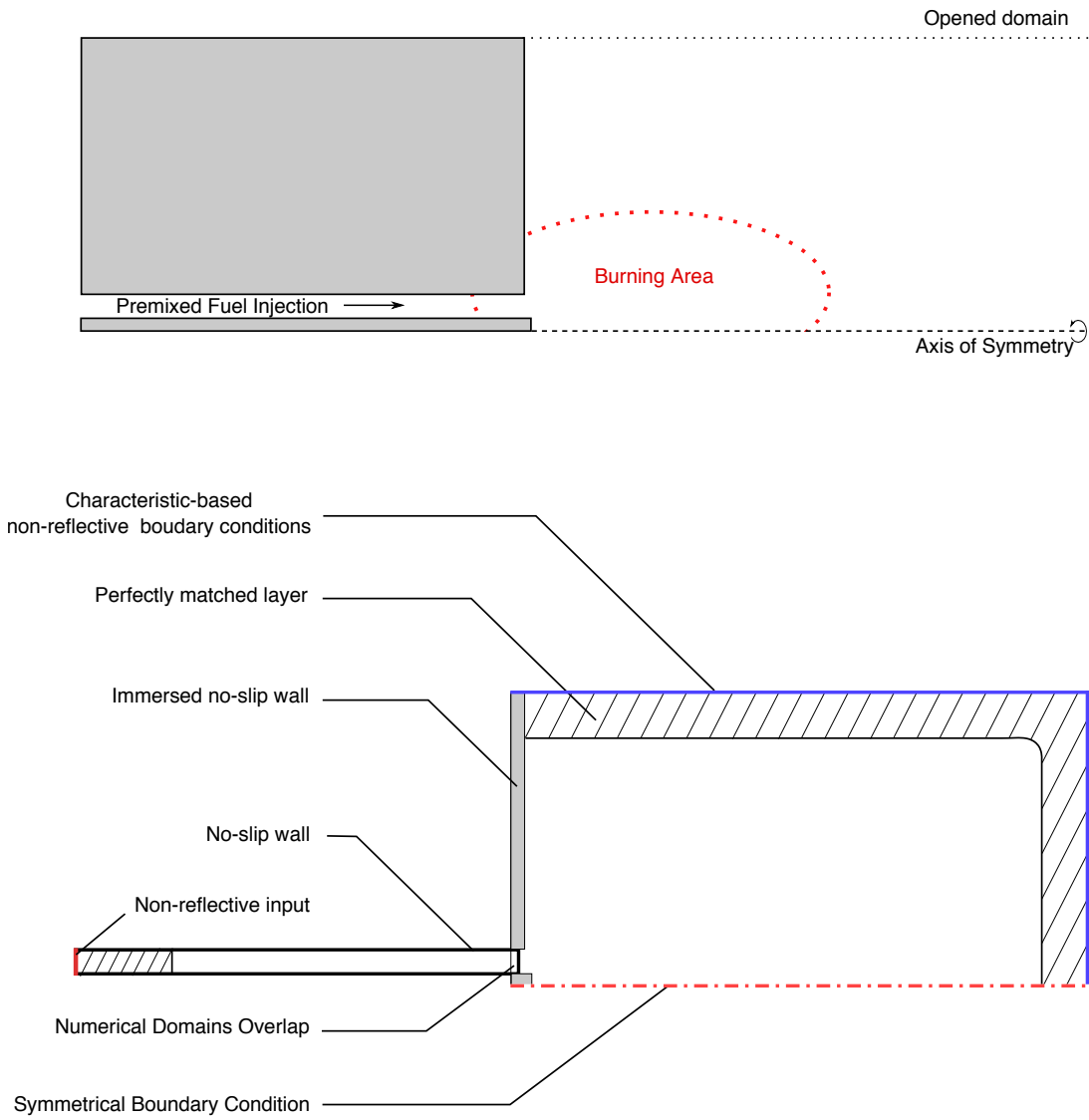


Figure 1.5: *Numerical Geometry used in CNS2D simulations. Top: reference case computed. Bottom: corresponding numerical implementation.*

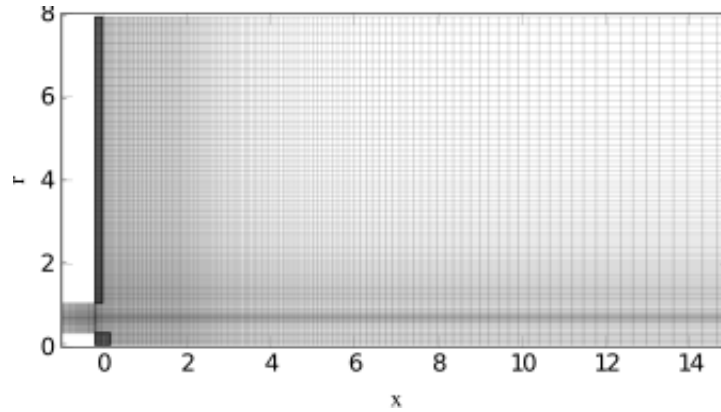


Figure 1.6: Typical M-flame mesh used in chapter 2, coarsened four times in each direction. The shaded regions are treated as non-slipping walls.

boundary conditions [Poinsot & Lele, 1992]. An overlap area with the second region ensures the continuity of the solution across both domains. The expansion area includes immersed boundary conditions for the injector's walls, shown in dark on figure 1.6; a symmetrical boundary on the jet axis; and characteristic-based non reflective boundary conditions at the open sides of the domain. When required, acoustic sources can be distributed inside the tube. A perfectly matched layer [Tam *et al.*, 1998] further damps exiting acoustic waves both at the inlet and at the outlet.

By definition, the tube external radius is set to $r_0=1$, the exit being located at $x_0=0$. In this work, and by analogy with Schuller *et al.* [2003a], the rod has a radius of $r_1=3/11$ and ends at $x_1=2/11$. Tube's dimensions were taken long enough to obtain a fully developed velocity profile. In chapter 2, an injector length of 60 was chosen as to contain a full acoustic wavelength at the hydrodynamic characteristic frequency. This setting helped validating the acoustic propagation computed by the code. In chapter 4, the tube length was reduced to 20.

Mesh convergence in the reaction area was the object of a specific care. A minimum of 15 points in the reaction layer was imposed in a first coarse mesh, and 20 points in a second thinner mesh. These levels correspond to respectively about 18 and 20 points in boundary layers, leading to 2.8 and 3.5 millions degrees of freedom respectively. The same non-linear simulation was computed with those two meshes. No difference on baseflow flame position was observed. The coarse mesh was used to compute acoustic forcing simulations presented in chapter 2, and is shown in figure 1.6. Results in chapter 3 are based on the thinnest mesh, as adjoint computations typically require very finely resolved meshes to suppress any spurious oscillation.

1.2.2 Baseflow

Linear simulations were led in the case of an M-flame. By definition, our baseflow is a solution of:

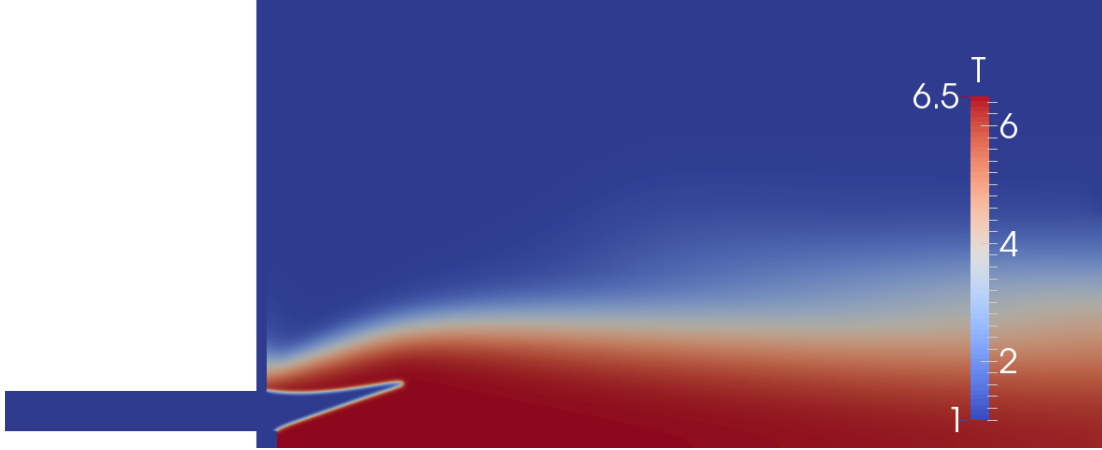


Figure 1.7: Chapter 2 M-flame baseflow temperature profile.

$$\nabla \cdot (\rho_0 \mathbf{u}_0) = 0, \quad (1.78)$$

$$\nabla \cdot (\rho_0 \mathbf{u}_0 \otimes \mathbf{u}_0) = -\nabla p_0 + \nabla \cdot \underline{\boldsymbol{\tau}}_0, \quad (1.79)$$

$$\nabla \cdot (\rho_0 \mathbf{u}_0 E_0) = \dot{\omega}_{f,0} \Delta h_f - \nabla \cdot \mathbf{q}_0 + \nabla \cdot (\underline{\boldsymbol{\tau}}_0 \cdot \mathbf{u}_0), \quad (1.80)$$

$$\nabla \cdot (\rho_0 \mathbf{u}_0 Y_{f,0}) = -\dot{\omega}_{f,0} + \nabla \cdot (\rho_0 D \nabla Y_{f,0}). \quad (1.81)$$

In order to obtain this state vector, the non-linear reactive Navier-Stokes equations were filtered with a Selective Frequency Damping technique [Åkervik *et al.*, 2006]. In this technique, if Υ_0 is the state space to be converged, and \mathcal{L} is the Navier-Stokes operator, an auxiliary variable $\tilde{\Upsilon}$ is introduced and the following set of equations is solved:

$$\dot{\Upsilon}_0 = \mathcal{L}(\Upsilon_0) + \tau (\tilde{\Upsilon} - \Upsilon_0) \quad (1.82)$$

$$\dot{\tilde{\Upsilon}} = \frac{1}{\delta} (\Upsilon_0 - \tilde{\Upsilon}) \quad (1.83)$$

The choice of τ and δ fix respectively the gain and the cut-off frequency of the method. If the system is destabilized by a mode with a finite frequency, there exist a set of parameters (τ, δ) that will make the system converge to a steady state. As an example, the baseflow used in chapter 2 was computed in about 4000 CPU hours with $\tau = 1$ and $\delta = 5$. The corresponding temperature profile is presented on figure 1.7.

1.2.3 Acoustic Sources

Creating clean acoustic waves is a complex procedure. By definition, the resulting waves should propagate at the speed of sound. The entropy and vorticity waves induced by our sources should also be negligible. By supposing acoustic sources are associated with an

entropy-free perturbation, the following forcing shape is found:

$$f(r, x) = \begin{pmatrix} \rho_f(x) \\ \rho_f(x)u_{x,0}(r, x) \\ \rho_f(x)u_{r,0}(r, x) \\ \rho_f(x) \left(\frac{c_0^2}{\gamma - 1} + 0.5(u_{x,0}^2 + u_{r,0}^2) \right) (r, x) \\ \rho_f(x)Y_0(r, x) \end{pmatrix} \quad (1.84)$$

with

$$\rho_f(x) = \frac{\rho_{loc}(x)}{\int_{-\infty}^{+\infty} \rho_{loc}(x') dx'}, \quad (1.85)$$

$$\rho_{loc}(x) = \exp\left(-\frac{(x - x_{ac})^2}{\sigma_{ac}^2}\right) \quad (1.86)$$

where x_{ac} refers to the axial position of the acoustic sources and σ_{ac} to the characteristic width of the forcing region. σ_{ac} should be taken as small as possible but large enough to ensure a good resolution of the shape of the forcing. In practice, the forcing area is taken at least ten points wide to enforce a smooth forcing shape. This form of sources was found to yield good results for linear simulations. It was also used in chapter in the computations presented in chapter 2.

Such sources however lead to the generation of significant vortical and entropy waves at high forcing amplitudes. In order to circumvent this problem, a fit on the form of the numerically observed acoustic waves in the tube was evaluated:

$$g(r) = (1 - \exp(-122.3\sqrt{u_0}r)) \quad (1.87)$$

$$u_{fit} = u_{x,0} + 0.6378u_{x,0}^2 + \frac{1}{\text{Ma}}g(1-r)g(r-r_{rod}) \quad (1.88)$$

$$f(r, x) = \begin{pmatrix} \rho_f(x) \\ \rho_f(x)u_{fit} \\ 0 \\ \rho_f(x) \left(\frac{c_0^2}{\gamma - 1} - 0.5(u_{x,0}^2 + u_{r,0}^2) + u_{x,0}u_{fit} \right) \\ \rho_f(x)Y_0(r, x) \end{pmatrix} \quad (1.89)$$

Those forcing values were found by numerically fitting an acoustic wave propagating in the injector. This fit is valid for our simulation Reynolds number only, i.e. for a Reynolds number of 1500. The comparison between these two forcing strategies is presented figure 1.8. The radial velocity, density and fuel mass fraction profiles are not shown as they are constant for all forcing techniques along the injector's cross section. The fits of the axial velocity and of the total energy are improved in this new technique. Besides, a filter on entropy and vortical waves was implemented in a small area downstream the sources. It takes the form of a perfectly matched layer penalizing any entropy or radial velocity fluctuation. These combined techniques proved efficient at generating a clean acoustic forcing in all non-linear simulations.

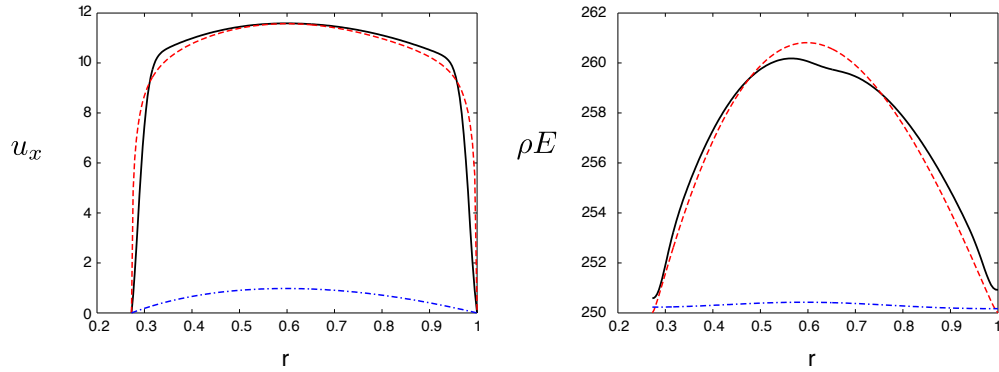


Figure 1.8: Acoustic forcing shapes in axial velocity (right) and total energy (left). Continuous black line: reference acoustic wave, computed with a linear simulation. Point-dotted blue line: linear acoustic forcing shape. Dotted red line: non-linear acoustic forcing shape.

1.3 Conclusion

In this chapter, the equations implemented in our main code, CNS2D, are presented. They set a layout for axisymmetric lean premixed flame computations. These equations can be solved within a non-linear or linear framework. Sensitivity analysis allows to carry out some optimization in a 2-norm sense. Specific attention has been paid to performances.

The geometry considered in this thesis is an opened annular burner handled in a multidomain approach. The baseflow corresponding to an M-flame was converged on this configuration. It can be submitted to various forcing shapes placed in the injection tube. Sound sources were in particular carefully designed to minimize the spurious hydrodynamic structures generated along with the intended acoustic waves.

In the next chapter, the linear dynamics of our M-flame submitted to acoustic perturbations will be considered in details.

Chapter 2

Linear Acoustic Forcing

*This chapter is divided in three parts. First, the framework of this study is recalled, along with the main results. The second part contains the full corresponding article published in *Physic of Fluids*. It explores the influence of flame heating on the resulting flow disturbances generated upstream acoustically forced premixed flames. The last part describes a fitting technique that allows to convert an impulse response to a high-precision, low order state-space model.*

2.1 Motivation

Prediction of thermoacoustic instabilities requires some knowledge on the frequency response of the combustion chamber. The detailed design of the engine is not known *ex ante*, neither its eigenfrequencies. For this reason, the acoustically forced combustor dynamic is often studied as a first step. This methodology was adopted here. In the following, a study of the perturbative dynamic of an M-flame submitted to an oscillating acoustic field is presented. The linear capacities of our numerical code were used both to conduct an efficient system identification and to set-up a physics-based operator decomposition.

Experimentally, the most natural way to study such systems is to evaluate the flame response to some acoustic harmonic forcing with a controlled shape, frequency and amplitude. A first range of techniques evaluates the combustor impedance matrix [Paschereit *et al.* \[2002\]](#). Alternatively, the flame transfer function can be evaluated [[Ducruix *et al.*, 2000](#)]. Both these methods can be used to evaluate the growth rate of a potential thermoacoustic instability, even in a complex combustor geometry [[Selle *et al.*, 2004](#); [Nicoud *et al.*, 2007](#)]. Ultimately, such flame linear reduced order models were typically used as a designing guide for active [Dowling & Morgans \[2005\]](#) or passive [Bellucci *et al.* \[2004\]](#) controllers.

Numerically, conducting a frequency-by-frequency parametric study is computationally expensive [[Poinsot, 2014](#)]. In a non-linear framework, specific, white-noise forcing methodologies were developed to evaluate the flame transfer function [[Tay-Wo-Chong *et al.*, 2010](#)]. However, such methodologies are limited by the potential non-linearities of the system, and fairly long time series are required for the system identification algorithms to converge. Alternatively, conducting a flame study in a linear framework may be seen as minimizing flame sensitivity to flow perturbations. Flames move, they are often unstable, and the flow in most combustion chambers is typically turbulent. However, from a theoretical point of view, much information can be extracted from such an analysis. In particular, acoustic

waves exhibit a linear behavior for a wide range of amplitudes [Pierce, 1989], and they are ubiquitous in flame dynamics. However, their interactions with the flow are quite challenging to study, as they can be analytically defined and identified for only very simple flows [Doak, 1973]. In non-linear simulations, specific post-processing procedures must be applied to isolate it from the ambient dynamic, relying on Fourier transform or wavelets analysis for instance [Grizzi & Camussi, 2012]. This difficulty stems from the energy transfers from and to acoustics in a wide variety of flow structures such as decaying vortices, shear layers or, of course, flames. Traditionally, non reactive linear flows are divided in three waves: acoustic, vortical and entropy wave. With the reaction from Eq. 1.35, a fuel mass fraction wave can be superimposed to these. These structures can interact, decay or be amplified by the baseflow. Understanding flow-acoustic interactions comes to understanding these energy transfers and their underlying dynamics. In particular, the role of flames in these processes deserves a close study.

Flames have an intrinsic multiscale dynamic and thus present specific difficulties. Very much like a boundary layer, each scales interact one with another. Flame structure is defined at diffusion scale, and predetermines the mesoscale flame stability properties [Zeldovich *et al.*, 1985]. Combustor's scale features pilots in turn flame dynamics. Burner's geometry or the thermal properties of its walls constitute key factors in determining the averaged flame position and its response to flow perturbations [Duchaine *et al.*, 2011; Cuquel *et al.*, 2013a]. These very rich interactions have recently been handled through LES simulations [Hermeth *et al.*, 2014], asymptotic expansion [Luzzato *et al.*, 2013] or global modes computation [Qadri, 2014]. However, distinguishing the direct effects of chemistry from hydrodynamic-related modes is often challenging. A mere question exemplifies this issue: if it was possible to maintain a strong local, subsonic temperature gradient without a chemical reaction, what would it dynamically change with respect to an actual flame? This question is important when considering reduced order models. Indeed, it is well known that flame heating has an important impact on the overall shape of the flame, on the flow streamlines [Zeldovich *et al.*, 1985] and on its flame transfer function [Cuquel *et al.*, 2013b]. Besides, recent studies [Fleifil *et al.*, 1996; Waugh *et al.*, 2013] have hypothesized that flame heating processes had a relevant effect on unsteady flame dynamics only when displacements were large enough to yield a parametric instability. This 'cold flame assumption' is worth considering in light of a linear study. More specifically, the impact on flame dynamics of a density variation through the reaction zone will be studied. Our analysis is based on the additivity properties of linear operators and separates purely chemical effects from the consequences of the baseflow's sharp temperature gradients. A model for the upstream flow perturbations will then be presented and validated. This work was published in Physics of Fluids [Blanchard *et al.*, 2015] and is reproduced in the following section.

2.2 Article: Response Analysis of a Laminar Premixed M-Flame to Flow Perturbations

Response analysis of a laminar premixed M-flame to flow perturbations using a linearized compressible Navier-Stokes solver

M. Blanchard¹, T. Schuller^{2,3}, D. Sipp⁴, and P.J. Schmid⁵

¹ LadHyX, CNRS and Ecole Polytechnique, 91128 Palaiseau, France

²CNRS, UPR 288, Laboratoire d'Energétique Moléculaire et Macroscopique Combustion (EM2C), Grande Voie des Vignes, 92290 Chatenay-Malabry, France

³ Centrale-Supélec, Grande Voie des Vignes, 92290 Chatenay-Malabry, France

⁴ONERA-DAFE, 8 rue des Vertugadins, 92190 Meudon, France

⁵Department of Mathematics, Imperial College London, London, SW7 2AZ, United Kingdom

March 2015

Abstract

The response of a laminar premixed methane-air flame subjected to flow perturbations around a steady state is examined experimentally and using a linearized compressible Navier-Stokes solver with a one-step chemistry mechanism to describe combustion. The unperturbed flame takes an M-shape stabilized both by a central bluff body and by the external rim of a cylindrical nozzle. This base flow is computed by a nonlinear direct simulation of the steady reacting flow, and the flame topology is shown to qualitatively correspond to experiments conducted under comparable conditions. The flame is then subjected to acoustic disturbances produced at different locations in the numerical domain, and its response is examined using the linearized solver. This linear numerical model then allows the componentwise investigation of the effects of flow disturbances on unsteady combustion and the feedback from the flame on the unsteady flow field. It is shown that a wrinkled reaction layer produces hydrodynamic disturbances in the fresh reactant flow field that superimpose on the acoustic field. This phenomenon, observed in several experiments, is fully interpreted here. The additional perturbations connected by the mean flow stem from the feedback of the perturbed flame sheet dynamics onto the flow field by a mechanism similar to that of a perturbed vortex sheet. The different regimes where this mechanism prevails are investigated by examining the phase and group velocities of flow disturbances along an axis oriented along the main direction of the flow in the fresh reactant flow field. It is shown that this mechanism dominates the low-frequency response of the wrinkled shape taken by the flame and, in particular, that it fully determines the dynamics of the flame tip from where the bulk of noise is radiated.

Keywords — flame dynamics, flame transfer function, linearized simulation

1 Introduction

This study is motivated by a general lack of understanding of the flame response to flow perturbations. This response is needed to determine the stability of combustors with respect to thermo-acoustic instabilities and to predict combustion noise emission from these systems Candel *et al.* (2009). These two issues cause several difficulties in the development of high-performance combustion systems, especially as improved efficiency and lower pollutant emission levels are concerned Lieuwen & Yang (2005); Lieuwen (2012). Gaining insight into the fundamental mechanisms that dominate the response of flames to unsteadiness is mandatory to reducing combustion noise emission and self-sustained combustion instabilities in real systems.

There are different ways to analyze the response of flames to flow perturbations which are briefly reviewed below. An alternative methodology is proposed in this work where the reacting base flow is calculated by direct simulations of the compressible Navier-Stokes, energy and species transport equations. The response of this flow to small perturbations is then computed by solving the linearized set of equations around this base state. This linearized solver allows the rapid determination of flame frequency and impulse responses to flow disturbances over the full frequency range of interest and the componentwise investigation of different contributions yielding large unsteady heat release rate fluctuations or maximum sound radiation. This approach offers a general framework for flow sensitivity analysis and optimal forcing.

Before proceeding, it is worth analyzing the current strategies used to infer the response of flames to flow perturbations. In realistic systems with complex geometries, many techniques have been developed to determine the flame frequency response to harmonic flow excitations. Acoustic characterizations are preferred when optical access is limited, as is often the case in real systems Paschereit *et al.* (2002); Schuermans *et al.* (2010b). When optical access is possible, this response is generally characterized experimentally by determining flame transfer functions or, more recently, flame describing functions relating heat release rate disturbances to flow rate or mixture composition oscillations produced at some location in the injector for different flow and excitation conditions Durox *et al.* (2009); Kim & Hochgreb (2011); Kim *et al.* (2010); Schuermans *et al.* (2010a); Palies *et al.* (2011a); Schimek *et al.* (2011); Kim & Hochgreb (2011); Bobusch *et al.* (2014). These characterizations have proven valuable for linear and nonlinear stability analyses of the system dynamics; in addition, they are used to determine stability charts as the operating conditions of the combustor are modified Bade *et al.* (2013a,b); Noiray *et al.* (2008); Schuermans *et al.* (2010b); Palies *et al.* (2011b); Krebs *et al.* (2013).

With the rapid development of high-performance computing resources, it is nowadays also possible to capture the response of flames to flow disturbances in complex combustor geometries by solving the compressible Navier-Stokes equations in multi-species reacting flows using Large-Eddy Simulation (LES) tools Krediet *et al.* (2012); Tay Wo Chong & Polifke (2013); Hermeth *et al.* (2014). These simulations, however, remain difficult and incur considerable computational costs. For this reason, they are often limited to the analysis of the system response to a single forcing frequency or to the simulation of the dynamics of self-sustained oscillations initiated from small or finite-level initial perturbations to a limit cycle Staffelbach *et al.* (2009); Iudiciani &

Duwig (2011); Franzelli *et al.* (2012). System identification tools have also been applied to LES simulations to estimate the flame transfer function Tay Wo Chong *et al.* (2010); Tay-Wo-Chong *et al.* (2012). These techniques are based on the forcing of the flame using a small-amplitude broadband noise, assuming the flame response to be linear. There is thus an ongoing effort to develop low-order numerical and analytical models aiming at improving the description of the flame dynamics in configurations of increasing complexities at reduced computational effort.

In the case of premixed flames, these low-order models generally rely on a level-set description of the flame front motion that is reduced to a flame sheet separating the fresh reactants from the burnt gases. This interface propagates in the normal direction with the flame speed and is also advected by the flow. Assuming simplified flow and flame topologies and prescribing different types of flow perturbations, it is possible in many cases to describe wrinkles produced along the flame sheet and deduce the resulting heat release rate disturbances. Analytical expressions for flame transfer functions and, more recently, flame impulse responses were determined using this level-set description in different generic laminar and turbulent flow configurations Fleifil *et al.* (1996); Dowling (1999); Schuller *et al.* (2003b); Cho & Lieuwen (2005); Preetham *et al.* (2008); Altay *et al.* (2009); Palies *et al.* (2011c). These models highlight the different physical mechanisms influencing the flame response to the excitation and yield the appropriate dimensionless groups to analyze the response of flames featuring different shapes and subjected to different types of perturbations. They are of undeniable value to guide experimental characterizations in practical systems and to suggest control strategies.

There are, however, several difficulties to extend this level-set description to real systems characterized by complex flow topologies and complex interactions of the unsteady flame with the combustion chamber boundaries. The base flow and the flame shape are generally difficult to describe with analytical models in real systems. The way perturbations are produced and transported by or propagating through the flow is also complex to model, in particular when these disturbances interact with shear layers Matveev & Culick (2003); Birbaud *et al.* (2006, 2007); Palies *et al.* (2011d); Acharya *et al.* (2012). One explored possibility has been to couple the level-set description of the flame reaction sheet with the Navier-Stokes equations and then compute the response of this flow to excitations Rhee *et al.* (1995); Hartmann *et al.* (2011); Hemchandra (2012); Kashinath *et al.* (2013). This type of approach, relying on direct simulations of the Navier-Stokes equations, only differs by the way combustion is modeled. More detailed combustion models are now commonly used to simulate the response of flames to flow forcing Kornilov *et al.* (2009); Auzillon *et al.* (2011); Duchaine *et al.* (2011); Kedia *et al.* (2011).

A different approach is undertaken in this work, where only the steady, reacting base flow is solved by direct simulation of the nonlinear Navier-Stokes equations assuming that chemistry proceeds through one irreversible reaction. The unsteady response of the flame is subsequently determined by solving a linearized version of these equations around this base state. This type of approach is well-known and widely used in sensitivity analyses of non-reacting flows Garnaud (2012), but has only recently been applied to reactive flows Lemke *et al.* (2014); Qadri (2014). This strategy also differs from the acoustic perturbation equation formulation that has been developed to

analyze combustion noise Bui *et al.* (2008). In this hybrid approach, the noise sources are extracted from Large-Eddy simulations and the sound field is computed with an aeroacoustic solver, but the flame does not respond to the incident sound field. In the linear method presented herein, a steady base flame is computed and perturbations are supposed to develop around this base state without modifying it. The methodology is validated in a generic laminar configuration by comparison with experiments. It is then used to improve our understanding of the interactions taking place between the unsteady flow and the flame in response to imposed excitations.

It is thus worth synthesizing the current state of knowledge of unsteady flames and flow-interactions leading to heat release rate disturbances. Only perturbation scales much larger than the chemical-reaction and thermal thicknesses are considered, such that the reaction layer where combustion takes place can legitimately be approximated by an infinitely thin interface separating the reactants from the combustion products Kerstein *et al.* (1988); Peters (2000). This approximation is valid because flames are known to act as low-pass filters for flow perturbations with a cut-off frequency much lower than frequencies associated with disturbances interfering with the flame's internal structure Ducruix *et al.* (2003). Most studies have considered the canonical problem of flame wrinkling produced by acoustic, hydrodynamic or mixture-composition perturbations. For flame sheets inclined with respect to the main direction of the flow, it has been shown that flame wrinkles are produced by disturbances normal to the reaction layer which are convected by the mean flow along the flame front Boyer & Quinard (1990). The flame motion corresponds then to a delayed system consisting of the convection of flame-root oscillations as well as flow disturbances integrated along the flame front Schuller *et al.* (2003b); Preetham *et al.* (2008). These wrinkles originate from all conceivable mechanisms altering the flame displacement speed or the velocity field. The physics associated with these different contributions is currently well described, and many effects can be captured by low-order models.

However, the interactions of flame wrinkles with the flow field are still an active field of research. The effects of gas expansion through the flame have been considered in the context of flame stability Zeldovich *et al.* (1985); Bychkov & Liberman (2000). These efforts led to an accurate description of the Landau-Darrieus instability through linear Pelce & Clavin (1982) and nonlinear Sivashinsky (1977); Pan & Fursenko (2008) analyses. When the system is stable, it is known from experiments that acoustically perturbed flames or flames in a steady flow subjected to oscillations of its anchoring points produce hydrodynamic disturbances in the vicinity of the reaction layer Birbaud *et al.* (2006); Kornilov *et al.* (2007). These disturbances have first been detected in velocity measurements along the symmetry axis of conical flames subjected to acoustic excitations Baillot *et al.* (1992). Three regimes have been identified Birbaud *et al.* (2006). At low frequencies, the phase lag of velocity fluctuations recorded in the fresh stream of reactants scales with the inverse of the injection flow velocity. At high frequencies, these disturbances propagate in the entire fresh stream at the speed of sound. At intermediate frequencies, transitions between these two regimes can be detected, with abrupt phase changes. The region where flow disturbances are convected narrows closer to the flame front as the forcing frequency increases. This type of feedback has also been identified for flames subjected to mixture-composition oscillations Birbaud *et al.* (2008); Hemchandra (2012). However, the detailed mech-

anisms by which the flame modifies the upstream, perturbed flow field remain to be determined and modeled. These issues constitute the second objective of the present work.

The article is organized as follows. Results of experiments conducted for a laminar premixed methane/air M-flame subjected to acoustic forcing are presented in section 2. The numerical methodology developed to capture the base flow is then presented in section 3 together with the simulations of the steady configuration. This section ends with the description of the linear solver. Results for the flame impulse and flame transfer functions are then compared to measurements in section 4. This comparison is used to validate the developed methodology and to identify the flow regions where large heat release rate fluctuations and noise emissions take place. Effects of the flame dynamics on the unsteady flow field are examined in section 5.

2 Reference experiments

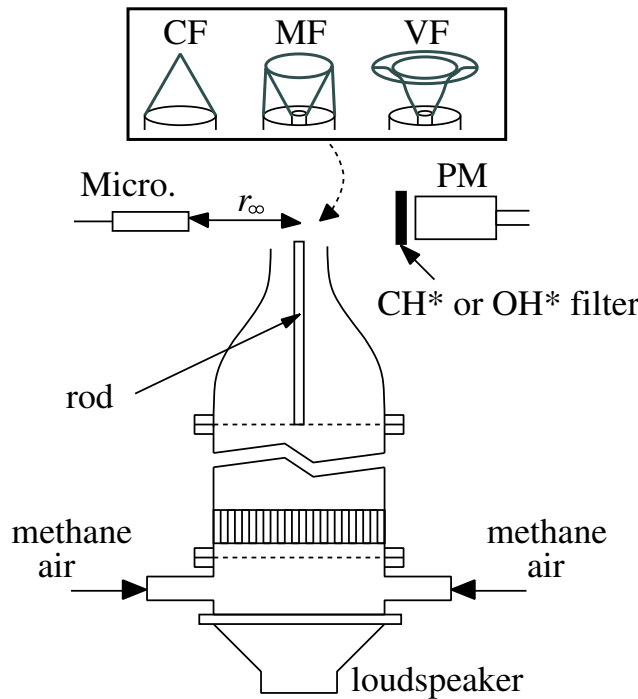


Figure 1: Experimental setup comprising a laminar burner with a central rod and a loudspeaker to modulate the flow. A photomultiplier (PM) with interferometric filters (OH^* or CH^*) collects the light emission from the flame. A microphone (M) records the radiated pressure at a distance r_∞ from the burner axis. A Laser Doppler Velocimeter (LDV) and an intensified CCD camera (ICCD), not shown here, are also placed around the setup to measure the flow velocity and to record flame images.

The configuration studied in this work is a laminar M-flame stabilized at the nozzle

outlet of a burner equipped with a central rod (MF in Fig. 1). A methane-air mixture is injected at the bottom of the burner. This mixture passes successively through a perforated plate, a laminarization honeycomb grid and a converging nozzle of $r_1 = 11$ mm outlet radius. A cylindrical, metallic rod of $r_0 = 3$ mm radius is placed on the burner axis. The flat top of this rod lies 2 mm above the nozzle outlet plane. This burner is used to anchor laminar flames featuring different flow topologies Schuller *et al.* (2003a); Durox *et al.* (2009). A conical, V- or M-flame can be stabilized depending on the injection and ignition conditions (Fig. 2). The case of a flame featuring an M-shape anchored both at the nozzle outlet rim and on the central rod is studied herein. This configuration has been selected because it is very sensitive to flow unsteadiness with large heat release rate fluctuations and large emission of noise Schuller *et al.* (2003a); Durox *et al.* (2009).

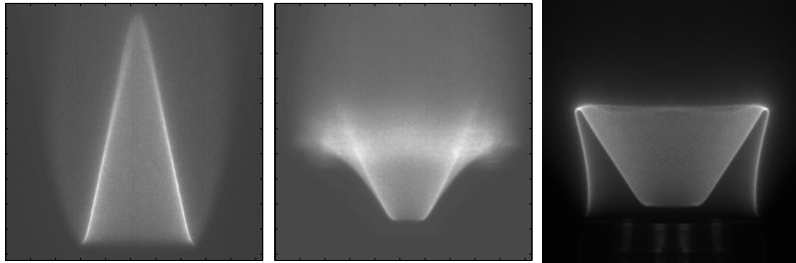


Figure 2: Flame topologies for different injection and ignition conditions. Left: conical flame, $\phi = 1.11$, $u_b = 1.7 \text{ m}\cdot\text{s}^{-1}$. Middle: V-flame, $\phi = 1.11$, $u_b = 2.3 \text{ m}\cdot\text{s}^{-1}$. Right: M-flame, $\phi = 1.04$, $u_b = 1.97 \text{ m}\cdot\text{s}^{-1}$.

An image of a nearly stoichiometric M-flame, with an equivalence ratio of $\phi = 1.04$, is shown in Fig. 2 for a bulk injection velocity $u_b = 1.97 \text{ m}\cdot\text{s}^{-1}$ at the annular nozzle outlet at room temperature. The flame height measured along the burner axis is $h = 16$ mm. In the absence of external forcing, the broadband noise level measured in the lab with a microphone set at $r_\infty = 0.25$ m away from the burner axis does not exceed 70 dB. A loudspeaker placed at the bottom of the burner and shown in Fig. 1 is used to modulate the flow with harmonic excitations. The axial-velocity perturbation produced at the burner outlet is measured by a Laser Doppler Velocimeter (LDV) $z = 2$ mm above the injection plane, i.e., at the same level as the top of the central rod, close to the center of the annular rim, $r = 7$ mm away from the burner axis. Images of the flame response were recorded with an intensified CCD camera (ICCD) equipped with a UV Nikkor objective that was triggered by the forcing signal sent to the loudspeaker.

When forced at a finite amplitude, the M-flame wrinkles as shown in Figure 3. Perturbations are convected along the flame front towards the flame tip. Relative fluctuations of the flame chemiluminescence intensity I'/I are plotted as a function of time in Fig. 3 for a harmonic velocity modulation $u'/u_b = 0.25$ at $f = 150$ Hz, where u' denotes the rms-fluctuations of the axial velocity. This signal already contains a large harmonic component and is out of phase with the sinusoidal velocity signal u at the burner outlet. Images (a) and (b) in Fig. 3 correspond to a pinching of the flame front leading to the release of a flame torus. This phenomenon leads to a sudden drop

of the flame chemiluminescence intensity I'/I in the oscillation cycle. This rapid rate of flame surface destruction corresponds to a pressure peak in the sound pressure $p'(t + \tau)$ recorded by the microphone, represented by the thick line in Fig. 3. The time lag $\tau = r_\infty/c_0$ corresponds to the propagation time of sound waves from the compact source region to the microphone location at the speed of sound $c_0 = 340$ m/s. The pressure predicted from combustion noise theory is represented by the thin line in Fig. 3. This estimate compares well with microphone measurements.

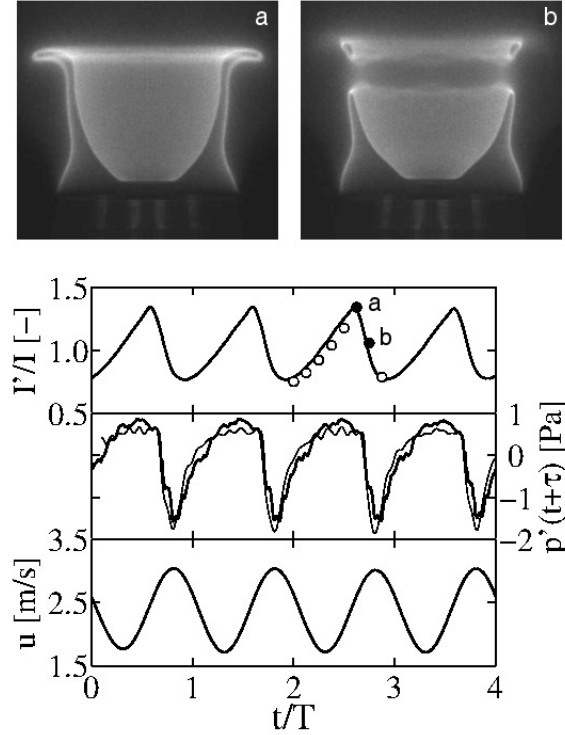


Figure 3: Top: Cyclic flame motion subjected to a flow modulation at $f = 150$ Hz with $\phi = 1.04$, $u_b = 1.97$ m/s and $u'/u_b = 0.25$. Snapshots are respectively taken at $3T/2$ (a) and $7T/8$ (b), where $T = 1/f$. Bottom: Corresponding input velocity signal $u(t)$, acoustic pressure $p'(t + \tau)$ and relative heat release rate fluctuations measured by relative flame light $I'(t)/\bar{I}$ oscillations as a function of time t/T . The delay $\tau = r_\infty/c_0$ coincides with the sound propagation time. The rate of change $dI'/dt(t - \tau)$ (thin line) is also superimposed on the acoustic pressure (thick line).

At small forcing amplitudes, effects of the forcing frequency are considered by determining the flame transfer function (FTF) between the upstream flow velocity and heat release rate disturbances. This response is calculated by only considering the signals at the fundamental frequency associated with the forcing frequency. Heat release rate disturbances were determined by recording the flame chemiluminescence intensity signal $I(t)$ collected by the PM equipped with a CH* interferometric filter. Flame surface, flame light intensity and heat release rate fluctuations were shown to be pro-

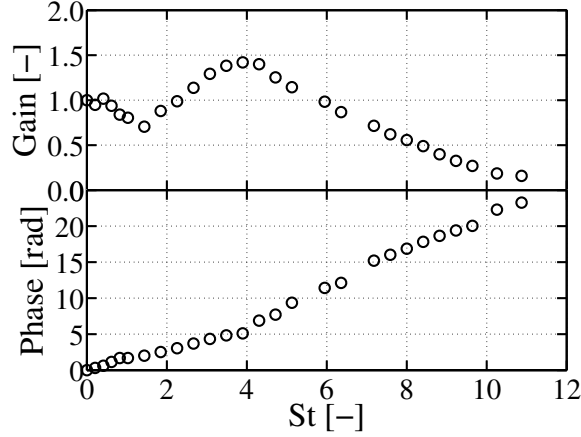


Figure 4: Gain (top) and phase lag (bottom) of the Flame Transfer Function (FTF) as a function of the Strouhal number $St = f(r_1 - r_0)/S_d$ for an M-flame with $\phi = 1.04$, $u_b = 1.97$ m/s, $u'/u_b = 0.08$, and $S_d = 0.39$ m/s.

portional Schuller *et al.* (2003a), and one may write

$$\frac{\tilde{\dot{Q}}}{\bar{\dot{Q}}} = \frac{\tilde{I}}{\bar{I}} = G \exp(i\varphi) \frac{\tilde{u}}{u_b} \quad (1)$$

where \tilde{a} denotes the Fourier components of the signal $a(t)$ examined at the forcing frequency and \bar{a} stands for the mean value of the signal. This frequency response was obtained by modifying the harmonic forcing frequency for a fixed velocity perturbation level $u'/u_b = 0.08$ at the burner outlet controlled by LDV.

Results for the gain G and phase lag φ of the flame transfer function (FTF) are presented in Fig. 4 in terms of a Strouhal number $St = f(r_1 - r_0)/S_d$ Schuller *et al.* (2003a) where St denotes the angular forcing frequency and S_d the laminar burning velocity of the combustible mixture. The FTF has a gain of unity at very low frequencies. It then takes on values lower than unity and reaches a minimum at about $St \simeq 1.5$. The gain then increases and takes on values larger than unity for $St \geq 2$ with a peak of about $G = 1.5$ at $St = 4$, indicating the amplification of the flow perturbations by the flame within this frequency range. Higher forcing frequencies are progressively filtered by the flame with a decrease in gain with increasing forcing frequencies. The gain is lower than unity for $St \geq 6$, and the FTF cut-off frequency, where the gain falls below 0.5, is equal to $St \simeq 8$.

The FTF phase lag between velocity and heat release rate disturbances starts from zero and steadily increases with the forcing frequency. One notes an inflection point when the gain reaches the small local minimum near $St \simeq 1.2$. The phase derivative is almost constant and equal to $v_\varphi = 1.2$ rad/St when $St \leq 4$. It then increases and takes on a slightly larger value $v_\varphi = 2.5$ rad/St for $St \geq 4$. This steadily increasing phase lag is characteristic of perturbations convected by the mean flow with a velocity proportional to the bulk injection velocity $u_b = 1.97$ m/s, see Schuller *et al.* (2003b);

Durox *et al.* (2009).

These responses in terms of FTF and noise radiated by the perturbed flame serve as reference experiments to validate the numerical solver developed below.

3 Numerical approach

The numerical approach chosen in this study is based on a linear computation. This technique allows for the study of the perturbations' dynamics without employing a reduced-order model. Strong linear couplings between the reaction layer, hydrodynamics and acoustics are also preserved. It is assumed that these interactions can account for most physical phenomena involved in thermoacoustic interactions. The numerical code was adapted from a compressible, inert gaseous flow solver developed in Ref. Garnaud (2012). The conservation equations are first presented, followed by the combustion model. Different approximations are introduced in this version of the solver for the description of species transport and combustion. They are listed below. Only the minimum material, needed to capture the response of laminar flames to small flow disturbances, was included in the numerical approach. These assumptions are assumed to retain the most important features of the laminar flame dynamics and are intended as a first step towards more complex models. This approach should highlight the principal physical mechanisms involved in acoustic amplification rather than lead to a close quantitative comparison.

3.1 Governing equations

A viscous, axisymmetric, compressible, reactive laminar flow is considered. Throughout this study, the Lewis number of all species is taken as unity. To simplify the problem, heat capacities are also kept equal and constant for all species. Species diffusion fluxes are modeled by Fick's law. The governing equations for density ρ , the velocity field \mathbf{u} , total energy E and the k^{th} species mass fraction Y_k are given as Poinso & Veynante (2012)

$$\frac{\partial \rho}{\partial t} + \nabla \cdot (\rho \mathbf{u}) = 0 \quad (2)$$

$$\frac{\partial \rho \mathbf{u}}{\partial t} + \nabla \cdot (\rho \mathbf{u} \otimes \mathbf{u}) = -\nabla p + \nabla \cdot \underline{\tau}, \quad (3)$$

$$\frac{\partial \rho E}{\partial t} + \nabla \cdot (\rho \mathbf{u} E) = -\nabla \cdot (p \mathbf{u}) + \dot{\omega}_T - \nabla \cdot \mathbf{q} + \nabla \cdot (\underline{\tau} \cdot \mathbf{u}) \quad (4)$$

$$\frac{\partial \rho Y_k}{\partial t} + \nabla \cdot (\rho \mathbf{u} Y_k) = -\dot{\omega}_k + \nabla \cdot (\rho D \nabla Y_k) \quad (5)$$

where

$$\dot{\omega}_T = \sum_k \dot{\omega}_k \Delta h_{f,k}^0 \quad (6)$$

and p is the pressure, D denotes the diffusion coefficient common to all species, $\underline{\tau}$ stands for the stress tensor, $\Delta h_{f,k}^0$ is the formation enthalpy of species k at the reference

temperature $T_0 = 300$ K, and $\dot{\omega}_k$ represents the production rate of species k . In our case, only the fuel mass fraction is explicitly computed and $k = 1$. In what follows, reaction rate and fuel mass fraction will be respectively designated with $\dot{\omega}_f$ and Y_f . A Newtonian fluid with viscosity μ , given by Sutherland's law, is considered to link the stress tensor to the velocity flow field. Details on the implementation of these equations for an axisymmetric configuration can be found in Refs. Garnaud (2012); Sandberg (2007).

3.2 Chemistry

A one-step, one-way chemistry was used to model the premixed flame. The flame is supposed to be stoichiometric, even though experiments were conducted at a slightly rich condition with a mixture ratio of $\phi = 1.04$. The fuel mass reaction rate is given by an Arrhenius model of the form

$$\dot{\omega}_f = A \rho Y_f \exp\left(-\frac{T_a}{T}\right) \quad (7)$$

where A is the Arrhenius prefactor and T_a is the activation temperature. These parameters were set to stabilize the flame on the burner at a prescribed displacement speed reproducing the same flame topology as shown in experiments, while keeping the flame thickness within a reasonable range. These conditions were obtained for an Arrhenius prefactor set to $A = 6.04 \cdot 10^5 \text{ St}^{-1}$ and for

$$\frac{T_b}{T_u} = 6.47 \quad \text{and} \quad \frac{T_a}{T_u} = 40 \quad (8)$$

where T_u denotes the temperature in the injection unit, fixed at 300 K, and T_b stands for the temperature of burnt gases. The associated Zeldovitch parameters are accordingly

$$\alpha = \frac{T_b - T_u}{T_b} = 0.845 \quad \text{and} \quad \beta = \alpha \frac{T_a}{T_b} = 5.23. \quad (9)$$

These parameters correspond to a flame of thickness $\delta \simeq 0.05$ mm stabilized on a burner of 0.7 mm in diameter. This flame is also faster $S_d \simeq 3.63$ m/s than the laminar burning velocity $S_d = 0.39$ m/s of the methane-air flame. The computed flame thus admits a bulk injection velocity of $u_b = 20.79$ m/s, which is rather high for air-combustion hydrocarbon flames, but reasonable for Oxy-flames. Stoichiometric methane-oxygen flames have a laminar burning velocity of 3.3m/s close to the value used in the simulations. In what follows, all quantities are expressed with respect to the tube radius $r_{tube} = 0.7$ mm, the tube bulk injection velocity u_b and the unburned gas temperature $T_u = 300$ K.

These choices were guided by a compromise between simulations of realistic, laminar flame configurations and optimization of the computational effort. It allowed for a validation of the methodology, before considering more challenging configurations and chemistries in future studies. It is however worth mentioning that, within the range of frequencies considered in this study, the flame remains compact with respect to acoustics. Indeed, the characteristic acoustic wavelength considered here is of order L/Ma ,

where L is the flame characteristic length. In our case, L is typically of the order of the tube radius. Furthermore, the Mach number is kept low, with a local value of $Ma \leq 0.1$, which enforces a length scale separation that should maintain the validity of our results for more complex cases.

3.3 Geometry

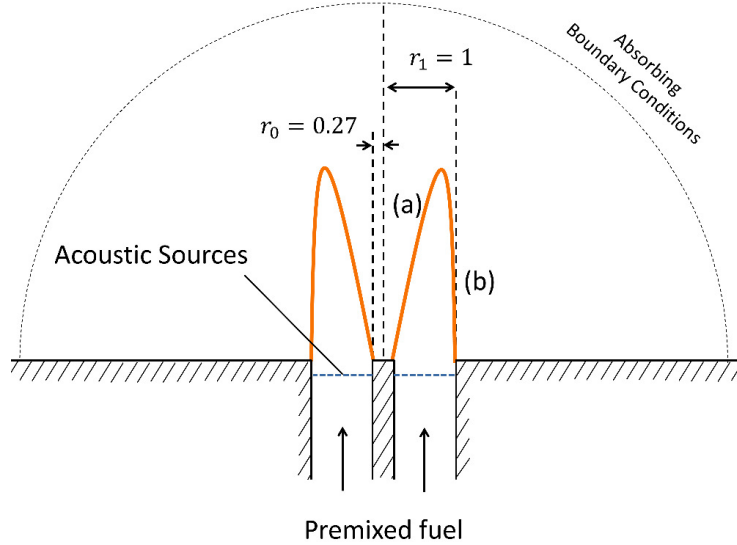


Figure 5: Sketch of the numerical configuration.

The numerical domain consists of an annular pipe expelling gases into a cylindrical region shown in Fig. 5 and 6. The combustible mixture is injected through the annular pipe of internal radius $r_0 = 0.27$ and external radius $r_1 = 1$ and burns at the exit. This computational domain was split into two regions, the first one containing the annular pipe, the second one containing the exit region. The burnt gases expand into the atmosphere via absorbing boundary conditions. The fresh reactants are injected through the annular tube which has been taken sufficiently long to contain one full period of an acoustic wave at the characteristic flame frequency $S_d/(r_1 - r_0)$, where S_d is the laminar burning velocity. In what follows, flame front (a) will be designated as the 'internal flame front', while flame front (b) will be referred to as the 'external flame front'.

Using the bulk injection velocity u_b and the outer radius r_1 as reference scales, the corresponding Reynolds number has been set to $Re = 950$, and the bulk Mach number in the tube at T_u to $Ma = 0.065$ for a maximum local injection mach number of $Ma_{\max} = 0.1$. The maximum base-flow velocity at the injection plane was measured as $u_{\max} = 1.54$. Compared to the reference experiment, this sets the Reynolds number of our simulation lower by a factor of two and the injection Mach number one order of magnitude higher. The choice of flow parameters and geometric dimensions, however, has been driven by computational limitations. In fact, the Courant-Friedrichs-Lewy

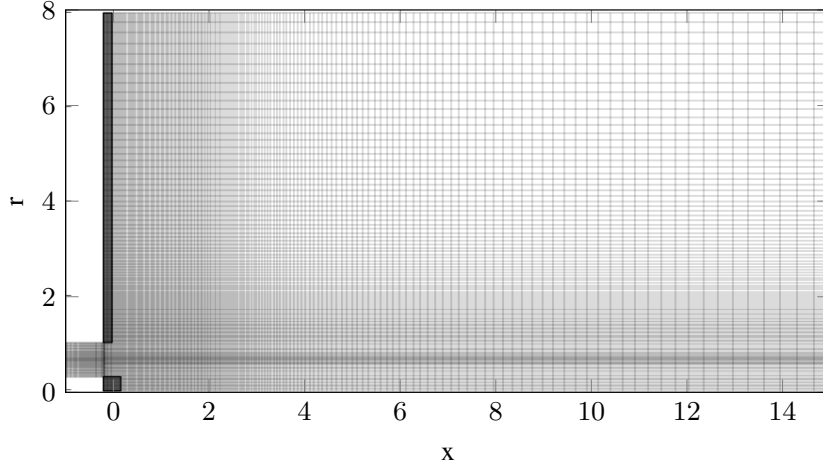


Figure 6: Typical mesh used in simulations, coarsened four times in each direction. The shaded regions are treated as non-slipping walls.

(CFL) condition locally imposes Courant *et al.* (1967)

$$dt \sim \frac{dx}{U_{0,loc} \left(1 + \frac{1}{Ma_{loc}}\right)} \quad (10)$$

for compressible computations, which imposes a rather stringent constraint on the Mach number.

In the following, we use the same Strouhal number to allow a compare between numerical results and experimental data. We thus define

$$St = \frac{f(r_1 - r_0)}{S_d}. \quad (11)$$

3.4 Numerical details

Spatial derivatives have been computed to third-order accuracy using a 11-point stencil, optimized in the Fourier domain Berland *et al.* (2007). Time integration has been performed using a 10-step, strongly stability-preserving, fourth-order Runge-Kutta method Gottlieb (2005); Ketcheson (2008). The flame has been fully resolved. For nonlinear simulations, an operator-splitting method has been used to solve for the chemistry. At each intermediate Runge-Kutta step, the following partial system is employed

$$\frac{\rho E(t+dt) - \rho E(t)}{dt} = \Delta h_f^0 \dot{\omega}_f(t+dt), \quad (12)$$

$$\frac{\rho Y_f(t+dt) - \rho Y_f(t)}{dt} = -\dot{\omega}_f(t+dt). \quad (13)$$

This system is solved for $(\rho E(t+dt), \rho Y_f(t+dt))$ using a Newton-Raphson technique, based on the time step dt of the global Runge-Kutta step. The resulting value of $\dot{\omega}_f(t+$

dt) is then used in equation (5). This method was observed to yield consistent, stable results for the range of time steps typically encountered in our simulations. In the worst case, this scheme locally decreases the temporal accuracy of the simulation to first order for the chemistry terms. This apparent loss in precision, however, has no impact on subsequent simulations, since the nonlinear computations were only used to establish a steady base flow. The discretized system contained a total of 2,785,280 degrees of freedom, and simulations were conducted at a CFL number of 1.18. An implementation on parallel architectures has been handled via the PETSc library Balay *et al.* (2013, 1997).

3.5 Base flow

In order to perform a linearized simulation, a steady-state solution is required. This base flow represents the solution of the system

$$\nabla \cdot (\rho_0 \mathbf{u}_0) = 0, \quad (14)$$

$$\nabla \cdot (\rho_0 \mathbf{u}_0 \otimes \mathbf{u}_0) = -\nabla p_0 + \nabla \cdot \underline{\boldsymbol{\tau}}_0, \quad (15)$$

$$\nabla \cdot (\rho_0 \mathbf{u}_0 E_0) = -\nabla \cdot (p_0 \mathbf{u}_0) + \dot{\omega}_{f,0} \Delta h_f - \nabla \cdot \mathbf{q}_0 + \nabla \cdot (\underline{\boldsymbol{\tau}}_0 \cdot \mathbf{u}_0), \quad (16)$$

$$\nabla \cdot (\rho_0 \mathbf{u}_0 Y_{f,0}) = -\dot{\omega}_{f,0} + \nabla \cdot (\rho D \nabla Y_{f,0}). \quad (17)$$

In all cases explored in this study, the nonlinear simulation showed that the flow is naturally convectively unstable. Indeed, the flame produces a hot shear layer associated with a Kelvin-Helmholtz instability. This is not surprising as hot jets at these working conditions are typically either convectively or absolutely unstable Huerre & Monkewitz (1985); Michalke (1984); Monkewitz & Sohn (1988); Lesshafft *et al.* (2006). This instability mostly influences the hot products downstream of the flame; it was further assumed to have a negligible impact in this study. In order to suppress this unsteady dynamical component, a selective frequency damping (SFD) technique Åkervik *et al.* (2006) has been applied. To this end, two linearly coupled equations are simultaneously advanced in time: the first equation associated with the field variables, the second equation describing an observer state. The observer is damped such that the dynamics of the field variable no longer retains the unstable, unsteady state. It is readily verified that, upon convergence of the procedure, a steady state of the nonlinear reactive compressible Navier-Stokes equations is obtained. This solution has been taken as the base flow and is presented in Fig. 7, visualized by temperature. In this figure, the shear layer is confined to the mixing layer (in grey) away from the flame.

4 Linear Response Analysis

4.1 Linearization

We proceed by carrying out a full, exact linearization about our base flow, using the direct numerical linearization technique developed in Ref. Fosas de Pando *et al.* (2012) which allows an efficient implementation and evaluation of the linear operator (about

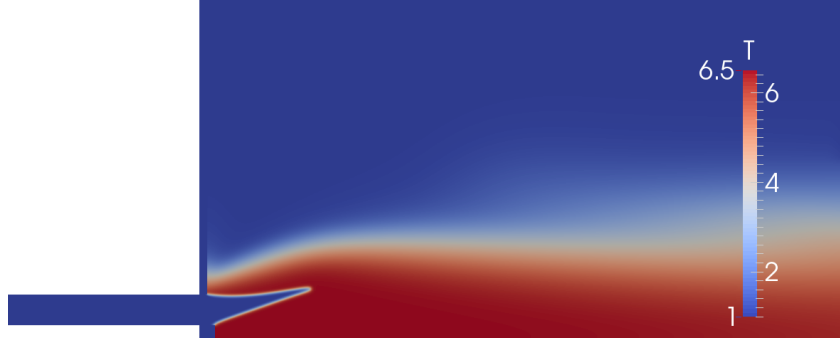


Figure 7: Base flow used for the linearization procedure, visualized by temperature ratio T/T_u with $T_u = 300$ K.

a given base flow) underlying a nonlinear numerical simulation. For the case of a reacting compressible flow, following a reordering of matrix components, this procedure provides numerical access to the linearized operator A_{full} , split into respective physical mechanisms. For example, we obtain

$$A_{full} = A_{flow} + A_{chem} \quad (18)$$

where A_{flow} is the operator associated with the compressible non-reactive flow dynamics, while A_{chem} is the operator associated with the linearization of $\dot{\omega}_T$ and $\dot{\omega}_f$ in equations (4) and (5). It is worth noting that, in a linearized simulation, the state vector is defined up to a multiplicative constant. This justifies the use of dimensionless numbers to express results.

4.2 Impulse response analysis of the system: the transfer function

In order to evaluate the effects of acoustic waves on the flame, a planar acoustic forcing is employed. The acoustic source distribution is presented in Fig. 5. The acoustic forcing is introduced as a set of source terms, uniform in the r -direction, with a Gaussian-shaped amplitude, centered about $x = -0.1$ upstream of the injection plane and with a characteristic width of 0.02, i.e.,

$$f(r, x) = \begin{pmatrix} \rho_f(x) \\ \rho_f(x)u_0(r, x) \\ \rho_f(x)v_0(r, x) \\ \rho_f(x) \left(c_0^2 / (\gamma - 1) + 0.5 (u_0^2 + v_0^2) \right) (r, x) \\ \rho_f(x)Y_0(r, x) \end{pmatrix} \quad (19)$$

with

$$\rho_f(x) = \frac{\rho_{loc}(x)}{\int_{-\infty}^{+\infty} \rho_{loc}(x') dx'}, \quad (20)$$

$$\rho_{loc}(x) = \exp \left(- (x + 0.1)^2 / 0.02^2 \right). \quad (21)$$

The above expressions define a set of density sources acting at constant entropy; such a set has been found to generate nearly pure, acoustic waves. The response of the flame to this forcing is determined by computing a numerical impulse response. In experiments, the linear flame response is typically inferred frequency-by-frequency using an harmonic forcing as in Fig. 4. In numerical simulations, a low-amplitude broadband signal, such as a random binary signal, can be applied to identify the system impulse response Tay-Wo-Chong *et al.* (2012). In our case, initial conditions have been applied using equation (19); in particular, a volume forcing is applied at $t = 0$ and thereafter set to zero, and the propagation of the resulting acoustic impulse is computed. Applying a Fourier transform to this impulse response yields the transfer function to our particular forcing defined by equation (19).

To allow comparison with experiments, this transfer function has been further modified according to

$$(\rho u)'_b = \frac{1}{\pi(r_1^2 - r_0^2)} \int_{r_0, x=-0.05}^{r_1} 2\pi r (\rho u)'_x(x, r) dr \quad (22)$$

as an input. In experiments with $Ma \ll 1$, we have $\tilde{u}/u_0 \gg \tilde{\rho}/\rho_0$ and $(\tilde{\rho u})/(\rho u)_0 \simeq \tilde{u}/u_0$. In our case, with $Ma = 0.1$, the density term has been retained; it introduces a correction of typically two percent to the transfer function. In addition, the transfer function, for a field variable g , has been formulated in the form

$$TF_g = \frac{\tilde{g}/g_0}{(\tilde{\rho u})'_b/(\rho u)_{b,0}} \quad (23)$$

where \tilde{g} denotes the Fourier transform of the impulse response of g .

In Fig. 4, the flame transfer function (FTF) consists of the computation of the transfer function associated with the relative CH* light intensity using the relative bulk velocity perturbation as an input. A numerical simulation allowing a direct access to the heat release rate, the relative variations of this quantity was used as an output here. For this reason, the variable g in the expression above has been taken as the volumetric integral of the heat release rate \dot{q} , i.e.,

$$g = \dot{q} = \int_{\Omega} \dot{\omega}_T d\Omega \quad (24)$$

where Ω stands for the computational domain. The corresponding transfer function TF_q , presented in Fig. 8, thus quantifies flame sensitivity to acoustics in the limit of infinitesimal perturbations.

Figures 4 can now be easily compared. Experiments show an asymptotic value of one for the transfer function as $St \rightarrow 0$, with a local minimum at $St = 1.5$ and a local maximum at $St = 4$; the phase is linearly increasing over the same range of frequencies, at a rate of $2.5 \text{ rad } St^{-1}$. The linear variation of the phase, present in both Fig. 4 and 8, is characteristic of the phase delay φ associated with wave propagation of the form

$$\varphi = kx = \frac{2\pi St}{U_c} x \quad (25)$$

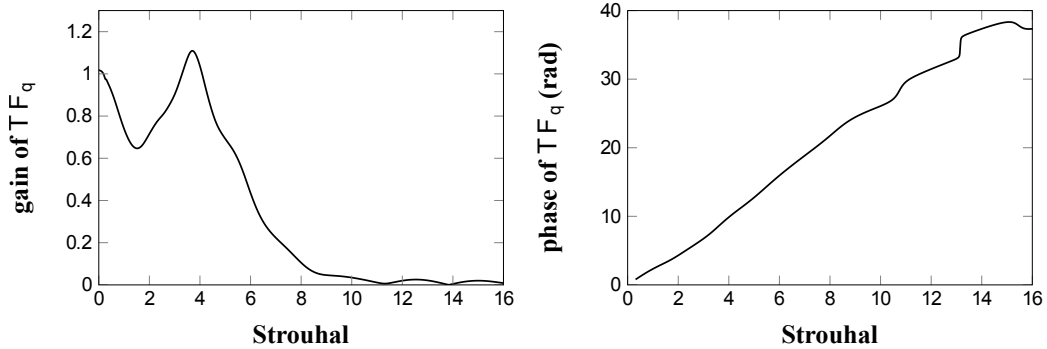


Figure 8: Amplitude and phase of the computed flame transfer function

where U_c is the characteristic velocity of the wave considered. Here, we have $U_c \approx 1$ which corresponds to a hydrodynamic velocity. The predicted phase is also linear in frequency with a coefficient proportional to the distance x from the injection plane. These relations are correctly predicted by the numerical simulation; however, quantitative differences appear in the values of the gain for the local maximum and minimum, as well as in the rate of decrease of the gain past its maximum. This may be attributed to insufficient accuracy of our chemistry model, to the length-scale separation between the simulated and the real flame, or to the finite amplitude of the perturbations used in experiments. As this study focuses on the physical mechanisms associated with flame/acoustic interactions, the above results seem adequate to validate our approach.

According to Rayleigh's criterion, if the unsteady rate of heat released is positively correlated to the pressure of the oscillation, thermoacoustic amplification will occur. We have

$$\lambda \propto \int_0^{2\pi/\omega} p_{in} \dot{q} dt \quad (26)$$

with λ as the pressure amplification and p_{in} as the forcing pressure. As presented in 8, an evaluation of the integral unsteady heat release phase and gain also allows the prediction of frequency ranges where amplification can be observed. However, this provides little information on which spatial regions are subject to large acoustic amplification due to chemistry. In addition, we also wish to identify (and visualize) the acoustic sources induced by unsteady chemistry.

Generating such a map in space for a given frequency requires us to compare pressure levels at different points, and, in doing so, compensation for propagation effects is necessary. In the far-field region, such comparisons are typically achieved using asymptotic expressions; in the near field, however, a different approach has to be used. Additionally, our strategy aims at isolating chemical unsteady heat release effects from linear computations, which ultimately allows for an isolation of the acoustic field induced by unsteady chemistry. We therefore perform two sets of computations: a first simulation with (linear) chemistry and a second one without reactive terms. In linear numerical studies, the base flow is typically assumed constant throughout the simulation, and ignoring flame effects on the linear acoustics is equivalent to keeping a react-

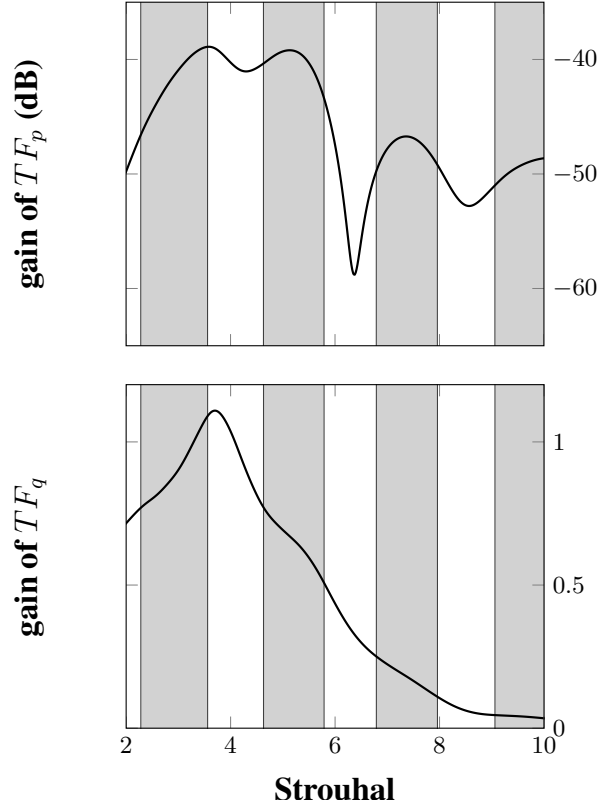


Figure 9: Top: pressure gain (in dB) at $x=4$, $r=1.5$, bottom: gain of the flame transfer function. Grey areas: frequency ranges corresponding to expected constructive interactions between heat release rate and pressure based on the Rayleigh's criterion.

ing baseflow (with strong temperature gradients) while switching off linear chemistry terms.

Following the previous formalism, the matrix

$$A_{full} = A_{flow} \quad (27)$$

is then used instead of equation (18), while keeping all other simulation parameters identical. Applying our system analysis technique to the full system with (18) then yields the full transfer function $TF_{p,full}$, while using (27) leads to the transfer function without linear chemistry $TF_{p,partial}$. The ratio between these two transfer functions, i.e.,

$$\Delta TF_p = \frac{TF_{p,full}}{TF_{p,partial}}, \quad (28)$$

then characterizes the amplification of acoustic waves by the flame, without being influenced by propagation effects or by interactions with the hydrodynamics.

Figure 10 presents, at the point $x = (4, 1)$, the transfer functions $TF_{p,full}$ and $TF_{p,partial}$, as well as a graphic interpretation of ΔTF_p . Two frequency ranges can be distinguished: for $St < 6$, strong acoustic amplifications due to unsteady chemistry

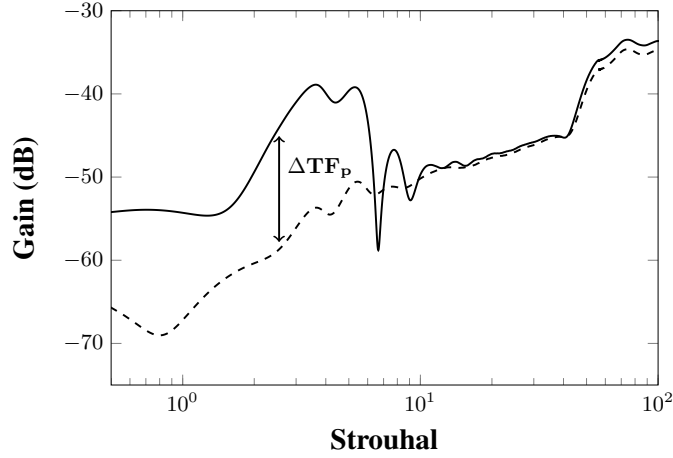


Figure 10: Comparison of the acoustic gain of $-Tf_{p,full}$ with chemistry and $-Tf_{p,partial}$ without linearized chemistry at $x=4$, $r=1$

occur, while for $St > 6$ both transfer function curves coincide. This observation is in agreement with the flame transfer function shown Fig. 8. At high forcing frequencies, the flame saturates and no amplification is observed; the same behavior is observed in Fig. 3.

4.3 Acoustic amplification map

Instead of considering the variation of acoustic amplification with frequency at a given location, our procedure allows for the comparison of the transfer function ΔTF_p for varying points in space at a prescribed frequency. This results in a spatial map of acoustic amplification, such as presented in Fig. 11, for $St = 3.54$ and for $St = 10.58$.

At both frequencies, the spatial structures related to acoustic amplification are comparable. However, the amplitudes in both cases are drastically different. Confirming previous observations, at $St = 3.54$, the gain reaches a maximum of 25 dB, while at $St = 10.6$, a maximum of 1.7 dB is obtained. Moreover, these local maxima of amplification are located at the flame tip, which is in agreement with experimental light intensity measurements in Fig. 3 (a) and (b). Indeed, the local nonlinear heat release rate at the flame front can be expressed as

$$d\dot{q} = \rho_1 S_f \Delta h dA \quad (29)$$

with ρ_1 as the upstream density, S_f as the normal flame front speed, defined with respect to the flow, Δh as the mass heat of reaction and dA as an infinitesimal flame surface element. According to Markstein's asymptotic analysis, the flame speed mostly depends on stretch, which in turn suggests that the heat release rate will be particularly affected by disturbances at regions of maximum curvature. Dilatation effects will thus be important at the flame tip and result in high acoustic amplitudes. The above figures also underline the necessity of taking local inhomogeneities of heat release into

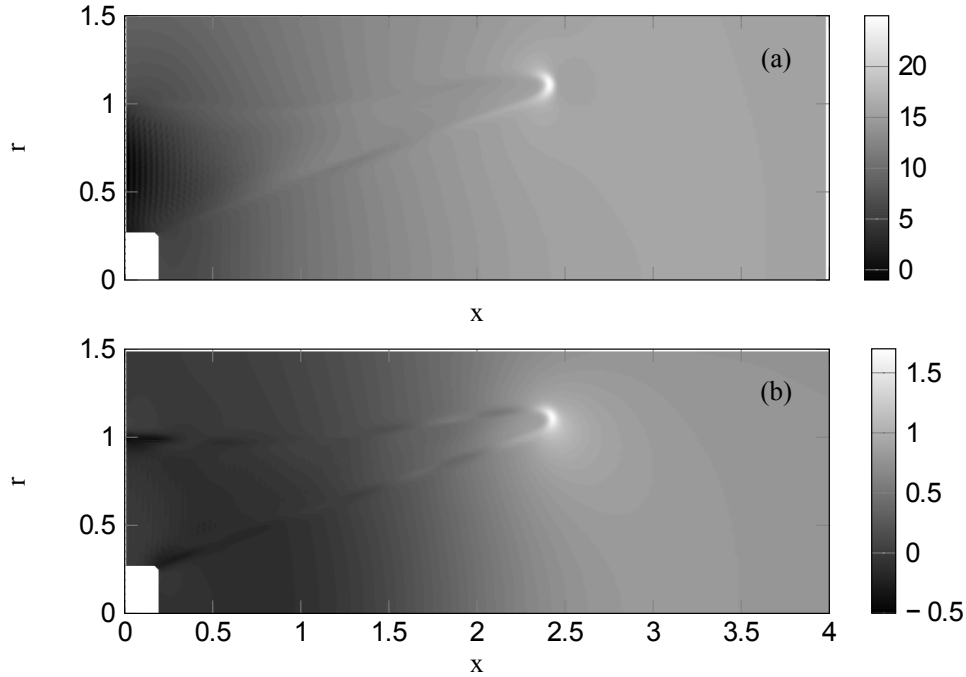


Figure 11: Mapping of the pressure amplification attributed to unsteady chemistry ΔTF_p . (a): $S_t = 3.54$; (b): $S_t = 10.58$. Gains are expressed in dB

account when estimating interactions between the flame and acoustics. In particular, an approach solely based on flame-surface computations may underestimate unsteady heat-release amplitudes by a significant amount Clavin & Siggia (1991); Talei *et al.* (2012).

Our operator decomposition method has the capability of delineating various physical mechanisms, which is certainly not restricted to only the estimation of pressure amplification. For instance, for flame instabilities it can isolate hydrodynamic effects from chemistry influences and help guide an analysis of the most prevailing mechanisms and physical processes. In our present study, this strategy has identified vorticity as a crucial component in the linear flame-front dynamics.

5 Acoustically induced vorticity at the flame front

5.1 Convective modes upstream of the flame

When a flame is acoustically forced, a coherent velocity mode appears in the region between the internal and external flame fronts, as shown in Fig. 12. The phenomenon appears either with (left subfigure) or without (right subfigure) unsteady chemistry. In what follows below, this mode is referred to as the flame-induced oscillatory mode (FIOM). The rise of this mode has been reported in experiments by Baillot *et al.* (Baillot *et al.*, 1992) for the case of a conical flame. Birbaud *et al.* (Birbaud *et al.*, 2006)

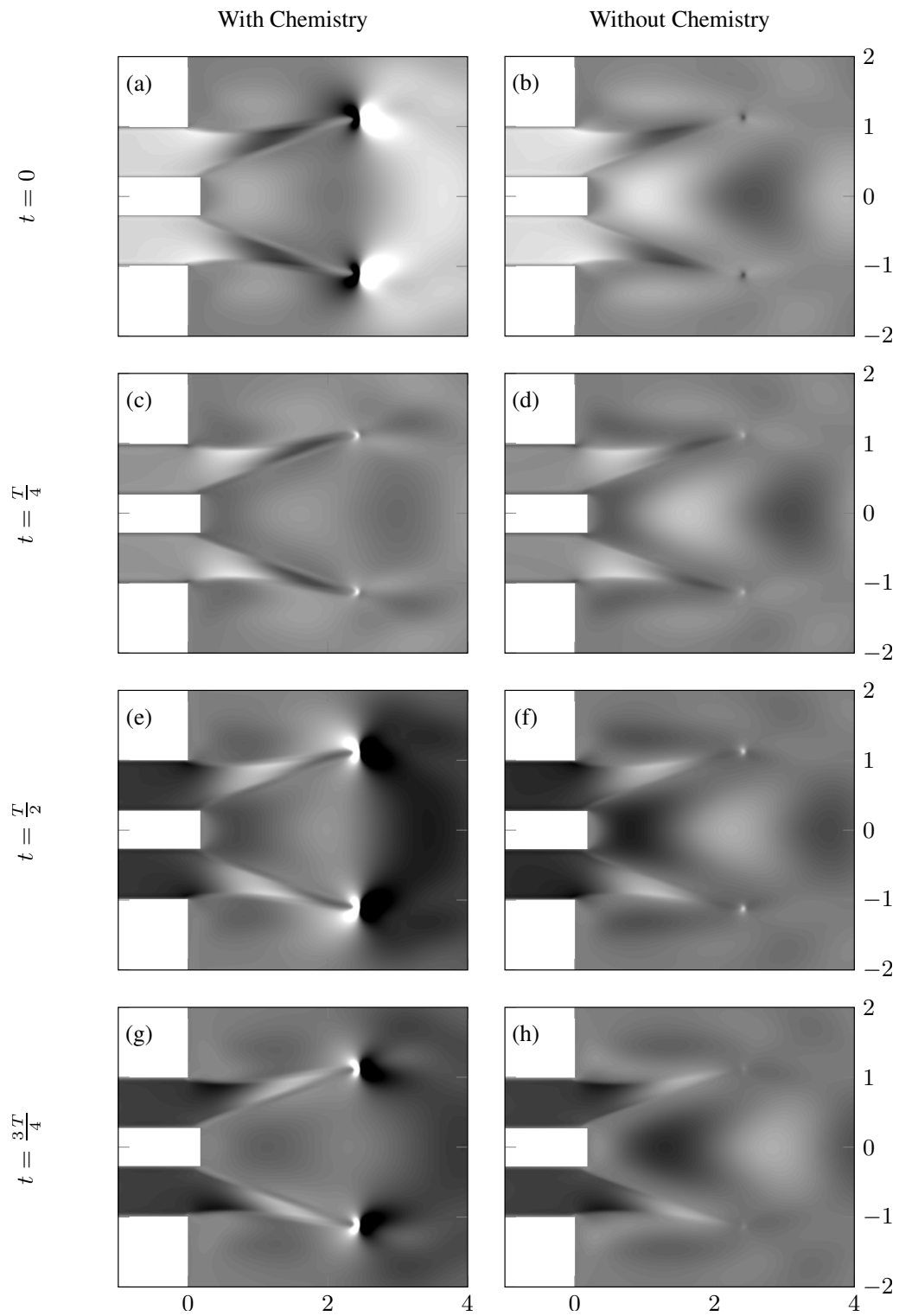


Figure 12: Longitudinal velocity for a linear forcing at $St=2.64$, in established regime, with (left) and without (right) linearized chemistry. The colormap is identical for all figures.

studied the change in apparent phase speed of the upstream velocity with frequency. Two characteristic behaviors have been observed with (i) a slow convective mode and (ii) a quick acoustic forcing. The transition between both modes in space could be very abrupt, and even associated with locally negative phase velocities. In this present study, the same approach is employed. The variation of the upstream values of the velocity have been interpolated from impulse response data on a line presented in Fig. 13. The obtained velocity was then projected onto this line and normalized according to

$$TF_{FIOM}(\tilde{s}, St) = \frac{\tilde{u}_t(\tilde{s}, St)}{\tilde{u}_t(\tilde{s} = 0, St)} \quad (30)$$

where \tilde{s} is the local arclength of the line, taken from upstream to downstream. The resulting transfer function TF_{FIOM} is then of the form $|TF_{FIOM}| \exp(i\varphi)$. Assuming that \tilde{u} is linked to a propagating wave allows us to define a pseudo-phase speed as

$$v_\varphi = \frac{\omega}{\partial\varphi/\partial\tilde{s}}. \quad (31)$$

The results of this decomposition (in norm and phase velocity) are presented in Fig. 14. Data is shown as a function of the axial position x and of the Strouhal number defined as previously.

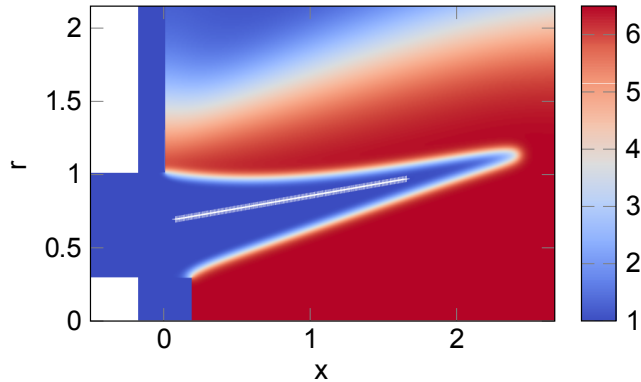


Figure 13: + symbols denote position of the extracted points (in white) for the characterization of the FIOM. Background colors are based on the temperature.

Typically, acoustic waves are faster than convective waves by a factor of $1/Ma$, equal to ten in our study. A phase speed of order one will thus be labelled as 'convective', while a phase speed of order ten will be referred to as 'acoustical'. Three behaviors can be distinguished. (i) At low Strouhal numbers ($St < 6.3$), a slow, convective mode dominates, characterized by dark blue regions in the phase-speed plot and by a stable amplitude in space. For instance, at $St = 5$, the phase speed is essentially constant and equal to 1.5 with a slowly varying gain. (ii) For mid-range Strouhal numbers ($6.3 < St < 32$), the amplitude of the velocity decreases along the line, as the convective wave vanishes. A convective and acoustic wave co-exist, which leads to locally negative phase speeds in agreement with previous observations Birbaud *et al.*

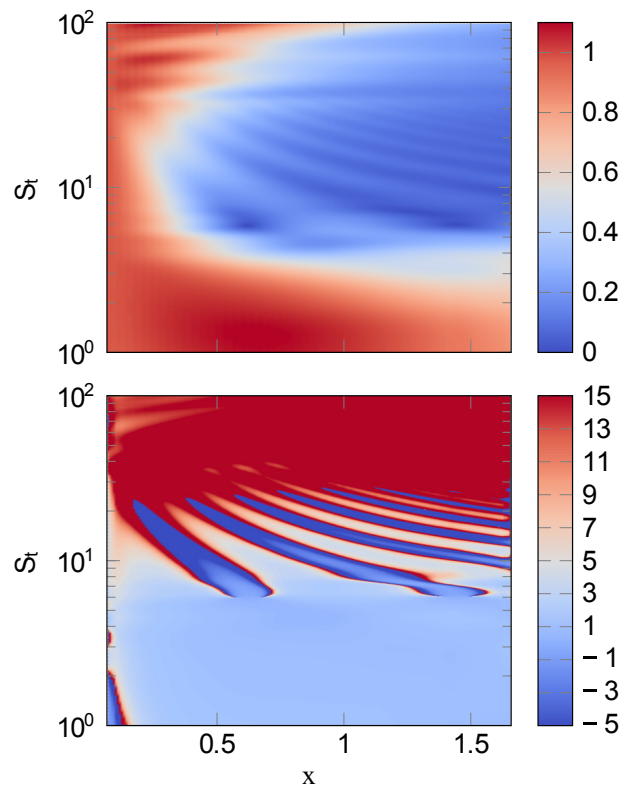


Figure 14: Norm (top) and phase speed (bottom) of the TF_{FIOM} computed from the impulse response.

(2006). Diagonals in the phase velocity map appear. They are related to the interference either between acoustic waves reflected by the flame surface or between acoustic and convective waves. In this regime, the flow becomes gradually dominated by the acoustic forcing as the frequency increases. This tendency is visualized by a shift in background turning from blue to red at $6.3 < St < 32$ in Fig. 14. (iii) For very high frequencies ($St > 32$), a detailed study of phase speeds shows that the flow is dominated by unreflected, propagating acoustic waves.

A small region of negative phase speeds appears at very low frequencies. It is believed that this region is associated with the frequency cut-off of the FIOM at low Strouhal numbers.

Given the richness of this dynamics, a direct analysis appears difficult. However, using the analysis technique developed in section 4, we are able to isolate the effects of unsteady chemistry.

5.2 Identification of vorticity sources

In this section, we focus on the low-frequency regime. All computations have been performed at $St = 2.64$, and unsteady chemistry has been considered.

In Fig. 15 the presence of a vorticity sheet confined to the flame-front region can be observed. As the flame is periodically pulsed, the internal and external flame fronts are in quasi-phase opposition; this situation is illustrated in Fig. 16.

Through their interaction, the two vorticity sheets induce a dominant longitudinal velocity, confined inside the flame region. The vortices are convected by the flow along the flame fronts. This induces and sets the speed for a convective mode appearing between the internal and external flame fronts. The same mechanism also seems to provide a satisfactory explanation for the FIOM.

In unsteady simulations with linear chemistry, the phase speeds of heat release and of vorticity dynamics are closely correlated, as shown in Fig. 15. This suggests that the above flame-induced vorticity is related to the flame-front dynamics. Moreover, in Fig. 12 a hydrodynamic velocity mode appears, both with and without linearized chemistry, in the region between the internal and external flame fronts, with a notable amplitude in all computations. The mechanism underlying the FIOM seems to be of a hydrodynamic nature, since its appearance only weakly depends on the unsteady chemistry associated with the flame. It can further be postulated that the FIOM is linked to the dynamics of the temperature discontinuity present in the base flow. To verify this latter hypothesis, an idealized model is considered. By presuming diffusion effects to be negligible ($Re \rightarrow \infty$), the flame becomes infinitely thin — a limit that allows the modeling of the flame using a G -equation.

5.3 Analytical development of the flame dynamics

The G -equation is based on a level-set method to represent the flame, where the flame front is identified as the zero-level of a globally defined function G , with $G > 0$ in the region of burned gases and $G < 0$ for fresh gases. This zero-level moves at a speed S_d

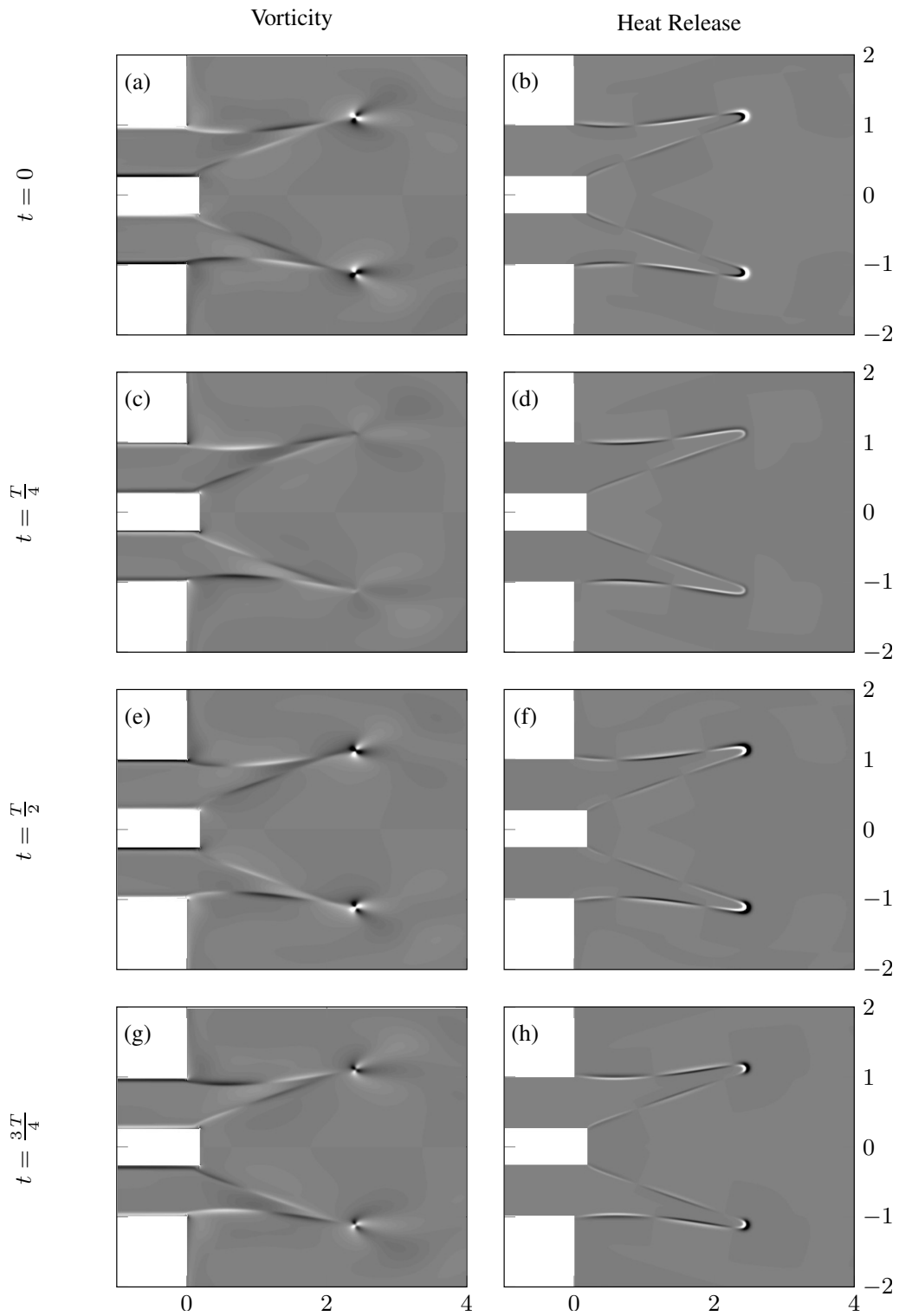


Figure 15: Vorticity field and unsteady heat release rate for a linear forcing at $St=2.64$, in established regime. Colormaps are identical respectively for all vorticity plots (between -3 and 3), and for all heat release rate plots (between -5000 and 5000)

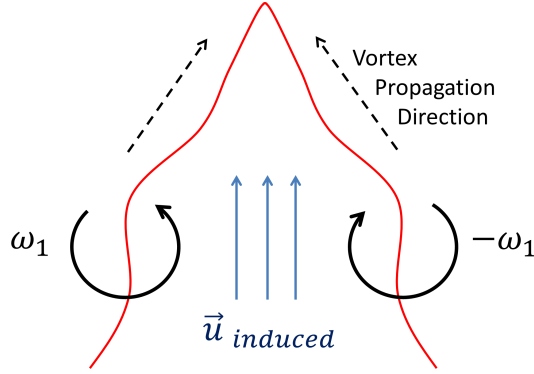


Figure 16: Effects of flame wrinkling-induced vorticity on the upstream flow.

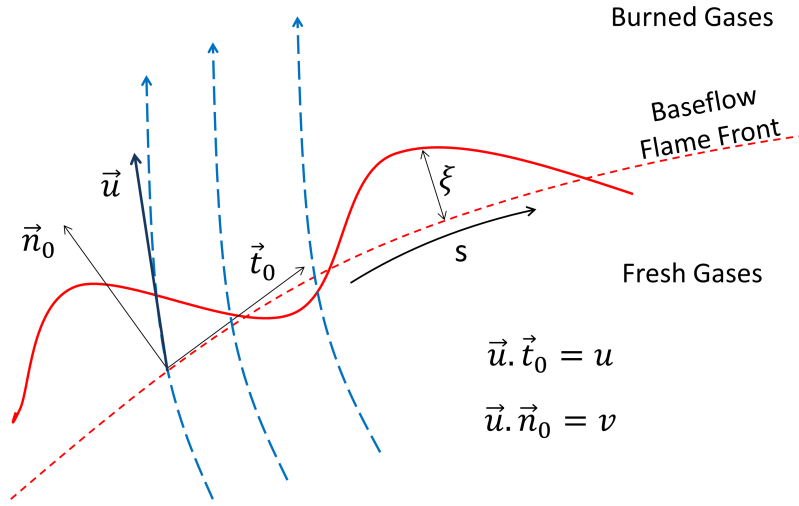


Figure 17: Conventions for the linearized G -equation.

normal to the flame front which leads to the equation

$$\frac{\partial G}{\partial t} + (\mathbf{u} \cdot \nabla) G = S_d |\nabla G| \quad (32)$$

on the flame front. In this formulation, the driving flame-front velocities are taken upstream of the flame.

As we adopt a perturbative approach, the variations of G around a steady position G_0 are considered next. To this end, all fields f are decomposed according to $f = f_0 + f'$ with f_0 as the base value of f and $f' \ll 1$ as an infinitesimal perturbation. Under the assumption that the flame front does not intersect itself, it is possible to define a local frame of reference $(\mathbf{t}_0, \mathbf{n}_0)$, with associated coordinates (X, Y) , such that \mathbf{t}_0 is tangent to the flame front and \mathbf{n}_0 is normal to it. The normal vector \mathbf{n}_0 points from fresh to burnt gases, such that $\mathbf{S}_{d,0} = -S_{d,0} \mathbf{n}_0$. A sketch of this geometric setup is depicted in Fig. 17. The projection of the speed onto $(\mathbf{t}_0, \mathbf{n}_0)$ is denoted by (u, v) .

Working in this frame of reference, it can be further deduced that $\partial G_0 / \partial \mathbf{n}_0 = 1$ for $G_0 \in \mathcal{C}^1$. Thus, at first order, we have

$$G \simeq G_0 - \xi(s, t), \quad \xi \ll 1, \quad (33)$$

$$\frac{\partial \xi}{\partial t} + u_0 \frac{\partial \xi}{\partial s} - v' = -S'_d. \quad (34)$$

In practice, this model corresponds to a geometrically unchanged surface of discontinuity, given implicitly by $G_0 = 0$, for which jumps depend on equation (34). This jump also represents the feedback of the flame dynamics on linear perturbations. Equation (34) is the trace of the base-flow discontinuity dynamics. In this model, unsteady chemistry is only accounted for via the forcing term S'_d . Besides, it is well-known Markstein (1964) that the flame structure and, in particular, the flame speed only depend on stretch and the equivalence ratio, in the limit of low stretching. This stretch is the consequence of flame curvature and of upstream velocity surface divergence Poinso & Veynante (2012). In the absence of fuel perturbations, unsteady heat release only has a weak effect on the flame dynamics modeled by equation (34). Any mechanism arising from this equation and involving weak relations to S'_d would also be compatible with the FIOM and its appearance in all our simulations. In particular, the continuity of the nonlinear tangential velocity

$$u_2 - u_1 = 0. \quad (35)$$

leads in our linear framework to the expression

$$u'_2 - u'_1 = -\frac{\partial \xi}{\partial s} (v_{0,2} - v_{0,1}). \quad (36)$$

This also implies that, at long distance, a wrinkled flame surface acts as a vorticity sheet of local perceived intensity $\partial \xi / \partial s (v_{0,2} - v_{0,1})$. This result is rather classical and has been accounted for in Refs. Zeldovich *et al.* (1985); Truffaut (1998) for the modeling of the Landau-Darrieus instability. Its effect on a planar flame has also been well-studied and reported. However, its influence on a flame composed of two flame fronts and a flame tip is not as well understood.

In order to validate the role of vorticity in the onset of the FIOM, equations (34) and (36) have been implemented in the form of a simplified simulation.

5.4 Implementation of the G -equation

Equation (34) was further developed, based on Ref. Poinso & Veynante (2012), to read

$$\frac{\partial \xi}{\partial t} + u_0 \frac{\partial \xi}{\partial s} - v' = -\kappa_1 S_{d,0} C'_u - \kappa_2 \nabla_t \cdot \mathbf{u}'_1 \quad (37)$$

where C'_u is the local linearized curvature of the flame front, ∇_t is the divergence operator associated with the flame surface, κ_1 and κ_2 are the Markstein lengths associated, respectively, with the curvature of the flame and with the local strain of the upstream

flow. For a given input, this equation allows for the computation of the local value of ξ and its action on the upstream flow.

The vorticity sheet is accounted for by the Biot-Savart law using conventions from Fig. 17 according to

$$\mathbf{u}'_{BS}(\mathbf{x}) = \frac{1}{4\pi} \int_S \frac{(\mathbf{x} - \mathbf{x}')}{|\mathbf{x} - \mathbf{x}'|^3} \times (\mathbf{t}_0 \times \mathbf{n}_0) \left(\frac{\partial \xi}{\partial s} (v_{0,2} - v_{0,1}) \right) dS(\mathbf{x}') \quad (38)$$

where S denotes the flame front. This self-induced vorticity has been superimposed on the acoustic forcing for the computation of equation (37). The forcing has been taken as a periodic acoustic wave with a fixed frequency; a vorticity sheet is generated on the wall at the injection plane. This correction models the anchor-point dynamics and provides a Neumann boundary condition for equation (37)

$$\omega_{in} = \frac{\partial \xi}{\partial s} (v_{0,2} - v_{0,1}) \quad (39)$$

where ω_{in} is the input-speed discontinuity at the flame anchor-point. The importance of pipe corners in vorticity generation can be appreciated by an analysis of the DNS (Direct Navier-Stokes Simulation) results presented in appendix A. Equations (37), (38) and (39) then form a closed set of linear equations.

The flame base-flow position has been set as the isolevel $\rho_0 = 0.7\rho_\infty$. This value has been found to reasonably well interpolate the linear vorticity layer in the flame. The flame speed has been inferred from the two-dimensional results. For a given density level set, it has been extrapolated using

$$S_{d,0} = (\mathbf{u}_{0,2D} \cdot \mathbf{n}_0) \frac{S_{ref}}{S} \quad (40)$$

where S is the surface of the considered isolevel, and S_{ref} is the surface of the level $\rho_0 = 0.99$, defined as the start of the preheating zone. This technique has been found to give consistent results for different density isolevels. The interpolated convective speed u_0 of equation (37) has been straightforwardly obtained with

$$u_0 = \mathbf{u}_{0,2D} \cdot \mathbf{t}_0. \quad (41)$$

The computation of the Markstein lengths has proven more challenging and has resulted in strong variations in the values estimated from base-flow analysis. The lengths were respectively set to $\kappa_1 = 0.05$ and $\kappa_2 = 0.005$. They are in qualitative agreement with observations from two-dimensional simulations. The direct implementation of a Biot-Savart law, like equation (38), is known to yield numerical instabilities and requires a desingularization step Krasny (1986) to produce a stable algorithm. The characteristic thickness of the sheet has been set to 1/3 of the flame thickness.

The last challenge in the implementation of this test case concerns the set-up of the acoustic forcing. In fully compressible reactive simulations, acoustic waves have been found to be reflected by the internal and external flame front because the flame acts as a wave guide. In a first approximation, this effect has been neglected. The forcing amplitude has been determined from the initialization of a linear acoustic forcing at

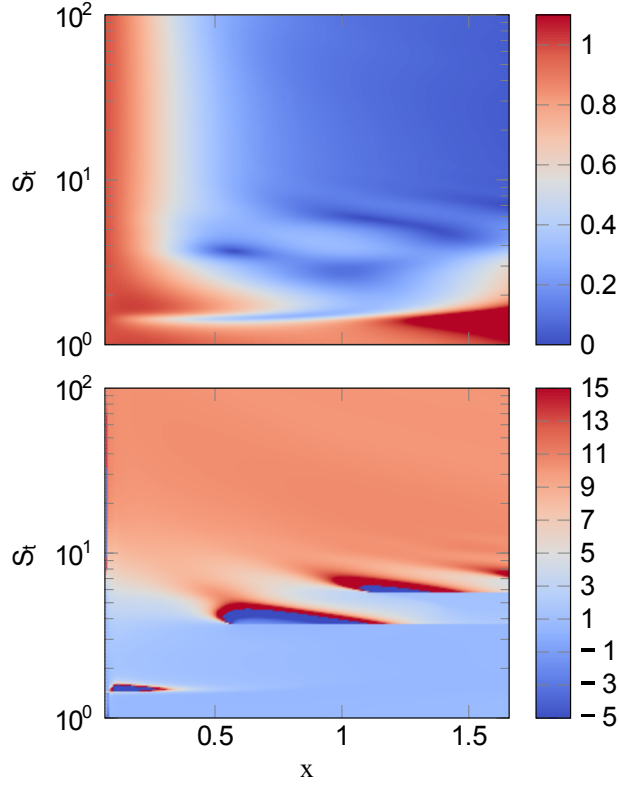


Figure 18: Norm (top) and phase speed (bottom) from the model.

$St = 2.64$. The phase has then been computed based on a delay model, assuming an acoustic wave propagating along the pipe axis, i.e.,

$$\varphi = St \left(t - \frac{x}{\text{Ma}} \right). \quad (42)$$

Lastly, the input vorticity ω_{in} has been calculated from the discontinuity of the axial velocity at wall corners. These techniques have not been able to predict the acoustic fringes observed in Fig. 14 and can only provide an estimate for the anchor-point dynamics. They are nonetheless intended as an illustration of the effect of vorticity on the upstream flow induced by flame deformations.

As the system is linear and forced at a chosen nondimensional frequency St , the solution can be decomposed as

$$\xi(s, t) = \hat{\xi}(s) \exp(i St t). \quad (43)$$

The equation for $\hat{\xi}$ is thus time-independent and has been solved using a preconditioned, iterative GMRES (Generalized Minimal Residual Method) algorithm Saad & Schultz (1986).

Results have been post-processed using the same methodology employed for Fig. 14. Both figures use the same colormap. As can be seen in Fig. 18, the model reproduces

the first low-frequency region observed in Fig. 14, in blue, in the phase diagram. The amplitude of the velocity in this region is nearly constant, except for $St = 1.4$, for which a quick decay is observed. This effect is likely due to the definition of TF_{FIOM} in Eq. (30) and associated with a spuriously high amplitude of $\tilde{u}(\tilde{s} = 0, St = 1.4)$. The critical Strouhal number has been shifted from 6.3 to 3.6.

The structure of the transitional region has been found to strongly depend on κ_1 and κ_2 and on the values of the critical Strouhal number to be closely related to the anchor-point boundary conditions. However, this region extends from $St = 5$ to $St = 10$; furthermore, it is qualitatively correctly identified in frequency. For $St > 10$, as in Fig. 14, the acoustics dominate.

Given the simplicity of our approach, these results are very encouraging and highlight the need for a careful modeling of forcing terms and flame parameters when using a G -equation to represent the flame front. Additionally, the model shows the importance of coupling any nonlinear G -equation with a resolved continuity equation, in order to take into account the effects of the flame front displacement on the upstream flow.

Lastly, this study demonstrated the efficiency of our linearization technique to analyze a physical process as complex as the one occurring in a flame. It enabled us to develop a model that has been found to correctly account for the bulk of the observed physical mechanisms.

6 Conclusion

Even though it is widely acknowledged that flames react sensitively to acoustic excitation, a frequency response analysis of flames to sources of sound and its dependence on governing parameters appears to be lacking. The present study is an attempt to propose a numerical approach based on linearized governing equations that provides insight into acoustically forced flame dynamics and delineates the role of hydrodynamics and reaction chemistry. To this end, the compressible Navier-Stokes equations, augmented by equations for species mass fraction and closed by a one-way, one-step chemistry model of Arrhenius type, have been linearized about an M-flame and used as a basis for a numerical frequency response analysis. The resulting flame transfer function has been found in good agreement with experimental data for a laminar premixed methane-air flame. The accuracy of the model over the considered frequency range is further corroborated by matching the heat-release fluctuations and sound emission to results from combustion noise theory.

The principal advantage of the numerical frequency response approach lies in its componentwise analysis of physical effects on a specific output quantity. In this manner, the role and dominance of purely hydrodynamic versus reactive processes can be determined and quantified independently. Furthermore, a pointwise input-output map is able to isolate regions in space that respond favorably and maximally to acoustic excitation at a given frequency.

This type of analysis, applied to the M-flame, confirmed the role of flame-front deformations in the production of hydrodynamic structures which dominate and co-exist with the acoustic field over a certain range of Strouhal numbers. In particular,

acoustically induced vorticity at the flame front is purely hydrodynamically driven for $St < 6.3$. For higher Strouhal numbers, the convective mode and the acoustic wave co-exist, before the acoustic wave prevails for Strouhal numbers above 32. In the low-Strouhal regime, the convective mode is induced by a varicose response of the internal and external flame front to the acoustic forcing and dominates the flame front dynamics. A linearized model based on the G -equation has been developed to provide additional insight into the flame dynamics in the convection-dominated Strouhal-number regime. In this approach the wrinkled flame sheet is modeled by a vorticity sheet which is driven by two linearized source terms capturing the effects of localized curvature and local strain. Supplemented by a Biot-Savart equation and an anchor-point boundary condition, this model has been able to qualitatively reproduce the observations of the frequency response analysis and to duplicate (even quantitatively) the regime-switching of the convective and acoustic modes as a function of the Strouhal number. The low-frequency response of the wrinkled M-flame is thus influenced by a feedback mechanism involving the convective mode which drives the dynamics of the flame tip and thus the majority of radiated noise.

Acknowledgement

We wish to acknowledge the computational resources of GENCI-CINES and TGCC (Grant 2014-2a6451).

Appendices

A Volume vorticity sources

In this section, all linear simulations take into account unsteady chemistry terms. Our analytical model relies on the assumption of an infinitely thin flame. However, in DNS computations, the flame has a finite thickness. This section intends to provide information on vorticity generation inside the finite-thickness flame front.

Only a small amount of vorticity is present in the reaction layer of the base flow, as can be seen in Fig. 19. The vorticity of the base flow is mostly associated with the acceleration of the flow between the internal and external flame fronts. The volume vorticity observed in linear simulations thus cannot be explained by a convection of base-flow vorticity. This linear vorticity field associated with an acoustic forcing at $St = 2.64$ is presented in Fig. 20. Identifying the main vorticity sources is also of interest.

The vorticity equation for compressible flow can be expressed as

$$\begin{aligned} \frac{\partial \boldsymbol{\omega}}{\partial t} + (\mathbf{u} \nabla) \boldsymbol{\omega} &= (\boldsymbol{\omega} \nabla) \mathbf{u} - \boldsymbol{\omega} (\nabla \cdot \mathbf{u}) + \\ &\quad \frac{1}{\rho^2} \nabla \rho \wedge \nabla p + \nabla \wedge \left(\frac{1}{\rho} \nabla \cdot \boldsymbol{\tau} \right) + \nabla \wedge \mathbf{F} \end{aligned} \quad (44)$$

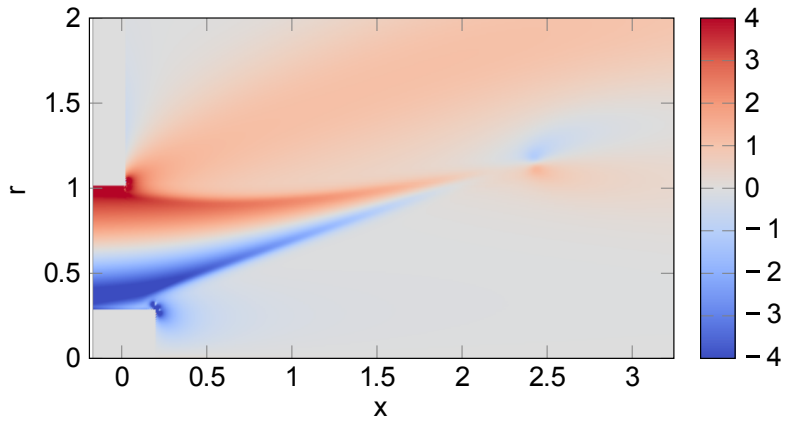


Figure 19: Base-flow vorticity.

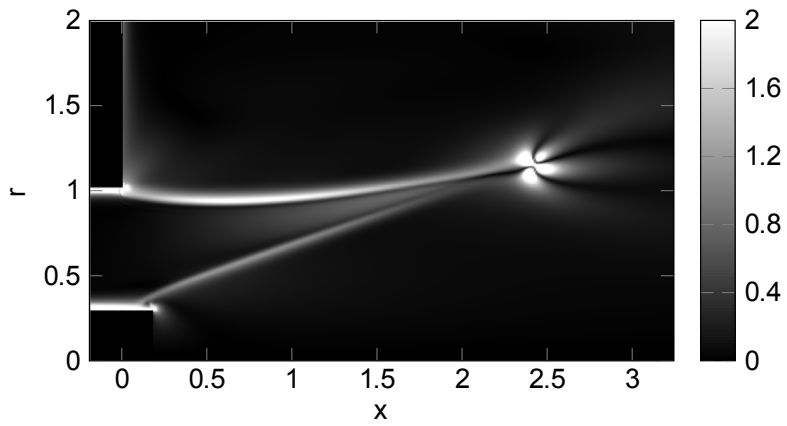


Figure 20: Absolute value of the permanent-regime linear vorticity, with an acoustic forcing at $St = 2.64$.

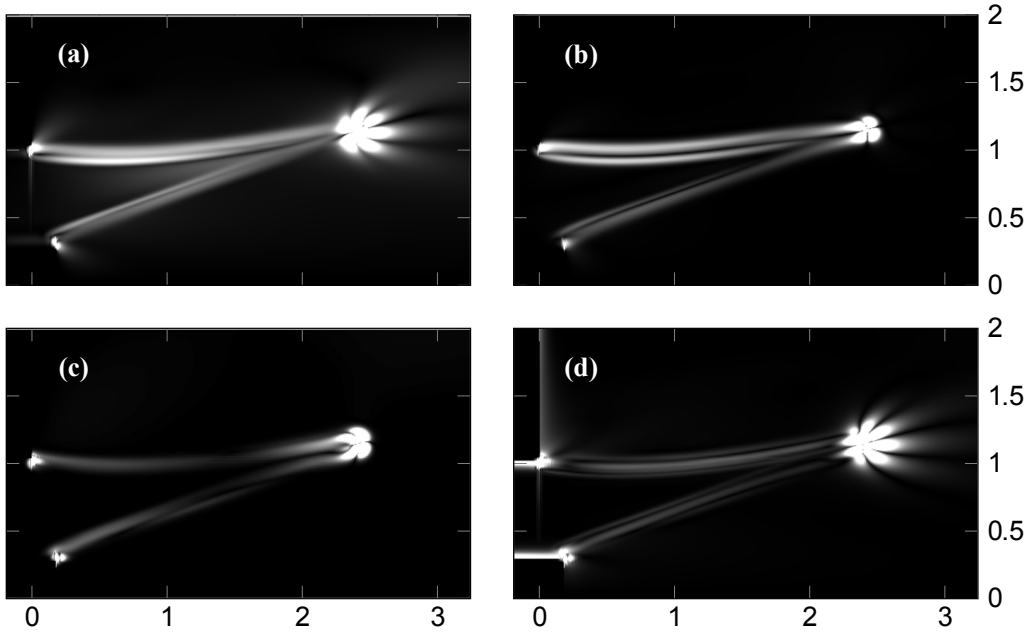


Figure 21: Absolute value of the components of the vorticity sources: (a): vorticity convection sources; (b): dilatation sources; (c): baroclinic sources; (d): viscous sources. The colormap is the same for all figures.

where ω is the vorticity, and \mathbf{F} stands for volume forces. In our case, gravity is neglected and $\mathbf{F} = 0$. Within an axisymmetric framework, it is convenient to group the first two terms of the right hand side; in the following, this first group will be referred to as the dilatation sources. The third term contains baroclinic vorticity sources, while the fourth captures viscous effects. A linearization of equation (44) about a steady state thus provides expressions for the different components of the linear vorticity equation. These terms have been separately evaluated and are presented in Fig. 21.

Three distinct regions can be distinguished: (i) the flame tip, (ii) the quasi-planar flame-front region, comprising the internal and external flame fronts, and (iii) the anchor-points area. The vorticity at the flame tip can straightforwardly be interpreted as the consequence of the local, high heat release rate. The strong dilatation occurring in a restricted region leads to a strong, but localized vorticity field. In the quasi-planar flame front region, the dilatation counteracts the convection in the direction normal to the flame front. This causes confinement of the vorticity layer inside the flame front. The vorticity is only convected in the tangential direction. In this region, baroclinic and viscous effects are negligible. Finally, in the anchor-point area, baroclinic and viscous effects are dominant (by two orders of magnitude). Moreover, locally, viscous sources are one order of magnitude higher than baroclinic sources. This suggests that the vorticity is mostly generated at the anchor-points, inside the boundary layer, by viscous effects.

A simple mechanism can be suggested for this vorticity generation. The acoustic boundary layer is much thinner than the fluid-based boundary layer. At the exit, a

strong radial gradient of axial velocity is thus induced at the corners. This shear generates vorticity through viscosity, which is subsequently convected along the flame front by the flow.

Bibliography

References

- ACHARYA, VISHAL, SHIN, DONG-HYUK & LIEUWEN, TIM 2012 Swirl effects on harmonically excited, premixed flame kinematics. *Combustion and Flame* **159** (3), 1139–1150.
- ÅKERVIK, ESPEN, BRANDT, LUCA, HENNINGSON, DAN S., HØEPFFNER, JÉRÔME, MARXEN, OLAF & SCHLATTER, PHILIPP 2006 Steady solutions of the navier-stokes equations by selective frequency damping. *Physics of Fluids* **18** (6), 068102–068106.
- ALTAY, H.M., PARK, S., WU, D., WEE, D., ANNASWAMY, A.M. & GHONIEM, A.F. 2009 Modeling the dynamic response of a laminar perforated-plate stabilized flame. *Proceedings of the Combustion Institute* **32**, 1359–1366.
- AUZILLON, P., FIORINA, B., VICQUELIN, R., DARABIHA, N., GICQUEL, O. & VEYNANTE, D. 2011 Modeling chemical flame structure and combustion dynamics in LES. *Proceedings of the Combustion Institute* **33** (1), 1331–1338.
- BADE, S., WAGNER, M., HIRSCH, C., SATTELMAYER, T. & SCHUERMANS, B. 2013a Design for thermo-acoustic stability: Modeling of burner and flame dynamics. *Journal of Engineering for Gas Turbine and Power* **135** (111502).
- BADE, S., WAGNER, M., HIRSCH, C., SATTELMAYER, T. & SCHUERMANS, B. 2013b Design for thermo-acoustic stability: Procedure and database. *Journal of Engineering for Gas Turbine and Power* **135** (121507).
- BAILLOT, F., DUROX, D. & PRUD'HOMME, R. 1992 Experimental and theoretical study of a premixed vibrating flame. *Combustion and Flame* **88**, 149–168.
- BALAY, SATISH, BROWN, JED, BUSCHELMAN, KRIS, EIJKHOUT, VICTOR, GROPP, WILLIAM D., KAUSHIK, DINESH, KNEPLEY, MATTHEW G., MCINNES, LOIS CURFMAN, SMITH, BARRY F. & ZHANG, HONG 2013 PETSc users manual. *Tech. Rep.* ANL-95/11 - Revision 3.5. Argonne National Laboratory.
- BALAY, SATISH, GROPP, WILLIAM D., MCINNES, LOIS CURFMAN & SMITH, BARRY F. 1997 Efficient management of parallelism in object oriented numerical software libraries. In *Modern Software Tools in Scientific Computing* (ed. E. Arge, A. M. Bruaset & H. P. Langtangen), pp. 163–202. Birkhäuser Press.

- BERLAND, JULIEN, BOGEY, CHRISTOPHE, MARSDEN, OLIVIER & BAILLY, CHRISTOPHE 2007 High-order, low dispersive and low dissipative explicit schemes for multiple-scale and boundary problems. *Journal of Computational Physics* **224** (2), 637–662.
- BIRBAUD, A. L., DUCRUIX, S., DUROX, D. & CANDEL, S. 2008 The nonlinear response of inverted “v” flames to equivalence ratio nonuniformities. *Combustion and Flame* **154** (3), 356–367.
- BIRBAUD, A. L., DUROX, D. & CANDEL, S. 2006 Upstream flow dynamics of a laminar premixed conical flame submitted to acoustic modulations. *Combustion and Flame* **146** (3), 541–552.
- BIRBAUD, A. L., DUROX, D., DUCRUIX, S. & CANDEL, S. 2007 Dynamics of free jets submitted to upstream acoustic modulations. *Physics of Fluids* **19** (1), 013602.
- BOBUSCH, B.C., COSIC, B., MOECK, J.P. & PASCHEREIT, C.O. 2014 Optical measurement of local and global transfer functions for equivalence ratio fluctuations in a turbulent swirl flame. *Journal of Engineering for Gas Turbine and Power* **136** (021506).
- BOYER, L. & QUINARD, J. 1990 On the dynamics of anchored flames. *Combustion and Flame* **82** (1), 51–65.
- BUI, T. PH., SCHRÖDER, W. & MEINKE, M. 2008 Numerical analysis of the acoustic field of reacting flows via acoustic perturbation equations. *Computers & Fluids* **37** (9), 1157–1169.
- BYCHKOV, V. V. & LIBERMAN, M. A. 2000 Dynamics and stability of premixed flames. *Physics Reports* **325** (4–5), 115–237.
- CANDEL, S., DUROX, D., DUCRUIX, S., BIRBAUD, A.-L., NOIRAY, N. & SCHULLER, T. 2009 Flame dynamics and combustion noise: progress and challenges. *International Journal of Aeroacoustics* **8** (1), 1–56.
- CHO, J.H. & LIEUWEN, T. 2005 Laminar premixed flame response to equivalence ratio oscillations. *Combustion and Flame* **140**, 116–129.
- CLAVIN, PAUL & SIGGIA, ERIC D. 1991 Turbulent premixed flames and sound generation. *Combustion Science and Technology* **78** (1-3), 147–155, 00083.
- COURANT, R., FRIEDRICHS, K. & LEWY, H. 1967 On the partial difference equations of mathematical physics. *IBM Journal of Research and Development* **11** (2), 215–234.
- DOWLING, A. P. 1999 A kinematic model of a ducted flame. *Journal of Fluid Mechanics* **394**, 51–72.
- DUCHAINE, F., BOUDY, F., DUROX, D. & POINSOT, T. 2011 Sensitivity of flame transfer functions of laminar flames. *Combustion and Flame* **158**, 2384–2394.

- DUCRUIX, S., SCHULLER, T., DUROX, D. & CANDEL, S. 2003 Combustion dynamics and instabilities: Elementary coupling and driving mechanisms. *Journal of Propulsion and Power* **19** (5), 722–734.
- DUROX, D., SCHULLER, T., NOIRAY, N. & CANDEL, S. 2009 Experimental analysis of nonlinear flame transfer functions for different flame geometries. *Proceedings of the Combustion Institute* **32** (1), 1391–1398.
- FLEIFIL, M., ANNASWAMY, A. M., GHONEIM, Z. A. & GHONIEM, A. F. 1996 Response of a laminar premixed flame to flow oscillations: A kinematic model and thermoacoustic instability results. *Combustion and Flame* **106** (4), 487–510.
- FRANZELLI, BENEDETTA, RIBER, ELEONORE, GICQUEL, LAURENT Y.M. & POINSOT, THIERRY 2012 Large eddy simulation of combustion instabilities in a lean partially premixed swirled flame. *Combustion and Flame* **159** (2), 621–637.
- GARNAUD, XAVIER 2012 Modes, transient dynamics and forced response of circular jets. PhD thesis, Ecole Polytechnique X.
- GOTTLIEB, SIGAL 2005 On high order strong stability preserving runge–kutta and multi step time discretizations. *Journal of Scientific Computing* **25** (1), 105–128.
- HARTMANN, D., MEINKE, M. & SCHROEDER, W. 2011 A level-set based adaptive-grid method for premixed combustion. *Combustion and Flame* **158**, 1318–1339.
- HEMCHANDRA, SANTOSH 2012 Premixed flame response to equivalence ratio fluctuations: Comparison between reduced order modeling and detailed computations. *Combustion and Flame* **159** (12), 3530–3543, 00016.
- HERMETH, S., STAFFELBACH, G., GICQUEL, L.Y.M., ANISIMOV, V., CIRIGLIANO, C. & POINSOT, T. 2014 Bistable swirled flames and influence on flame transfer functions. *Combustion and Flame* **161** (1), 184–196.
- HUERRE, P. & MONKEWITZ, P. A. 1985 Absolute and convective instabilities in free shear layers. *Journal of Fluid Mechanics* **159**, 151–168.
- IUDICIANI, P. & DUWIG, C. 2011 Large eddy simulation of the sensitivity of vortex breakdown and flame stabilisation to axial forcing. *Flow, Turbulence and Combustion* **86**, 639–666.
- KASHINATH, KARTHIK, HEMCHANDRA, SANTOSH & JUNIPER, MATTHEW P. 2013 Nonlinear thermoacoustics of ducted premixed flames: The influence of perturbation convection speed. *Combustion and Flame* **160** (12), 2856–2865, 00008.
- KEDIA, K. S., ALTAY, H. M. & GHONIEM, A. F. 2011 Impact of flame-wall interaction on premixed flame dynamics and transfer function characteristics. *Proceedings of the Combustion Institute* **33** (1), 1113–1120.
- KERSTEIN, ALAN R., ASHURST, WILLIAM T. & WILLIAMS, FORMAN A. 1988 Field equation for interface propagation in an unsteady homogeneous flow field. *Physical Review A* **37** (7), 2728–2731.

- KETCHESON, DAVID I. 2008 Highly efficient strong stability-preserving runge–kutta methods with low-storage implementations. *SIAM Journal on Scientific Computing* **30** (4), 2113–2136.
- KIM, K.T., LEE, J.G., QUAY, B.D. & SANTAVICCA, D.A. 2010 Response of partially premixed flames to acoustic velocity and equivalence ratio perturbations. *Combustion and Flame* **157**, 1731–1744.
- KIM, K. T. & HOCHGREB, S. 2011 The nonlinear heat release response of stratified lean-premixed flames to acoustic velocity oscillations. *Combustion and Flame* **158** (12), 2482–2499, 00035.
- KORNILOV, V.N., ROOK, R., TEN THIJE BOOKKAMP, J.H.M. & DE GOEY, L.P.H. 2009 Experimental and numerical investigation of the acoustic response of multi-slit bunsen burners. *Combustion and Flame* **156** (10), 1957–1970.
- KORNILOV, V. N., SCHREEL, K. R. A. M. & DE GOEY, L. P. H. 2007 Experimental assessment of the acoustic response of laminar premixed bunsen flames. *Proceedings of the Combustion Institute* **31**, 1239–1246.
- KRASNY, ROBERT 1986 Desingularization of periodic vortex sheet roll-up. *Journal of Computational Physics* **65** (2), 292–313.
- KREBS, W., KREDIET, H., PORTILLO, E., HERMETH, S., POINSOT, T., SCHIMEK, S. & PASCHEREIT, C. O. 2013 Comparison of nonlinear to linear thermoacoustic stability analysis of a gas turbine combustion system. *Journal of Engineering for Gas Turbine and Power* **135** (081503).
- KREDIET, H. J., BECK, C. H., KREBS, W., SCHIMEK, S., PASCHEREIT, C. O. & KOK, J. B. W. 2012 Identification of the flame describing function of a premixed swirl flame from LES. *Combustion Science and Technology* **184** (7-8), 888–900.
- LEMKE, MATHIAS, REISS, JULIUS & SESTERHENN, JÖRN 2014 Adjoint based optimisation of reactive compressible flows. *Combustion and Flame* **10** (161), 2552–2564.
- LESSHAFFT, LUTZ, HUERRE, PATRICK, SAGAUT, PIERRE & TERRACOL, MARC 2006 Nonlinear global modes in hot jets. *Journal of Fluid Mechanics* **554**, 393–409.
- LIEUWEN, TIM C. 2012 *Unsteady Combustor Physics*. Cambridge University Press.
- LIEUWEN, T. C. & YANG, V., ed. 2005 *Combustion instabilities in gas turbines, Operational experience, Fundamental mechanisms, and Modeling, Progress in Astronautics and Aeronautics*, vol. 210. American Institute of Aeronautics and Astronautics, Inc.
- MARKSTEIN, G.H. 1964 *Nonsteady flame propagation*. Pergamon.
- MATVEEV, K.I. & CULICK, F.E.C. 2003 A model for combustion instability involving vortex shedding. *Combustion Science and Technology* **175**, 1059–1083.

- MICHALKE, ALFONS 1984 Survey on jet instability theory. *Progress in Aerospace Sciences* **21**, 159–199.
- MONKEWITZ, PETER A & SOHN, KIHOD 1988 Absolute instability in hot jets. *AIAA journal* **26** (8), 911–916.
- NOIRAY, N., DUROX, D., SCHULLER, T. & CANDEL, S. 2008 A unified framework for nonlinear combustion instability analysis based on the flame describing function. *Journal of Fluid Mechanics* **615**, 139–167.
- PALIES, P., DUROX, D., SCHULLER, T. & CANDEL, S. 2011*a* Experimental study on the effect of swirler geometry and swirl number on flame describing functions. *Combustion Science and Technology* **183** (7), 704–717.
- PALIES, P., DUROX, D., SCHULLER, T. & CANDEL, S. 2011*b* Nonlinear combustion instabilities analysis based on the flame describing function applied to turbulent premixed swirling flames. *Combustion and Flame* **158**, 1980–1991.
- PALIES, P., SCHULLER, T., DUROX, D. & CANDEL, S. 2011*c* Modeling of swirling flames transfer functions. *Proceedings of the Combustion Institute* **33**, 2967–2974.
- PALIES, P., SCHULLER, T., DUROX, D., GICQUEL, L.Y.M. & CANDEL, S. 2011*d* Acoustically perturbed turbulent premixed swirling flames. *Physics of Fluids* **23** (037101), (15 pages).
- PAN, KUO-LONG & FURSENKO, ROMAN 2008 Characteristics of cylindrical flame acceleration in outward expansion. *Physics of Fluids* **20** (9), 094107.
- FOSAS DE PANDO, MIGUEL, SIPP, DENIS & SCHMID, PETER J. 2012 Efficient evaluation of the direct and adjoint linearized dynamics from compressible flow solvers. *Journal of Computational Physics* **231** (23), 7739–7755.
- PASCHEREIT, C. O., SCHUERMANS, B., POLIFKE, W. & MATTSON, O. 2002 Measurement of transfer matrices and source terms of premixed flames. *Journal of Engineering for Gas Turbine and Power* **124**, 239–247.
- PELCE, PIERRE & CLAVIN, PAUL 1982 Influence of hydrodynamics and diffusion upon the stability limits of laminar premixed flames. *Journal of Fluid Mechanics* **124**, 219–237.
- PETERS, N. 2000 *Turbulent combustion*. Cambridge University Press.
- POINSOT, THIERRY & VEYNANTE, DENIS 2012 *Theoretical And Numerical Combustion - Third Edition*. R.T. Edwards, Inc.
- PREETHAM, HEMCHANDRA, S. & LIEUWEN, T. 2008 Dynamics of laminar premixed flames forced by harmonic velocity disturbances. *Journal of Propulsion and Power* **24** (6), 1390–1402.
- QADRI, UBAID ALI 2014 Global stability and control of swirling jets and flames. Thesis, University of Cambridge.

- RHEE, C. W., TALBOT, L. & SETHIAN, J. A. 1995 Dynamical behaviour of a premixed turbulent open v-flame. *Journal of Fluid Mechanics* **300**, 87–115.
- SAAD, Y. & SCHULTZ, M. 1986 GMRES: A generalized minimal residual algorithm for solving nonsymmetric linear systems. *SIAM Journal on Scientific and Statistical Computing* **7** (3), 856–869.
- SANDBERG, RICHARD D. 2007 Governing equations for a new compressible navier-stokes solver in general cylindrical coordinates. Monograph AFM-07/07. School of Engineering Sciences, University of Southampton.
- SCHIMEK, S., MOECK, J.P & PASCHEREIT, C.O. 2011 An experimental investigation of the nonlinear response of an atmospheric swirl-stabilized premixed flame. *Journal of Engineering for Gas Turbine and Power* **133** (10), 101502.
- SCHUERMANS, B., GUETHE, F. & MOHR, W. 2010a Optical transfer function measurements for technically premixed flames. *Journal of Engineering for Gas Turbine and Power* **132** (081501).
- SCHUERMANS, B., GUETHE, F., PENNEL, D., GUYOT, D. & PASCHEREIT, C.O. 2010b Thermoacoustic modeling of a gas turbine using transfer functions measured at full engine pressure. *Journal of Engineering for Gas Turbines and Power* **132** (11), 11503 (9 pages).
- SCHULLER, T, DUROX, D & CANDEL, S 2003a Self-induced combustion oscillations of laminar premixed flames stabilized on annular burners. *Combustion and Flame* **135** (4), 525–537.
- SCHULLER, T., DUROX, D. & CANDEL, S. 2003b A unified model for the prediction of laminar flame transfer functions: comparisons between conical and v-flame dynamics. *Combustion and Flame* **134** (1–2), 21–34.
- SIVASHINSKY, G. I. 1977 Nonlinear analysis of hydrodynamic instability in laminar flames—i. derivation of basic equations. *Acta Astronautica* **4** (11–12), 1177–1206.
- STAFFELBACH, G., GICQUEL, L.Y.M., BOUDIER, G. & POINSOT, T. 2009 Large eddy simulation of self excited azimuthal modes in annular combustors. *Proceedings of the Combustion Institute* **32**, 2909–2916.
- TALEI, MOHSEN, BREAR, MICHAEL JOHN & HAWKES, EVATT ROBERT 2012 A parametric study of sound generation by premixed laminar flame annihilation. *Combustion and Flame* **159** (2), 757–769.
- TAY-WO-CHONG, L., BOMBERG, S., ULHAQ, A. & POLIFKE, W. 2012 Comparative validation study on identification of premixed flame transfer function. *Journal of Engineering for Gas Turbine and Power* **134** (2), 021502 (8 pages).
- TAY WO CHONG, LUIS, KOMAREK, THOMAS, KAESS, ROLAND, FOLLER, STEPHAN & POLIFKE, WOLFGANG 2010 Identification of flame transfer functions from LES of a premixed swirl burner. *Proceedings of ASME Turbo Expo 2010* pp. 623–635.

- TAY WO CHONG, L. & POLIFKE, W. 2013 Large eddy simulation-based study of the influence of thermal boundary condition and combustor confinement on premix flame transfer functions. *Journal of Engineering for Gas Turbine and Power* **135**, 021502 (9 pages).
- TRUFFAUT, JEAN-MARIE 1998 Étude expérimentale de l'origine du bruit émis par les flammes de chalumeaux. PhD thesis, Université de Provence - Aix-Marseille I.
- ZELDOVICH, IA B., BARENBLATT, G. I., LIBROVICH, V. B. & MAKHVILADZE, G. M. 1985 *Mathematical theory of combustion and explosions*. Consultants Bureau, New York, NY.

2.3 Going Further with Linear Results

The previous section showed some specific aspects of the flame dynamics occurring during an acoustic forcing. More pieces of information can be deduced from this Input/Output analysis. A fast evaluation technique of the impulse response was presented in section 2.2. Impulse responses then allow to recover the dynamic of a linear system subjected to any forcing history through a mere convolution. Moreover its Fourier transform generates the frequency response of the input/output relation considered. In theory, all these characteristics are sufficient to fully describe a system. In particular, a naive state space equation can directly be inferred from the impulse response. As an example, it can be numerically formulated as:

$$\begin{aligned} X_{n+1} &= \tilde{A}_{ss}X_n + \tilde{B}_{ss}f_n \\ Y_n &= \tilde{C}_{ss}X_n \end{aligned} \quad (2.1)$$

with:

$$\tilde{A}_{ss} = \begin{pmatrix} 0 & 0 & \cdots & 0 & 0 \\ 1 & 0 & \cdots & 0 & 0 \\ 0 & 1 & \cdots & 0 & 0 \\ \vdots & \vdots & \cdots & \vdots & \vdots \\ 0 & 0 & \cdots & 1 & 0 \end{pmatrix} \quad (2.2)$$

$$\tilde{B}_{ss} = \begin{pmatrix} 1 \\ 0 \\ \vdots \\ 0 \end{pmatrix} \quad \tilde{C}_{ss} = Imp^* \quad (2.3)$$

where Imp denotes the impulse response, X_n denotes the state space variable, f_n is the input and Y_n the output at the n -th time step. This method has however three main disadvantages: if the impulse response is oscillating, it is poorly conditioned; no physical information is included in \tilde{A}_{ss} ; the impulse is likely to contain a lot of redundant pieces of information. Indeed, this model has just as many modes as the numerical impulse response has points. These issues make it a poor candidate for generating a state space equation. Integrating it in a combustor model would lead at best to slow or at worst to imprecise results. As an example, we can consider the case of the integral heat release rate stemming from the M-flame acoustic impulse response. This time series, presented in figure 2.1, is about 10 000 points long. However, it is visually rather obvious that a good state-space approximation could be obtained with a limited number of modes.

Linear algebra analysis can help infer the natural form a physics-based model should take. A good start is the linear operator definition:

$$\frac{\partial \Upsilon}{\partial t} = A\Upsilon(t) + f(t) \quad (2.4)$$

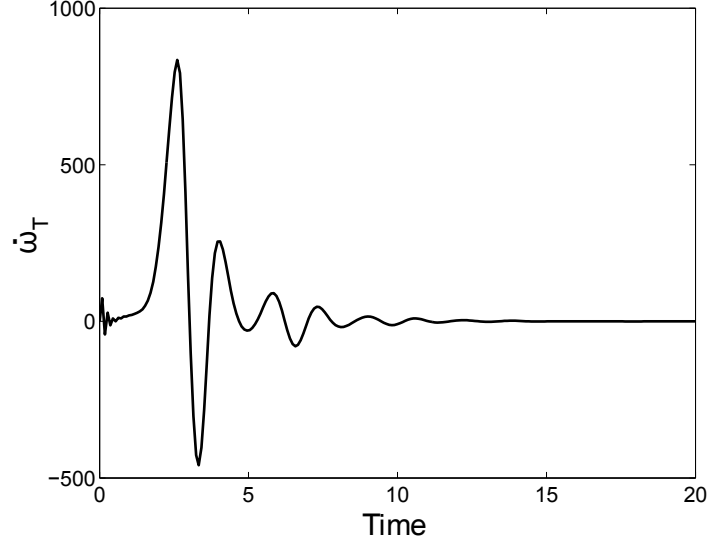


Figure 2.1: Linear heat release rate response to an acoustic impulse for an M -flame.

As we are working in finite dimension, A is a matrix. By making the hypothesis that A is real and diagonalizable, there exists an invertible P matrix such that:

$$A = P^{-1} \begin{pmatrix} E_1 & 0 & \cdots & 0 \\ 0 & E_2 & \cdots & 0 \\ \vdots & \vdots & \ddots & \vdots \\ 0 & 0 & \cdots & E_k \end{pmatrix} P \quad (2.5)$$

where E_j is the subspace associated with the j -th eigenvalue of A , λ_j . As an example, E_j can take the form:

$$E_j = \begin{pmatrix} \lambda_j \end{pmatrix} \quad \text{if} \quad \text{Im}(\lambda_j) = 0 \quad (2.6)$$

$$E_j = \begin{pmatrix} 2\text{Re}(\lambda_j) & -|\lambda_j|^2 \\ 1 & 0 \end{pmatrix} \quad \text{if} \quad \text{Im}(\lambda_j) \neq 0 \quad (2.7)$$

Using this definition, the matrix A takes the form of a set of harmonic oscillators acting simultaneously, in parallel, on the system. Building a linear reduced order model can also consist in carefully selecting the relevant subspaces E_j . In the following, a constant shape forcing f_0 and a varying forcing amplitude $\alpha(t)$ are assumed. Besides, we suppose the variations of $\alpha(t)$ have a bounded frequency content. The Fourier transform of α is also negligible for $\omega > \omega_{max}$. In this case, selecting E_j can be accomplished by examining the eigenvalues on the one hand and on the other hand the projection of the forcing shape on the eigenvectors. First, the value of λ_j can filter some subspaces. Indeed, if the linear operator A has an eigenvalue λ_j , the corresponding eigenvalue of the resolvent at the angular frequency ω is $1/(\lambda_j - i\omega)$. If λ_j is very large compared to ω , the response corresponding to the subspace E_j will also be negligible. However, this criteria is very rough and can only eliminate fairly high wavenumbers. It is then necessary to consider the projection of the forcing shape f_0 on E_j . This projection results from a linear combination of the projection of f_0 on the eigenvector Υ_j and its conjugate. Equivalently, the contribution of Υ_j to the output can be used as a supplementary criteria.

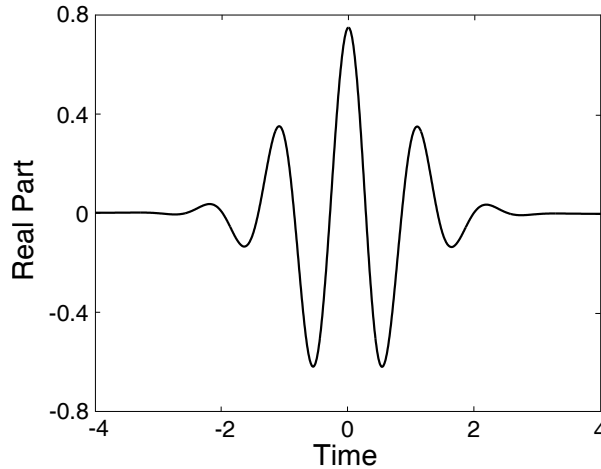


Figure 2.2: Real part of a Morlet wavelet, $\sigma=5$.

2.3.1 State Space Identification Algorithm Layout

All these arguments are rather theoretical and would be heavy to implement as they require a perfect knowledge of the eigenvalues and eigenvectors of A . Instead, we are going to attempt reducing the system resulting from the impulse response into a set of parallel harmonic oscillators. Each one of these oscillators has a unique characteristic angular frequency ω_i . The output signal can also be decomposed as

$$Imp = \sum_i \alpha_i(t) e^{i\omega_i t} \quad (2.8)$$

where α_i denotes the time-varying amplitude associated with the frequency ω_i . Our algorithm will also attempt to:

- Identify the dominant frequencies ω_i .
- Compute the instantaneous amplitude α_i associated with these oscillations.
- Use the two previous pieces of information to estimate the coefficients of a corresponding harmonic oscillator.

Our decomposition technique uses the convolution of wavelets with the impulse response. Wavelets have been successfully used over the past to analyze complex time series [Grizzi & Camussi, 2012]. They have the property to be localized both in time and in frequency. In this study, they will be used to evaluate the local evolution of the amplitude associated with predefined characteristic frequencies.

2.3.2 Detailed Description of the Wavelets Used

In the following, we are going to consider Morlet wavelets [Ashmead, 2012]. They typically take the form presented in figure 2.2. These wavelets are defined in the Fourier domain by:

$$\tilde{\psi}(\sigma, \omega) = \left(1 + e^{-\sigma^2} - 2e^{-\sigma^2 3/4}\right)^{-1/2} \pi^{-1/4} \left(e^{-(\sigma-\omega)^2/2} - e^{-(\omega^2+\sigma^2)/2}\right) \quad (2.9)$$

Where σ characterizes the time/frequency localization trade-off associated with the wavelet. Its main angular frequency ω_{main} is defined as the solution of:

$$(\omega_{main} - \sigma)^2 - 1 - (\omega_{main}^2 - 1)e^{-\sigma\omega_{main}} = 0 \quad (2.10)$$

A good use of wavelets also supposes to carefully choose σ for a given ω_{main} . In our case, a good frequency localization is required; $\sigma = 30$ is kept when possible, otherwise we impose $\sigma \geq 5$. More precisely, the following functions are used in the algorithm:

For a signal of length N , of time-step dt , let define:

$$\omega_1 = \frac{2\pi}{Ndt} \quad (2.11)$$

$$\sigma_{max} = 30 \quad (2.12)$$

$$0 = (\omega_{ref} - \sigma_{max})^2 - 1 - (\omega_{ref}^2 - 1)e^{-\sigma_{max}\omega_{ref}} \quad (2.13)$$

where ω_1 is the lowest angular frequency for which a wavelength is fully included in the time series. In order to keep $\sigma \geq 5$, the smallest analyzable frequency is thus $4\omega_1$. For a given angular frequency $\omega_{main} \geq 4\omega_1$ we compute the corresponding σ_{init} :

$$\left(\frac{\omega_{main}}{\omega_1} - \sigma_{init}\right)^2 - 1 - \left(\frac{\omega_{main}^2}{\omega_1^2} - 1\right)e^{-\sigma_{init}\omega_{main}/\omega_1} = 0 \quad (2.14)$$

Then the following values are used:

$$\delta = 1, \quad \sigma = \sigma_{init} \quad \text{if} \quad \sigma_{init} \leq \sigma_{max} \quad (2.15)$$

$$\delta = \frac{\omega_{main}}{\omega_{ref}}, \quad \sigma = \sigma_{max} \quad \text{if} \quad \sigma_{init} > \sigma_{max} \quad (2.16)$$

Finally, the following expression for the wavelet is used:

$$g(\omega) = \exp\left[-\left(\sigma - \frac{\omega}{\delta\omega_1}\right)^2/2\right] - \exp\left[-\left(\left(\frac{\omega}{\delta\omega_1}\right)^2 + \sigma^2\right)/2\right] \quad (2.17)$$

$$\tilde{\psi}(\omega_{main}, \omega) = \frac{g(\omega) \sqrt{N}}{\left(\|g\|_n^2 \sqrt{\delta}\right)} \quad (2.18)$$

where $\|\cdot\|_n^2$ is the numerical 2-norm. This scaling preserves the maximum value of the inverse Fourier transform of $\tilde{\psi}$ with varying ω_{main} , while the \sqrt{N} factor is an optional factor enforcing a consistency of the measured amplitudes with varying time series length.

2.3.3 Detailed Description of the Algorithm

The previous wavelets family sets the framework for our algorithm. By computing the convolution of a given wavelet with the impulse response signal, a specific angular frequency ω_{main} is selected: the filtered signal is also of the form $\alpha(t) \exp(i\omega_{main}t)$. If ω_{main} corresponds to one of the ω_i from Eq. 2.8, α will be an approximation for α_i . However, wavelet convolution induces a phase and amplitude shift on the initial signal. For instance, the filtering of a periodic $\exp(i\omega_{main}t)$ signal creates:

$$\psi(\omega_{main}, t) \otimes e^{i\omega_{main}t} = \xi e^{i\omega_{main}(t+\tau)} \quad (2.19)$$

where ξ and τ are the amplitude and the corresponding time shift. These parameters only depend on $\psi(\omega_{main})$. To compensate for this phenomenon, the input is filtered as well to compute the state space estimate.

The identification algorithm is then rather straightforward. A frequency bandwidth is first defined. The minimum angular frequency should be at least $4\omega_1$, i.e. the impulse response should contain 4 full periods of the minimum angular frequency. A set of frequencies regularly spaced in log scale between the minimum and the maximum frequency is generated. The corresponding wavelets are first convoluted with the impulse response. The

signal with the largest 1-norm is then selected: in the following, this will be the output. The corresponding wavelet is convoluted with the initial impulse input signal to generate the input used in the system identification step. Please note that a tolerance exists on the shape of the initial impulse input signal. A second order state space is then identified with the ‘srest’ function from Matlab (©The MathWorks, Inc.).

Using wavelets limits the identification to oscillatory modes. To circumvent this issue, a first order model is separately estimated, based on a 2-norm fit of a decaying exponential. The fit thus obtained is compared with the error made by the second order model, the best one being then retained. This supplementary step increases precision and enforces the convergence of the algorithm.

Finally, the impulse response of this second order state space is computed and subtracted to the initial signal. After looping, this procedure converges to a state space model with all its characteristic frequencies between the initially fixed minimum and maximum frequencies. The overall algorithm is presented in figure 2.3.

2.3.4 Validation Test Case

The reconstructed impulse response resulting from our algorithm applied on the signal presented in figure 2.1, for an order $k' = 40$, is shown in figure 2.4. The agreement is excellent, with an overall 2-norm error lower than 4%. This algorithm is also very efficient at identifying a state space model from an impulse response. Several limitations are however worth being explicitly stated. First, if the energy contained in the frequency range chosen gets of the same order as the energy out of this bandwidth, the algorithm saturates. This is observable at the very start of the signal in figure 2.4 where high frequency oscillations are not well captured. A second limitation is the absence of delay in our model. The algorithm supposes an instantaneous response of the system. If present, a delay will have to be added as a pre-processing step. However, we believe this limitation is not too steep as impulse responses provide an immediate, explicit access to delays.

The output of our algorithm is also in the form we were looking for. If the i -th identified state space is written:

$$\dot{x}_i = A_i x_i + B_i u \quad (2.20)$$

$$y = C_i x_i \quad (2.21)$$

where A_i is a 1-by-1 or 2-by-2 matrix, then the final state space identified:

$$\dot{x} = A_{ss} x + B_{ss} u \quad (2.22)$$

$$y = C_{ss} x \quad (2.23)$$

is such that:

$$A_{ss} = \begin{pmatrix} A_1 & 0 & \cdots & 0 \\ 0 & A_2 & \cdots & 0 \\ \vdots & \vdots & \ddots & \vdots \\ 0 & 0 & \cdots & A_k \end{pmatrix} \quad (2.24)$$

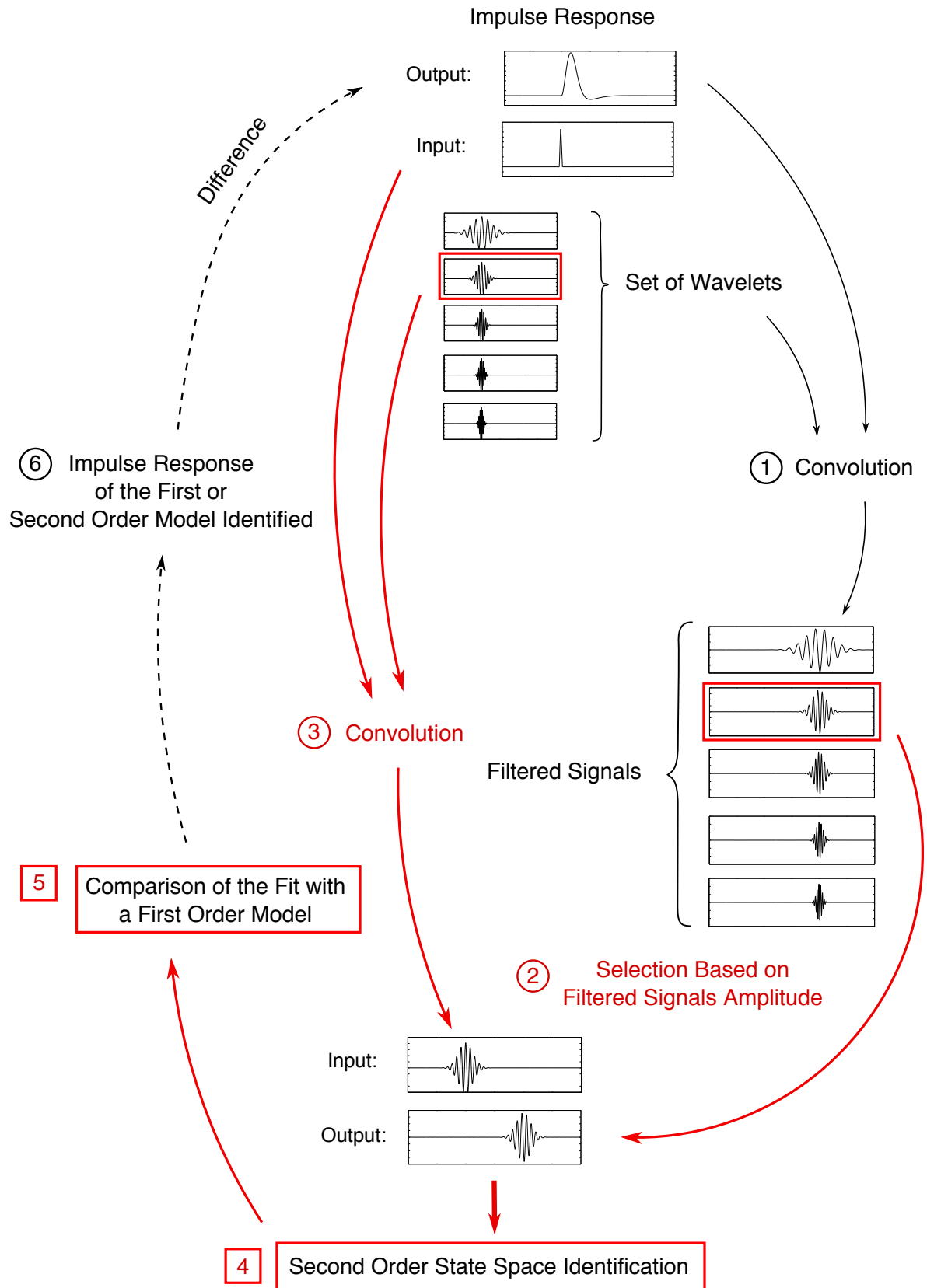


Figure 2.3: Impulse Response to State Space Algorithm. Continuous black arrows: preprocessing steps. Red arrows: identification steps. Dotted black arrows: post-processing steps.

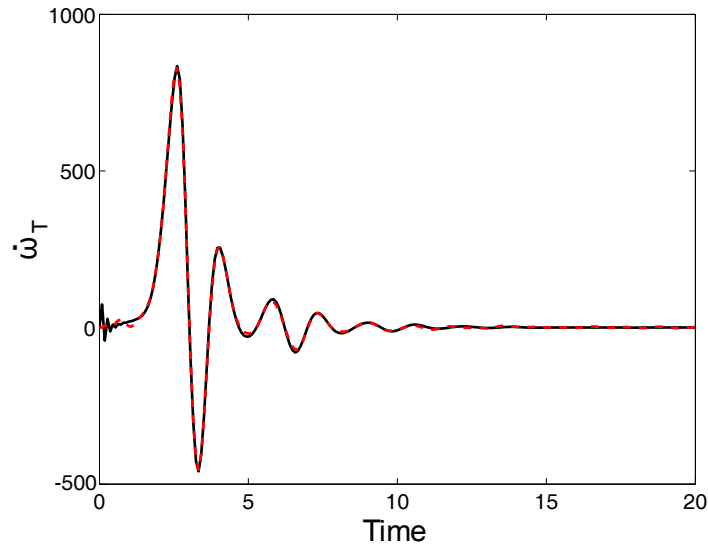


Figure 2.4: Comparison of the initial signal and the reconstructed impulse response using our algorithm, with an order $k' = 40$. The 2-norm error is of 4%. Black: initial signal. Dotted red: reconstructed signal.

$$B_{ss} = \begin{pmatrix} B_1 \\ B_2 \\ \vdots \\ B_k \end{pmatrix} \quad (2.25)$$

$$C_{ss} = (C_1, C_2, \dots, C_k) \quad (2.26)$$

The A_i matrices are approximations for the E_i submatrices of Eq. 2.5. The identified dynamical system takes the wished form of a set of harmonic oscillators or first-order ordinary differential equations placed in parallel. An interesting property of this formulation is its filtering behaviour at high forcing frequency. Outside the selected frequency range, each oscillator acts as a first or second order low pass filter. The non-resolved forcing frequencies are also damped.

Our procedure is however less efficient than Matlab's build-in corresponding function ('imp2ss'). Matlab's algorithm leads to a 0.01% error on the reconstructed impulse. However, the main interests of our method lie in the structure of the A matrix, presented in the form of a set of harmonic oscillators, and in the identification of amplitude equations. Besides, the most natural expression of non-linearities is in state-space form. This methodology can also be a first step toward more precise non linear models. The challenges associated with finite amplitude flames dynamics will thus be considered in chapter 4.

2.4 Conclusion

In this chapter, the linear dynamics of an acoustically forced M-flame was studied. It was shown that, even in the linear limit, flame heating effects have a strong impact on

flame dynamics. Acoustic fluctuations induce the propagation of vorticity waves along the flame front. These perturbations generate in turn an upstream velocity fluctuation called here Flame Induced Oscillatory Mode (FIOM). This structure needs to be included in flow models to reproduce the correct flame shape and flame transfer function when submitted to an acoustic forcing. This conclusion was reached using linear tools. In particular, results from impulse responses were used. A method to convert these signals into a low-order, high precision linear dynamical system was finally presented

These results may ease the development of reduced order models for the prediction of flame response to flow perturbations. It is interesting to explore the limits of our combustion noise model. Indeed, our entire analysis of acoustic waves generation has been so far based on the assumption that most noise stems from linear heat release rate. Our tools allow us to explore the limits of this hypothesis by evaluating which flow structure generates the largest sound levels in the M-flame. In the next chapter, an optimization algorithm will thus be applied to investigate this issue. A 1-D axisymmetric analysis will then provide the tools to understand our optimization results.

Chapter 3

Optimal Linear Acoustic Generation

Flame noise essentially originates from unsteady heat release rate sources [Strahle, 1978]. However, this observation is based on a far field asymptotic analysis. This chapter tackles the issue of close field acoustic generation. More precisely, its purpose is to revisit the way flame fronts generate noise using linear optimizations tools.

3.1 Motivation

Optimizing an input/output relation in linear fluid dynamics is a classical procedure. The resolvent operator $R(\omega)$, described in the introduction of this thesis, has properties in common with the linear operator. Assuming the multiplicity of the eigenvalues λ of the linear operator to be one, both share the same eigenvectors, with the eigenvalues of the resolvent being shifted according to $\tilde{\lambda} = 1/(\lambda - i\omega)$. For this reason, it has been used in linear stability analysis [Schmid & Henningson, 2001; Garnaud, 2012]. When combined with the adjoint, it is possible to carry out output optimizations in a 2-norm sense. This method is, for instance, at the base of modern airfoil shape optimization [Reuther *et al.*, 1999]. It has been used as well to study the amplification of streaks by a turbulent flow [Hwang & Cossu, 2010], or the generation of acoustic waves by an harmonically forced jet [Garnaud, 2012]. This chapter will focus on the maximization of the acoustic output of flames.

In the first part, a study of the optimal forcing of an M-flame is carried out. The forcing shape is localized in the injection tube upstream the flame. An algorithm is run to optimize its shape first with respect to the norm of the full perturbation field in the flame region and second with respect to the pressure field. It is then shown that a vast part of the sound generated by flames stems from the tip dynamics as often observed in experiments. This result highlights a need for a local analysis of the pressure generation mechanisms at the flame front at both low and high flame curvatures. The second part of this chapter corresponds to an article tackling this issue. Last, a synthesis of the main results is carried out to link both approaches.

In this chapter, fields are decomposed in a baseflow and a linear perturbation part. For instance, in $q_{nl} = q_0 + q$, q_{nl} denotes the non linear field value, q_0 the baseflow value and q the linear perturbation field.

Our first step is also a noise generation maximization in the 2-norm sense based on our software CNS2D.

3.2 Optimal Forcing of the M-flame

3.2.1 Presentation of the Optimization Procedure

The optimization procedure consists in maximizing the response of the system in a specified region to a localized normalized volumetric harmonic forcing. The algorithm used was presented in section 1.1.4.

We wish to understand how the nature of disturbances convected by the injector affects the flame acoustic output. For this reason, the forcing was located in a region comprised between 0.5 and 2.5 radii upstream the injection plane. The normalization was then carried out using a physics-based norm for compressible flows following [Chu \[1965\]](#) and [Hanifi *et al.* \[1996\]](#). We have

$$\begin{aligned} \|\mathbf{q}\|_{\text{comp}}^2 = & \int \int \int_{\Omega} \rho_0 (|u_r|^2 + |u_{\theta}|^2) + \frac{p_0}{\rho_0} |\rho|^2 \\ & + \frac{\rho_0^2}{\gamma^2(\gamma - 1)Ma^4 p_0} (|T|^2 + |\Delta Q Ma^2(\gamma - 1)Y_f|^2) d\Omega, \end{aligned} \quad (3.1)$$

properly augmented to account for reactive terms. The parameter ΔQ denotes the formation enthalpy of the reaction per unit mass. This formulation of the compressible norm has the advantage to minimize the influence of acoustic propagation in the norm, thus focusing on hydrodynamic and acoustic sources. The coefficient associated with Y_f is estimated from the temperature variation induced by a perturbation of the fuel mass fraction. For a mono-dimensional flame with a one-way, one species chemical reaction and a completely burnt fuel, we have [\[Poinsot & Veynante, 2012\]](#)

$$T_{b,nl} = T_{u,nl} + \Delta Q Ma^2(\gamma - 1)Y_{f,nl} \quad (3.2)$$

where $T_{u,nl}$ denotes the unburnt gases temperature, $T_{b,nl}$ the burnt gases temperature and $Y_{f,nl}$ the fuel mass fraction. A linear variation Y_f of the fuel mass fraction would also induce a variation of temperature of

$$T_b = \Delta Q Ma^2(\gamma - 1)Y_f \quad (3.3)$$

in the burnt gases. This temperature is used as a reference for our compressible norm.

The definition of the output is more complex. No general method for the separation of acoustic waves from pseudo-sound is currently available. Two different strategies were tested. First, a full field optimization strategy was set-up. The optimized area was then simply set as the domain containing the flame, measured with the norm stemming from Eq. 3.1. This choice leads to a maximization of the flame modes, with the acoustic waves playing a secondary role. In this strategy, acoustics is a by-product of the maximized flame activity. A second technique, in which pressure levels are maximized in half a sphere of radius 6, was then tried. Both configurations are presented in figure 3.1.

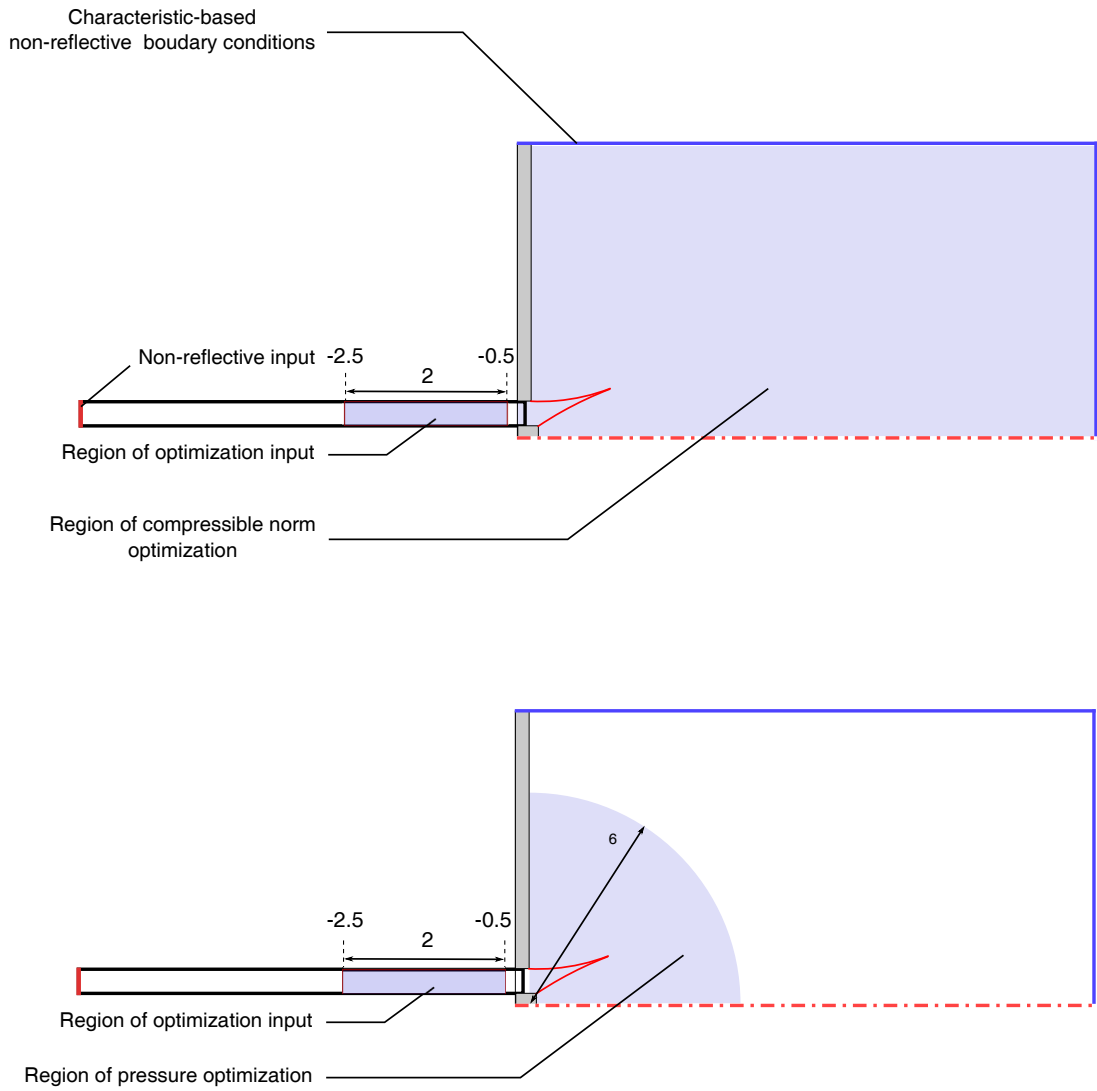


Figure 3.1: Setup of the optimal forcing computations. Top: full field optimization. Bottom: pressure optimization.

Other choices of input/output relations would have been possible. The forcing and output region can for instance be superimposed, which is especially useful in unstable configurations [Garnaud, 2012]. For instance, convectively unstable flows naturally amplify perturbations along their unstable modes, independently of the initial perturbation. The choice of overlapped input and output regions becomes relevant. However, in our case, the flow is linearly stable. Perturbations impinging on the flame are first filtered by the ambient flow. Choosing a forcing located in the injection tube allows this filtering to happen. This guarantees that the optimal modes found are somehow physically meaningful.

3.2.2 Full Field Approach

First, full field optimizations were carried out for the angular frequencies $\omega = 2, 3, 4.5, 6.75, 10.125, 15.19$ and 22.78 . In this approach, the objective function is described by Eq. 3.1 with a domain of integration corresponding to the jet expansion region, as shown figure 3.1 (top). A minimum of 7 forcing periods was imposed for each time integration phase. Eigenvectors were assumed converged when a relative error of 0.01 was reached.

The forcing shapes of u_r, u_z, ρ, p, Y_f for $\omega = 3$ are presented in figure 3.2. The forcing is typically dominated by a vortical mode, with negligible density and fuel mass fraction inputs. Most of the pressure present in the forcing is of hydrodynamic nature, i.e. is related to pseudo-noise. Forcings are spatially arranged along a repeated pattern of inclined waves. This configuration is comparable to the structure stemming from the Orr mechanism in boundary layers [Orr, 1907; Monokrousos *et al.*, 2010]. The forcing shapes repeat themselves along the axial direction, due to the quasi 1D shape of the injection tube. The delay observed between two axial positions is mostly controlled by the local hydrodynamic velocity in the injector. When the frequency increases, the wavelength of the space patterns decreases accordingly, as shown in figure 3.3 for $\omega = 10.125$. In this case, the forcing intensity gets concentrated in the middle of the annulus, away from the walls. It can be hypothesized that, at shorter wavelengths, wrinkles get more damped by viscous effects when the perturbations are convected along the flame front. The eigenvalues corresponding to these optimal forcing computations are plotted in figure 3.4. Over four order of magnitudes separate the largest and the smallest amplification factors. A global maximum is obtained for $\omega = 3$.

These computations are interesting as they exhibit a low-pass filtering behavior much in agreement with the Flame Transfer Function (FTF) computations presented in chapter 2. Using the same Strouhal number definition

$$St = \frac{f(r_1 - r_0)}{S_d} \quad (3.4)$$

the cut-off frequency at 12 dB (i.e. for a norm of the output half the maximum norm) is here at $St \simeq 6$. This frequency corresponds to the cut-off frequency of the FTF. There is however a fundamental difference between both results. The FTF is based on a volume integral of the heat release rate. Two flame elements can have contributions that cancel each other. On the contrary, in the case of an optimal forcing, the eigenvalues are based on the computation of a norm. Such cancellation effect does not occur. Two phenomena are also in competition in the FTF: an integration effect, characterized by the periodicity of the perturbations, and an hydrodynamic mode amplification effect, characterized by the

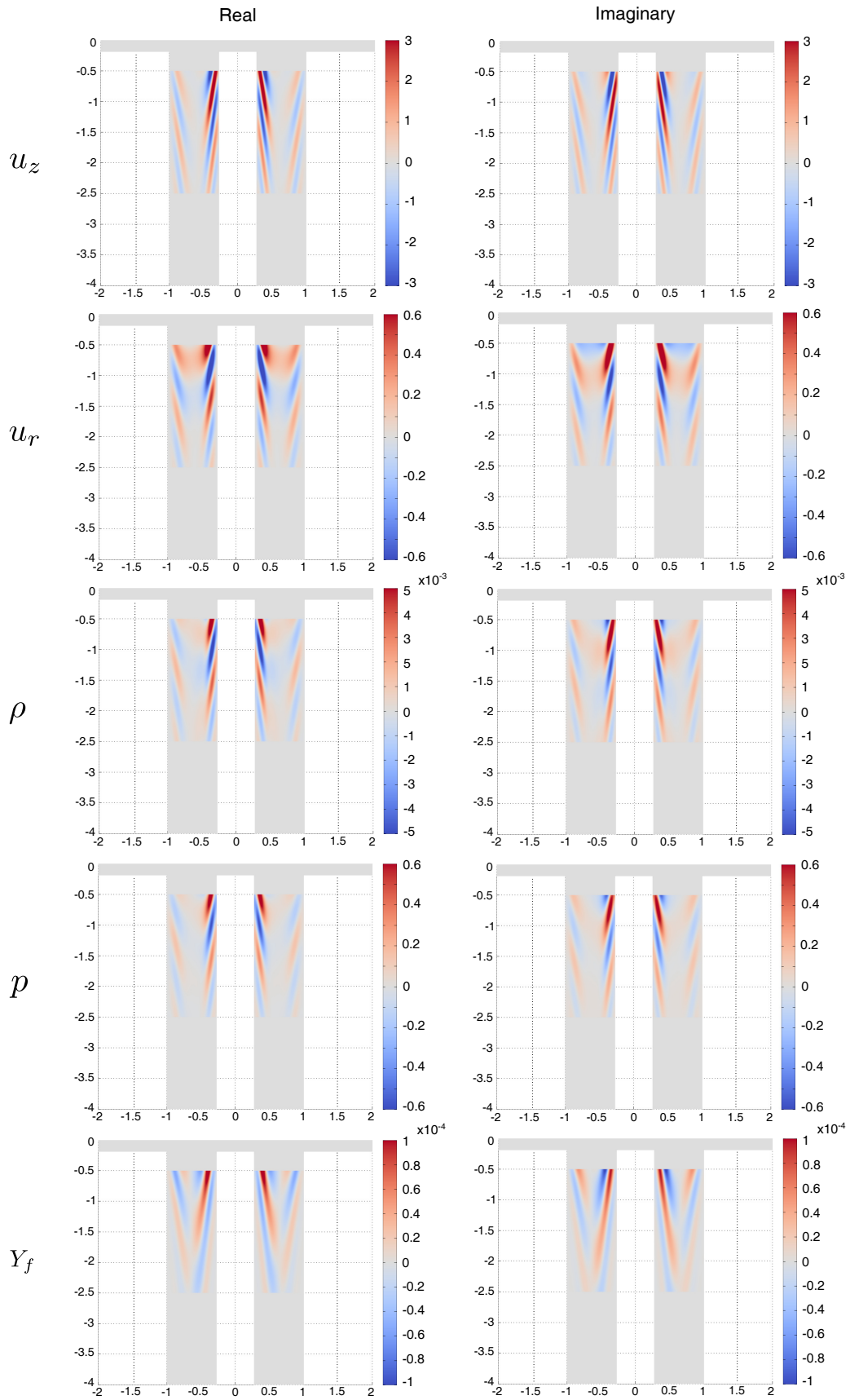


Figure 3.2: Optimal forcing shapes for a full field maximization, $\omega = 3$, presented in (r, z) coordinates.

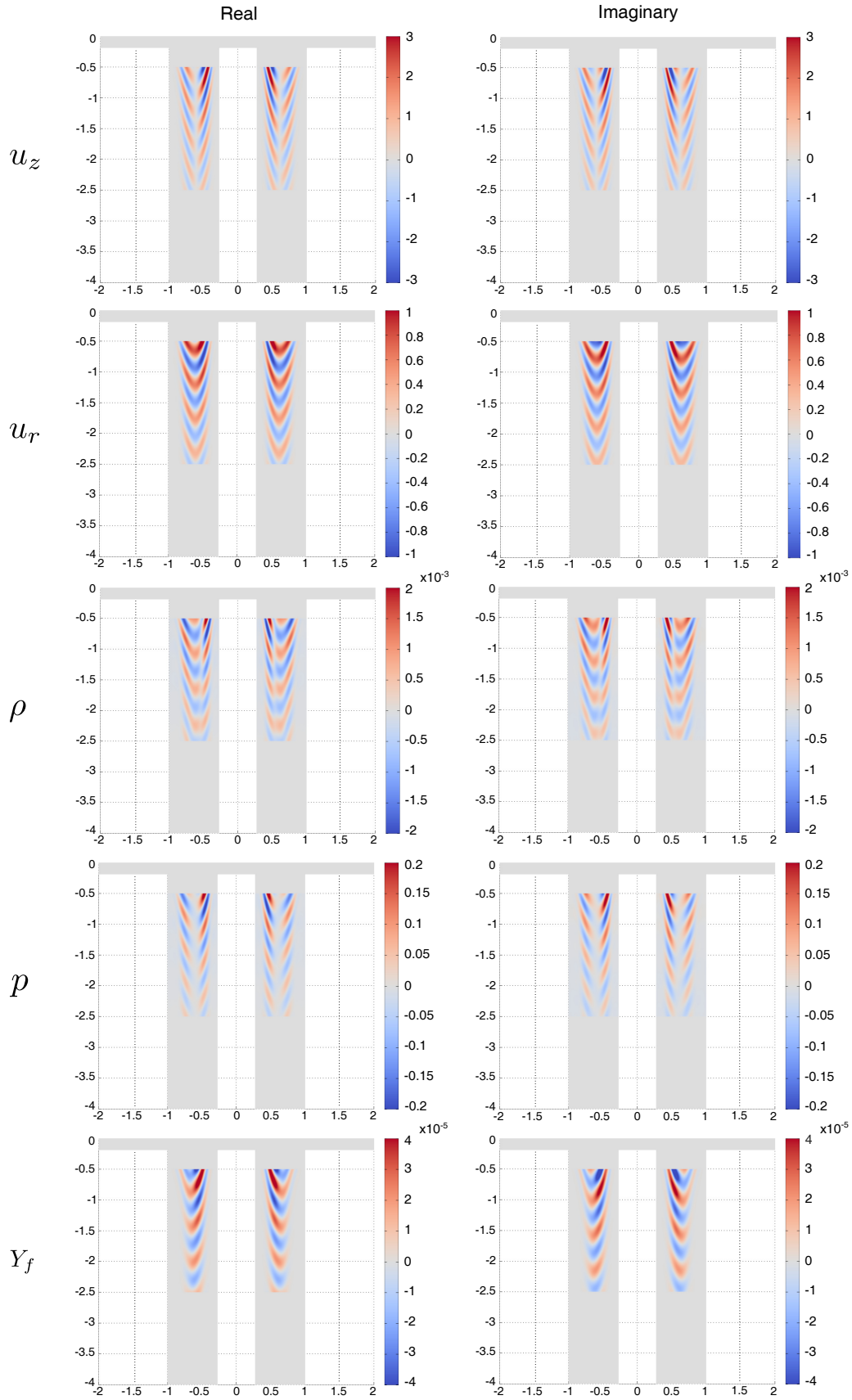


Figure 3.3: Optimal forcing shapes for a full field maximization, $\omega = 10.125$, presented in (r, z) coordinates.

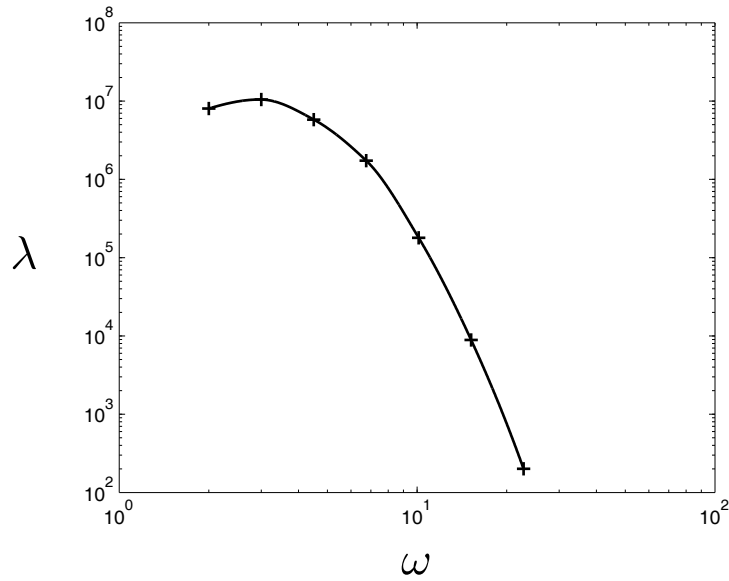


Figure 3.4: *Optimal forcing eigenvalues for a full field optimization.*

amplitude of the perturbations. These results suggest that the overshoot present on the FTF of the M-Flame presented in chapter 2 and by Schuller *et al.* [2003a] is related to an amplification of flame modes.

However, flame perturbations generated by acoustic waves and by these forcing are structured quite differently. This is shown in figure 3.5. In the case of the full field optimal forcing, the density waves on the two sides of the flame front are in phase opposition while for an acoustic forcing they are in phase. Flame tip dynamic is also radically different in both cases. Pressure radiates much more clearly from the flame tip for the optimal forcing than for the acoustic forcing. This situation is even more marked at higher frequency. For $\omega = 10.25$, the acoustic field radiates directly from the flame tip in the optimal forcing computations while it propagates from the tube exit in the case of the acoustic forcing, as can be seen in figure 3.6. Moreover, density perturbations are concentrated around the flame tip in the optimal configuration while they are quickly damped when leaving the flame base for acoustic perturbations.

3.2.3 Pressure Optimization Approach

In order to further investigate the generation of acoustic waves by the flame, two further optimizations were conducted at $\omega = 3$ and $\omega = 10.125$. We wish to investigate which type of forcing leads to a maximal pressure output using the setup presented in figure 3.1 (bottom). For this procedure, the objective function is changed to

$$\mathcal{J} = \int_{S_{ph}} |p|^2 d\Omega \quad (3.5)$$

where S_{ph} refers to the half sphere of radius 6 presented figure 3.1.

Forcing shapes at $\omega = 3$ are presented in figure 3.7. The colormaps used are identical to figure 3.2. It can be observed that the change of optimization target leads to little

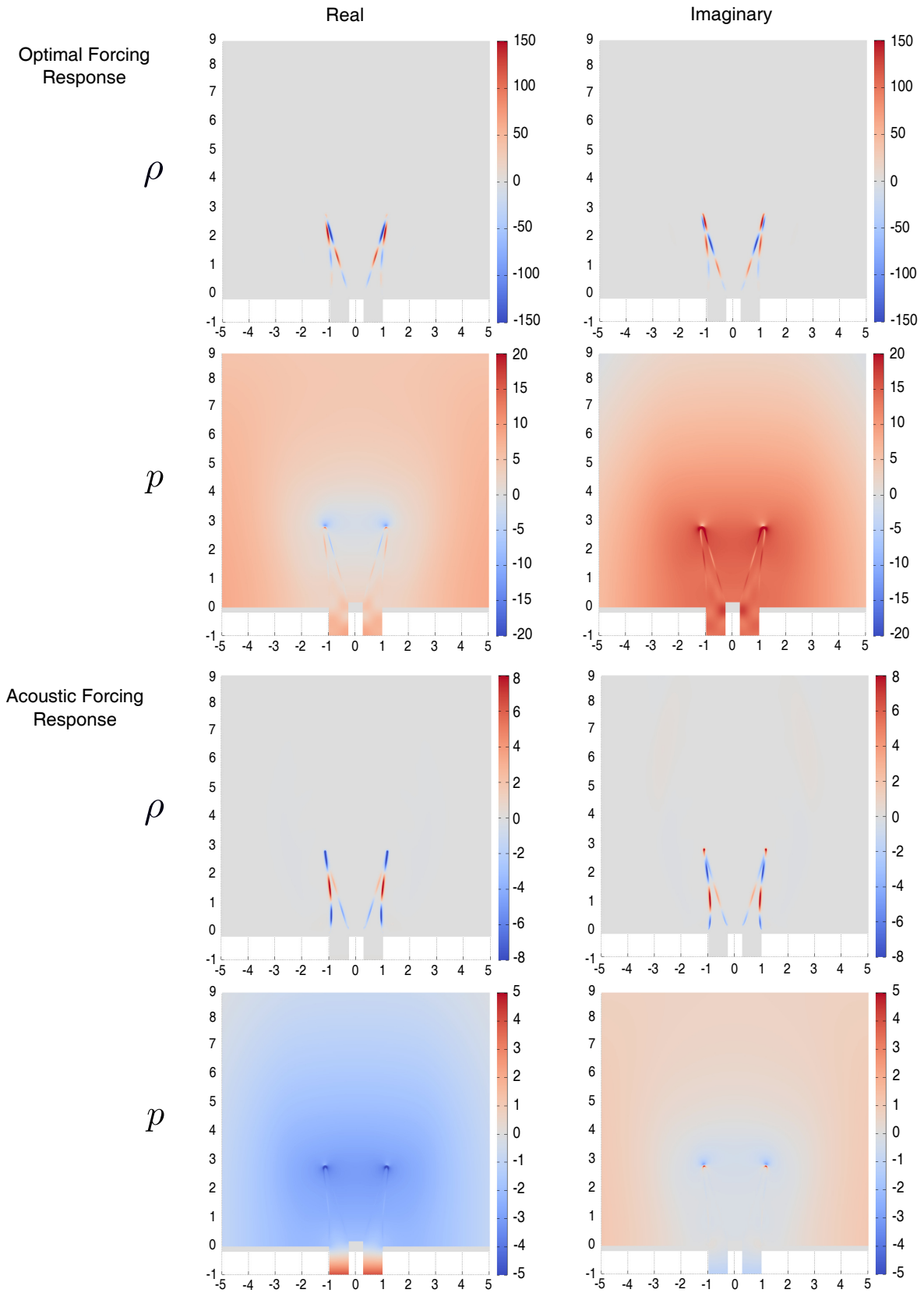


Figure 3.5: Comparison of the pressure and density outputs at $\omega = 3$ for an optimal (top) and an acoustic (bottom) forcing.

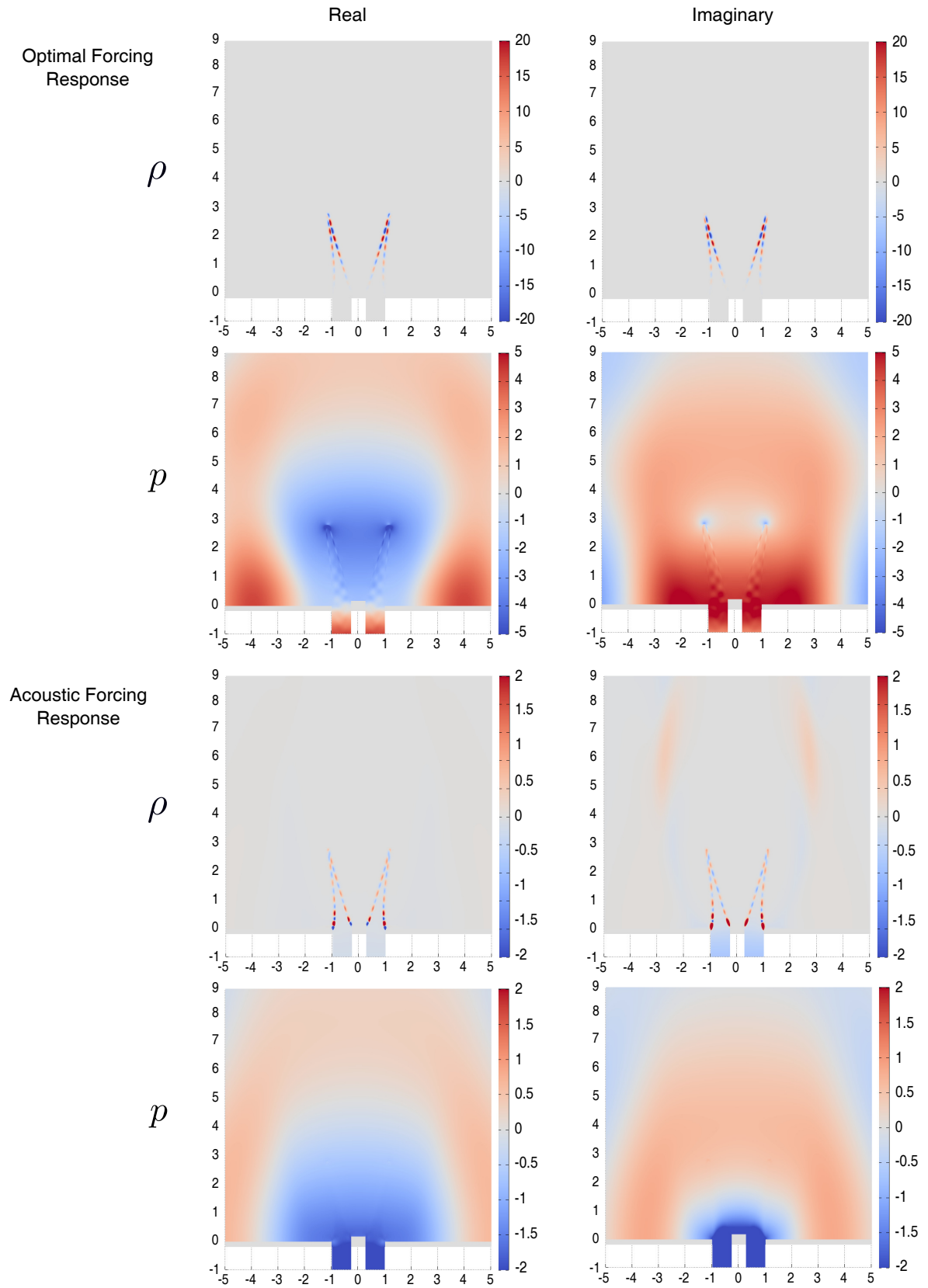


Figure 3.6: Comparison of the pressure and density outputs at $\omega = 10.125$ for an optimal (top) and an acoustic (bottom) forcing.

modifications of the forcing. Vorticity waves are still dominant, and the space structures of figures 3.2 and 3.7 are rather similar. This observation is confirmed by comparing the absolute value of the output heat release rate \dot{q} and of the corresponding pressure with both forcing, presented in figure 3.8. The heat release rate is slightly more intense on the inner side of the flame front than on the outer part. Besides, the heat release rate fluctuation is much larger at the tip when pressure is optimized. This result is consistent with the classical combustion noise theory [Strahle, 1971] that attributes most of the noise radiated by flames to the unsteady heat release rate. In Lighthill's equation, presented in Eq. 10 in the introduction, the term

$$\tilde{\mathcal{T}}_4 = \frac{\gamma - 1}{c_0^2} \frac{\partial \dot{q}}{\partial t} \quad (3.6)$$

is typically assumed responsible for the largest part of the far-field combustion noise. A larger heat release rate at the tip also leads to larger radiated acoustic amplitudes. For $\omega = 10.125$, the difference between inner and outer flame fronts is even more remarkable as can be seen in figure 3.9. Besides, the heat release rate is strongly concentrated at the flame tip. Once again, acoustic waves seem to radiate from the tip.

At first glance, these results seem in good agreement with the classical combustion noise theory. However, a closer analysis may question this approach. First, pressure fields in figures 3.8 and 3.9 exhibit a close-range directionality around the flame tip in apparent contradiction with monopolar heat release rate sources [Strahle, 1971]. Second, the correlation of the integral heat release rate with the near-field pressure seems to vary with frequencies. In order to characterize these phenomena, the following estimate is chosen

$$\tilde{\lambda} = \frac{\int_{S_{ph}} |p|^2 d\Omega}{\left| \int_{\Omega} \tilde{\mathcal{T}}_4 d\Omega \right|^2} = \frac{J(q)}{\left| \int_{\Omega} \tilde{\mathcal{T}}_4 d\Omega \right|^2} \quad (3.7)$$

This modified eigenvalue depends on the near-field pressure distribution, but should be of order 1 and almost constant for all the frequencies if p is exclusively generated by heat release rate. The values of $\tilde{\lambda}$ corresponding to all the computed optimized fields are presented in figure 3.10. Both optimization techniques lead to similar results. A strong variation of $\tilde{\lambda}$ is observed. Even though this estimate does not separate hydrodynamic noise from acoustics, this observation once more questions the dominance of heat release rate on near-field sound generation. In order to obtain a more definitive answer, a careful analysis of local pressure sources at flame fronts is required. In particular, this analysis needs to tackle the subtle issue of flame tip dynamic. A new methodology was developed to this end and is presented in the next section. It is based on the analysis of pressure sources resulting from a perturbed imploding flame.

3.3 Article: Pressure waves generation from perturbed premixed flames

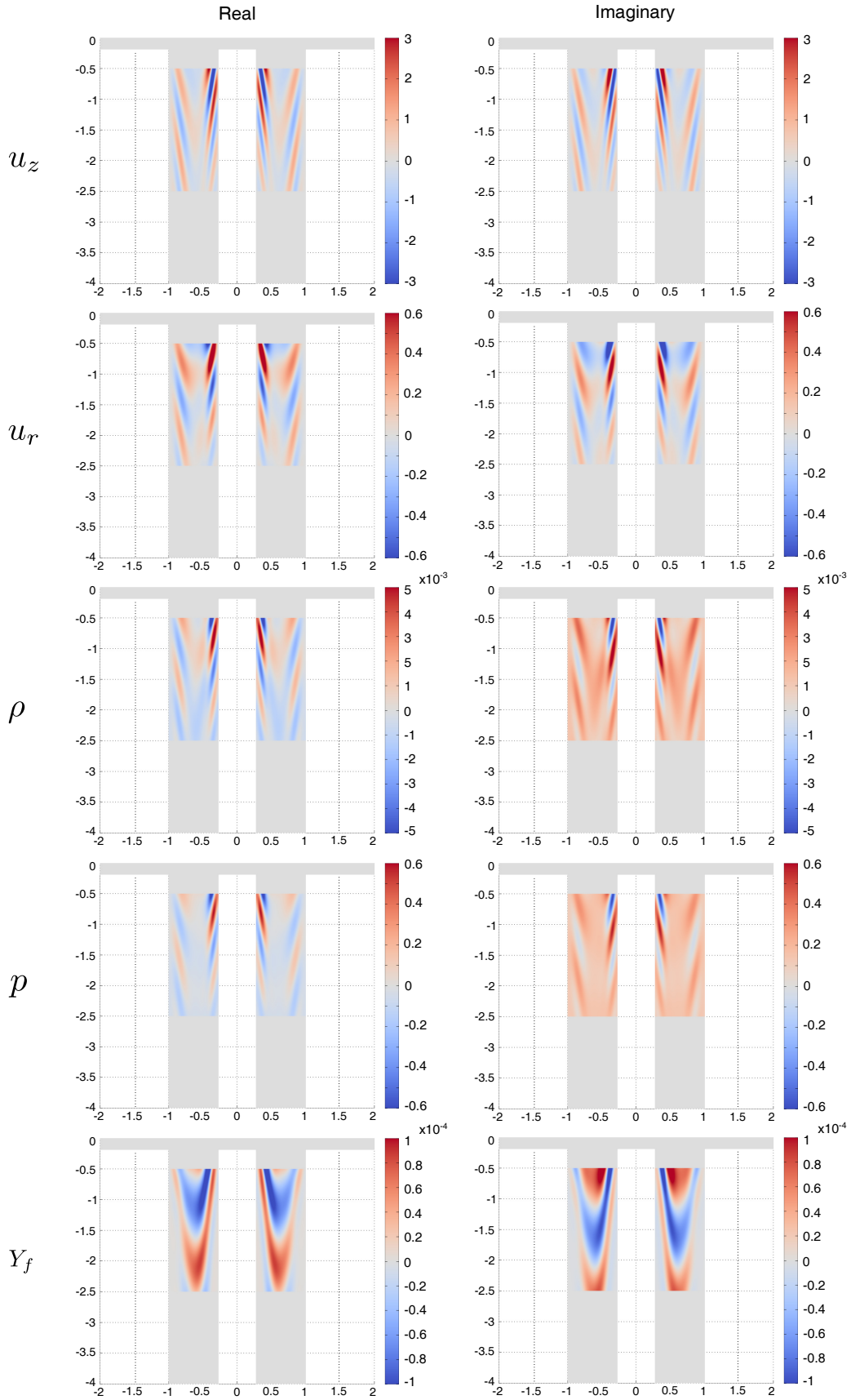


Figure 3.7: Optimal forcing shapes for the pressure maximization, $\omega = 3$, presented in (r, z) coordinates.

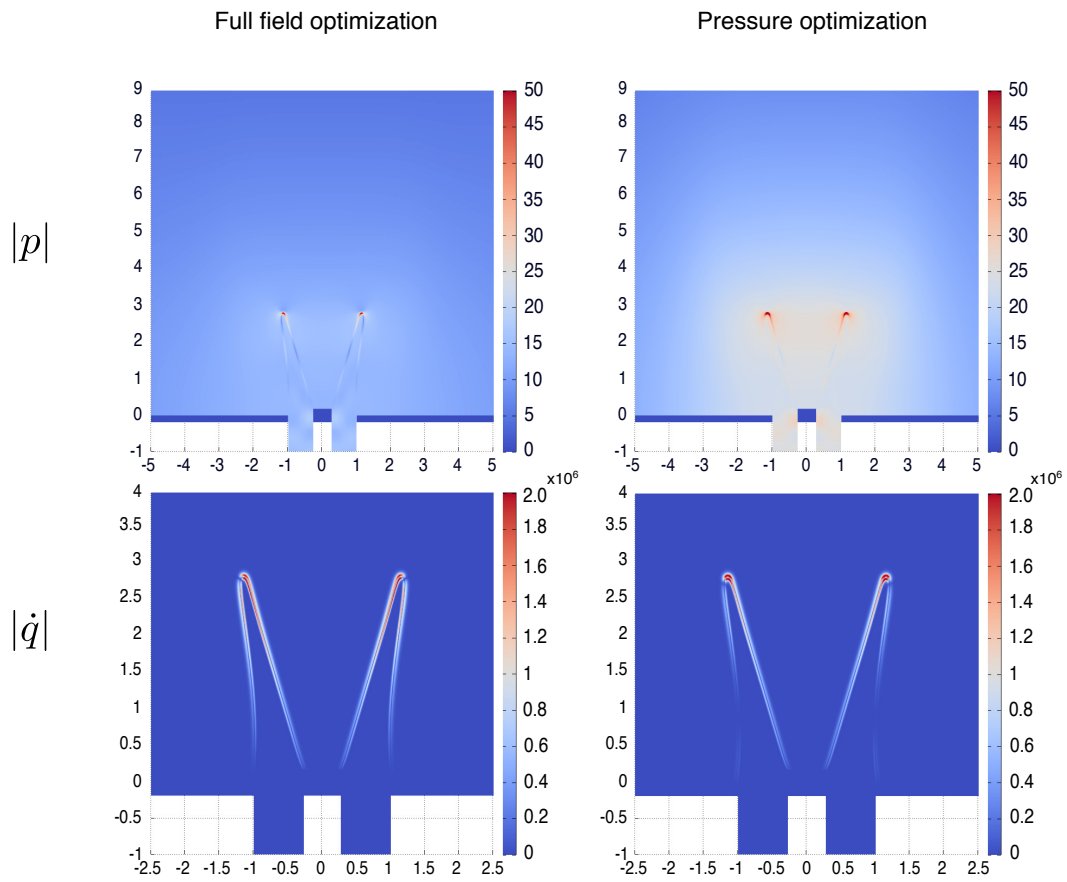


Figure 3.8: Optimal forcing pressure and heat release rate output for a pressure-optimized forcing at $\omega = 3$, presented in (r, z) coordinates.

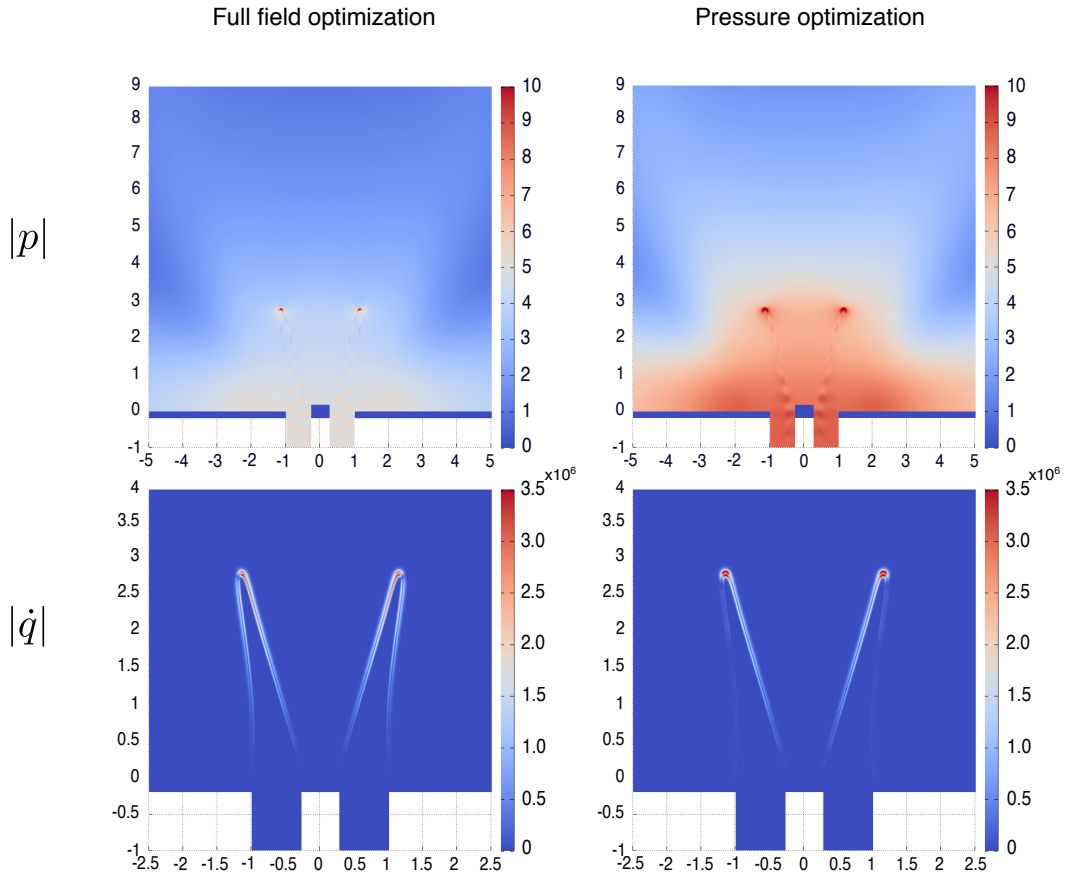


Figure 3.9: Optimal forcing pressure and heat release rate output for a pressure-optimized forcing at $\omega = 10.125$, presented in (r, z) coordinates.

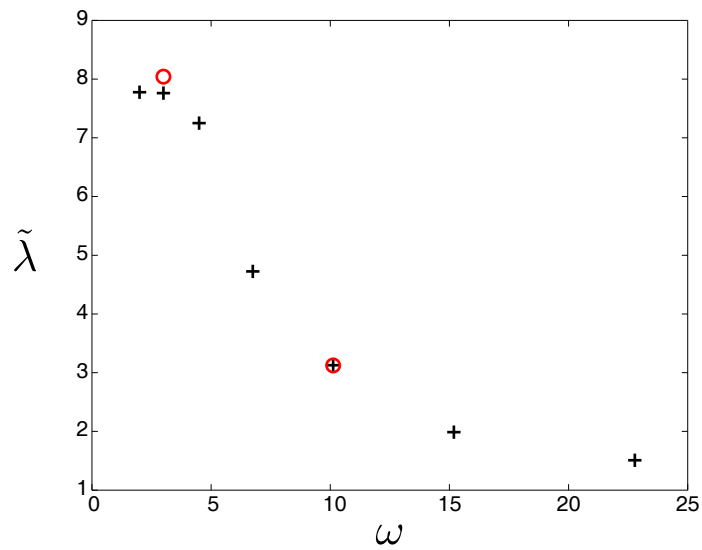


Figure 3.10: Values of $\tilde{\lambda}$ for: black cross, full field optimization; red circle, pressure optimization.

Pressure waves generation from perturbed premixed flames

By **Mathieu Blanchard**¹, **Peter J. Schmid**², **Denis Sipp**³ and **Thierry Schuller**^{4,5}

¹Laboratoire d'Hydrodynamique (LadHyX), Ecole Polytechnique, F-91128 Palaiseau, France

²Department of Mathematics, Imperial College London, London SW7 2AZ, United Kingdom

³ONERA-DAFE, 8 rue des Vertugadins, F-92190 Meudon, France

⁴CNRS, UPR 288, Laboratoire d'Energie Moléculaire et Macroscopique Combustion (EM2C), Grande Voie des Vignes, 92290 Chtenay-Malabry, France

⁵Centrale-Suplec, Grande Voie des Vignes, 92290 Chtenay-Malabry, France

(Received ?; revised ?; accepted ?.)

Numerical simulations and perturbation analysis of a radially imploding premixed flame are used to study the mechanisms responsible for the generation of acoustic waves at flame fronts. The relative importance of mechanisms based on unsteady heat release and on vorticity is investigated using an optimization methodology. Particular attention is paid to the influence of non-axisymmetric conditions and local flame curvature. It is shown that vorticity-based noise generation is prevailing for high wavenumber non-axisymmetric disturbances at all curvatures, while heat-release-driven noise generation dominates the axisymmetric and low wavenumber regimes. These results indicate that short wavelength vorticity waves actively participate in flame acoustic activity and can surpass acoustic output mechanisms based on heat-release fluctuations.

1. Introduction

Turbulent flames are noisy (Mahan & Karchmer, 1991; Dowling & Mahmoudi, 2015), which in turn may lead to thermo-acoustic instabilities in many energy conversion systems that involve combustion (Candel *et al.*, 2009). Theoretical studies of combustion noise indicate that heat release disturbances constitute the main source of noise radiated by flames (Strahle, 1971). In this case, the local sound pressure level is proportional to the rate of change of the volumetric heat release rate. The associated disturbances originate from flame-surface density fluctuations (Abugov & Obrezkov, 1978; Clavin & Siggia, 1991) and from local changes of the burning rate (Kidin *et al.*, 1984; Talei *et al.*, 2011). In stationary operating systems, it is generally found that mechanisms yielding flame-surface destruction produce far more acoustic output than mechanisms associated with flame-surface creation (Candel *et al.*, 2004). Local regions characterized by reaction layers with strong curvatures, like the flame tip, are responsible for intense noise emission. Also in these regions, mutual annihilation of flame elements lead to rapid changes in heat release. The problem of sound generation in premixed turbulent flames, and its underlying physical mechanisms, have been thoroughly studied using experiments and, more recently, direct numerical simulations (Zhao & Frankel, 2001; Shalaby *et al.*, 2009; Swaminathan *et al.*, 2011). During flame annihilation, these studies confirm that the acceleration of the burning rate at the final stage of combustion is caused by interpenetrating thermal and species-diffusion layers of neighbouring flame elements that generate strong acoustic output (see e.g. Talei *et al.* (2011)).

In a turbulent flow, mutual flame annihilation is also influenced by hydrodynamic disturbances. Flame-vortex interactions represent a canonical component when modelling turbulent combustion processes (Driscoll, 2008). When the size of these vortical structures is large compared to

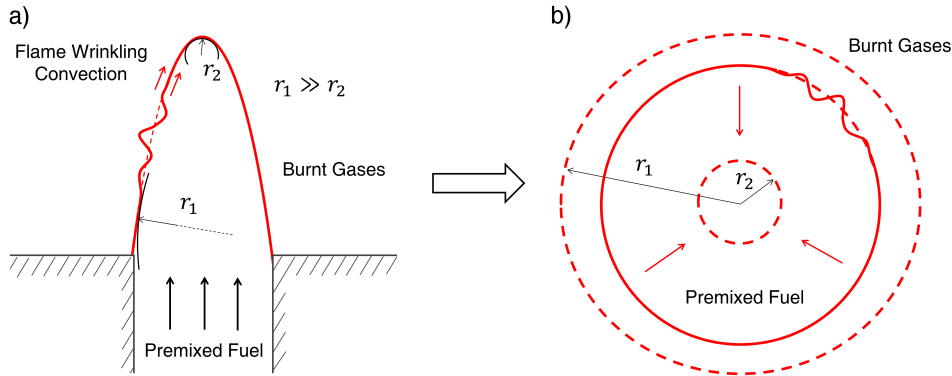


FIGURE 1. Sketch of a flame-front perturbation propagating along an axisymmetric, two-dimensional anchored flame (a) and a simplified model of an axisymmetrically imploding, cylindrical flame (b), devised to capture the same essential flow features. The local mean flame-front curvature radii, r_1 and r_2 , at different positions are indicated. The propagation of a flame wrinkle along the flame front (in (a)) translates into a study of azimuthal perturbations superimposed on the respective mean-curvature radii (in (b)).

the flame thickness, the flame rolls up around the vortex while its internal structure is not altered during the interaction (Renard *et al.*, 2000). A different picture emerges for flames interacting with hydrodynamic structures of smaller size. Vortices which width is 10 to 100 times the flame thickness generate large diffusion fluxes within the internal flame structure (Roberts & Driscoll, 1991). This interaction may subsequently be associated with strong acoustic sources. This latter mechanism has yet not been considered as a noise-generation process during mutual flame annihilation.

The objective of this study is to use numerical techniques and linear perturbation analysis on a simplified combustion model of a radially imploding flame to examine the effects of size of hydrodynamic disturbances and local flame front curvature on the generation of acoustic waves.

2. Configuration, modelling approach, numerical details

Let consider the propagation of small-amplitude perturbations along an axisymmetric, two-dimensional anchored flame; a sketch of this configuration is shown in figure 1(a). The geometric outline of the flame is such that the perturbation exhibits a progressively larger flame front mean-curvature as it approaches the flame tip. When analyzing physical effects imposed on the perturbation by the moving flame, three principal components remain: (i) strain due to the tangential flow velocity, (ii) a continuous change in the flame curvature and (iii) a change in the local flame speed. In this study, we neglect the influence of strain and, instead, concentrate on the latter two effects. Under the reasonable assumption that the perturbation moves at a slowly varying velocity along the flame front, a relative change of reference frame that keeps the perturbation fixed, but the flame moving, seems advantageous. A further simplification of the flame dynamics, that nonetheless capture the main features, is introduced by representing our configuration as a one-dimensional, axisymmetrically imploding cylindrical flame, as in figure 1(b). In this situation a flame front propagates towards the center while burning homogeneously premixed fuel (see, e.g., Talei *et al.*, 2011).

In our approach, a direct-simulation, fully compressible, reactive Navier-Stokes solver has been used, coupled to a one-step, one-way chemistry model of Arrhenius type with a local reaction rate of the form

$$\dot{\omega}_f = A\rho Y_f T^\beta \exp\left(-\frac{T_a}{T}\right) \quad (2.1)$$

where ρ is the flow density, Y_f is the fuel mass fraction, T_a is the activation temperature and T is the local fluid temperature. Coefficients A and β are kept constant. The time-independent planar flame thickness δ_f is defined in the limit of small local curvature according to

$$\delta_f = \frac{T_b - T_u}{\max|\partial T/\partial r|} \quad (2.2)$$

with T_u denoting the temperature of the fresh gases and T_b the temperature of the burnt products. In what follows, the reference length is taken as δ_f , the reference velocity as the laminar burning velocity, and the reference temperature as the temperature of the unburned gases at T_u . With this choice, we consider the parameters $A = 6.3 \cdot 10^{10}$, $\beta = 0.35$ and $T_a = 120$ which yield a reference Reynolds number of $Re = 5.56$ in fresh gases, a reference Mach number of $Ma = 0.006$ and a constant Prandtl number of $Pr = 0.72$. The heat release of the reaction is set to enforce $T_b = 6.5$. Differential diffusion is taken into account by Fick's law at a constant, unit Lewis number. Finally, the temperature dependence of the viscosity is modelled by Sutherland's law with $\mu = \mu_{\text{ref}} (T/T_u)^{0.65}$.

A chemistry model of this type has been used by Williams (1985) to analytically study planar flame fronts. Details about the numerical discretization of our governing equations can be found in Sandberg (2007) and Blanchard *et al.* (2015). Our simulations use a conservative formulation of the state variable $\mathbf{q} = (\rho, \rho u_r, \rho u_\theta, \rho E, \rho Y_f)^T$ with (u_r, u_θ) as the radial and angular velocity, respectively, and ρE as the total energy. The computational mesh is adapted to ensure a minimum of 25 grid points throughout the reaction layer and a proper convergence in the diffusive regions. Absorbing boundary conditions at a large outer radius are employed using a perfectly matched layer along with characteristic boundary conditions (Poinsot & Lele, 1992).

Our flow analysis consists of a two-step procedure. First, a nonlinear axisymmetric simulation is performed, from which snapshots are extracted at discrete time instants t_i corresponding to a set of radial positions $r_0(t_i)$ that satisfy $Y_f(r_0) = 0.5$ and $0.4 \leq r_0 \leq 160$. In a second step, we compute the maximum amount of pressure that can be generated by a linear perturbation superimposed on the extracted flow field at the specific radii. The next section presents more details about this second step.

3. Linear analysis and optimization of acoustic output

The linear operator A , describing the temporal evolution of perturbations superposed on a reference state \mathbf{q}_0 , can formally be defined as $A = \partial \mathbf{F}(\mathbf{q})/\partial \mathbf{q}|_{\mathbf{q}_0}$ where \mathbf{F} stands for the nonlinear reactive Navier-Stokes operator and \mathbf{q}_0 is taken as the state vector associated with a particular snapshot (Schmid & Henningson, 2001).

Our setup centers around the nonlinear, non-periodic dynamics of the imploding flame. Consequently, \mathbf{q}_0 changes in time, and eigenmodes, finite time optimizations or resolvents associated with A poorly describe the system's intrinsic dynamics; instead, a physically motivated technique may be more relevant. Applying the decomposition of Chu & Kovásznyai (1958), a general perturbation in a compressible flow can be divided into a vortical, an entropy and an acoustic structure. The same decomposition can be augmented by a mixture composition structure when dealing with reactive flows. In this work, we are especially interested in energy transfers from vortical, entropy and mixture composition modes to acoustics. For this reason, we will attempt to generate a maximum instantaneous sound output from an initial condition as free of acoustics as possible. This approach is based on three assumptions. First, the pressure sources located at the flame front are assumed to be directly associated with the radiated acoustics. This hypothesis is admittedly rather harsh. In actual configurations, acoustic pressure is only one component of the pressure field. It is assumed here that a maximization of the total pressure is equivalent to an optimization of the pressure output. Second, since the acoustic wavelengths generated by

combustion processes are typically much larger than the flame thickness, only the integral of the pressure sources over the compact flame front will be considered. Considering an integral of acoustic sources suppresses the need for the computation of eigenvalues associated with typical 2-norm optimal perturbations computations (Schmid & Henningson, 2001). Third, this integration shall be carried out over the radial direction only. This last hypothesis relies on the vanishing character of any volume integral for a non-zero azimuthal wavenumber m . In addition, fixing an arbitrary angle of integration would induce spurious angular-based amplifications or damping that are of little interest in this study, as we focus on local phenomena.

Within this framework, our objective is to maximize the short-time acoustic energy production at the flame front starting from an acoustic-free initial condition. To do so, we wish to maximize the pressure $p'(0^+)$ starting from a normalized initial perturbation $\mathbf{q}'(0^-)$ such that $p'(0^-) = 0$. We measure the perturbation \mathbf{q}' using a physics-based norm for compressible flows following Chu (1965) and Hanifi *et al.* (1996). We have

$$\|\mathbf{q}'\|_{\text{comp}}^2 = \int_0^\infty \rho_0 (|u_r'|^2 + |u_\theta'|^2) + \frac{p_0}{\rho_0} |\rho'|^2 + \frac{\rho_0^2}{\gamma^2(\gamma-1)Ma^4 p_0} (|T'|^2 + |\Delta Q Ma^2(\gamma-1)Y_f'|^2) r dr, \quad (3.1)$$

properly augmented to account for reactive terms. In this expression, ΔQ is the heat of the reaction per unit mass of mixture. The premultiplying coefficient for the perturbed fuel mass fraction Y_f' identifies a variation in mixture composition with its corresponding temperature variation T' in the burned gases. In order to focus our study on the flame front dynamics, the initial perturbation is localized in $[r_0 - 2, r_0 + 2]$. For a given r_0 :

$$\mathbf{q}'(r) = 0 \quad \text{if } r < r_0 - r_{\text{lim}} \quad \text{or} \quad r > r_0 + r_{\text{lim}} \quad (3.2)$$

The corresponding projector is referred to as M_{loc} in the following. A traditional strategy would then consist in maximizing $\partial\|p'\|_{\text{comp}}^2/\partial t$ by solving an eigenvalue problem (Schmid & Henningson, 2001). We propose a new methodology based on the maximization of the objective function \mathcal{J}

$$\mathcal{J}(\mathbf{q}') = \frac{1}{\sqrt{r_0}} \left| \int_0^\infty \frac{\partial p'}{\partial t} g(r, r_0) r dr \right| \quad (3.3)$$

where \mathbf{q}' is the perturbation state vector, p' is the corresponding pressure disturbance. The factor $1/\sqrt{r_0}$ scales the result to obtain a constant optimal value of $\mathcal{J}(\mathbf{q}')$ for large radii by ensuring a scaling compatibility between the 2-norm based normalization $\|\cdot\|_{\text{comp}}$ of the input and the form of the objective function. The masking function $g(r, r_0)$ ensures information extraction from the flame front and is designed to satisfy $g(r, r_0) = 1$ at the flame front, and to smoothly decrease towards zero elsewhere in the domain. The shape of $g(r)$ for $r_0 = 48.4$ is presented by the black line in figure 2. The results stemming from (3.3) and a more classical 2-norm optimization were compared for axisymmetric configurations and found to agree down to 1%. Maximization of (3.3) was also preferred as it does not require any eigenvalue computation, making it much faster. Converting our problem to a linear, discretized formulation, we have the following system of equations

$$\frac{d}{dt}\mathbf{q}' = \mathbf{A}\mathbf{q}' \quad \mathbf{p}' = \mathbf{M}_p\mathbf{q}' \quad \|\mathbf{q}'\|_{\text{comp}} = \|\mathbf{M}_{\text{norm}}\mathbf{q}'\|_2 \quad (3.4)$$

$$\mathbf{q}'_p = \mathbf{M}_{q,p}\mathbf{q}' \quad (3.5)$$

$$\int_0^\infty f g(r, r_0) r dr \approx (\mathbf{g}_{\text{int}})^H \mathbf{f} \quad (3.6)$$

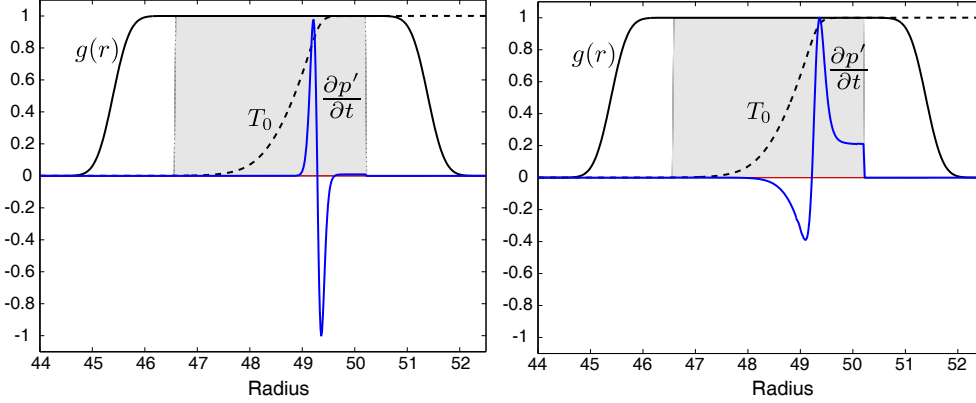


FIGURE 2. Shape of the output optimal pressure production associated with (a) axisymmetric disturbances at $r_0 = 48.4$, and (b) non-axisymmetric disturbances with $m = 40$, $\lambda = 7.5$ and $r_0 = 48.2$. Real part of the pressure (in blue), imaginary part (in red); dashed line: rescaled base flow temperature; black line: output window $g(r, r_0)$; in gray: input window implemented by M_{loc} .

involving the system matrix A , the matrix M_p computing the pressure field from the state vector and the matrix M_{norm} implementing the weights given by the norm above. Equation (3.5) extracts the pressure-related part of the perturbation \mathbf{q}' . Vector \mathbf{q}'_p also has the same dimensionality as \mathbf{q}' , and is equal in our case to $(0, 0, 0, p'/(\gamma - 1), 0)^T$. The last equation recasts the integral of a quantity f and the masking function g in discretized form as a simple scalar product, with \mathbf{f} as the discretized equivalent of f ; the complex conjugate operation is denoted by H . All the above matrices and vectors depend on the snapshot \mathbf{q}_0 and are parameterized by the azimuthal wavenumber m . Based on this notation, our optimization problem can be stated as

$$\tilde{\mathbf{q}} = \operatorname{argmax}_{\|\mathbf{q}_1\|_2=1} \mathbf{g}_{int}^H M_p A (I - M_{q,p}) M_{norm}^{-1} M_{loc} \mathbf{q}_1, \quad (3.7a)$$

$$\mathbf{q}'_{opt} = (I - M_{q,p}) M_{norm}^{-1} M_{loc} \tilde{\mathbf{q}}. \quad (3.7b)$$

The first equation, reading from right to left, seeks a normalized perturbation \mathbf{q}_1 that, when localized in space (by M_{loc}), converted to the physical space (by M_{norm}^{-1}) and its pressure component removed (by $I - M_{q,p}$), maximizes its time rate of change of pressure (by $M_p A$) within the confines of the flame front (by multiplication with the masking vector \mathbf{g}_{int}). The perturbation that maximizes this expression is denoted by $\tilde{\mathbf{q}}$. The second line retrieves the physical state corresponding to this optimal solution and removes the pressure component. The solution to the above optimization problem is straightforwardly given by

$$\tilde{\mathbf{q}} = \frac{(M_p A (I - M_{q,p}) M_{norm}^{-1} M_{loc})^H \mathbf{g}_{int}}{\|(M_p A (I - M_{q,p}) M_{norm}^{-1} M_{loc})^H \mathbf{g}_{int}\|_2}. \quad (3.8)$$

The above expression shows that no large-scale and costly matrix manipulations are required so long as a multiplication with the adjoint matrix is provided; this makes the computation of optimal perturbations very efficient and fast. The cost functional measuring the overall acoustic output is then given for the optimal (pressure-free) perturbation by

$$\mathcal{J}_{opt} \equiv \mathcal{J}(\mathbf{q}'_{opt}) = \frac{1}{\sqrt{r_0}} \|(M_p A (I - M_{q,p}) M_{norm}^{-1} M_{loc})^H \mathbf{g}_{int}\|_2 \quad (3.9)$$

The quantity determines the maximally achievable acoustic radiation from pressure-free initial perturbations; it is a valuable instrument in identifying regions of increased acoustic activity along the flame front. A second quantity will help us determine the *manner* in which this optimal

acoustic output is generated. We allow small variations δA of the system matrix A and record its first order variation of the cost functional,

$$\delta \mathcal{J}_{\text{opt}}(\delta A) = \frac{1}{r_0 \mathcal{J}_{\text{opt}}} \text{Real} \left[\tilde{\mathbf{q}}^H (M_p \delta A (I - M_{q,p}) M_{\text{norm}}^{-1} M_{\text{loc}})^H \mathbf{g}_{\text{int}} \right], \quad (3.10)$$

thus constructing a sensitivity measure for the optimal perturbation which will be used to assess the contributions of various terms in the system matrix to the optimal acoustic output.

4. Results

4.1. Axisymmetric disturbances

As a first step, we will establish a base case and assume axisymmetric perturbations, where we will find that acoustic sources are independent of vortical components and the optimal perturbation \mathbf{q}'_{opt} is dominated by a superposition of entropy and fuel mass-fraction modes. Indeed, in an axisymmetric configuration, the angular derivative $\partial \cdot / \partial \theta$ is null: azimuthal velocity and vorticity waves lose all influence on the rest of the flow field.

The measure \mathcal{J}_{opt} is shown, for this case, in figure 3 by the black continuous curve, demonstrating a strong preference of the flame tip (i.e., small radii of curvature) for the generation of acoustic waves. This behaviour is compatible with heat release rate-induced pressure waves. Chemical activity indeed intensifies with the mean curvature (Kidin *et al.*, 1984; Talei *et al.*, 2011). This finding is further corroborated by considering the sensitivity of \mathcal{J}_{opt} to small variations in the operator A_{chem} describing the chemistry of the combustion process. We define A_{chem} as the linearised operator associated with reaction rate terms in our governing equations: it is given by a combination of fuel sources due to modifications in the reaction rates and of energy sources due to variations of the corresponding heat release rate. In a further step, we assume a multiplicative (scaling) change in this operator according to $\delta A_{\text{chem}} = \epsilon A_{\text{chem}}$, with $\epsilon \ll 1$. The corresponding relative linear change in \mathcal{J}_{opt} due to this latter scaling can be defined as

$$\delta \mathcal{J} = \frac{\delta \mathcal{J}_{\text{opt}}(\delta A_{\text{chem}})}{\delta \mathcal{J}_{\text{chem}}}. \quad (4.1)$$

The quantity $\delta \mathcal{J}_{\text{chem}}$ denotes the expected variation of \mathcal{J}_{opt} if \mathcal{J}_{opt} is proportional to the chemistry operator A_{chem} . Here, $\delta \mathcal{J}_{\text{chem}} = \epsilon \mathcal{J}_{\text{opt}}$ as $\delta A_{\text{chem}} = \epsilon A_{\text{chem}}$. A value of $\delta \mathcal{J} = 1$ indicates that all changes in the chemistry terms convert into acoustic energy and thus points towards acoustic output based entirely on unsteady heat release in the flame.

The results for $\delta \mathcal{J}$ are shown in figure 3. The continuous black line presents the special case of axisymmetric disturbances which, except at the smallest radius, confirms $\delta \mathcal{J} = 1$ and thus a pure generation of acoustic radiation due to reactive processes. In other words, at the flame front, unsteady chemistry is responsible for the coupling of entropy and fuel modes with the acoustics. This finding is in agreement with experiments (Hurle *et al.*, 1968; Candel *et al.*, 2009). The observed increase in optimally generated noise at small radii r_0 can be largely accounted for by the acceleration of the flame front due to diffusive effects (Talei *et al.*, 2011).

4.2. Non-axisymmetric disturbances

We proceed by allowing a non-zero azimuthal dependence of the flame front, physically describing wrinkles in the flame front propagating towards the flame tip. This step introduces an azimuthal wavenumber m . Due to this new degree of freedom, the optimal \mathbf{q}'_{opt} depends not only on the flame radius, but also on this azimuthal wavenumber. In order to maintain a connection between the convection of a flame wrinkle and a varying flame curvature radius (see figure 1), a meaningful choice of scale is based on considering a perturbation of constant size. For a flame

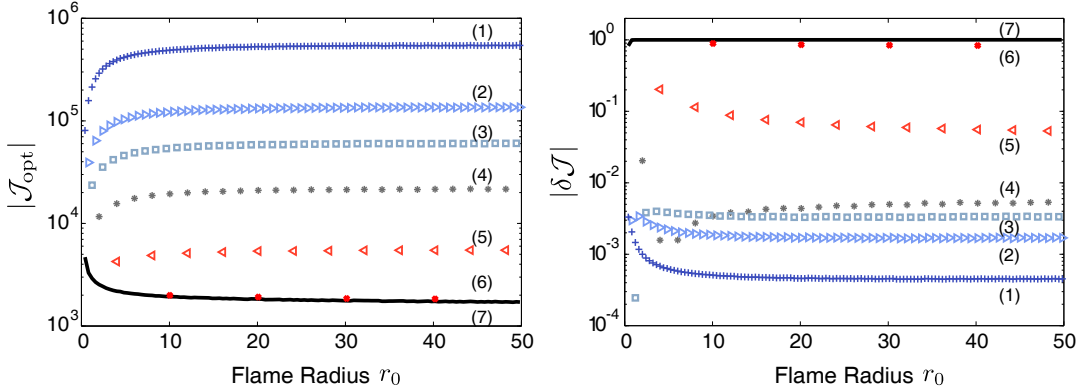


FIGURE 3. Left: Comparison of optimal acoustic generation for various characteristic wavelengths and axisymmetric perturbations. Right: Relative sensitivity $\delta\mathcal{J}$ of \mathcal{J}_{opt} with respect to changes in the chemistry operator A_{chem} . A value of $|\delta\mathcal{J}| = 1$ indicates that the acoustic output is solely generated by the unsteady heat release rate. Symbols: non-axisymmetric cases with $\lambda = 2.5$ (1), $\lambda = 5.0$ (2), $\lambda = 7.5$ (3), $\lambda = 12.6$ (4), $\lambda = 25.1$ (5), $\lambda = 62.8$ (6); black, solid line: axisymmetric reference case (7).

of radius r_0 and a wrinkle described by a wavenumber m , the characteristic wavelength of a perturbation is given by

$$\lambda = \frac{2\pi r_0}{m}. \quad (4.2)$$

This choice enforces a balance between the azimuthal derivative operator and the radius of curvature

$$\frac{1}{r} \frac{\partial f}{\partial \theta} \propto \frac{m}{r_0} f = \frac{2\pi}{\lambda} f. \quad (4.3)$$

In the limit of large λ , azimuthal derivative terms vanish and the optimal perturbations should asymptotically approach the axisymmetric solutions. Figure 3, showing \mathcal{J}_{opt} versus the flame radius, confirms this limit: for values of λ greater than 50 times the flame thickness, the optimal acoustic output coincides with the axisymmetric case (represented by the black, solid line). For values of $\lambda < 50$, non-axisymmetric effects become important. The curves separate. In the non-axisymmetric regime, optimal perturbation q' may be composed of any combination of an entropy mode, a mixture composition mode, or a vortical mode. This fact provides additional degrees of freedom for the optimization, which explains why non-axisymmetric configurations achieve higher acoustic output $|\mathcal{J}_{\text{opt}}|$ than axisymmetric ones in figure 3. Moreover, the generation of acoustic output may rely on complex mechanisms involving more than solely unsteady heat release rates. This effect is reflected in the variation of $|\delta\mathcal{J}|$, presented in figure 3: for $\lambda < 50$, the values of $|\delta\mathcal{J}|$ strongly deviate from one and converge towards zero, indicating a diminishing contribution of reactive processes (i.e., linearized chemistry) to the generation of acoustic output. This change of physics has an impact on the composition of the modes and their amplitudes at high flame curvature. We also note from inspection of figure 3 that axisymmetric disturbances achieve their maximum acoustic output at low values of r_0 (i.e., near the flame tip for a conical flame), while non-axisymmetric produce their maximum for large radii (i.e., for planar flames). Furthermore, the shape of the pressure sources are modified as well at high λ , as demonstrated in figure 2 for two representative cases. In the axisymmetric case, the pressure sources are attached to the reaction zone, whereas for large azimuthal wavenumbers the pressure sources are spread across the diffusion zone and even extend into the region of burnt gases. For all cases, output pressure sources were found to have a uniform phase along r : this is a consequence of the integral form of our objective function \mathcal{J} .

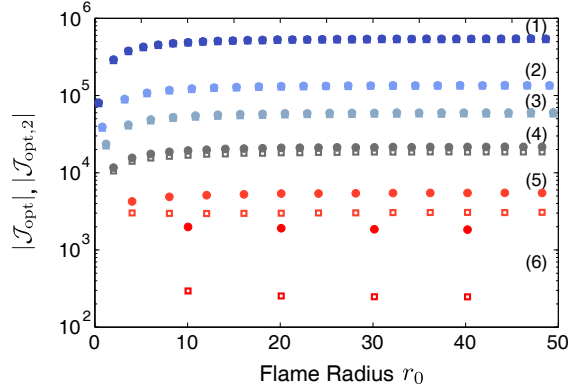


FIGURE 4. Comparison of acoustic output for modes optimizing \mathcal{J} (round symbols) and modes with maximal vorticity changes optimizing \mathcal{J}_2 (square symbols) for different values of λ : $\lambda = 2.5$ (1), $\lambda = 5.0$ (2), $\lambda = 7.5$ (3), $\lambda = 12.6$ (4), $\lambda = 25.1$ (5), $\lambda = 62.8$ (6).

Understanding this transition is of importance and warrants further analysis. To this end, we propose a vortex-sound mechanism (see, e.g. Powell, 1964) as the dominant process for the generation of pressure output at low wavelength and investigate the validity of this assumption. Hence, a new objective function is introduced according to

$$\mathcal{J}_2(q') = \frac{1}{\sqrt{r_0}} \left| \int_0^\infty \frac{\partial \zeta'}{\partial t} g(r, r_0) r dr \right| \quad (4.4)$$

where ζ' denotes the vorticity of the linear perturbation. The maximization of this cost function leads to an optimal pressure-free perturbation $\mathbf{q}'_{\text{opt},2}$. The acoustic output computed by optimizing either the previous cost functional (emphasizing pressure generation processes) $\mathcal{J}_{\text{opt}} = \mathcal{J}(\mathbf{q}'_{\text{opt}})$ or the above cost functional (emphasizing vorticity-based process) $\mathcal{J}_{\text{opt},2} = \mathcal{J}(\mathbf{q}'_{\text{opt},2})$ is compared in figure 4. In this figure, round symbols are identical to markers shown in figure 3 (left).

At low values of λ , we observe an excellent agreement between the two optimization problems, indicating a dominant contribution of vorticity to the generation of sound. This may also suggest a behavior of the modes at low values of r_0 : when the mean flame curvature is important, vortices interact strongly, resulting in a decrease in acoustic activity. At higher values of λ , at least one order of magnitude separates the values of \mathcal{J} computed by the two methods and, the pressure field generated by vorticity variations becomes negligible.

As a conclusion, for large-scale perturbations, the unsteady heat release rate constitutes the dominant source of sound, while for disturbance wavelengths of the order of the planar flame thickness, vorticity dynamics becomes the prevailing mechanism in acoustic waves generation.

5. Discussion and conclusions

In this article the influence of mean flame curvature r_0 and small-amplitude flame wrinkles (characterized by a wavelength λ) on production of acoustic output has been addressed by posing an optimization problem for a generic configuration. More specifically, the flame dynamics has been studied by considering an axisymmetric, laminar, imploding flame front, upon which azimuthal disturbances have been superimposed and their dynamics along the flame front has been investigated. The choice of optimization variable (in our case, unsteady heat release rate or vorticity) has allowed us to quantify the contribution of various noise-generation mechanisms to the overall acoustic output.

The main characteristic length of the problem is the flame thickness δ_f , and the wavelength λ studied above has been non-dimensionalized using δ_f (as have all other spatial scales). From our analysis, two distinct behaviors can be observed. For large-scale perturbations (with $\lambda > 50$), the unsteady heat-release rate is the dominant contributor to acoustics. As a consequence, the maximum of our objective functional \mathcal{J}_{opt} was observed to increase with flame front curvature for $r_0 < 10$. In contrast, for small perturbations (with $\lambda < 8$), changes in vorticity become the prevalent sources of pressure fluctuations and thus acoustics. The values of \mathcal{J}_{opt} then decrease for high mean-curvature ($r_0 < 10$). This transition between two contrasting behaviors has important physical implications.

The importance of vortex in regards to generation of noise is well-known for non-reactive flows (Powell, 1964). In combustion systems, the contribution of vorticity to acoustics is far less established. Indeed, experimentally, a flame submitted to the influence of a large-scale vortex ($\lambda \gg 1$) will roll up (Renard *et al.*, 2000). However, at smaller scales, Poinso *et al.* (1991) and Roberts & Driscoll (1991) showed that, keeping a constant vortex strength, vortices were unable to disrupt the flame front. The corresponding transition was observed for $3 < \lambda < 100$. This transitional range of λ found in our study is compatible with these simulations and experiments. Our results also suggest two distinct scenarios. At large scales, flame-vortex interaction may lead to an increased flame surface variation, and, consequently, to the generation of sound through the heat release rate. At small scales, the vortex is unable to disrupt the flame front, is partly absorbed by the flame structure and generates high local pressure levels.

If confirmed by further experiments or simulations, this physical phenomenon will strongly influence root-mean-square values of the near-field pressure. Moreover, our analysis shows that the flame diffusion thickness δ_f plays an essential role as the crucial characteristic length. The effects of complex chemistry also needs to be assessed. Energy exchanges between entropy, vorticity, mixture fraction and acoustic modes at the flame surface is a complex and sensitive issue, and non-linear effect quickly appear in flames. A proper validation of these results in non linear simulations or experiments would also push our understanding of combustion noise and flame dynamics one step further.

Acknowledgment

We would like to thank Gaetan Lerisson for providing the initial impulse behind this project.

References

- ABUGOV, D.I. & OBREZKOV, O.I. 1978 Acoustic noise in turbulent flames. *Combustion, Explosions and Shock Waves* **14**, 606–612, 00028.
- BLANCHARD, M., SCHULLER, T., SIPP, D. & SCHMID, P. J. 2015 Response analysis of a laminar premixed M-flame to flow perturbations using a linearized compressible Navier-Stokes solver. *Physics of Fluids (1994-present)* **27** (4), 043602, 00000.
- CANDEL, S., DUROX, D., DUCRUIX, S., BIRBAUD, A.-L., NOIRAY, N. & SCHULLER, T. 2009 Flame dynamics and combustion noise: progress and challenges. *International Journal of Aeroacoustics* **8** (1), 1–56.
- CANDEL, S., DUROX, D. & SCHULLER, T. 2004 Flame interactions as a source of noise and combustion instabilities. In *Proceedings of the AIAA/CEAS Aeroacoustics Conference 2004*. 10th AIAA/CEAS Aeroacoustics Conference, Manchester, United Kingdom, May 10–12., 00031.
- CHU, BOA-TEH & KOVÁSZNAY, LESLIE S. G. 1958 Non-linear interactions in a viscous heat-conducting compressible gas. *Journal of Fluid Mechanics* **3** (05), 494–514.

- CHU, PROF DR BOA-TEH 1965 On the energy transfer to small disturbances in fluid flow (Part I). *Acta Mechanica* **1** (3), 215–234.
- CLAVIN, P. & SIGGIA, E.D. 1991 Turbulent premixed flames and sound generation. *Combust. Sci. Technol.* **78**, 147–155, 00088.
- DOWLING, A.P. & MAHMOUDI, Y. 2015 Combustion noise. *Proceedings of the Combustion Institute* **35**, 65–100, 00016.
- DRISCOLL, J.F. 2008 Turbulent premixed combustion: Flamelet structure and its effect on turbulent burning velocities. *Progress in Energy and Combustion Science* **34**, 91–134, 00301.
- HANIFI, ARDESHIR, SCHMID, PETER J. & HENNINGSON, DAN S. 1996 Transient growth in compressible boundary layer flow. *Physics of Fluids (1994-present)* **8** (3), 826–837.
- HURLE, I. R., PRICE, R. B., SUGDEN, T. M. & THOMAS, A. 1968 Sound Emission from Open Turbulent Premixed Flames. *Proceedings of the Royal Society of London A: Mathematical, Physical and Engineering Sciences* **303** (1475), 409–427, 00242.
- KIDIN, N., LIBROVICH, V., ROBERTS, J. & VUILLERMOZ, M. 1984 On Sound Sources in Turbulent Combustion. *Progress in Astronautics and Aeronautics, AIAA* **95**, 343–355, 00013.
- MAHAN, J.R. & KARCHMER, A. 1991 Aeroacoustics of Flight Vehicles: Theory and Practice. Volume 1: Noise Sources. *Tech. Rep. NASA-L-16926-VOL-1*. NASA. Langley Research Center, NASA RP-1258, 00005.
- POINSOT, T.J. & LELE, S.K. 1992 Boundary conditions for direct simulations of compressible viscous flows. *Journal of Computational Physics* **101** (1), 104–129.
- POINSOT, T., VEYNANTE, D. & CANDEL, S. 1991 Quenching processes and premixed turbulent combustion diagrams. *Journal of Fluid Mechanics* 00377.
- POWELL, ALAN 1964 Theory of Vortex Sound. *The Journal of the Acoustical Society of America* **36** (1), 177–195.
- RENARD, P.H., THÉVENIN, D., ROLON, J.C. & CANDEL, S. 2000 Dynamics of flame-vortex interactions. *Prog. Energ. Combust. Sci.* **26**, 225–282, 00215.
- ROBERTS, W.L. & DRISCOLL, J.F. 1991 A laminar vortex interacting with a premixed flame: measured formation of pockets of reactants. *Comb. Flame* **87**, 245–256, 00115.
- SANDBERG, RICHARD D. 2007 Governing equations for a new compressible Navier-Stokes solver in general cylindrical coordinates. Monograph AFM-07/07. School of Engineering Sciences, University of Southampton.
- SCHMID, PETER J. & HENNINGSON, DAN S. 2001 *Stability and Transition in Shear Flows*. Springer Science & Business Media, 01533.
- SHALABY, H., LAVERDANT, A. & THÉVENIN, D. 2009 Direct numerical simulation of a realistic acoustic wave interacting with a premixed flame. *Proceedings of the combustion institute* **32**, 1473–1480, 00005.
- STRAHLE, WARREN C. 1971 On combustion generated noise. *Journal of Fluid Mechanics* **49** (02), 399–414.
- SWAMINATHAN, N., XU, G., DOWLING, A. P. & BALACHANDRAN, R. 2011 Heat release rate correlation and combustion noise in premixed flames. *Journal of Fluid Mechanics* **681**, 80–115.
- TALEI, MOHSEN, BREAR, MICHAEL J. & HAWKES, EVATT R. 2011 Sound generation by laminar premixed flame annihilation. *Journal of Fluid Mechanics* **679**, 194–218.
- WILLIAMS, GARETH 1985 *Combustion Theory*. Addison-Wesley.
- ZHAO, W. & FRANKEL, S.H. 2001 Numerical simulations of sound radiated from an axisymmetric premixed reacting jet. *Physics of Fluids* **13**, 2671–2681, 00016.

3.4 From near-field to far-field combustion noise

The previous section showed how, locally, vorticity-induced sources can lead to pressure sources orders of magnitude more intense than unsteady heat-release rate acoustic sources. However, this leads to a paradox: numerous studies have proven that far-field combustion noise is dominated by heat release rate sources [Hurle *et al.*, 1968; Kidin & Librovich, 1983; Kidin *et al.*, 1984; Candel *et al.*, 2004]. In our optimal forcing computations, it has been shown that heat release rate does not provide a full picture of near-field acoustic generation. This section will investigate this issue in more details.

We first need to analyze the origin of the far-field acoustic waves generated by the M-flame investigated in this study. However, the size of our numerical domain does not allow proper far-field conditions. This analysis needs thus to be carried out indirectly.

At low frequency, the output pressure field is dominated by flame-induced noise, both when the flame is forced acoustically or with an optimal forcing, as can be seen for $\omega = 3$ in figure 3.5. We also define the rescaled pressure as

$$p_1 = \frac{p}{\int_{\Omega} \tilde{\mathcal{T}}_4 d\Omega} \quad (3.8)$$

If in the far flame-induced acoustic field, pressure originates from heat release rate sources, far-field values of p_1 should be independent from the detailed shape of the forcing. Besides, if the repartition of the sources across the flame are comparable, this identity should hold at much closer range. We also define the ratio

$$p_2 = \frac{p_{1,opt}}{p_{1,ac}} \quad (3.9)$$

where $p_{1,ac}$ denotes the p_1 acoustic field stemming from an acoustic forcing and $p_{1,opt}$ the values associated with an optimal forcing. If the pressure stems from the integral heat release rate, p_2 should be close to 1 for a mid-field range. Values of p_2 are plotted in figure 3.11. It is observed that $|p_2|$ is comprised between 0.94 and 1.05 for $x^2 + r^2 > 5^2$. This also suggests that $\int_{\Omega} \tilde{\mathcal{T}}_4 d\Omega$ is the correct scaling for the far and mid field acoustic pressure.

In order to explain the variations of rescaled near-field pressure values observed in figure 3.10, a closer comparison between the pressure field stemming from both optimal forcing strategies at $\omega = 3$ and $\omega = 10.125$ is required. In section 3.3, we proved that two phenomena were responsible for major contributions to the near-field pressure at flame fronts. At large wavelength, heat release rate dominates; at short wavelength, vorticity destruction generates more pressure. We have just shown that most of the far-field acoustics is radiated by heat-release rate sources. Suppressing the radiated sound in the far field also cancels most of the heat release rate sources, thus isolating a part of the vorticity-induced noise. This cancellation procedure was accomplished by taking advantage of the very similar flame disturbance structures between full field and pressure optimal forcings. It consists in using the pressure p_{ref} at a reference point (r, z) to cancel far field acoustics. The corresponding non-radiating pressure field can be defined as

$$p_3 = \frac{p_{tot}}{p_{ref,tot}} - \frac{p_{press}}{p_{ref,press}} \quad (3.10)$$

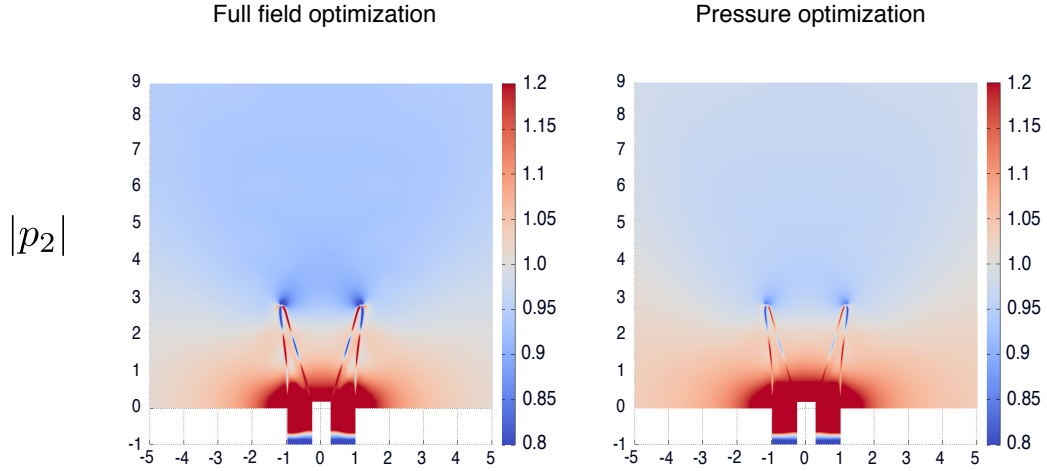


Figure 3.11: p_2 values, computed for pressure fields from full field optimization (left) and pressure optimization (right), at $\omega = 3$.

where the $_{tot}$ subscript refers to the output pressure from the full field optimization and the $_{press}$ subscript refers to the output pressure from the pressure maximization. This computation leads to the fields presented in figure 3.12 for $(r = 5, z = 9)$. The pressure p_3 can then be split in three parts for both frequencies. In the unburnt gases, disturbances propagate at hydrodynamic velocity. At the flame front, a flame mode generates some pseudo-sound. Finally, in the burnt gases, acoustic waves are radiated along a characteristic dipolar shape. Several origins are possible for this structure. It could result from a superposition of monopoles, of dipoles of same axis but different intensities, of dipoles of different axis but similar intensities or from a combination of these effects. In order to evaluate their importance in our optimal acoustic fields, it is necessary to come back to the initial pressure field. Keeping the same value of p_{ref} , the rescaled pressure and vorticity fields for both optimization procedures at $\omega = 3$ are presented in figure 3.13. A mask has been applied on pressure when $\rho Y_0 > 0.001$, which selects unburnt gases. The dipolar structures are clearly present on all pressure fields, with comparable intensities but slightly different central axis angles. A perturbation in the vorticity field is observed near the estimated center of the dipole. Its inclination varies as well by approximately the same angle as the acoustic dipole. A vorticity variation would also be compatible with the generation of a dipolar source close to the flame tip.

If it is assumed that these dipolar sources originate from the destruction of vorticity at the flame front, these observations are in good agreement with the results presented in section 3.3. Flame wrinkles, associated with long wavelength disturbances, generate monopolar acoustic sources that radiates in the far-field. When optimizing near-field pressure sources, disturbances at flame tip are enhanced while generating locally short spatial wavelengths. This leads to the creation of dipolar sources that contribute to a large part of the near-field acoustics. However, their contribution quickly decays in space as axisymmetric dipolar sources have a negligible impact afar.

It should be noted that the dipolar structure of these probably vortex-induced pressure sources was rather unexpected. The vortex sound theory [Powell, 1964] typically states that vortices induce quadrupolar sources. Coming back to Lighthill's theory, three hypothesis

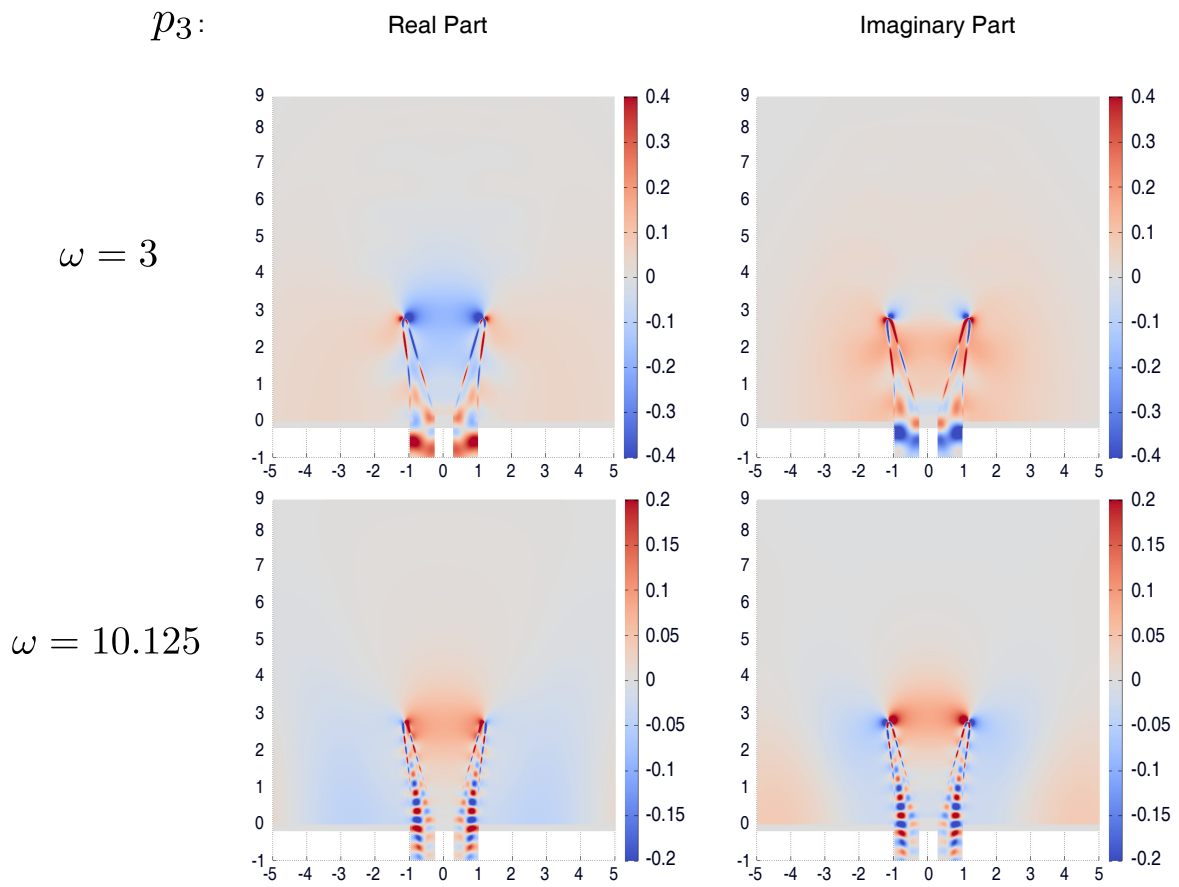


Figure 3.12: p_3 values, computed for $\omega = 3$ (top) and $\omega = 10.125$ (bottom).

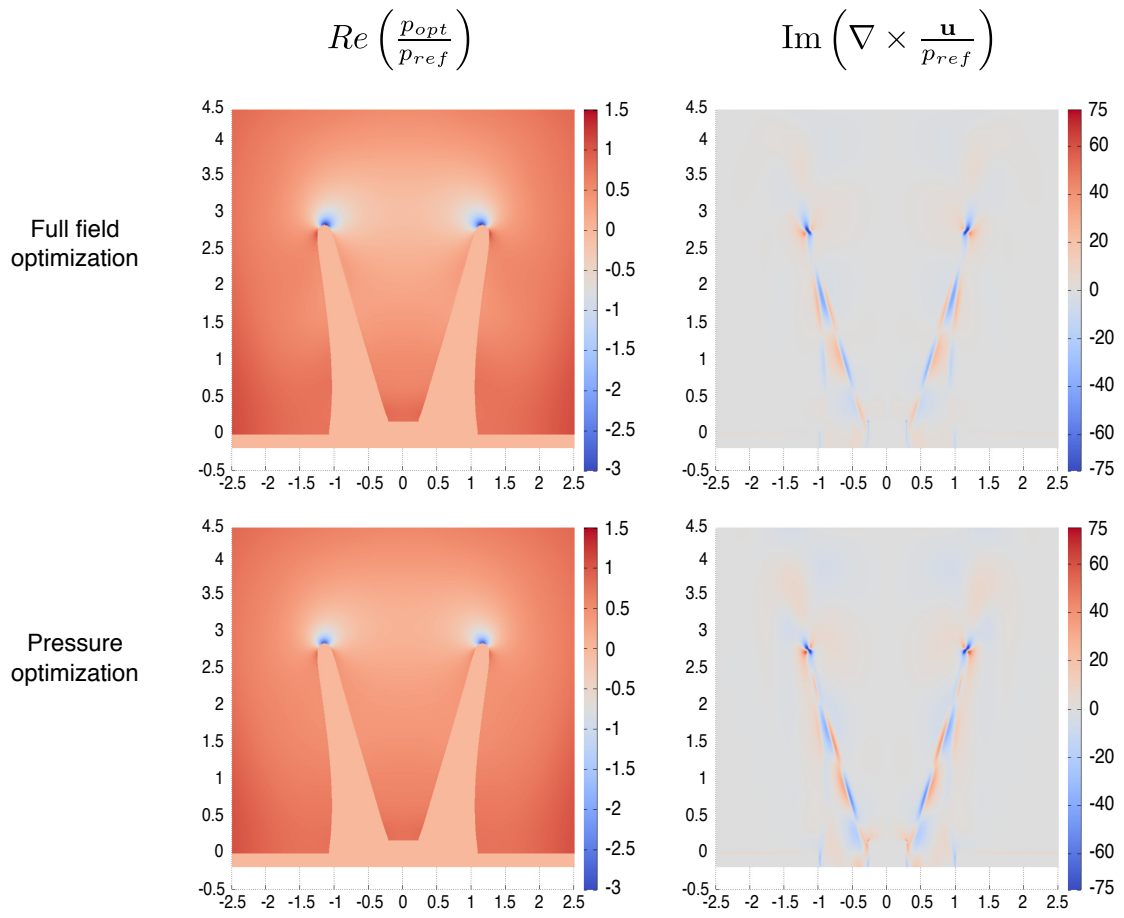


Figure 3.13: Left: masked pressure field. Right: vorticity. All field results from optimization procedures at $\omega = 3$.

may be formulated:

- The acoustic sources originate from the same mechanism as in Powell's theory. However, a dominant direction of gradients at flame front transforms an initially quadrupolar source into a dipole.
- Acoustic waves are generated by a different mechanism, activated by the destruction of vorticity at the flame front.
- The acoustic dipole observed here is unrelated to the observations from section 3.3 on vorticity destruction. This last possibility is the least probable as in all optimal forcing cases, locally intense vorticity disturbances were observed at flame tip.

3.5 Conclusion

In this chapter, the mechanisms dominating the close-field acoustic generation from laminar unsteady flames were investigated using linear optimization tools. First, the noise radiated by an M-flame was maximized using two different objective functions. All results consistently highlighted the important role of flame tip dynamics in the radiation of sound. A 1-D model was then developed to carry out a local study of flame front pressure generation. The specific and important role of vorticity waves in this process was thus highlighted. Finally, these vortical acoustic sources were shown to generate bipolar sources in the M-flame configuration considered.

These observations open the path for a non-linear extension of this theory using numerical simulations or experiments; besides, they call for more detailed theoretical and experimental analysis of the sound generated by flame fronts.

Overall, this study quantitatively proves the validity of the assumption that the heat release rate is responsible for the major part of the acoustics radiated at far and mid distances from the flame. This justifies the use of non-linear reduced order model based on integral heat release rate for the computation of the radiated sound field and of thermoacoustic instabilities.

Chapter 4

Heating Effects with a G-Equation

This chapter presents an implementation of a level set methods that models the flame as an infinitely thin surface with some heating corrections. This model is then validated with experimental results. Two system identification algorithms are finally tested on a conical flame setup computed with this new code.

4.1 Motivation

In chapter 2, it has been shown that flame heating has a major impact on flame dynamics. In chapter 3, the main local pressure sources have been verified as being the result of the heat release rate. Using these pieces of information, it is then possible to design a reduced order simulation capable of capturing the main characteristics of flame dynamics and of acoustics generation. In this chapter, the flame is represented as an iso-level of a G-equation. This methodology was introduced by Markstein [1964]. Since then, it has been applied in numerous works [Piana *et al.*, 1997; Schuller *et al.*, 2002a; Luzzato *et al.*, 2013]. One of the major difficulties arising when developing such a code is the implementation of heating effects. Some studies have attempted to include such corrections by modifying the local flame propagation equation in order to induce both an absolute instability and a saturation effect [D'angelo *et al.*, 2000; Pan & Fursenko, 2008]. However, these approaches have a domain of validity limited to close range interactions. In order to obtain a full, complete model, an evaluation of the influence of density gradients must be considered. This implies to evaluate the shape of the surrounding flow perturbations. Using the G-equation to generate heat sources constitutes a first solution [Piana *et al.*, 1997; Creta & Matalon, 2011]. This technique leads to smooth velocity gradients, but provides little computational advantage over a thickened flame model. Another possibility is the use of asymptotic expansion to express the relations between the various scales of the flame [Luzzato *et al.*, 2013]. However, this technique is mathematically difficult, and limited to non-pinching flames. Our method mixes both approaches, with an iso-level representing here both the reaction zone and the thermal diffusion layer.

The objective of this chapter is also to present this algorithm, implemented on GPU, along with some of the subsequent results. The equations solved are an extension of the G-equation coupled with a simplified Navier-Stokes solver. The resulting software, called G-FLOX (from the ancient Greek $\varphi\lambda\acute{o}\xi$, flame), is designed to allow for a quick but precise validation of non-linear system identification and control techniques on laminar axisymmetric premixed flames. It can be run on an individual computer equipped with an NVidia

GPU card. In the first section, the equations solved are briefly presented. In the second part, details are given on the solver and the test cases that were computed. Last, a system identification is carried out on a confined conical flame configuration.

4.2 Governing Equations

4.2.1 Flow Equations

In this simulation, an infinitely thin flame is considered. The configuration is assumed axisymmetric, with no azimuthal velocity. Besides, we place ourselves in a low Mach number approximation, with variable density. In this case, the mass balance reduces to

$$\nabla \cdot \rho \mathbf{u} = 0 . \quad (4.1)$$

The stream function ψ and the potential φ are introduced as:

$$\nabla \times \boldsymbol{\psi} + \nabla \varphi = \rho \mathbf{u} \quad (4.2)$$

This leads to the equations:

$$\boldsymbol{\zeta} = \nabla \times \rho \mathbf{u} \quad (4.3)$$

$$\Delta \boldsymbol{\psi} = -\boldsymbol{\zeta} \quad (4.4)$$

$$\Delta \varphi = \kappa \quad (4.5)$$

where κ denotes dilatation sources. In the following, $\boldsymbol{\zeta}$ will be designated as the compressible vorticity.

At this point, these equations are still rather general. A stronger assumption is then made. The flow is divided in three regions: a flame region separating burnt gases on the one hand and fresh reactants on the other hand. In burnt and fresh gases, the density is supposed to be respectively equal to ρ_b and ρ_u . Gravity is neglected. Using these hypothesis, a simplified equation for $\boldsymbol{\zeta}$ can be written:

$$\frac{\partial \boldsymbol{\zeta}}{\partial t} + \nabla \boldsymbol{\zeta} \cdot \mathbf{u} = \nu \Delta \boldsymbol{\zeta} \quad (4.6)$$

The flame is localized using a level-set method. A function G is computed, its zero-isolevel representing the flame front [Sethian, 1999]. The G-equation implemented follows:

$$\frac{\partial G}{\partial t} + \nabla (G) \cdot \mathbf{u} = S_d |\nabla G| \quad (4.7)$$

where the flame speed S_d is taken as

$$S_d = S_L (1 + \mathcal{L}C) \left(1 - \epsilon_{Sf} \tanh \left(\frac{G}{\epsilon_G} \right) \right) \tanh \left(\frac{d_{wall}}{\epsilon_{wall}} \right) \quad (4.8)$$

where S_L denotes the laminar burning velocity, \mathcal{L} the (first) Marstein length, C the curvature of the local isolevel of G [Peters, 2000]. The last two terms in parenthesis in Eq. 4.8 have no direct physical meaning and are introduced to circumvent numerical issues at the flame anchoring points. The distance d_{wall} is the distance to the nearest wall, ϵ_{wall} is a

parameter of the order of \mathcal{L} allowing the flame to stabilize in boundary layers. The parameters ϵ_{Sf} and ϵ_G are two real strictly positive constants introduced to handle the singularity of Eq. 4.7 at $G = 0$. This technique suppresses any need for a re-initialization of the G-equation while keeping a correct expression of the flame velocity away from the walls. This representation cannot fully capture the flame base dynamics of acoustically forced flames [Cuquel *et al.*, 2013a], but will be shown to capture the main flame features at low forcing frequency. The second Markstein length, associated with the tangential strain [Poinsot & Veynante, 2012] is neglected in the current implementation of the code.

4.2.2 Boundary Conditions

In this chapter, a conical flame configuration is considered. Its general layout is presented in figure 4.1. The associated boundary conditions are presented in figure 4.2. All the non-penetrating boundary conditions are implemented with conditions on ψ and ϕ . The non-slip part of wall boundary conditions is handled by injecting some vorticity in the interior of the domain.

Non-Penetrating Boundary Conditions

There are two type of walls in our configuration: walls corresponding to a domain's limit on one hand, and on the other hand walls immersed within the numerical domain.

On the sides of the numerical domain, boundary conditions are imposed using ghost nodes. For this reason, on the exterior walls, the non-penetrating condition is imposed with Neumann boundary conditions on the streamfunction, the Dirichlet boundary condition on the potential flow being set to 0:

$$\nabla \times \boldsymbol{\psi} \cdot \mathbf{t} = 0 \quad (4.9)$$

$$\nabla \varphi \cdot \mathbf{t} = 0 \quad (4.10)$$

where \mathbf{t} denotes the unit vector tangent to the wall.

Non-penetrating boundary conditions at the walls inside the domain are handled using immersed boundary conditions. At each time step, two linear systems are solved:

$$A_{BC,1} \tilde{\zeta} = -\tilde{u}_n \quad (4.11)$$

$$A_{BC,2} \tilde{\kappa} = 0 \quad (4.12)$$

where $\tilde{\zeta}$ denotes the sources for the Poisson equation for ψ to add at blue nodes in figure 4.3, $\tilde{\kappa}$ denotes the sources for the Poisson equation for φ to add at blue nodes, and \tilde{u}_n is the penetrating velocity we wish to compensate at the same wall nodes.

In those two cases, non-penetrating boundary conditions are imposed by setting some constraints on φ and ψ .

Non-Slip Boundary Conditions

The non-slip part of the boundary conditions is much more complex to handle. Numerous strategies were developed to implement it in a vorticity-streamfunction formulation

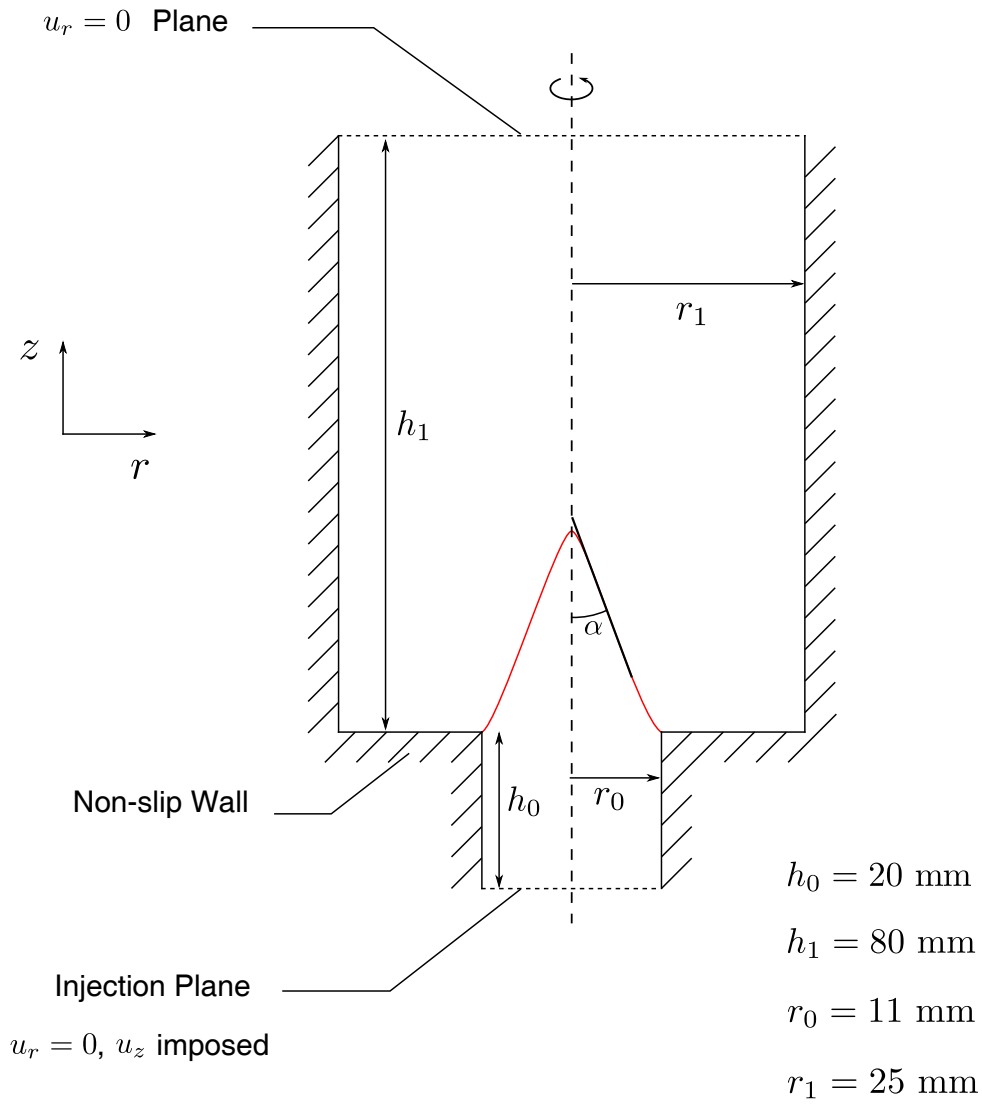


Figure 4.1: Set-up used for a weakly confined axisymmetric flame. α is defined as the half cone angle of the flame.

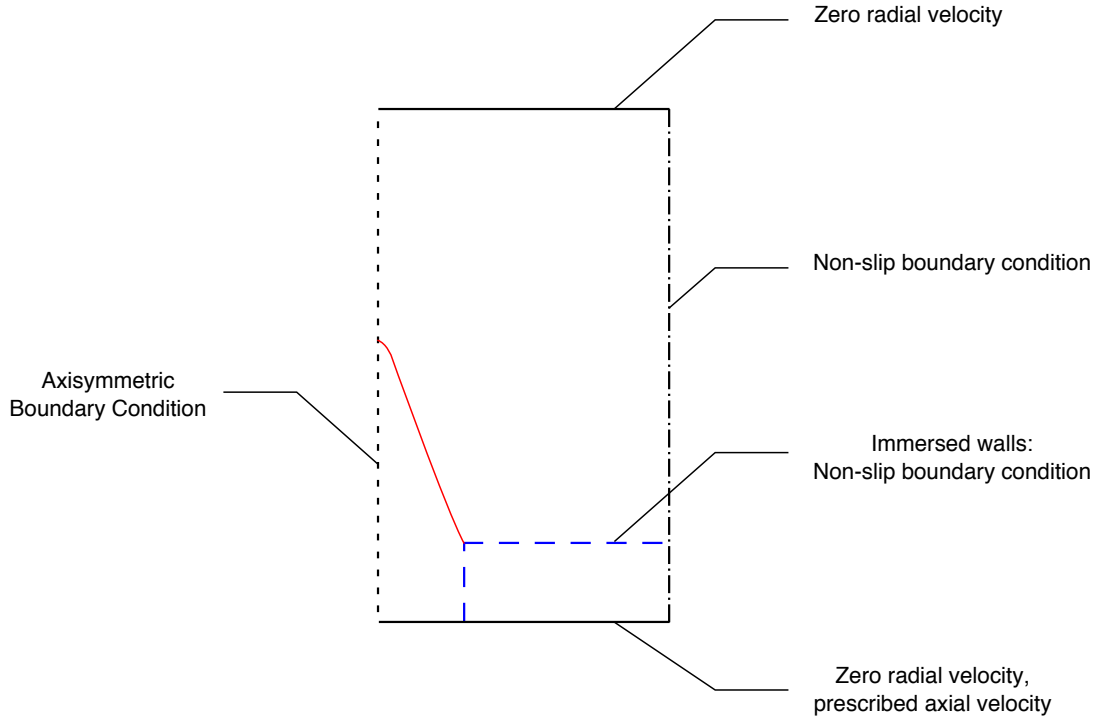


Figure 4.2: Boundary conditions implemented, along with the indicative position of the flame (in red). Boundary conditions on the sides of the domain (black lines) are implemented with ghost nodes. Inner walls non-slip boundary conditions are implemented with immersed boundary conditions.

[Koumoutsakos *et al.*, 1994; Davies & Carpenter, 2001]. The technique used in this code is adapted from Ploumhans & Winckelmans [2000]. It consists in injecting some vorticity inside the domain. To do so, some compressible vorticity is added to the points immediately close to the wall, shown as red circles in figure 4.3. The blue nodes are updated such that

$$\nabla \zeta \cdot \mathbf{n} = 0 \quad (4.13)$$

where \mathbf{n} denotes the unit vector normal to the wall. In order to impose both conditions simultaneously, a linear system is solved at each time steps with the slip velocity \tilde{u}_{slip} computed on blue nodes as a source term:

$$A_{BC,3} \tilde{\zeta} = \begin{bmatrix} -\tilde{u}_{slip} \\ 0 \end{bmatrix} \quad (4.14)$$

Where $\tilde{\zeta}$ denotes the vorticity values at the blue and red nodes.

In our formulation, the non-slip part of wall boundary conditions is also handled by adding some vorticity in the domain. This vorticity appears as a source term in the ψ Poisson equation.

Besides, the matrices $A_{BC,1}$, $A_{BC,2}$ and $A_{BC,3}$ are evaluated and inverted as a pre-processing step. This computation is carried out only once per geometry, making it rather inexpensive.

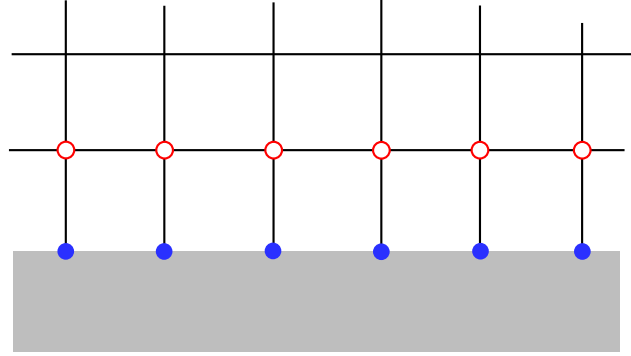


Figure 4.3: Local mesh in the vicinity of a wall. Grey: wall. Blue dots: wall nodes. Red circles: interior wall points.

Inlet, Outlet and Axis of Symmetry

At the inlet of the numerical domain, the axial velocity is imposed with Dirichlet boundary conditions on the streamfunction, the Neumann boundary condition on the potential flow being set to 0

$$\nabla \times \boldsymbol{\psi} \cdot \mathbf{n} = u_{x,in} \quad (4.15)$$

$$\nabla \varphi \cdot \mathbf{n} = 0 \quad (4.16)$$

where \mathbf{n} denotes the normal to the inlet. At the outlet, the tangential velocity is set to 0 with Neumann boundary conditions on $\boldsymbol{\psi}$ and Dirichlet boundary conditions on φ

$$\nabla \times \boldsymbol{\psi} \cdot \mathbf{t} = 0 \quad (4.17)$$

$$\nabla \varphi \cdot \mathbf{t} = 0 \quad (4.18)$$

where \mathbf{t} denotes the tangent to the outlet.

Finally, symmetrical boundary conditions are imposed on φ and G , antisymmetrical boundary conditions are set for $\boldsymbol{\psi}$ and ζ on the axis of symmetry.

G-Equation

The boundary condition for G at walls is a mere Neumann boundary condition

$$\nabla G \cdot \mathbf{n} = 0 \quad (4.19)$$

Besides, the flame velocity was reduced in the vicinity of the walls according to Eq. 4.8 to prevent the G-equation from diverging.

4.2.3 Flame Region

When assuming an infinitely thin flame, it is possible to evaluate the corresponding jump conditions for the flow variables across the flame [Chu, 1953; Matalon & Matkowsky, 1982; Matalon *et al.*, 2003]. In particular, the conditions on velocity can be expressed as

$$[[\mathbf{u}]] \cdot \mathbf{n}_f = (E - 1)S_d \quad (4.20)$$

$$[[\mathbf{u}]] \cdot \mathbf{t}_f = 0 \quad (4.21)$$

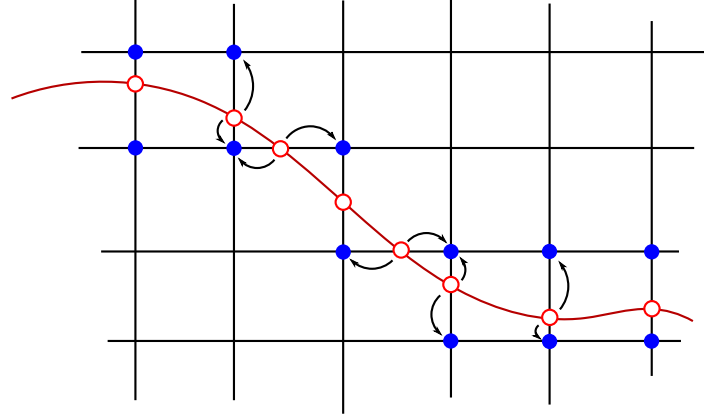


Figure 4.4: Interpolation of sources from the flame front to the mesh. Black lines: initial mesh. Red line: Flame Front. Blue dots: mesh compressible vorticity or dilatation sources. Red circles: flame front compressible vorticity or dilatation sources. Arrows: linear interpolation from flame front to mesh sources.

where \mathbf{t}_f and \mathbf{n}_f respectively denote the tangent and the normal to the flame, while E is the volumetric expansion ratio, i.e. the ratio of unburnt to burnt densities ($E \geq 1$). This can be equivalently written as:

$$\llbracket \rho \mathbf{u} \rrbracket \cdot \mathbf{n}_f = \frac{E-1}{E} \rho_u (S_d - \mathbf{u}_u \cdot \mathbf{n}_f) \quad (4.22)$$

$$\llbracket \rho \mathbf{u} \rrbracket \cdot \mathbf{t}_f = -\frac{E-1}{E} \rho_u \mathbf{u}_u \cdot \mathbf{t}_f = -\tilde{\zeta}_f \quad (4.23)$$

where the subscript $_u$ refers to unburnt gases. Equation 4.22 can then be translated into dilatation sources κ_f for the φ -Poisson equation, while Eq. 4.23 is equivalent to the presence of a vorticity layer of intensity $\tilde{\zeta}_f$. These terms were implemented by transforming those Dirac-like sources into volumetric sources. For instance, if a tangential jump of 1 on $\rho \mathbf{u}$ is intended, a compressible vorticity of intensity $ds/dr/dx$ would be added at the flame front, where ds is the length of the local flame front element, dr and dx are the local mesh spacings in both directions. This technique leads to a collection of sources located on the flame front that are transferred back to the initial mesh using bilinear interpolation as presented in figure 4.4. On this figure, the red circles represent the points where vorticity and dilatation sources are computed from Eqs. 4.22 and 4.23. The blue dots are the points of the mesh where the sources are projected to. This interpolation phase enforces an identical volume integral between flame front sources (red) and mesh sources (blue). This interpolation technique is adapted from previous vortex-in-cell methods [Couët *et al.*, 1981; Cottet, 1987; Cocle *et al.*, 2008].

This procedure results in a dilatation field κ and a compressible vorticity field ζ_f . The flame-induced sources ζ_f are added to ζ for the streamfunction evaluation, but they are neither diffused nor convected.

Last, the jump conditions on vorticity are largely simplified. Hayes [1957] developed a full theory of the vorticity jump across a gasdynamic discontinuity. Matalon *et al.* [2003] showed that the two dominant terms in these equations were the damping due to heating effects

and vorticity generation by baroclinic effects. In this study, baroclinic vorticity production will be neglected. As a consequence, the jump conditions on compressible vorticity is

$$\llbracket \zeta \rrbracket = -\frac{E^2 - 1}{E^2} \mathbf{n}_f \times (\zeta \times \mathbf{n}_f) \quad (4.24)$$

According to this last equation, for a reasonable value of $E = 6$, about 97% of the compressible vorticity is absorbed by the flame. This observation is in agreement with our DNS computations, where most of the incoming vorticity -and compressible vorticity- disappears at the flame front. This last jump condition was implemented through a sponge layer placed in the flame thickness.

Overall, this set of techniques intrinsically leads to a flame with a thermal thickness between 2 and 4 points wide. Finite flame thickness effects only appear through the Markstein length \mathcal{L} . The main drawback of this technique is its absence of mesh convergence. If the mesh is twice more resolved, the flame is simply twice thinner. Besides, detailed flame structure effects such as diffusive instabilities are not solved. Only bulk hydrodynamic properties are retained.

Even though the previous assumptions strongly simplify the handling of chemistry, computations are still too complex to be carried out on a mono-processor configuration. However, it is possible to take advantage of recent advances in hardware to fit all computations on a single machine equipped with a high performance Graphic Processing Unit (GPU).

4.3 Implementation on GPU

4.3.1 Algorithm Structure

After an optional preprocessing step computing $A_{BC,1}^{-1}$, $A_{BC,2}^{-1}$, $A_{BC,3}^{-1}$ the main algorithm structure is presented in figure 4.5. The functions G and ζ are used for initialization. The rest of the time step is separated in 3 modules. The ζ_f and κ_f fields are initialized to 0.

- First, the position of the flame front is interpolated. The identified coordinates are filtered using a local average in order to suppress any grid-induced oscillation of the local flame front curvature.
- Second, the velocity is computed: if $E = 1$, only ψ is estimated as φ is identically null. If $E > 1$, the computation of φ and ψ requires a convergence of the flame sources. Using $\zeta + \zeta_f$ and κ_f sources, ψ and φ are computed. The momentum $\rho \mathbf{u}$ is then estimated. The density ρ is corrected in the flame region to impose $\mathbf{u} \cdot \mathbf{t}_f$ constant through the flame thickness. The corresponding values of u_r and u_z are then estimated and used to update ζ_f and κ . This procedure is repeated until convergence.
- Last, G and ζ are convected and diffused assuming constant velocities throughout the time step.

The convection of ζ is integrated in time with a second-order Adam-Bashforth scheme [Stoer & Bulirsch, 2002]. Its diffusion is evaluated using a second-order implicit Adams-Moulton method [Stoer & Bulirsch, 2002]. Last, the convection of G is accomplished with a second order 10-step Strong Stability Preserving Runge Kutta time stepper [Gottlieb, 2005]. All space gradients are computed using second order centred finite difference. This strategy contrasts with traditional G-equations formulations that typically rely on Weighted Essentially Non-Oscillatory schemes [Adams & Shariff, 1996]. This was allowed by the

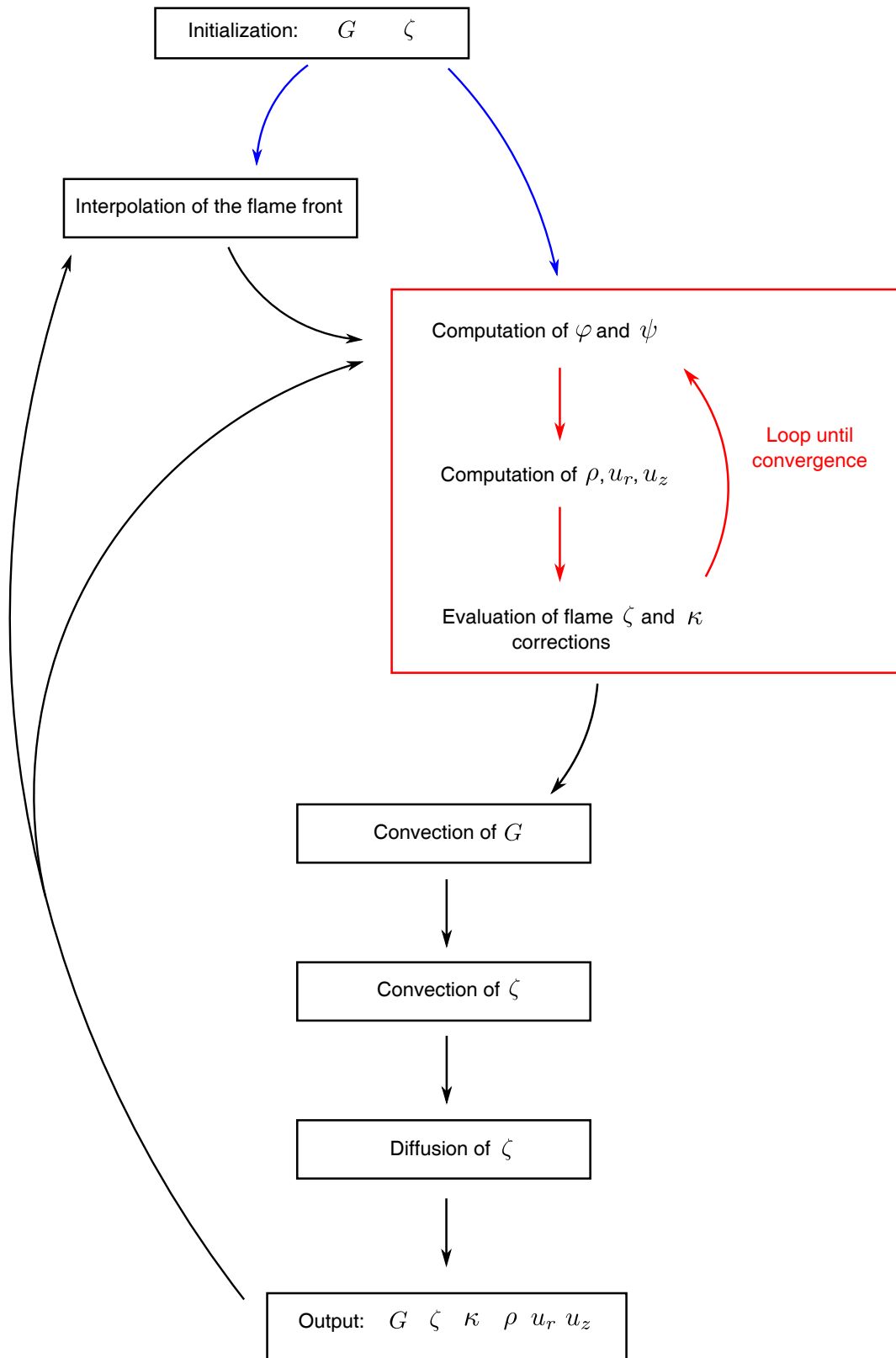


Figure 4.5: Main integration loop. Blue arrows: initialization. Red: internal convergence procedure.

modified expression of the flame velocity S_d presented in Eq. 4.8. Because of its dependence in the values of G , our current G-equation does not create a shock.

4.3.2 Poisson Solver

Over the last decades, GPU have become a fairly attractive solution for parallel computing. At equal performance and compared to MPI, the hardware and energy costs are both typically one order of magnitude cheaper. The objective of this section is not to provide a detailed description of the specificities of GPU computations, but rather to provide some insight into key elements implemented in our code.

The most fundamental difference between CPUs and GPUs is their intrinsically parallel architecture. GPUs split a given task between ‘threads’. Those threads are launched simultaneously by ‘warps’, grouping typically 32 threads. Several warps can be launched simultaneously. In these warps, computations must be as synchronized as possible, and memory accesses must be as aligned as possible. In order to keep a good synchronization, and to take advantage of it, warps are grouped in ‘blocks’, as presented in figure 4.6. It is possible to synchronize threads at a block level. This is useful as each block is assigned to its own local memory. Blocks are in turn grouped in a ‘grid’. Threads have access to five types of memories:

- Its own register, very fast.
- The local block memory, almost as fast as the register when accesses are aligned.
- The constant register, very fast as well.
- The global memory, quite slow.
- Texture memory, typically slightly faster than global memory. It was initially intended for 3D rendering, and is optimized for data accesses spatially grouped on hardware.

Finally, it is possible to transfer data from and to CPU. CPU/GPU transfers typically offer a few Gb/s fluxes while global memory/threads transfers are done at a few hundreds Gb/s. This very efficient handling of memory by GPUs and their large number of computational cores are at the heart of their performance. As a consequence, the efficiency of GPU algorithms is typically measured in terms of memory flux (in bit/s) and latency (the time during witch threads are idle, in %). Due to this rather complex memory structure, it is quite clear that GPU programming leaves a large room for optimization. This is an active field of research, and can be extremely time-consuming. For this reason, only a few procedures were actively optimized.

The most critical routine of our algorithm is the Poisson solver. It is used for the computation of φ , ψ and the diffusion of ζ . The algorithm is based on a multigrid V-cycle approach [Hackbusch, 1985; Stoer & Bulirsch, 2002] described in figure 4.7. The general idea of this algorithm is to relax the solution using an over-relaxed Gauss-Seidel iteration (Successive Over-Relaxation, SOR), and to restrict the residual of the equation on a coarser grid. This operation is recursively repeated until the coarsest grid is reached. This is the descending phase of the method. During the ascending phase, the solution is expanded on the finer grid, added to the local solution and relaxed. All these operations are straightforwardly realized on GPU as all data are accessible on the same device. The performance-sensitive task is also the SOR algorithm.

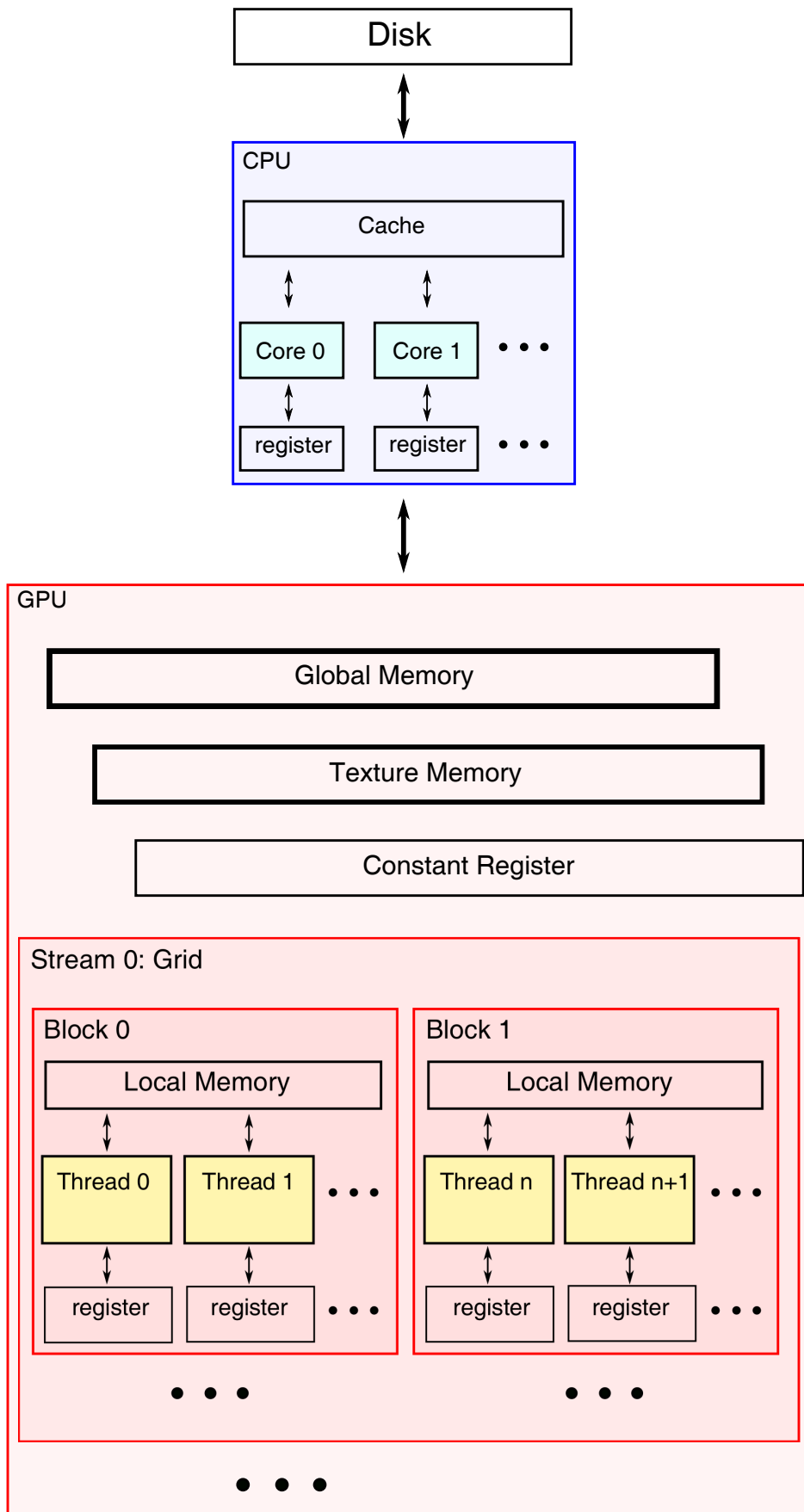


Figure 4.6: CPU/GPU memory structure.

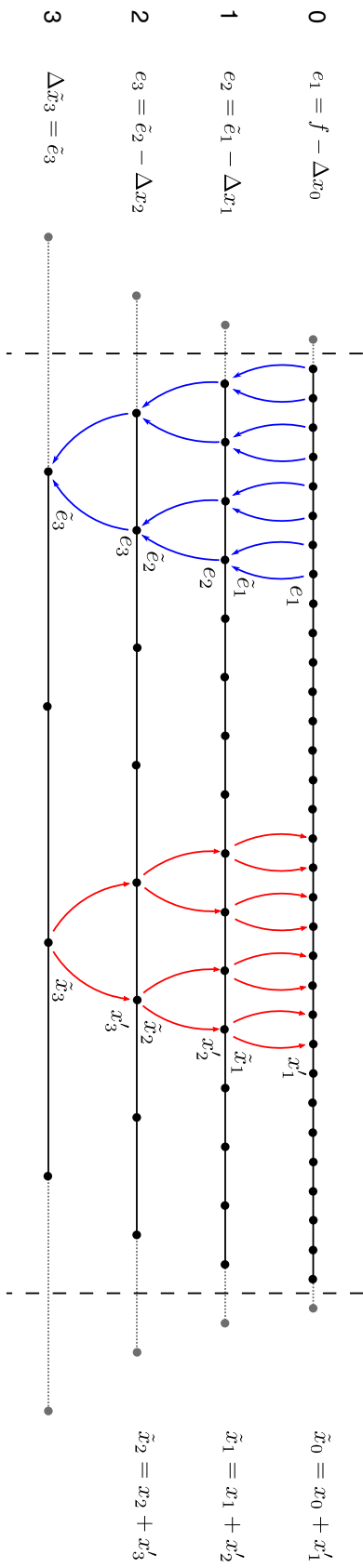


Figure 4.7: V-cycle multigrid method for a 1D-problem. Blue arrows: restriction step. Red arrows: expanding step. Black points: interior nodes. Grey points: ghost nodes. Descending operations are described on the left, ascending operations on the right. Relaxation using an SOR algorithm is performed before restrictions, after expansions and at the coarsest level.

In a parallel configuration, a variation of the classical sequential SOR algorithm needs to be used, the SOR algorithm in Red-Black ordering [Yavneh, 1996; Konstantinidis & Cotronis, 2013]. In this technique, nodes are separated in two sets, respectively called ‘black’ and ‘red’. The corresponding chessboard-like repartition is presented in figure 4.8. Both sets are alternatively updated during smoothing steps: black values are for instance updated using red nodes, red values are updated using black nodes... Computationally, this problem is interesting as the color sets are not aligned in memory. For the 2D poisson equation, for instance, when solving $\Delta\zeta = -f$ on a uniform mesh of spacing dx and dy , the update of the (i,j) node looks like:

$$\tilde{\zeta}_{i,j} = \left(\frac{\zeta_{i+1,j} + \zeta_{i-1,j}}{dx^2} + \frac{\zeta_{i,j+1} + \zeta_{i,j-1}}{dy^2} + f_{i,j} \right) / \left(\frac{2}{dx} + \frac{2}{dy} \right) \quad (4.25)$$

$$\zeta_{i,j} = (1 - \sigma) \zeta_{i,j} + \sigma \tilde{\zeta}_{i,j} \quad (4.26)$$

where $\sigma \geq 1$ is the over-relaxation parameter. A naive implementation would result in a succession of non-aligned global memory reads. A solution is to transfer the vector on which the method is iterated to texture memory. This memory is fast and intended to allow for a quick access to memory locations grouped on hardware. This method leads to a 20% speed-up in the code. Much more sophisticated techniques can be set-up to accelerate this procedure [Konstantinidis & Cotronis, 2013], but they usually require a preprocessing step to reorder the data. This was found here too costly as only 5 to 10 relaxation steps are accomplished in a row to ensure the convergence of the multigrid method. The next important performance critical task is a careful choice of the σ parameter, as choosing a near-optimal value leads to significant performance improvements at no extra computing cost. The values chosen here follow a procedure similar to Ehrlich [1972]; Schmid [2008]. The relaxation parameter σ is updated at each red or black update according to

$$r_J = 0.95 \cos \left(\frac{\pi}{2 \min(n_x, n_y)} \right) \quad (4.27)$$

$$\sigma_0 = 1 \quad (4.28)$$

$$\sigma_{1/2} = \frac{1}{1 - r_J^2/2} \quad (4.29)$$

$$\sigma_{n+1/2} = \frac{1}{1 - \sigma_n r_J^2/4} \quad \text{for } n \geq \frac{1}{2} \quad (4.30)$$

where a $1/2$ increment is added to indices after a red or black update. A speed-up of a factor 35 was observed between this algorithm and the corresponding sequential C-code, computed on a i7 1.6 GHz equipped with a NVidia Tesla C2075 GPU.

Using these numerical techniques, the on-site fast simulation of flames becomes accessible, providing an easier, instantaneous access to computations’ output.

4.4 Non-Linear Acoustic Forcing of a Conical Flame

The most prominent characteristic of our formulation is its capacity to generate a Darrieus-Landau mechanism. It is especially interesting as most G-equation based studies assume a forcing of the form [Schuller *et al.*, 2003b]:

$$u' = v' \sqrt{2} \cos \left(\omega \left(t - \frac{x}{\bar{u}} \right) \right) \quad (4.31)$$

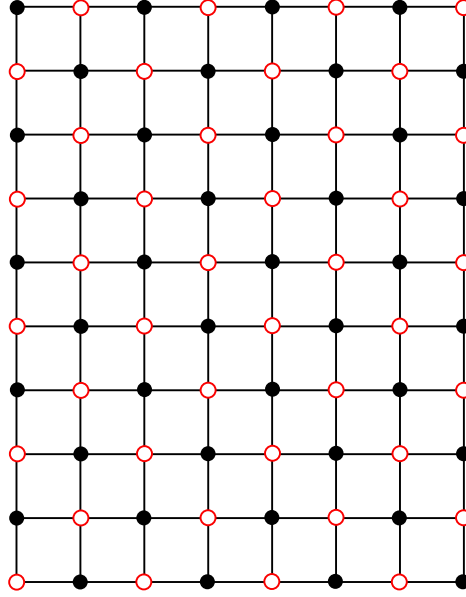


Figure 4.8: *Red-Black ordering for over-relaxed Gauss-Seidel operations.*

where x refers to the axial direction, ω to the angular forcing frequency, v' to the root-mean-square perturbation level and \bar{u} denotes a constant of the same order as the injection velocity. In more sophisticated models, this forcing can be made divergence-free or decaying in space [Schuller *et al.*, 2002a; Preetham *et al.*, 2008; Cuquel, 2013]. However, it is usually decoupled from the flame response. No explanation is then given for the transformation of an initially acoustic wave of characteristic length c/ω to an hydrodynamic disturbance of length \bar{u}/ω [Baillot *et al.*, 1992; Birbaud *et al.*, 2006]. We showed in chapter 2 that a proper inclusion of heat effects could solve this issue in a simplified linear framework [Blanchard *et al.*, 2015]. We wish to apply this modelling to a fully non-linear axisymmetric case.

To do so, the set-up presented in figure 4.1 was implemented. It consists in an axisymmetric injector on which a conical flame is attached. The combustion chamber is confined to suppress the need for an excessively large computational domain. Besides, following Cuquel [2013], the exterior radius r_1 was chosen large enough to weakly effect flame dynamics. Injector length allows the flow to stabilize. The combustion chamber length was taken long enough to minimize boundary conditions feedback. Throughout the computations carried out in this chapter, the burnt to unburnt temperature ratio E was set to 6.

Two techniques were employed to validate our methodology: first, harmonic forcing simulations were computed. Second, the linear transfer function of the flame was estimated using a random binary signal technique. Both approaches were compared to experiments carried out by Cuquel *et al.* [2013b]; Cuquel [2013] in similar conditions.

The numerical parameters were evaluated to fit the experimental flame's aspect ratio for a given bulk injection velocity v_{bulk} . Two flames were considered, the first one, noted flame a), is used for harmonic forcing comparisons. The main characteristics of this configuration are presented in table 4.1. The flame aspect ratio is defined as the ratio of the averaged flame height over the flame base radius, and ϕ denotes here the equivalence ratio of the CH₄/air

	configuration	v_{bulk} (m.s ⁻¹)	ϕ	S_L (m.s ⁻¹)	Aspect Ratio
Experiments	confined	0.89	0.86	0.37	2.7
Numerics	confined	0.89	-	0.28	2.7

Table 4.1: *Experimental and numerical parameters for the flame (a).*

	configuration	v_{bulk} (m.s ⁻¹)	ϕ	S_L (m.s ⁻¹)	Aspect Ratio
Experiments	opened	1.56	1.03	0.41	3.5
Numerics	confined	1.56	-	0.41	3.5

Table 4.2: *Experimental and numerical parameters for the flame (b).*

mixture used in the experiments. In this table, a discrepancy is observed between the experimental and the numerical laminar burning velocities. This can be easily explained as the value given by [Cuquel *et al.* \[2013b\]](#) is deduced from the equivalence ratio of the CH₄/air mixture at room temperature and atmospheric pressure [[Vagelopoulos *et al.*, 1994](#)]. In numerical simulation, an effective, corrected flame velocity is used that reproduces the correct flame shape observed in experiments. This effective laminar burning velocity takes into account the heat loss effects at the flame base and the structure of the jet, that has a top hat velocity profile near the outlet with a boundary layer thickness of about 1 mm. [Cuquel \[2013\]](#) did not carry out a white noise forcing of this confined conical flames. Instead, a second flame configuration b) was considered. The corresponding flame parameters are presented in table 4.2. In this case, [Cuquel \[2013\]](#) estimated an effective laminar burning velocity from aspect ratio measurements which is the value indicated in the table. The numerical and experimental values then agree.

4.4.1 Harmonic Forcing

For harmonic forcing excitations, flame (a) is considered. The effective laminar burning velocity is set to $S_L = 0.28$ m.s⁻¹ and the Markstein length \mathcal{L} to $5 \cdot 10^{-4}$ m. Any smaller value of the Markstein length leads to a global flame instability. A constant kinematic viscosity of $\nu = 1.57 \cdot 10^{-5}$ m.s⁻² was considered. This overall corresponds to a Reynolds number based on the injector diameter of 1247. This set of parameters leads to the steady flame presented in figure 4.9. A good agreement between the numerical and experimental shapes is observed. Harmonic forcing were implemented by imposing an oscillating input velocity at 20, 30, 40, 55, 70, 80, 150 and 200 Hz. The forcing root-mean-square (rms) level v' was chosen as 10% of the bulk velocity. This level corresponds to a peak-to-peak amplitude of 14.1%. The general aspect of the flame at 80 Hz is presented in figure 4.10 for both our numerical simulation and for experiments with flame (a) [Cuquel *et al.* \[2013b\]](#). The agreement with the measurements is satisfying, except of course for azimuthal perturbations, absent in our model. Cusps in the azimuthal direction are visible in experiments, especially in the vicinity of the axis of symmetry. They are due to a well-known thermo-diffusive instability [[Joulin & Clavin, 1979](#)]. Overall, the dispersion relation associated with flame wrinkling propagation is well respected. This agreement is confirmed by a comparison of the experimental and numerical Flame Transfer Functions presented in figure 4.11. On this plot, the reduced frequency $\omega^* = \omega r_0 / S_L^* \cos(\alpha)$ is used. The experimental theoretical laminar burning velocity, $S_L = 0.37$ m.s⁻¹, was retained as the reference flame velocity

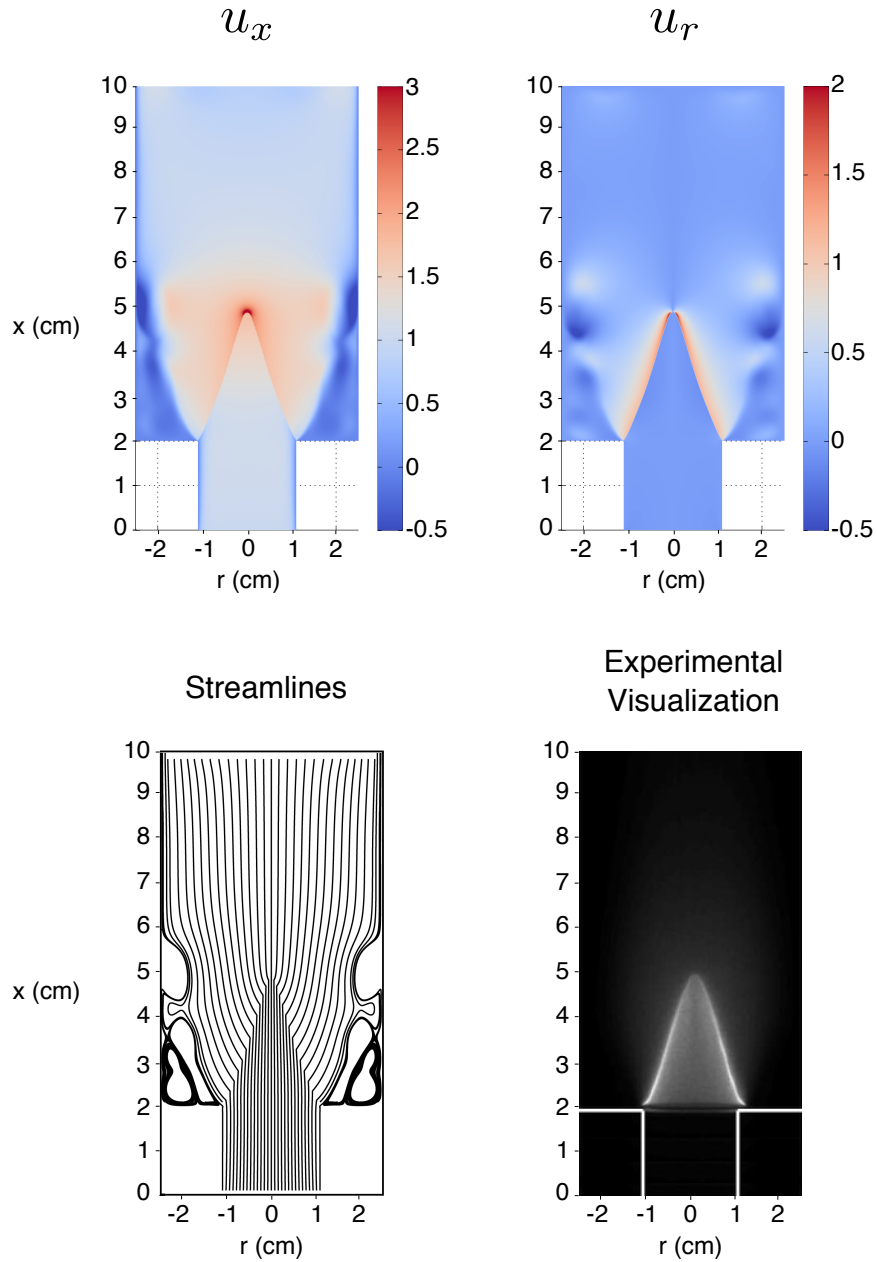


Figure 4.9: Longitudinal velocity (top left), radial velocity (top right) and streamlines (bottom left) of the flame harmonically forced of flame (a). $v_{bulk} = 0.89 \text{ m.s}^{-1}$, $S_L = 0.28 \text{ m.s}^{-1}$, $\mathcal{L} = 5.10^{-4} \text{ m}$. Bottom right: corresponding experimental flame configuration from [Cuquel et al. \[2013b\]](#), $v_{bulk} = 0.89 \text{ m.s}^{-1}$, $\phi = 0.86$.

S_L^* . For $\omega^* < 4\pi$, the agreement between both approaches is excellent. For larger forcing frequencies, as the flame base dynamic becomes more important, the datasets diverge [Cuquel *et al.*, 2013a]. This is to be expected as our numerical method neglects the thermal diffusion layer, dominant in the vicinity of the walls and has an ad-hoc model for the flame speed in boundary layers to circumvent numerical issues.

In order to evaluate the impact of the forcing frequency on the upstream flow, the leading Fourier mode of the longitudinal velocity \tilde{v}_x was extracted. Its phase β , evaluated on the axis of symmetry, is plotted in figure 4.12. The scaling with frequency allows a direct comparison of the slope of the different curves. Indeed, the phase velocity of the wave can be estimated by

$$v_\beta = \frac{\omega}{k} = \frac{2\pi f}{|\nabla\beta|} \quad (4.32)$$

Moreover,

$$|\nabla\beta| = \left| \frac{\partial\beta}{\partial x} \right| \quad (4.33)$$

on the axis of symmetry. Figure 4.12 shows a strong variation of phase velocity with the frequency. The forcing at 200 Hz is the only one exhibiting a characteristic acoustic, flat phase profile over the distance considered. All the others are the result of a superposition of multiple modes. For instance, at 55 Hz (curve (c)), an acoustic phase velocity is observable close to the injector but is replaced by an hydrodynamic mode downstream. The 40 Hz curve exemplifies the complexity of these interactions. An hydrodynamic phase velocity is observable throughout the plot, but with a change of sign between $x = 0.028$ m and $x = 0.032$ m. The corresponding surface results are presented in figure 4.13. The gain exhibits a typical decrease close to the injector exit, but increases when approaching the flame tip. On phase velocity profiles, large white areas denote regions where acoustic waves are dominant. Two limit regimes are observable. At high frequency, the flame saturates and the flow is dominated by acoustics. At very low frequency, flame-induced vorticity waves have a limited impact. The flame merely adapts its height to the changing mass flow rate, very little flame wrinkling dynamics is observed. In between, flame wrinkling is amplified and strong hydrodynamic modes are generated. All these features are consistent with previous experimental analysis from Birbaud *et al.* [2006].

These results show how the addition of heating effects to a G-equation is sufficient to induce a very rich and relevant dynamic in the fresh reactants that fully reproduces previous observations [Birbaud *et al.*, 2006] and previous direct numerical simulations of the flame response with a more sophisticated combustion model [Schlimpert *et al.*, 2015]. These details are required for the proper computation of realistic numerical flames. In the next part, we wish to test on this configuration some well-known linear system identification techniques: the ARMarkov (AutoRegressive model with Markov parameters) algorithm and the Wiener filtering technique [Ljung, 1987; Akers & Bernstein, 1997; Tay-Wo-Chong, 2012]. The theoretical limitations of these procedures are well known. Employing them then allows to estimate the robustness of purely linear approaches to flame system identification.

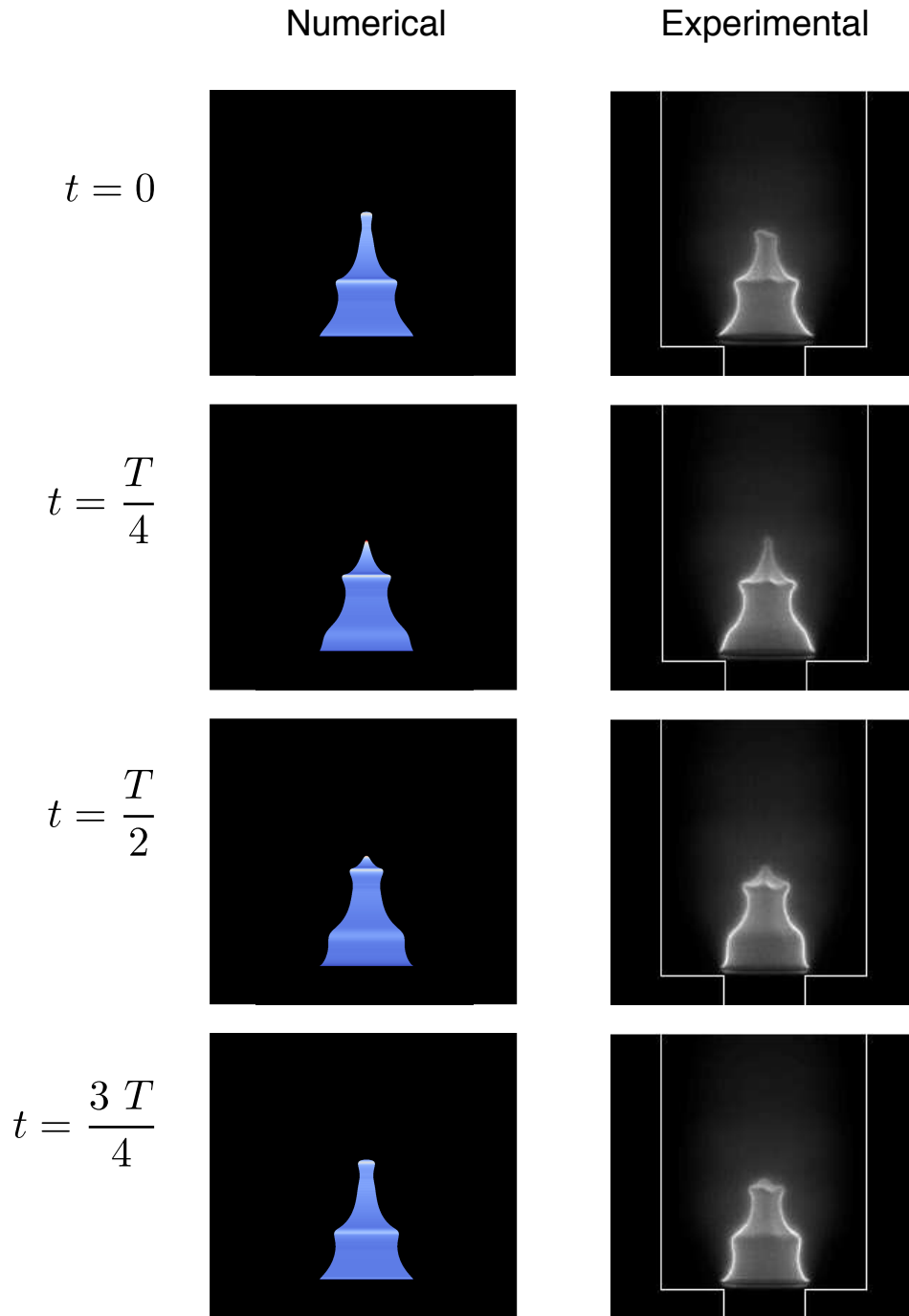


Figure 4.10: Comparison of numerical (left) and experimental (right) flames forced at a rms level $v'/v_{bulk} = 10\%$, with $v_{bulk} = 0.89 \text{ m.s}^{-1}$. Left: $S_L = 0.28 \text{ m.s}^{-1}$, $\mathcal{L} = 5.10^{-4} \text{ m}$. Color is based on local flame velocity, scaled between 0.2 and 0.93 m.s^{-1} . Axisymmetry is enforced to generate 3D visualizations. Right: methane-air flame, $v_{bulk} = 0.89 \text{ m.s}^{-1}$, $\phi = 0.86$. White lines indicate the solid walls location.

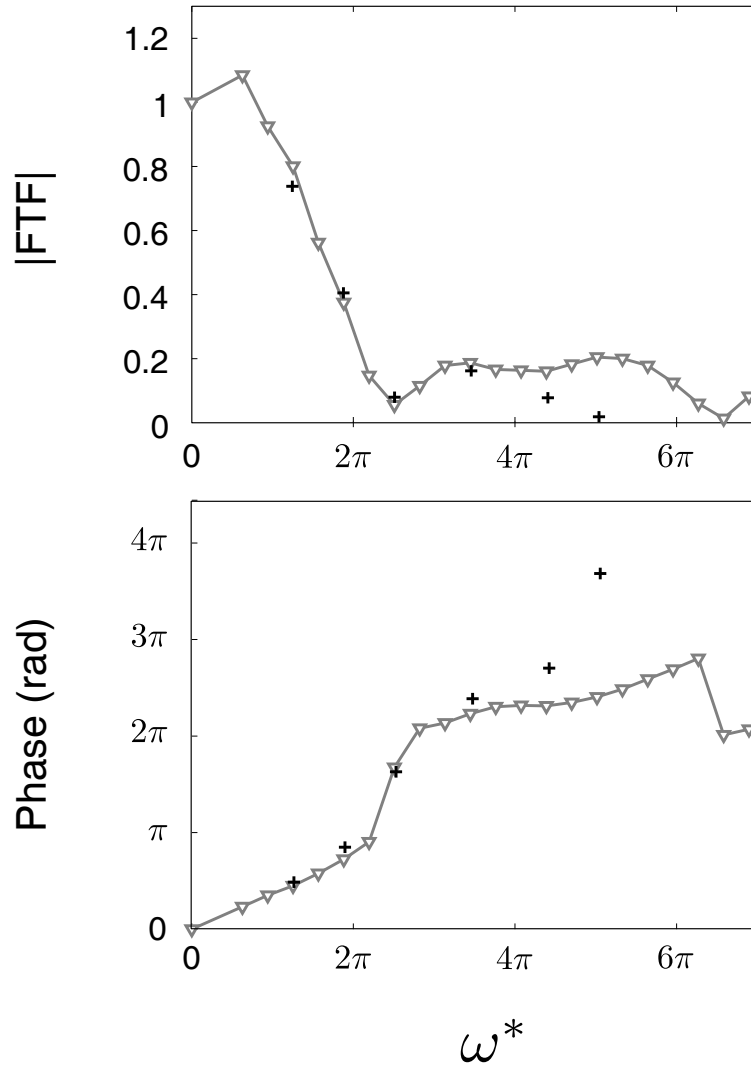


Figure 4.11: Comparison of numerical (crosses) and experimental (triangles) flame transfer function, with $v_{bulk} = 0.89 \text{ m.s}^{-1}$. Numerical parameters: $S_L = 0.28 \text{ m.s}^{-1}$, $\mathcal{L} = 5.10^{-4} \text{ m}$, flame is forced at 10 %. Experiment: methane-air flame, $v_{bulk} = 0.89 \text{ m.s}^{-1}$, $\phi = 0.86$.

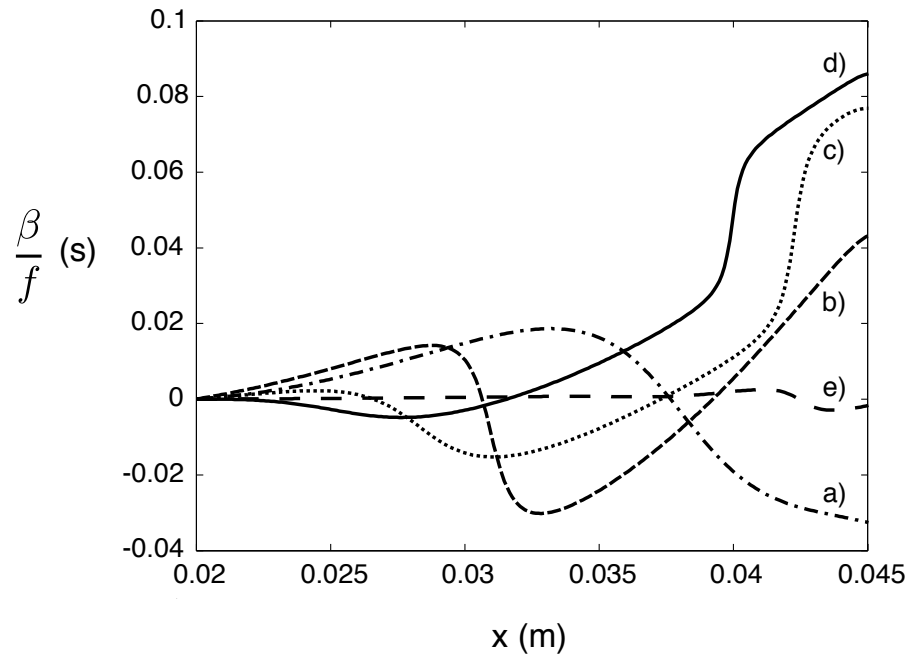


Figure 4.12: Phase of the principal longitudinal velocity mode on the axis of symmetry upstream the flame, rescaled with forcing frequency at a rms level $v'/v_{bulk} = 10\%$. a): 20 Hz, b): 40 Hz, c): 55 Hz, d): 80Hz, e): 200Hz. $x = 0.02$ m corresponds to the injector exit plane. In this computation, the average position of the flame tip is at $x = 0.05$ m.

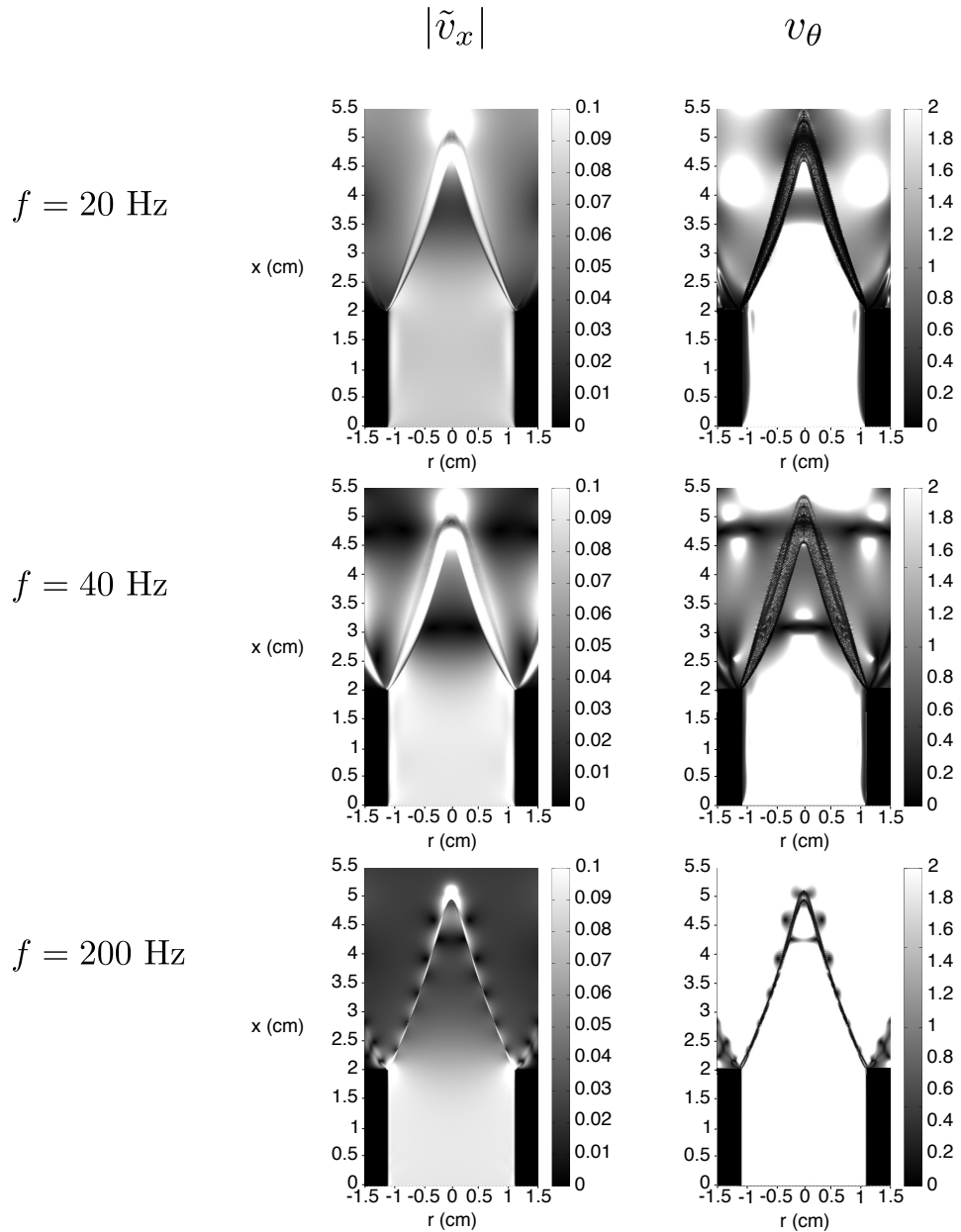


Figure 4.13: Phase of the principal longitudinal velocity mode on the axis of symmetry upstream the flame, rescaled with forcing frequency at a rms level $v'/v_{\text{bulk}} = 10\%$. a): 20 Hz, b): 40 Hz, c): 55 Hz, d): 80Hz, e): 200Hz. $x = 0.02 \text{ m}$ corresponds to the injector exit plane. In this computation, the average position of the flame tip is at $x = 0.05 \text{ m}$.

4.4.2 Impulse Response Identification

4.4.2.1 ARMarkov Algorithm

Two algorithms were tested to estimate the linear impulse response of the system: the ARMarkov model and a Wiener filter. In this chapter, a single input-single output (SISO), linear, time-invariant system will be considered. Starting from these assumptions, autoregressive models are among the most straightforward descriptions developed. They express an output y at a discrete time t as the result of a linear superposition of inputs u at different time in history along with some autoregressive terms

$$y(t) = a_0 u(t) + a_1 u(t-1) + \dots + a_n u(t-n) + a_{n+1} y(t-1) + \dots + a_{n+\mu} y(t-\mu) \quad (4.34)$$

where n denotes the length of the (pseudo-)impulse response computed and μ the number of autoregressive terms. A variation of this AR model is the ARMarkov model. The previous formula is then slightly modified to

$$y(t) = a_0 u(t) + a_1 u(t-1) + \dots + a_n u(t-n) + a_{n+1} u(t-n-1) + \dots + a_{n+\mu} u(t-n-\mu) + a_{n+\mu+1} y(t-n-1) + \dots + a_{n+2\mu} y(t-n-\mu) \quad (4.35)$$

The advantage of introducing a delay between the explicit and the autoregressive parts of the computation lies in the time separation between the impulse response and the autoregressive terms. Contrary to the AR model, $[a_0 \dots a_n]$ is an excellent approximation for the unfiltered impulse response provided that $n \gg \mu$. More details on the mathematical aspects of this model can be found in [Akers & Bernstein \[1997\]](#); [Venugopal & Bernstein \[2000\]](#).

These equations can be expressed in a matrix form, starting from a time series of length $N \gg n + \mu$

$$\mathbf{y} = M_u \mathbf{a} \quad (4.36)$$

where $\mathbf{y} = (y(n+\mu), \dots, y(N))^T$, $\mathbf{a} = (a_0, \dots, a_{n+2\mu})^T$ and M_u is a matrix coding Eq. 4.35 for times ($t = n + \mu, \dots, t = N$). This equation is solved in a least-square sense to obtain the coefficients \mathbf{a} , knowing u and y time series. This formulation is quite convenient as it can be directly implemented from the input and output vectors. However, if the forcing u is dominated by a given frequency, the resulting coefficients will emphasize the precision of the model on this mode. The pseudo-inversion of M_u indeed optimizes \mathbf{a} in a 2-norm sense based on an unfiltered y output. Besides, if the time series is long, or if n is large, M_u quickly gets fairly heavy and quite intractable on typical modern computers. Both of these limitations can be circumvented by using a Wiener filter on the data.

4.4.2.2 Wiener-filtered impulse response

We wish to identify the impulse response of the system while minimizing the numerical error on the whole time series. The output predicted by an impulse response (a_0, \dots, a_n) is obtained by computing the convolution of \mathbf{a} with the input u

$$y^*(t) = \sum_{k=0}^n a_k u(t-k) \quad (4.37)$$

The error at time t is

$$e(t) = y(t) - y^*(t) = y(t) - \sum_{k=0}^n a_k u(t - k) \quad (4.38)$$

The square of the 2-norm of the error on all predictable time steps is thus

$$\|e\|^2 = \sum_{t=n}^N \left[y(t) - \sum_{k=0}^n a_k u(t - k) \right]^2 \quad (4.39)$$

This norm can be minimized with respect to each a_k parameter. After differentiation, this leads to the equations for $k=0, \dots, n$

$$c_k = \sum_{t=n}^N [y(t)u(t - k)] \quad (4.40)$$

$$\Gamma_{k,j} = \sum_{t=n}^N u(t - k)u(t - j) \quad (4.41)$$

$$c_k = \sum_{j=0}^n \Gamma_{k,j} a_j \quad (4.42)$$

This set of equations can be written in a matrix form as

$$\mathbf{c} = \Gamma \mathbf{a} \quad (4.43)$$

Another possibility to obtain this relation is to multiply Eq. 4.36, in the case of $\mu = 0$, by M_u^T . Once again, this expression is numerically inverted to obtain \mathbf{a} . This method requires a computationally heavy but light in memory pre-processing procedure to compute the $\Gamma_{k,j}$ and c_k coefficients. It can compensate potential imperfections in a random forcing \mathbf{u} , but becomes very ill-conditioned when \mathbf{u} off-diagonal auto-correlation coefficients become large. Conversely, in the specific case of a forcing with an auto-correlation function equal to a Dirac function, the Γ matrix becomes unity and $\mathbf{c} = \mathbf{a}$.

4.4.2.3 Impulse Response Estimate of a Conical Flame: the Problem of Flame Instabilities.

We wish to apply both previous algorithms on a practical case.

First, as a test case, the random binary signal forcing of flame (a), presented in table 4.1, computed with a larger Markstein length value of $\mathcal{L} = 9 \cdot 10^{-4}$ m was carried out. The interest of increasing the damping term \mathcal{L} is to enforce the stability of the Darrieus-Landau mechanism, thus leading to a cleaner output signal. The rms velocity forcing level was set to 5.6%, with a forcing randomly changing between the maximum and minimum values at a frequency of 8190 Hz. The signal was computed for a duration of 2 s. The results of both algorithms are presented in figure 4.14. For edibility, only the first 0.1 s out of 0.25 s of the impulse response is plotted. As expected, the results are very clean, and both algorithms give the same result up to 4% in a 2-norm sense. Overall, this impulse predicts 80% of the output from a convolution with the input. The behaviour of the FTF is close to the one expected, with a low-pass filtering behaviour, and a succession of local maxima occurring at higher frequencies [Cuquel *et al.*, 2013b]. The gain values of these local maxima -up to 0.55- is however larger than what is expected from comparable flames -typically 0.4-. This may be the sign that neglecting the Markstein length associated with the tangential strain may significantly affect the linear damping of the Darrieus-Landau instability.

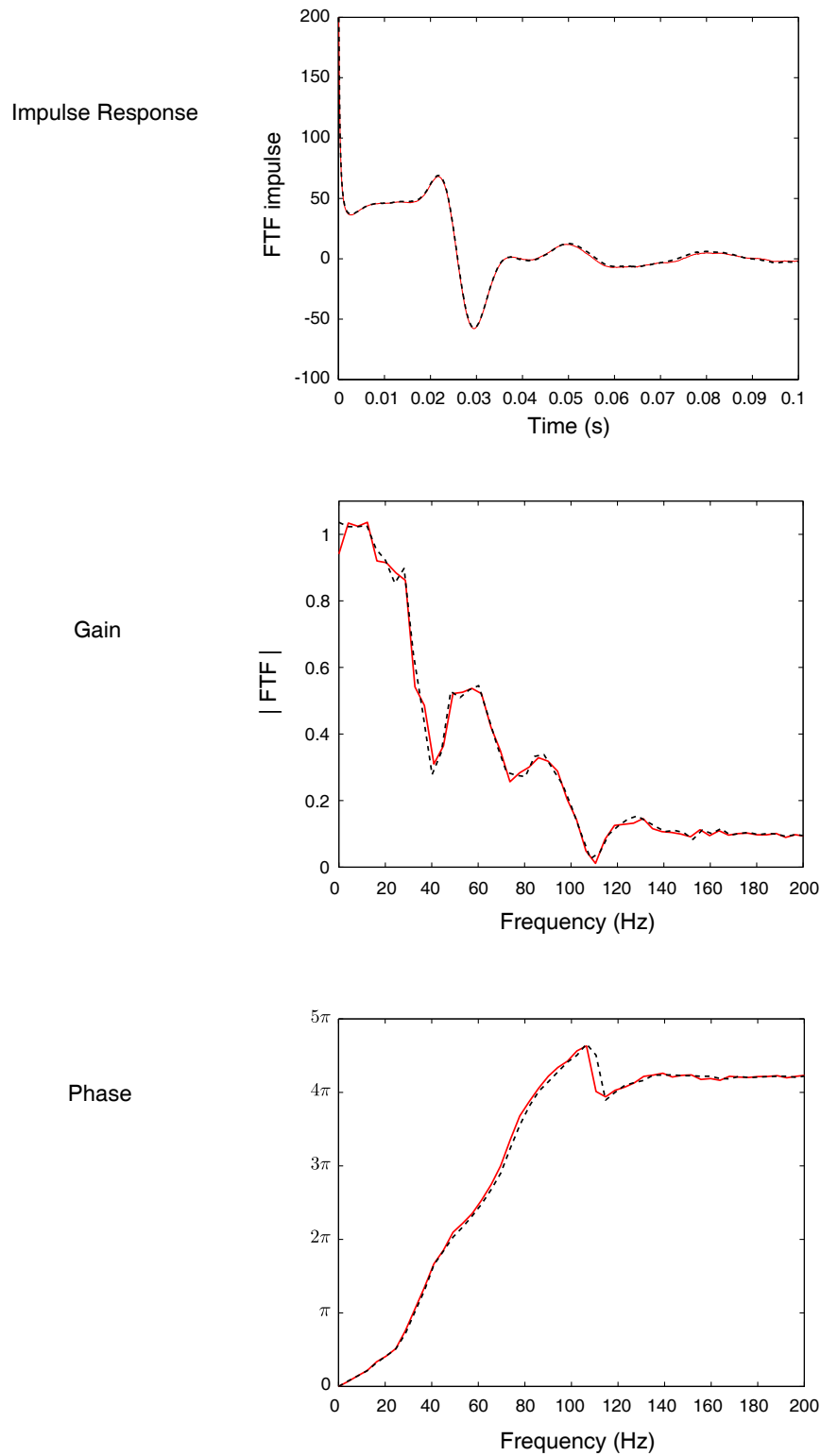


Figure 4.14: Results of both system identification techniques for an over-damped flame. $v_{bulk} = 0.89 \text{ m.s}^{-1}$, $S_L = 0.28 \text{ m.s}^{-1}$, $\mathcal{L} = 9.10^{-4} \text{ m}$. Dotted black: output from the ARMarkov algorithm, $n=2000$, $\mu = 40$. Red: output from the Wiener Filter, $n=2000$.

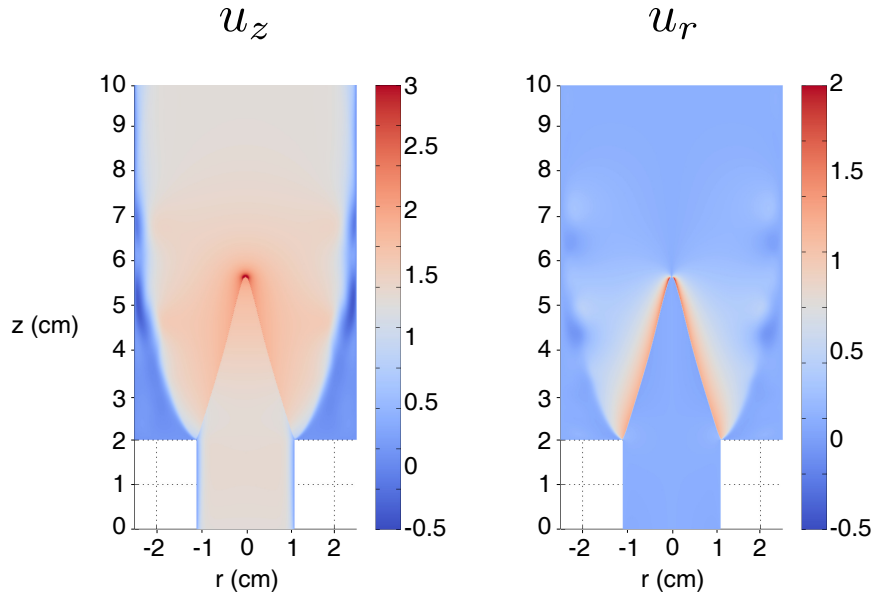


Figure 4.15: Longitudinal and radial velocity of flame (b). $v_{bulk} = 1.56 \text{ m.s}^{-1}$, $S_L = 0.41 \text{ m.s}^{-1}$, $\mathcal{L} = 5.10^{-4} \text{ m}$.

These algorithms were then tested on the flame (b), with the parameters presented in table 4.2. The bulk velocity was also set to $av_{bulk} = 1.56 \text{ m.s}^{-1}$ and the laminar burning velocity to $S_L = 0.41 \text{ m.s}^{-1}$ while the Markstein length from the previous computations of $\mathcal{L} = 5.10^{-4} \text{ m}$ was kept. The corresponding baseflow is presented in figure 4.15. A forcing rms level of 3.2% is considered, the other forcing parameters remaining identical to the previous case. The Markstein length value chosen is quite realistic, and leads to a low amplitude, self-sustained Darrieus-Landau instability. This phenomenon can be seen in figure 4.16. The impulse response is dominated at long times by persistent oscillations at 150 Hz. This prevents the impulse response from correctly converging to a zero value. Once again, the limitations of the code are quite obvious. The corresponding experimental Flame Transfer Function is presented in figure 4.17. The addition of the second Markstein length or of a gravity correction to the code may lead to a much better low-amplitude flame behaviour.

However, the issue of an hydrodynamic instability jeopardizing the quality of the system identification is far from being limited to numerical questions. In practice, flames are very often subject to global instabilities. For instance, the Wiener filtering technique was applied on the measurements from Cuquel [2013] of the OH^* signal of flame (b) forced with white noise velocity perturbations of various amplitudes, leading to the results presented in figure 4.18. The corresponding impulse responses exhibit a quite coherent, 14 Hz oscillation. This frequency has been identified as flame flickering [Buckmaster & Peters, 1988; Yuan *et al.*, 1994] for the conical flame investigated. They reveal a persistent presence of this oscillation in the impulse response. A fairly high rms forcing level of 15% needs to be achieved before this unstable mode gets masked by the impulse's measurement noise.

Handling such instabilities in a system identification model is difficult, as the frequency, growth rate and saturation mechanisms need to be understood prior to any further in-

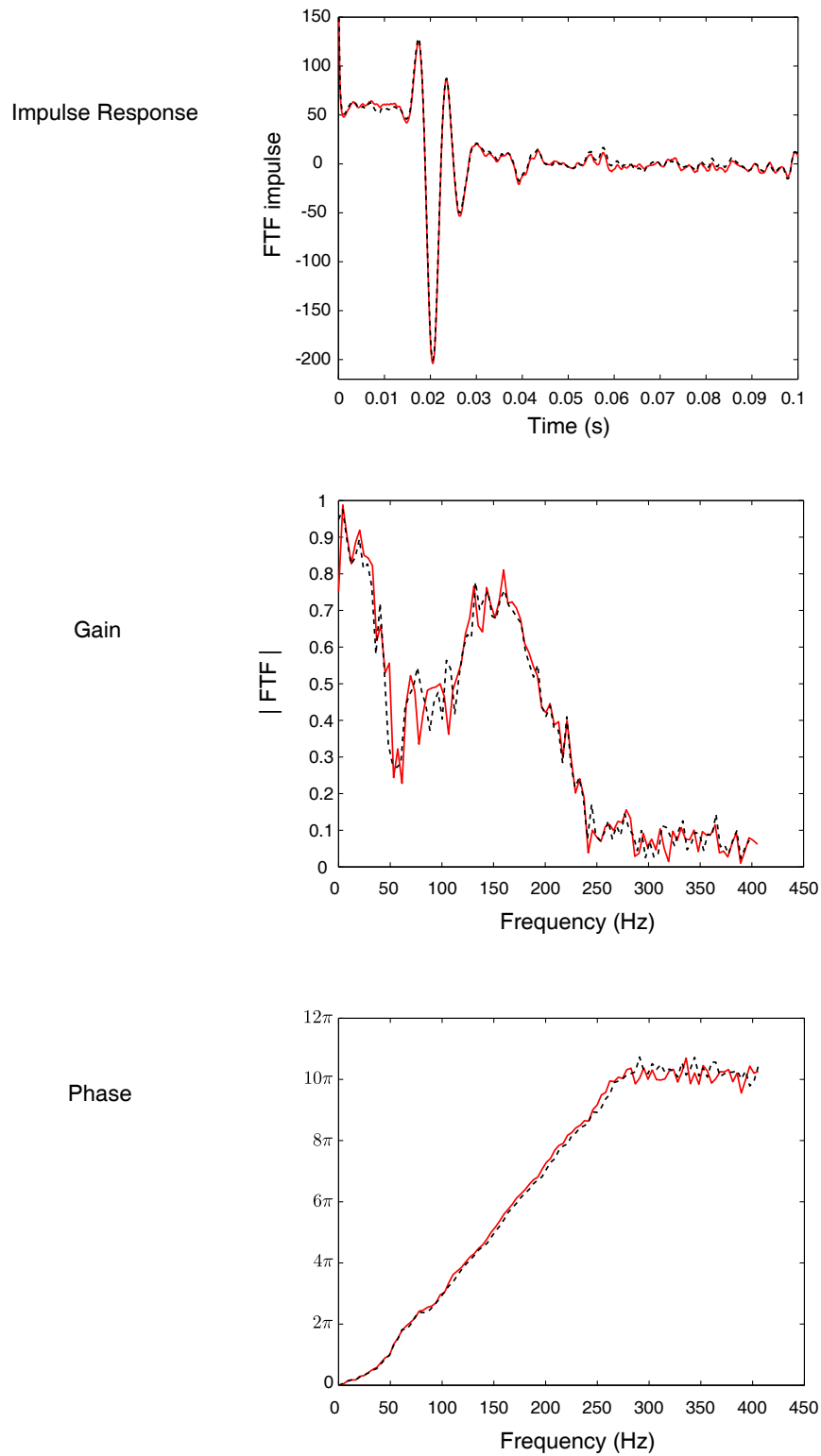


Figure 4.16: Results of both system identification techniques for an over-damped flame. $v_{bulk} = 1.56 \text{ m.s}^{-1}$, $S_L = 0.41 \text{ m.s}^{-1}$, $\mathcal{L} = 5.10^{-4} \text{ m}$. Dotted black: output from the ARMarkov algorithm, $n=2000$, $\mu = 40$. Red: output from the Wiener Filter, $n=2000$.

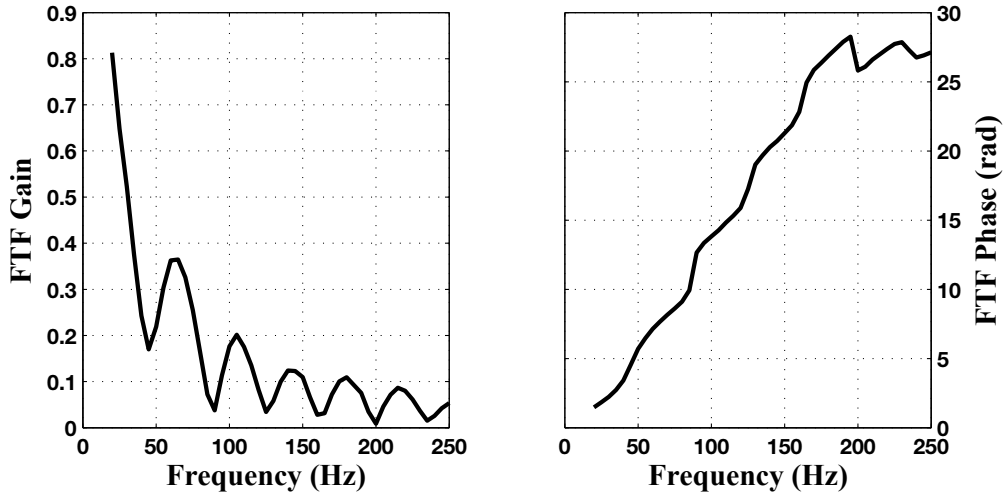


Figure 4.17: Flame Transfer Function obtained from discrete harmonic forcing of a methane-air flame at $\phi = 1.03$, $v_{bulk} = 1.56 \text{ m.s}^{-1}$. Data from [Cuquel \[2013\]](#).

vestigation. [Noiray & Schuermans \[2013\]](#) suggested to fit a Van der Pol oscillator on the measured dynamics. The instability contribution η to the time series is modelled as

$$\frac{d^2 \eta}{dt^2} + (-\nu + \kappa \eta^2) \frac{d \eta}{dt} + \omega_0 \eta = \Gamma_1 f + \Gamma_2 \frac{d f}{dt} \quad (4.44)$$

Where f denotes the instantaneous forcing intensity, ν the linear growth rate of the instability, κ the saturation parameter, ω_0 the pseudo-characteristic frequency of the oscillation, Γ_1 and Γ_2 the input forcing gains. Such a model was successfully applied on a jet instability [[Li & Juniper, 2013](#)]. But identifying these parameters is quite challenging, especially on noisy experimental data. [Noiray & Schuermans \[2013\]](#) proposed an approach based on output analysis. An amplitude equation is formulated and the Van-Der-Pol parameters are identified from its statistical properties. The system identification algorithm presented in chapter 2 provides an access to such time-varying amplitudes. This method could also be applied to our case, but several issues remain to be solved. In particular, evaluating the Γ_1 and Γ_2 factors is crucial and strongly influence the quality of the model. The corresponding detailed methodology is also a subject of active research, and is left for further studies.

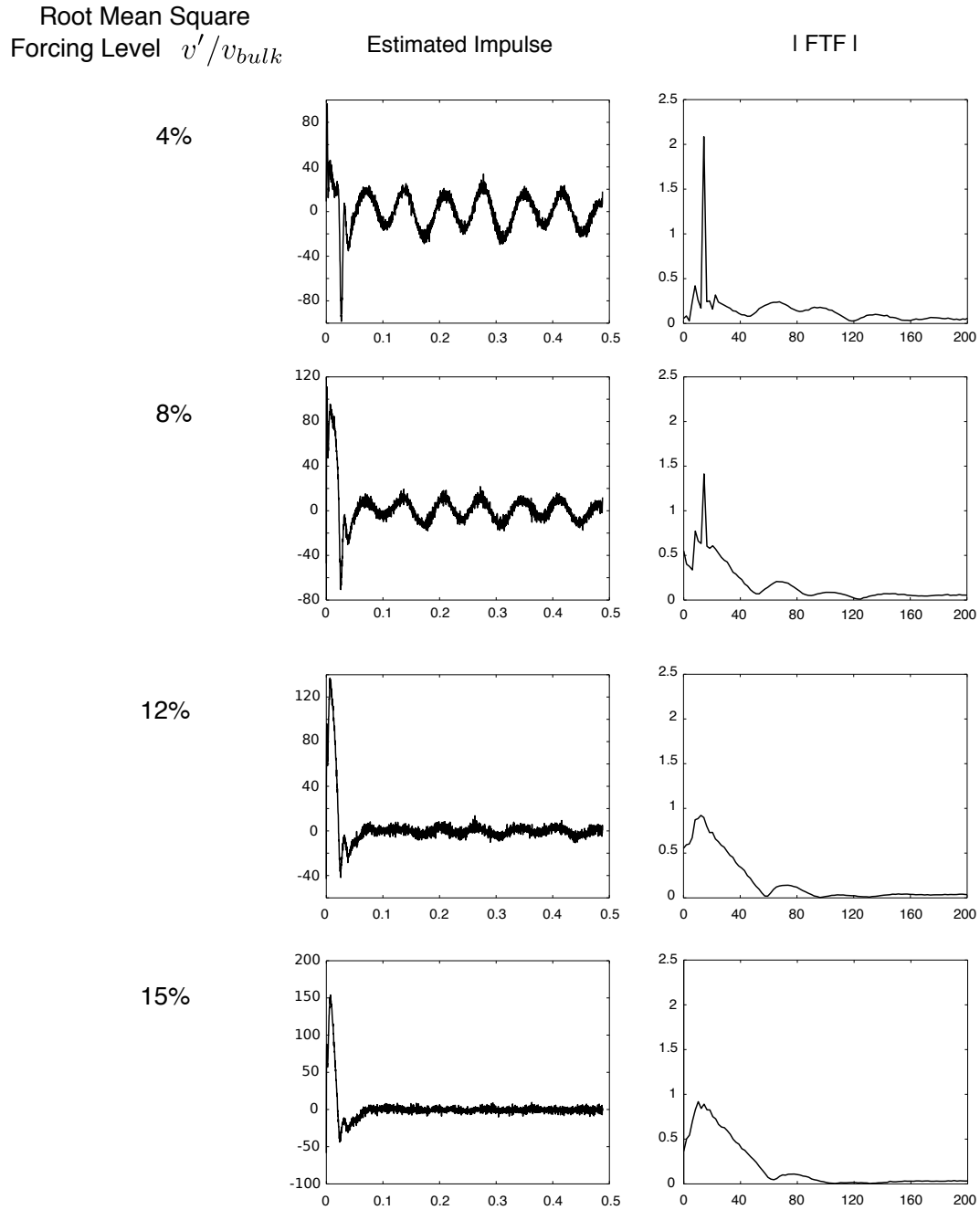


Figure 4.18: Flame Transfer Function obtained from discrete harmonic forcing of a methane-air flame at $\phi = 1.03$, $v_{bulk} = 1.56 \text{ m.s}^{-1}$. Data from *Cuquel [2013]*.

4.5 Conclusion

In this chapter, a novel strategy to incorporate heating effects in a level-set description of the flame dynamics subjected to acoustic forcing was presented. An implementation on GPU was carried out, leading to a high-efficiency numerical procedure. The results were compared with experimental data. A good quantitative agreement at low frequency was obtained between simulation and measurements for the flame shape and flame transfer function for finite amplitude perturbation levels. Finally, two system identification techniques were applied to numerical and experimental data. It was shown that, in the tested operating conditions, both methodologies were highlighting the influence of hydrodynamic instabilities naturally present in the flow on the measured output. Their existence prevented the algorithm from converging properly at low forcing amplitudes. At higher forcing levels, an impulse response can be obtained, but the domain of validity of such a linear approach to high amplitude forcings may be questioned. Finally, a perspective on the identification of a Van-der-Pol oscillator to model these instabilities was outlined. Creating a non-linear model in flames is fairly complex, and requires the identification of numerous parameters. This imposes a need for fast, accurate simulations compatible with try-and-error approaches. Our GPU code is also very well adapted for the incoming development of these new strategies in the combustion community.

Conclusion

This thesis had for objective to improve the understanding and modelling of the dynamics of premixed laminar flames submitted to an acoustic forcing. The specificity of this approach was to adapt numerical methods, initially applied to non-reactive flows, to combustion. Those numerical tools, developed at LadHyX, provide an access to powerful flow analysis capacities. They typically rely on non linear and linear direct simulations of the Navier and Stokes equations. They allow to carry out eigenvalues computations, sensitivity analysis, or linear system identifications. By applying these techniques to the analysis of flame response to incoming flow perturbations and flame sound generation, we were able to rigorously confirm some existing theories, provide theoretical elements that reproduce experimental observations and extend previous modelling of flame-acoustic interactions. This linear approach was completed with direct simulations of an original flame model that handles flow thermal expansion to explore the effects of finite amplitude perturbations on flame dynamics.

Summary of the Main Results

The local dynamics of planar flames are understood rather well, while the effects of the mutual interaction of flame fronts in a closed setting are not nearly as clearly explained. The study of an M-flame, acoustically forced within a linear regime, helps to understand these effects. Using linear tools allowed us to delineate the effects of chemistry from the effects of temperature gradients. This decomposition constitutes an important step beyond current understanding. In combustion systems, we encounter a very rich dynamics owing to the presence of multiple physical phenomena, and establishing a link between cause and effect in such a complex setting proves challenging. By switching off chemistry terms, we were able to show that the dominant contribution to the hydrodynamic perturbations induced by the flame were associated with the heat release rate. In other words, within the limits of linear thermoacoustics about a valid baseflow, the details of chemical reactions are negligible compared to the local heat release rate. This result also considerably simplifies our problem, and allows us to use a level-set method, or G-equation, to model the flame dynamics. A comparison of this method and our DNS results showed that the assumption of an infinitely thin flame generates acceptable results within a linear framework, provided heating effects has been taken into account.

Despite computing the flame dynamics, the acoustic level generated by our configuration cannot be analyzed without the identification of the prevalent acoustic sources. It is well-known that the long-range unsteady pressure field is dominated by the heat release rate noise. However, this long-range limit is measured with respect to the acoustic wavelengths, and is rarely achieved in practice. The second part our study thus focuses on the

identification of the acoustic sources dominating the close-range pressure field. To this end, an optimization of noise generated by an M-Flame within a linear limit has been carried out. This optimization has been based on a direct-adjoint methodology and consisted of optimizing the forcing shape acting on the flame from the inside of the injector. A complex superposition of entropy, vorticity and fuel mass fraction waves were generated. These waves excited the flame front and caused the corresponding perturbations to be convected towards the flame tip. There, large-amplitude acoustic waves could be generated. This latter process is quite challenging to interpret, as flame-tip behavior is rather poorly understood. Flame tips correspond to regions in which normal and transverse diffusion and convection processes are all of the same order. Determining whether flame-tip generated noise has been the result of an instability — with the energy of the perturbation amplified through the baseflow — or of an energy transfer from linear waves — with the energy extracted from pre-existing hydrodynamic structures — is an important component of a detailed analysis. To address this issue, a one-dimensional, axisymmetric model has been developed. By modulating the characteristic size of the azimuthal disturbances, it could be shown that disturbances with a length-scale of the order of the flame thickness generate high local pressure amplitudes. By modulating the content of these disturbances, it has been established that these sources are related to the destruction of vorticity waves. In other words, when disturbances are large, the dominant noise mechanism is based on the heat release rate; when they are small, of the order of the flame thickness, vorticity destruction is more important for close-range noise generation. An observation of the DNS-based optimization results confirmed this result. A dipolar source linked to a local variation in vorticity has therefore been observed. The corresponding acoustic field however quickly fades in space. Beyond two tube radii from the source, no effect on the pressure could be observed.

This finding has important implications on the flame stability: the destruction of vorticity waves by the flame front is prone to generating a close-range feedback process. It quantitatively confirms that the assumption that the bulk of the flame-generated noise is due to the unsteady heat-release rate, provides an excellent approximation even at mid-range distances. This element constitutes the final building block in our attempt to build a rigorous reduced-order flame model.

The results presented thus far had been obtained by invoking a linear framework. Based on them, a nonlinear model can now be proposed. It relies on two main assumptions: first, the flame is treated as an infinitely thin, moving interface; second, it does not generate any vorticity downstream, but rather only absorbs it. Starting from these hypotheses, a formulation in terms of a ‘hot’ G-equation has been presented and implemented on Graphic Processing Units (GPUs) in order to take advantage of the improved performances of this modern hardware. Specific attention has been directed towards the Poisson solver. The computations can treat pinching and heating effects and include a curvature correction applied to the flame velocity. This code has been validated against experimental results from a conical flame configuration. The response to a random binary signal, forcing of the numerical flame, has then been computed. However, the presence of hydrodynamic instabilities prevented the two chosen identification algorithms, ARMarkov and Wiener filtering, from converging.

The issue created by saturated instabilities is inherent to flame system identification, as the majority of combustion systems is afflicted with global instabilities. Within a linear

framework, computing an impulse response is rather straightforward. Using our linear DNS, this has been accomplished directly, i.e., without any need for an intermediate algorithm. Starting from this impulse response, it is then possible to determine a state-space model representing the underlying dynamics. This can be computed very accurately, e.g., with pre-existing $\text{\textcircled{R}}$ Matlab routines. Alternatively, a new methodology based on wavelet identification has been developed. This strategy aims at obtaining a set of amplitude equations associated with the dominant frequencies, which are subsequently converted to harmonic oscillators' responses. These harmonic oscillators, arranged in parallel, reproduce the overall system's dynamics. This strategy is proposed as a first step towards a more general system identification techniques, in particular for flows exhibiting a single, mono-frequency instability.

Perspectives

This study offers interesting perspectives for future studies of the flame dynamics, as well as the application of system identification and control. In particular, linear tools could contribute to our understanding of flame instabilities:

- A weakly nonlinear extension of our resolvent computations may help understand the nonlinear effects that arise when a flame is optimally forced.
- Numerous instabilities related to the interaction of flames with hydrodynamic structures are still poorly understood. In particular, the flame-shear layer interaction driving the V-flame dynamics would be an interesting case study in terms of local and global flame stability issues.
- As stated throughout this thesis, flames are prone to global instabilities. Some of these instabilities, such as flickering, are well understood, while others are frequently observed but not fully explained yet. For instance, when swirl is added to the flow, under certain conditions, a Precessing Vortex Core (PVC) is generated [Syred, 2006]. The instability generating this scenario and this structure is part of an ongoing research effort [Terhaar *et al.*, 2013].
- Lastly, the nonlinear dispersion relation related to flame wrinkling — and the Darrieus-Landau instability — should be mentioned. A study of this topic, based on a weakly nonlinear framework, could clarify how a flame with a saturated instability can link disturbances with different frequencies through triadic interactions.

Handling nonlinearities in flame system identification is quite complex, and the exact methodology to generate such a model poses a great challenge. However, from the results presented in this thesis, some potential approaches can be suggested:

- Assuming that the instabilities behave as separate systems, it may be possible to model them as Van-der-Pol oscillators [Li & Juniper, 2013; Noiray & Schuermans, 2013]. By cancelling their contribution to the output, linear tools could identify the remainder of the full dynamics.
- This approach could then be extended to a weakly nonlinear formulation, by representing the system as a network of nonlinearly coupled Van-der-Pol oscillators. The main problem is then to identify the nonlinear parameters. Novel system identification methodologies such as deep learning [Hinton *et al.*, 2006], one of the latest developments in the field of machine learning [Goldberg & Holland, 1988], may help tackle this issue. However, these techniques require some physical and mathematical

insight as well as long time series. Our GPU computations have been developed to satisfy this constraint.

- The integration of this model into acoustic network models such as Oscilos [[Jingxuan & Morgans, 2014](#)] would provide access to accurate estimates of limit cycle amplitudes.

Bibliography

- ADAMS, N. & SHARIFF, K. 1996 A High-Resolution Hybrid Compact-ENO Scheme for Shock-Turbulence Interaction Problems. *Journal of Computational Physics* **127** (1), 27–51. (p. 23, 122)
- AHN, K. & KENNETH, H. Y. 2012 Effects of Damköhler number on vortex–flame interaction. *Combustion and Flame* **159** (2), 686–696. (p. 12)
- AKERS, J. C. & BERNSTEIN, D. S. 1997 ARMARKOV least-squares identification. In *American Control Conference, 1997. Proceedings of the 1997*, , vol. 1, pp. 186–190 vol.1. (p. 131, 136)
- ÅKERVIK, E., BRANDT, L., HENNINGSON, D. S., HEPFFNER, J., MARXEN, O. & SCHLATTER, P. 2006 Steady solutions of the Navier-Stokes equations by selective frequency damping. *Physics of Fluids* **18** (6), 068102–068106. (p. 34)
- ASHMEAD, J. 2012 Morlet Wavelets in Quantum Mechanics. *Quanta* **1** (1), 58–70. (p. 80)
- BAILLOT, F., DUROX, D. & PRUD’HOMME, R. 1992 Experimental and theoretical study of a premixed vibrating flame. *Combustion and Flame* **88**, 149–168. (p. 128)
- BAUERHEIM, M., PARMENTIER, J.-F., SALAS, P., NICLOUD, F. & POINSOT, T. 2013 An analytical model for azimuthal thermoacoustic modes in an annular chamber fed by an annular plenum. *Combustion and Flame* . (p. 8)
- BELLUCCI, V., FLOHR, P., PASCHEREIT, C. O. & MAGNI, F. 2004 On the Use of Helmholtz Resonators for Damping Acoustic Pulsations in Industrial Gas Turbines. *Journal of Engineering for Gas Turbines and Power* **126** (2), 271–275. (p. 9, 37)
- BENEDDINE, S., METTOT, C. & SIPP, D. 2015 Global stability analysis of underexpanded screeching jets. *European Journal of Mechanics - B/Fluids* **49, Part B**, 392–399. (p. 6)
- BERLAND, J., BOGEY, C., MARSDEN, O. & BAILLY, C. 2007 High-order, low dispersive and low dissipative explicit schemes for multiple-scale and boundary problems. *Journal of Computational Physics* **224** (2), 637–662. (p. 23, 25)
- BIRBAUD, A. L., DUROX, D. & CANDEL, S. 2006 Upstream flow dynamics of a laminar premixed conical flame submitted to acoustic modulations. *Combustion and Flame* **146** (3), 541–552. (p. 14, 128, 131)
- BLANCHARD, M., SCHULLER, T., SIPP, D. & SCHMID, P. J. 2015 Response analysis of a laminar premixed M-flame to flow perturbations using a linearized compressible Navier-Stokes solver. *Physics of Fluids (1994-present)* **27** (4), 043602. (p. 38, 128)

- BÖHM, H., HESSE, D., JANDER, H., LÜERS, B., PIETSCHER, J., WAGNER, H. G. G. & WEISS, M. 1989 The influence of pressure and temperature on soot formation in premixed flames. *Symposium (International) on Combustion* **22** (1), 403–411. (p. 1)
- BOUDY, F., DUROX, D., SCHULLER, T. & CANDEL, S. 2013 Analysis of limit cycles sustained by two modes in the flame describing function framework. *Comptes Rendus Mécanique* **341** (1–2), 181–190. (p. 9)
- BOURGOUIN, J.-F., DUROX, D., MOECK, J. P., SCHULLER, T. & CANDEL, S. 2013 Self-Sustained Instabilities in an Annular Combustor Coupled by Azimuthal and Longitudinal Acoustic Modes. *ASME Turbo Expo 2013: Turbine Technical Conference and Exposition* **1** (04), 7–20. (p. 10)
- BOURGOUIN, J.-F., DUROX, D., MOECK, J. P., SCHULLER, T. & CANDEL, S. 2014 Characterization and Modeling of a Spinning Thermoacoustic Instability in an Annular Combustor Equipped With Multiple Matrix Injectors. *Journal of Engineering for Gas Turbines and Power* **137** (2), 021503–021503. (p. 10)
- BOURGOUIN, J. F., DUROX, D., MOECK, J. P., SCHULLER, T. & CANDEL, S. 2015 A new pattern of instability observed in an annular combustor: The slanted mode. *Proceedings of the Combustion Institute* **35** (3), 3237–3244. (p. 10)
- BOYER, L. & QUINARD, J. 1990 On the dynamics of anchored flames. *Combustion and Flame* **82** (1), 51–65. (p. 10)
- BREAR, M. J., NICOUD, F., TALEI, M., GIAUQUE, A. & HAWKES, E. R. 2012 Disturbance energy transport and sound production in gaseous combustion. *Journal of Fluid Mechanics* **707**, 53–73. (p. 3)
- BUCKMASTER, J. & PETERS, N. 1988 The infinite candle and its stability—A paradigm for flickering diffusion flames. *Symposium (International) on Combustion* **21** (1), 1829–1836. (p. 8, 139)
- BYCHKOV, V. V. & LIBERMAN, M. A. 2000 Dynamics and stability of premixed flames. *Physics Reports* **325** (4–5), 115–237. (p. 8)
- CAMBRAY, P. & JOULIN, G. 1994 Length-Scales of Wrinkling of Weakly-Forced, Unstable Premixed Flames. *Combustion Science and Technology* **97** (4–6), 405–428. (p. 8)
- CANDEL, S. 2002 Combustion dynamics and control: Progress and challenges. *Proceedings of the Combustion Institute* **29** (1), 1–28. (p. 2)
- CANDEL, S., DUROX, D., DUCRUIX, S., BIRBAUD, A.-L., NOIRAY, N. & SCHULLER, T. 2009 Flame dynamics and combustion noise: progress and challenges. *International Journal of Aeroacoustics* **8** (1), 1–56. (p. 3, 12)
- CANDEL, S., DUROX, D. & SCHULLER, T. 2004 Flame Interactions as a Source of Noise and Combustion Instabilities. In *10th AIAA/CEAS Aeroacoustics Conference*, pp. 1444–1454. American Institute of Aeronautics and Astronautics. (p. 12, 110)
- CHU, B.-T. 1953 On the generation of pressure waves at a plane flame front. *Symposium (International) on Combustion* **4** (1), 603–612. (p. 120)

- CHU, B.-T. 1965 On the energy transfer to small disturbances in fluid flow (Part I). *Acta Mechanica* **1** (3), 215–234. (p. 88)
- CHU, B.-T. & KOVÁSZNAY, L. S. G. 1958 Non-linear interactions in a viscous heat-conducting compressible gas. *Journal of Fluid Mechanics* **3** (05), 494–514. (p. 5)
- CLANET, C. & SEARBY, G. 1996 On the “tulip flame” phenomenon. *Combustion and Flame* **105** (1–2), 225–238. (p. 2)
- CLAVIN, P., PELCÉ, P. & HE, L. 1990 One-dimensional vibratory instability of planar flames propagating in tubes. *Journal of Fluid Mechanics* **216**, 299–322. (p. 2)
- COCLE, R., WINCKELMANS, G. & DAENINCK, G. 2008 Combining the vortex-in-cell and parallel fast multipole methods for efficient domain decomposition simulations. *Journal of Computational Physics* **227** (21), 9091–9120. (p. 121)
- COTTET, G.-H. 1987 Convergence of a vortex in cell method for the two-dimensional Euler equations. *Mathematics of Computation* **49** (180), 407–425. (p. 121)
- COUËT, B., BUNEMAN, O. & LEONARD, A. 1981 Simulation of three-dimensional incompressible flows with a vortex-in-cell method. *Journal of Computational Physics* **39** (2), 305–328. (p. 121)
- CRETA, F. & MATALON, M. 2011 Propagation of wrinkled turbulent flames in the context of hydrodynamic theory. *Journal of Fluid Mechanics* **680**, 225–264. (p. 8, 115)
- CRIGHTON, D. G., DOWLING, A. P., FLOWERS WILLIAMS, J. E., HECKL, M. & LEPINGTON, F. G. 1992 Thermoacoustic Sources and Instabilities. In *Modern Methods in Analytical Acoustics*, pp. 378–405. Springer London. (p. 3, 6)
- CROW, S. C. & CHAMPAGNE, F. H. 1971 Orderly structure in jet turbulence. *Journal of Fluid Mechanics* **48** (03), 547–591. (p. 6)
- CUQUEL, A. 2013 *Dynamics and nonlinear thermo-acoustic stability analysis of premixed conical flames*. Châtenay-Malabry, Ecole centrale de Paris. (p. xiv, 9, 128, 129, 139, 141, 142)
- CUQUEL, A., DUROX, D. & SCHULLER, T. 2013a Impact of flame base dynamics on the non-linear frequency response of conical flames. *Comptes Rendus Mécanique* **341** (1–2), 171–180. (p. 14, 38, 117, 131)
- CUQUEL, A., DUROX, D. & SCHULLER, T. 2013b Scaling the flame transfer function of confined premixed conical flames. *Proceedings of the Combustion Institute* **34**, 1007–1014. (p. xiii, 14, 38, 128, 129, 130, 137)
- D’ANGELO, Y., JOULIN, G. & BOURY, G. 2000 On model evolution equations for the whole surface of three-dimensional expanding wrinkled premixed flames. *Combustion Theory and Modelling* **4** (3), 317–338. (p. 8, 115)
- DARRIEUS, G. 1938 Propagation d’un front de flamme. In *La Technique Moderne*. France. (p. 7)

- DAVIES, C. & CARPENTER, P. W. 2001 A Novel Velocity–Vorticity Formulation of the Navier–Stokes Equations with Applications to Boundary Layer Disturbance Evolution. *Journal of Computational Physics* **172** (1), 119–165. (p. 119)
- DAVIS, S. G., QUINARD, J. & SEARBY, G. 2002a Determination of Markstein numbers in counterflow premixed flames. *Combustion and Flame* **130** (1–2), 112–122. (p. 7)
- DAVIS, S. G., QUINARD, J. & SEARBY, G. 2002b Markstein numbers in counterflow, methane- and propane- air flames: a computational study. *Combustion and Flame* **130** (1–2), 123–136. (p. 7)
- DOAK, P. E. 1973 Analysis of internally generated sound in continuous materials: 3. The momentum potential field description of fluctuating fluid motion as a basis for a unified theory of internally generated sound. *Journal of Sound and Vibration* **26** (1), 91–120. (p. 5, 38)
- DOWLING, A. P. & MORGANS, A. S. 2005 Feedback Control of Combustion Oscillations. *Annual Review of Fluid Mechanics* **37** (1), 151–182. (p. 9, 37)
- DUCHANE, F., BOUDY, F., DUROX, D. & POINSOT, T. 2011 Sensitivity analysis of transfer functions of laminar flames. *Combustion and Flame* **158** (12), 2384–2394. (p. 14, 38)
- DUCRUIX, S., DUROX, D. & CANDEL, S. 2000 Theoretical and experimental determinations of the transfer function of a laminar premixed flame. *Proceedings of the Combustion Institute* **28** (1), 765–773. (p. xi, 8, 9, 11, 37)
- DUCRUIX, S., SCHULLER, T., DUROX, D. & CANDEL, S. 2003 Combustion dynamics and instabilities: Elementary coupling and driving mechanisms. *Journal of Propulsion and Power* **19** (5), 722–734. (p. 7, 9, 10)
- DUROX, D., SCHULLER, T., NOIRAY, N. & CANDEL, S. 2009 Experimental analysis of nonlinear flame transfer functions for different flame geometries. *Proceedings of the Combustion Institute* **32** (1), 1391–1398. (p. 9, 14, 15)
- EHRlich, L. W. 1972 Coupled harmonic equations, SOR, and Chebyshev acceleration. *Mathematics of Computation* **26** (118), 335–343. (p. 127)
- EMMERT, T., BOMBERG, S. & POLIFKE, W. 2015 Intrinsic thermoacoustic instability of premixed flames. *Combustion and Flame* **162** (1), 75–85. (p. 7, 9)
- EVESQUE, S. & POLIFKE, W. 2002 Low-Order Acoustic Modelling for Annular Combustors: Validation and Inclusion of Modal Coupling. *ASME Turbo Expo 2002: Power for Land, Sea, and Air* **1**, 321–331. (p. 10)
- FLEIFIL, M., ANNASWAMY, A. M., GHONEIM, Z. A. & GHONIEM, A. F. 1996 Response of a laminar premixed flame to flow oscillations: A kinematic model and thermoacoustic instability results. *Combustion and Flame* **106** (4), 487–510. (p. 9, 38)
- GARNAUD, X. 2012 Modes, transient dynamics and forced response of circular jets. PhD thesis, École polytechnique. (p. 4, 18, 22, 87, 90)

- GARNAUD, X., LESSHAFFT, L., SCHMID, P. J. & CHOMAZ, J.-M. 2012 A relaxation method for large eigenvalue problems, with an application to flow stability analysis. *Journal of Computational Physics* **231** (10), 3912–3927. (p. 5)
- GHADDAR, N. K., KORCZAK, K. Z., MIKIC, B. B. & PATERA, A. T. 1986 Numerical investigation of incompressible flow in grooved channels. Part 1. Stability and self-sustained oscillations. *Journal of Fluid Mechanics* **163**, 99–127. (p. 4)
- GHIRARDO, G., ČOŠIĆ, B., JUNIPER, M. P. & MOECK, J. P. 2015 State-space realization of a describing function. *Nonlinear Dynamics* pp. 1–20. (p. 10)
- GOLDBERG, D. E. & HOLLAND, J. H. 1988 Genetic Algorithms and Machine Learning. *Machine Learning* **3** (2-3), 95–99. (p. 147)
- GOTTLIEB, S. 2005 On High Order Strong Stability Preserving Runge–Kutta and Multi Step Time Discretizations. *Journal of Scientific Computing* **25** (1), 105–128. (p. 122)
- GRIZZI, S. & CAMUSSI, R. 2012 Wavelet analysis of near-field pressure fluctuations generated by a subsonic jet. *Journal of Fluid Mechanics* **698**, 93–124. (p. 38, 80)
- HACKBUSCH, W. 1985 General Multi-Grid Iteration. In *Multi-Grid Methods and Applications*, Springer Series in Computational Mathematics 4, pp. 80–97. Springer Berlin Heidelberg. (p. 124)
- HAN, X., LI, J. & MORGANS, A. S. 2015 Prediction of combustion instability limit cycle oscillations by combining flame describing function simulations with a thermoacoustic network model. *Combustion and Flame* **162** (10), 3632–3647. (p. 9)
- HANIFI, A., SCHMID, P. J. & HENNINGSON, D. S. 1996 Transient growth in compressible boundary layer flow. *Physics of Fluids (1994-present)* **8** (3), 826–837. (p. 88)
- HAYES, W. D. 1957 The vorticity jump across a gasdynamic discontinuity. *Journal of Fluid Mechanics* **2**, 595–600. (p. 121)
- HERMETH, S., STAFFELBACH, G., GICQUEL, L. Y. M., ANISIMOV, V., CIRIGLIANO, C. & POINSOT, T. 2014 Bistable swirled flames and influence on flame transfer functions. *Combustion and Flame* **161** (1), 184–196. (p. 38)
- HERNANDEZ, V., ROMAN, J. E. & VIDAL, V. 2005 SLEPc: A Scalable and Flexible Toolkit for the Solution of Eigenvalue Problems. *ACM Transactions on Mathematical Software (TOMS)* **31** (3), 351–362. (p. 29)
- HINTON, G. E., OSINDERO, S. & TEH, Y.-W. 2006 A Fast Learning Algorithm for Deep Belief Nets. *Neural Computation* **18** (7), 1527–1554. (p. 147)
- HUERRE, P. & MONKEWITZ, P. A. 1985 Absolute and convective instabilities in free shear layers. *Journal of Fluid Mechanics* **159**, 151–168. (p. xi, 4)
- HUERRE, P. & MONKEWITZ, P. A. 1990 Local and global instabilities in spatially developing flows. *Annual Review of Fluid Mechanics* **22**, 473–537. (p. 4)
- HURLE, I. R., PRICE, R. B., SUGDEN, T. M. & THOMAS, A. 1968 Sound Emission from Open Turbulent Premixed Flames. *Proceedings of the Royal Society of London A: Mathematical, Physical and Engineering Sciences* **303** (1475), 409–427. (p. 110)

- HWANG, Y. & COSSU, C. 2010 Amplification of coherent streaks in the turbulent Couette flow: an input–output analysis at low Reynolds number. *Journal of Fluid Mechanics* **643**, 333–348. (p. 5, 87)
- JINGXUAN, L. & MORGANS, A. S. 2014 Open Source Combustion Instability Low Order Simulator (OSCILOS–Long) Technical report. *Tech. Rep.*. Imperial College. (p. 148)
- JOSEPH, D. D. 1976 Stability of fluid motions. I, II. *NASA STI/Recon Technical Report A* **77**, 12423. (p. 4)
- JOULIN, G. & CLAVIN, P. 1979 Linear stability analysis of nonadiabatic flames: Diffusional-thermal model. *Combustion and Flame* **35**, 139–153. (p. 8, 129)
- KADOWAKI, S. & HASEGAWA, T. 2005 Numerical simulation of dynamics of premixed flames: flame instability and vortex–flame interaction. *Progress in Energy and Combustion Science* **31** (3), 193–241. (p. 12)
- KASKAN, W. E. 1953 An investigation of vibrating flames. *Symposium (International) on Combustion* **4** (1), 575–591. (p. 2)
- KETCHESON, D. I. 2008 Highly Efficient Strong Stability-Preserving Runge–Kutta Methods with Low-Storage Implementations. *SIAM Journal on Scientific Computing* **30** (4), 2113–2136. (p. 25)
- KIDIN, N., LIBROVICH, V., ROBERTS, J. & VUILLERMOZ, M. 1984 On Sound Sources in Turbulent Combustion. *Progress in Astronautics and Aeronautics, AIAA* **95**, 343–355. (p. 9, 10, 110)
- KIDIN, N. I. & LIBROVICH, V. B. 1983 Sound radiation mechanism in a turbulent gas flame. *Combustion, Explosion and Shock Waves* **19** (4), 380–383. (p. 6, 110)
- KLEBANOFF, P. S., TIDSTROM, K. D. & SARGENT, L. M. 1962 The three-dimensional nature of boundary-layer instability. *Journal of Fluid Mechanics* **12** (01), 1–34. (p. 4)
- KONSTANTINIDIS, E. & COTRONIS, Y. 2013 Graphics processing unit acceleration of the red/black SOR method. *Concurrency and Computation: Practice and Experience* **25** (8), 1107–1120. (p. 127)
- KOUMOUTSAKOS, P., LEONARD, A. & PÉPIN, F. 1994 Boundary Conditions for Viscous Vortex Methods. *Journal of Computational Physics* **113** (1), 52–61. (p. 119)
- KREDIET, H. J., BECK, C. H., KREBS, W., SCHIMEK, S., PASCHEREIT, C. O. & KOK, J. B. W. 2012 Identification of the Flame Describing Function of a Premixed Swirl Flame from LES. *Combustion Science and Technology* **184** (7-8), 888–900. (p. 9)
- LANDAU, L. D. 1944 On the theory of slow combustion. *Acta Physicochimica URSS* **19**, 77–85. (p. 7)
- LEFEBVRE, A. H. 1998 *Gas Turbine Combustion, Second Edition*. CRC Press. (p. 1)
- LEWIS, B. & ELBE, G. v. 2012 *Combustion, Flames and Explosions of Gases*. Elsevier. (p. 1)

- LI, L. K. B. & JUNIPER, M. P. 2013 Lock-in and quasiperiodicity in a forced hydrodynamically self-excited jet. *Journal of Fluid Mechanics* **726**, 624–655. (p. 141, 147)
- LIEUWEN, T. C. & YANG, V., ed. 2005 *Combustion instabilities in gas turbines, Operational experience, Fundamental mechanisms, and Modeling, Progress in Astronautics and Aeronautics*, vol. 210. American Institute of Aeronautics and Astronautics, Inc. (p. 2)
- LIGHTHILL, M. J. 1952 On Sound Generated Aerodynamically. I. General Theory. *Proceedings of the Royal Society of London A: Mathematical, Physical and Engineering Sciences* **211** (1107), 564–587. (p. 3, 6)
- LJUNG, L. 1987 System Identification: Theory for the user. *PTR Prentice Hall Information and System Sciences Series* **198**. (p. 131)
- LUZZATO, C. M., ASSIER, R., MORGANS, A. & WU, X. 2013 Modelling thermo-acoustic instabilities of an anchored laminar flame in a simple lean premixed combustor: including hydrodynamic effects. In *19th AIAA/CEAS Aeroacoustics Conference*. American Institute of Aeronautics and Astronautics. (p. 10, 38, 115)
- MANTIČ-LUGO, V., ARRATIA, C. & GALLAIRE, F. 2014 Self-Consistent Mean Flow Description of the Nonlinear Saturation of the Vortex Shedding in the Cylinder Wake. *Physical Review Letters* **113** (8), 084501. (p. 5)
- MARKSTEIN, G. H. 1964 *Nonsteady flame propagation*. Pergamon. (p. 7, 9, 10, 115)
- MARQUET, O., SIPP, D. & JACQUIN, L. 2008 Sensitivity analysis and passive control of cylinder flow. *Journal of Fluid Mechanics* **615**, 221–252. (p. 28)
- MATALON, M., CUI, C. & BECHTOLD, J. K. 2003 Hydrodynamic theory of premixed flames: effects of stoichiometry, variable transport coefficients and arbitrary reaction orders. *Journal of Fluid Mechanics* **487**, 179–210. (p. 120, 121)
- MATALON, M. & MATKOWSKY, B. J. 1982 Flames as gasdynamic discontinuities. *Journal of Fluid Mechanics* **124**, 239–259. (p. 7, 120)
- MERK, H. J. 1956 Sixth Symposium (International) on Combustion. *The Combustion Institute, Pittsburgh* pp. 500–512. (p. 9)
- MICHALKE, A. 1984 Survey on jet instability theory. *Progress in Aerospace Sciences* **21**, 159–199. (p. 4)
- MIGUEL ÁNGEL FOSAS DE PANDO 2012 Génération d’ondes acoustiques à fréquences discrètes autour d’un profil d’aile : analyse de stabilité globale. PhD thesis, École polytechnique. (p. 6)
- MONKEWITZ, P. A. & SOHN, K. 1988 Absolute instability in hot jets. *AIAA Journal* **26** (8), 911–916. (p. 4)
- MONOKROUSOS, A., ÅKERVIK, E., BRANDT, L. & HENNINGSON, D. S. 2010 Global three-dimensional optimal disturbances in the Blasius boundary-layer flow using time-steppers. *Journal of Fluid Mechanics* **650**, 181–214. (p. 90)
- MORGANS, A. S. & STOW, S. R. 2007 Model-based control of combustion instabilities in annular combustors. *Combustion and Flame* **150** (4), 380–399. (p. 8)

- MUELLER, C. J., DRISCOLL, J. F., REUSS, D. L., DRAKE, M. C. & ROSALIK, M. E. 1998 Vorticity generation and attenuation as vortices convect through a premixed flame. *Combustion and Flame* **112** (3), 342–358. (p. 12)
- NATHAN, G. J., MI, J., ALWAHABI, Z. T., NEWBOLD, G. J. R. & NOBES, D. S. 2006 Impacts of a jet's exit flow pattern on mixing and combustion performance. *Progress in Energy and Combustion Science* **32** (5–6), 496–538. (p. 1)
- NICHOLS, J. W. & SCHMID, P. J. 2008 The effect of a lifted flame on the stability of round fuel jets. *Journal of Fluid Mechanics* **609**, 275–284. (p. 7)
- NICOUD, F., BENOIT, L., SENSIAU, C. & POINSOT, T. 2007 Acoustic Modes in Combustors with Complex Impedances and Multidimensional Active Flames. *AIAA Journal* **45** (2), 426–441. (p. 8, 37)
- NICOUD, F. & POINSOT, T. 2005 Thermoacoustic instabilities: Should the Rayleigh criterion be extended to include entropy changes? *Combustion and Flame* **142** (1–2), 153–159. (p. 3)
- NISHIOKA, M. & MORKOVIN, M. V. 1986 Boundary-layer receptivity to unsteady pressure gradients: experiments and overview. *Journal of Fluid Mechanics* **171**, 219–261. (p. 6)
- NOIRAY, N., DUROX, D., SCHULLER, T. & CANDEL, S. 2008 A unified framework for nonlinear combustion instability analysis based on the flame describing function. *Journal of Fluid Mechanics* **615**, 139–167. (p. 8, 9)
- NOIRAY, N. & SCHUERMANS, B. 2013 Deterministic quantities characterizing noise driven Hopf bifurcations in gas turbine combustors. *International Journal of Non-Linear Mechanics* **50**, 152–163. (p. 141, 147)
- NORUM, T. D. 1983 Screech suppression in supersonic jets. *AIAA Journal* **21** (2), 235–240. (p. 6)
- ORR, W. M. F. 1907 The stability or instability of the steady motions of a perfect liquid and of a viscous liquid. Part II: A viscous liquid. In *Proceedings of the Royal Irish Academy. Section A: Mathematical and Physical Sciences*, pp. 69–138. Hodges, Figgis, & Co. (p. 90)
- PALIES, P., DUROX, D., SCHULLER, T. & CANDEL, S. 2010 The combined dynamics of swirler and turbulent premixed swirling flames. *Combustion and Flame* **157** (9), 1698–1717. (p. 8, 9)
- PALIES, P., DUROX, D., SCHULLER, T. & CANDEL, S. 2011 Nonlinear combustion instabilities analysis based on the Flame Describing Function applied to turbulent premixed swirling flames. *Combustion and Flame* **158**, 1980–1991. (p. 8)
- PAN, K.-L. & FURSENKO, R. 2008 Characteristics of cylindrical flame acceleration in outward expansion. *Physics of Fluids* **20** (9), 094107. (p. 115)
- FOSAS DE PANDO, M., SIPP, D. & SCHMID, P. J. 2012 Efficient evaluation of the direct and adjoint linearized dynamics from compressible flow solvers. *Journal of Computational Physics* **231** (23), 7739–7755. (p. 23, 28)

- PARLIAMENT, E. & OF THE EUROPEAN UNION, C. 2007 Regulation (EC) No 715/2007 of the European Parliament and of the Council. (p. 1)
- PASCHEREIT, C. O., SCHUERMANS, B., POLIFKE, W. & MATTSON, O. 2002 Measurement of transfer matrices and source terms of premixed flames. *Journal of Engineering for Gas Turbine and Power* **124**, 239–247. (p. 8, 37)
- PELCE, P. & CLAVIN, P. 1982 Influence of hydrodynamics and diffusion upon the stability limits of laminar premixed flames. *Journal of Fluid Mechanics* **124**, 219–237. (p. 7, 8)
- PETERS, N. 2000 *Turbulent combustion*. Cambridge University Press. (p. 116)
- PETERSEN, R. E. & EMMONS, H. W. 1961 Stability of Laminar Flames. *Physics of Fluids (1958-1988)* **4** (4), 456–464. (p. 10)
- PIANA, J., VEYNANTE, D., CANDEL, S. & POINSOT, T. 1997 Direct Numerical Simulation Analysis of The G-Equation in Premixed Combustion. In *Direct and Large-Eddy Simulation II* (ed. Jean-Pierre Chollet, Peter R. Voke & Leonhard Kleiser), *ERCOTAC Series* 5, pp. 321–330. Springer Netherlands. (p. 8, 10, 115)
- PIERCE, A. D. 1989 *Acoustics: An Introduction to Its Physical Principles and Applications*. Melville, NY: Acoustical Society of America. (p. 38)
- PLOUMHANS, P. & WINCKELMANS, G. S. 2000 Vortex Methods for High-Resolution Simulations of Viscous Flow Past Bluff Bodies of General Geometry. *Journal of Computational Physics* **165** (2), 354–406. (p. 119)
- POINSOT, T. 2014 Control and simulation of thermoacoustic instabilities. *Bulletin of the American Physical Society* **59**. (p. 37)
- POINSOT, T. & VEYNANTE, D. 2012 *Theoretical And Numerical Combustion - Third Edition*. R.T. Edwards, Inc. (p. 1, 2, 8, 9, 17, 19, 88, 117)
- POINSOT, T. J. & LELE, S. K. 1992 Boundary conditions for direct simulations of compressible viscous flows. *Journal of Computational Physics* **101** (1), 104–129. (p. 33)
- POLIFKE, W., PONCET, A., PASCHEREIT, C. O. & DÖBBELING, K. 2001 Reconstruction of Acoustic Transfer Matrices by Instationary Computational Fluid Dynamics. *Journal of Sound and Vibration* **245** (3), 483–510. (p. 9)
- POWELL, A. 1953 On the Mechanism of Choked Jet Noise. *Proceedings of the Physical Society. Section B* **66** (12), 1039. (p. 6)
- POWELL, A. 1964 Theory of Vortex Sound. *The Journal of the Acoustical Society of America* **36** (1), 177–195. (p. 111)
- PREETHAM, HEMCHANDRA, S. & LIEUWEN, T. 2008 Dynamics of laminar premixed flames forced by harmonic velocity disturbances. *Journal of Propulsion and Power* **24** (6), 1390–1402. (p. 128)
- QADRI, U. A. 2014 Global stability and control of swirling jets and flames. PhD thesis, University of Cambridge. (p. 7, 38)

- RAYLEIGH, J. W. S. 1878 The explanation of certain acoustical phenomena. *Nature* **18** (455), 319–321. (p. 3)
- RENARD, P. H., THÉVENIN, D., ROLON, J. C. & CANDEL, S. 2000 Dynamics of flame-vortex interactions. *Progress in Energy and Combustion Science* **26** (3), 225–282. (p. 12)
- REUTHER, J. J., JAMESON, A., ALONSO, J. J., RIMLLINGER, M. J. & SAUNDERS, D. 1999 Constrained Multipoint Aerodynamic Shape Optimization Using an Adjoint Formulation and Parallel Computers, Part 2. *Journal of Aircraft* **36** (1), 61–74. (p. 5, 87)
- RIJKE, P. L. 1859 On the vibration of the air in a tube open at both ends. *The London, Edinburgh and Dublin Philosophical Magazine and Journal of Science* **17**, 419–422. (p. 2)
- SANDBERG, R. D. 2007 Governing equations for a new compressible Navier-Stokes solver in general cylindrical coordinates. Monograph AFM-07/07. School of Engineering Sciences, University of Southampton. (p. 18, 19)
- SATTELMAYER, T. & POLIFKE, W. 2003 Assessment of methods for the computation of the linear stability of combustors. *Combustion Science and Technology* **175** (3), 453–476. (p. 9)
- SCHIMEK, S., MOECK, J. P. & PASCHEREIT, C. O. 2011 An Experimental Investigation of the Nonlinear Response of an Atmospheric Swirl-Stabilized Premixed Flame. *Journal of Engineering for Gas Turbines and Power* **133** (10), 101502–101502. (p. 9)
- SCHLIMPERT, S., HEMCHANDRA, S., MEINKE, M. & SCHRÖDER, W. 2015 Hydrodynamic instability and shear layer effect on the response of an acoustically excited laminar premixed flame. *Combustion and Flame* **162** (2), 345–367. (p. 131)
- SCHMID, P. J. 2008 *Mécanique des fluides numériques*. École Polytechnique Éditions. (p. 127)
- SCHMID, P. J. & HENNINGSON, D. S. 2001 *Stability and Transition in Shear Flows*. Springer Science & Business Media. (p. 4, 87)
- SCHULLER, T., DUCRUIX, S., DUROX, D. & CANDEL, S. 2002a Modeling tools for the prediction of premixed flame transfer functions. *Proceedings of the Combustion Institute* **29** (1), 107–113. (p. 115, 128)
- SCHULLER, T., DUROX, D. & CANDEL, S. 2002b Dynamics of and noise radiated by a perturbed impinging premixed jet flame. *Combustion and Flame* **128** (1–2), 88–110. (p. 10)
- SCHULLER, T., DUROX, D. & CANDEL, S. 2003a Self-induced combustion oscillations of laminar premixed flames stabilized on annular burners. *Combustion and Flame* **135** (4), 525–537. (p. xi, 10, 14, 15, 33, 93)
- SCHULLER, T., DUROX, D. & CANDEL, S. 2003b A unified model for the prediction of laminar flame transfer functions: comparisons between conical and V-flame dynamics. *Combustion and Flame* **134** (1–2), 21–34. (p. 14, 127)

- SELLE, L., LARTIGUE, G., POINSOT, T., KOCH, R., SCHILDMACHER, K.-U., KREBS, W., PRADE, B., KAUFMANN, P. & VEYNANTE, D. 2004 Compressible large eddy simulation of turbulent combustion in complex geometry on unstructured meshes. *Combustion and Flame* **137** (4), 489–505. (p. 37)
- SETHIAN, J. A. 1999 *Level set methods and fast marching methods: evolving interfaces in computational geometry, fluid mechanics, computer vision, and materials science*, vol. 3. Cambridge University Press. (p. 116)
- SILVA, C. F., NICOUD, F., SCHULLER, T., DUROX, D. & CANDEL, S. 2013 Combining a Helmholtz solver with the flame describing function to assess combustion instability in a premixed swirled combustor. *Combustion and Flame* **160** (9), 1743–1754. (p. 8)
- SIPP, D. & LEBEDEV, A. 2007 Global stability of base and mean flows: a general approach and its applications to cylinder and open cavity flows. *Journal of Fluid Mechanics* **593**, 333–358. (p. 5)
- STOER, J. & BULIRSCH, R. 2002 *Introduction to Numerical Analysis*. Springer. (p. 122, 124)
- STRAHLE, W. 1978 Combustion noise. *Progress in Energy and Combustion Science* **4**, 157–176. (p. 87)
- STRAHLE, W. C. 1971 On combustion generated noise. *Journal of Fluid Mechanics* **49** (02), 399–414. (p. 3, 9, 14, 96)
- SYRED, N. 2006 A review of oscillation mechanisms and the role of the precessing vortex core (PVC) in swirl combustion systems. *Progress in Energy and Combustion Science* **32** (2), 93–161. (p. 147)
- TALEI, M., HAWKES, E. R. & BREAR, M. J. 2013 A direct numerical simulation study of frequency and Lewis number effects on sound generation by two-dimensional forced laminar premixed flames. *Proceedings of the Combustion Institute* **34** (1), 1093–1100. (p. xi, 10, 13)
- TAM, C. K., AURIAULT, L. & CAMBULI, F. 1998 Perfectly Matched Layer as an Absorbing Boundary Condition for the Linearized Euler Equations in Open and Ducted Domains. *Journal of Computational Physics* **144** (1), 213–234. (p. 33)
- TAY-WO-CHONG, L. 2012 Numerical Simulation of the Dynamics of Turbulent Swirling Flames. PhD thesis, Technische Universität München, Garching, Germany. (p. 9, 131)
- TAY-WO-CHONG, L., KOMAREK, T., KAESS, R., FOLLER, S. & POLIFKE, W. 2010 Identification of Flame Transfer Functions From LES of a Premixed Swirl Burner. *Proceedings of ASME Turbo Expo 2010* pp. 623–635. (p. 37)
- TERHAAR, S., REICHEL, T. G., SCHRÖDINGER, C., RUKES, L., PASCHEREIT, C. O. & OBERLEITNER, K. 2013 Vortex Breakdown and Global Modes in Swirling Combustor Flows With Axial Air Injection. *AIAA Paper* **0** (0748-4658). (p. 147)
- TREFETHEN, L. N., TREFETHEN, A. E., REDDY, S. C. & DRISCOLL, T. A. 1993 Hydrodynamic Stability Without Eigenvalues. *Science* **261** (5121), 578–584. (p. 5)

- TRUFFAUT, J.-M., SEARBY, G. & BOYER, L. 1998 Sound emission by non-isomolar combustion at low Mach numbers. *Combustion Theory and Modelling* **2** (4), 423–428. (p. 6)
- VAGELOPOULOS, C. M., EGOLFOPOULOS, F. N. & LAW, C. K. 1994 Further considerations on the determination of laminar flame speeds with the counterflow twin-flame technique. *Symposium (International) on Combustion* **25** (1), 1341–1347. (p. 129)
- VENUGOPAL, R. & BERNSTEIN, D. 2000 Adaptive disturbance rejection using AR-MARKOV/Toeplitz models. *IEEE Transactions on Control Systems Technology* **8** (2), 257–269. (p. 136)
- WAUGH, I., ILLINGWORTH, S. & JUNIPER, M. 2013 Matrix-free continuation of limit cycles for bifurcation analysis of large thermoacoustic systems. *Journal of Computational Physics* **240**, 225–247. (p. 38)
- WILLIAMS, F. 1985a Turbulent Combustion. In *The Mathematics of Combustion*, , vol. 2, pp. 267–294. SIAM. (p. 1)
- WILLIAMS, G. 1985b *Combustion Theory*. Addison-Wesley. (p. 2)
- WORTH, N. A. & DAWSON, J. R. 2013 Self-excited circumferential instabilities in a model annular gas turbine combustor: Global flame dynamics. *Proceedings of the Combustion Institute* **34** (2), 3127–3134. (p. 10)
- YAVNEH, I. 1996 On Red-Black SOR Smoothing in Multigrid. *SIAM Journal on Scientific Computing* **17** (1), 180–192. (p. 127)
- YUAN, T., DUROX, D. & VILLERMAUX, E. 1994 An analogue study for flame flickering. *Experiments in Fluids* **17** (5), 337–349. (p. 8, 139)
- ZELDOVICH, I. A., BARENBLATT, G. I., LIBROVICH, V. B. & MAKHVILADZE, G. M. 1985 *Mathematical theory of combustion and explosions*. Consultants Bureau, New York, NY. (p. 1, 2, 5, 7, 8, 38)

